UNIVERSITAT DE BARCELONA

Structure versus Magnetism in Magnetic Nanoparticles

Carlos Moya Álvarez

Programa de Doctorat en Nanociències

Structure versus Magnetism in Magnetic Nanoparticles

Tesi que presenta en **Carlos Moya Álvarez**

per optar al títol de Doctor per la Universitat de Barcelona

Director de la Tesi:

Dr Amílcar Labarta Rodríguez

Grup de Nanomaterials Magnètics

Departament de Física Fonamental

Institut de Nanociència i Nanotecnologia (IN^{2}UB)

Universitat de Barcelona

UNIVERSITAT DE BARCELONA

CONTENTS

Chapter 1.Introduction

1.1. Magnetic nanoparticles

1.1.1. Overview

Magnetic materials in the nanometre scale exhibit fascinating properties when they are compare with their bulk-counterparts such as giant magnetoresistance,[1-5] superparamagnetism,[6,7] large coercitivities and quantum tunnelling of the magnetization,[8,9] which are due to finite-size and surface effects together with collective phenomena arising from interparticle interactions.[1] In addition and because of the unique combination of small size and exotic properties, magnetic nanoparticles (NPs) can be used for technological applications such as data recording, magnetic sealing in motors, magnetic inks for bank checks, magneto-optical and biotechnology applications.[10,11] Within these fields, magnetic storage has played a key role in audio, video and computer development.[12] Since IBM built the first magnetic hard disk drive in 1956, featuring a total storage capacity of 5 MB at a recording density of 2 kbit/in^{-2}, the density area has increased more than 20 million-fold in modern disk drives and currently doubles every year (see Figure 1).[13] However, one of the most significant drawbacks of using magnetic NPs in storage data is the thermal effect limit that determines the minimum size of a magnetic element and is known as superparamagnetism. Currently, there are experimental approaches to overcome those effects of the thermal fluctuations on the stability of the particle magnetization. For example, the synthesis of materials with high magnetic anisotropy consequence of their specific shape or crystal structure such as needle-like FeCo nanoparticulate and metallic alloys of about 100 x 15 nm or FePt alloys that crystallize in the tetragonal phase.[14]

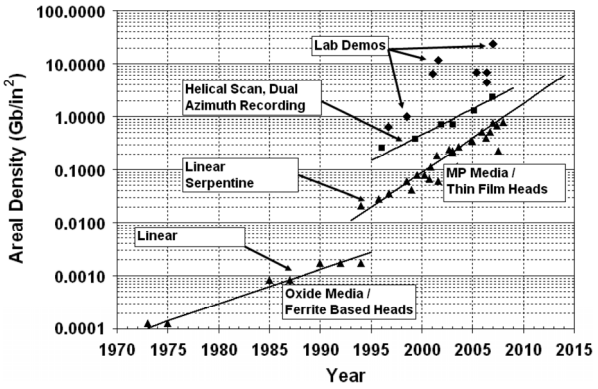

Figure 1. Areal density of magnetic disk storage *versus* year of IBM product introduction.

Another application in which the use of magnetic NPs is relevant is in magneto-optics such as transparent magnetic materials, which could potentially be used as sensors based on the Faraday effect. For instance, γ-Fe_2O_3 NPs embedded in transparent matrices such as transparent polymers, sol gel derived silica or Vycor glasses are examples of this kind of magneto-optical materials.[10,15] However, where magnetic NPs offer very attractive possibilities is for applications in biotechnology since their dimensions are comparable to the biological elements (see Figure 2), they are easily manipulated by an external magnetic field gradient and they have a large surface which can be properly modified to attach biological agents.[16-20] Special interest deserves the use of colloids based on magnetic NPs as contrast enhancement agents in magnetic resonance imaging (MRI).[21-23] Because of their larger magnetic moment in comparison to paramagnetic ions, particulate contrast agents produce enhanced relaxation rates of the spin of the proton in the hydrogen atoms of the water molecule at significantly lower doses.[24,25] Finally, magnetic nanoparticles exposed to an alternating magnetic field might act as localized heat sources at certain target regions inside the human body for cancer therapy (hyperthermia).[26-28]

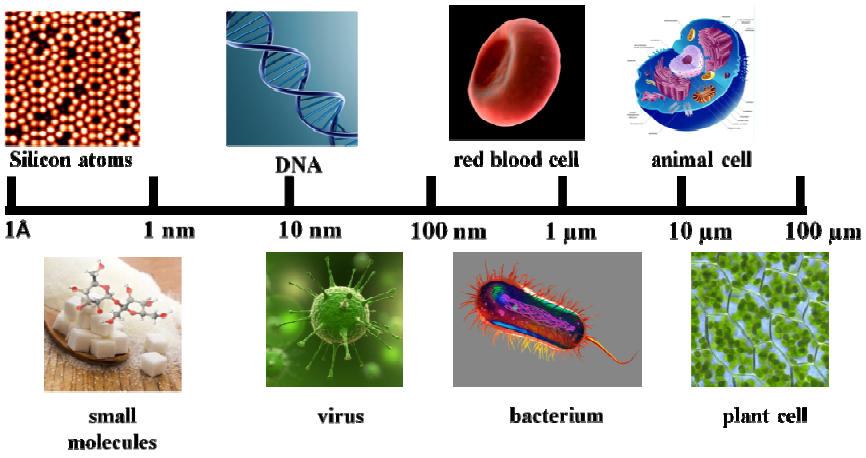

Figure 2. Artistic representations of different biological elements ranging from 1Å to 100 µm. Magnetic NPs are in the same scale of size that DNA or viruses.

1.1.2. Ferrite nanoparticles with composition MFe_2O_4 (M= Co,Fe)

MFe_2O_4 NPs are among the frequently chosen systems for studies of nanomagnetism and they are ideal candidates in technological applications.[16-32] This is due to the large variability of the magnetic properties of MFe_2O_4 with a simple change in the chemical identity of the

M^{2+} ion, together with the easy production by chemical and/or physical routes. [33-42] For example, because of the high saturation magnetization at room temperature, and low magnetic anisotropy and biocompatibility (see Table 1), magnetite ($Fe_{3-x}O_4$) particles have been used widely, not only as ferrofluids in sealing position sensing but also as promising candidates for applications in biomedicine such as drug delivery, MRI contrast agent, hyperthermia and separation agents.[16-32] Other remarkable nanomaterials are Co-ferrite ($Co_xFe_{3-x}O_4$) NPs, having high values of magnetic anisotropy induced for a variation in the electronic density, and the existence of defects and vacancies in the crystal structure (see Table 1), which make them potential candidates for future highly sensitive magnetic nanodevices.[43,44]

Compound name	Magnetite	Cobalt ferrite
Crystal structure	Cubic	Cubic
Formula units per unit cell, Z	8	8
Spatial group	Fd3m	Fd3m
Density (g cm^{-3})	5.24	5.29
Colour	black	black
Type of magnetism	Ferrimagnetism	Ferrimagnetism
Curie Temperature (°C)	585	520
Ms at 5 K (emu/g)	98	92
Ms at 300 K (emu/g)	92	80
Anisotropy constant (erg cm^{-3})	$1.1 \cdot 10^5$	$20.0 \cdot 10^5$

Table1. Summary of magnetic and structural properties of Fe_3O_4 and $CoFe_2O_4$.

1.1.3. Structural and magnetic properties

Typically, the crystal structure of ferrites is an inverse spinel where oxygen atoms form an fcc close packing structure and M^{2+} and Fe^{3+} occupy either tetrahedral or octahedral interstitial sites.[43-45] The distribution of the ions in the unit cell is as follows: 32 O^{2-} ions form the structure and 16 Fe^{3+} are distributed the same way in tetrahedral and octahedral sites, and 8 M^{2+} occupy entirely octahedral sites ($(A_8)(B_8A_8)O_{32} = A(AB)O_4$). Figure 3 shows a scheme of the structure where two types of cubic building units are inside of an fcc Fe^{2+}/Co^{2+} lattice filling all 8 octants.

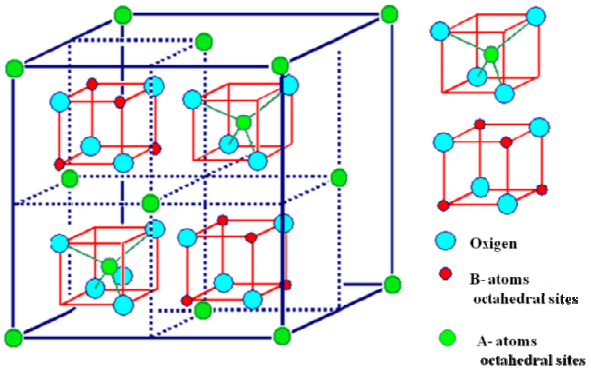

Figure 3. Representation of a spinel structure; two types of cubic building units are filling in a fcc lattice built up by part of the tetrahedral sites.

It is well known that the ferrimagnetic behaviour of an spinel is intrinsically related to the alignment of the cation spins and their environment. Therefore, the total magnetic moment will depend on the electronic configuration, the environment of each cation and the coupling between cations.[43,44] The crystal field theory (CFT) explains satisfactorily the spin configuration of metals with *d* orbitals.[46,47] In tetrahedral sites, the energy of e_g levels are lower than the t_{2g} levels because of the direct electrostatic repulsion between the d_{xy}, d_{yz} and d_{zx} orbitals and the surrounding anion orbitals. However, the order is reversed in the octahedral environment as the d_z^2 and $d_{x^2-y^2}$ orbitals are directly repelled. In this case, the electronic configuration depends on the relative strength of the CFT and the intra-atomic exchange field (EF).

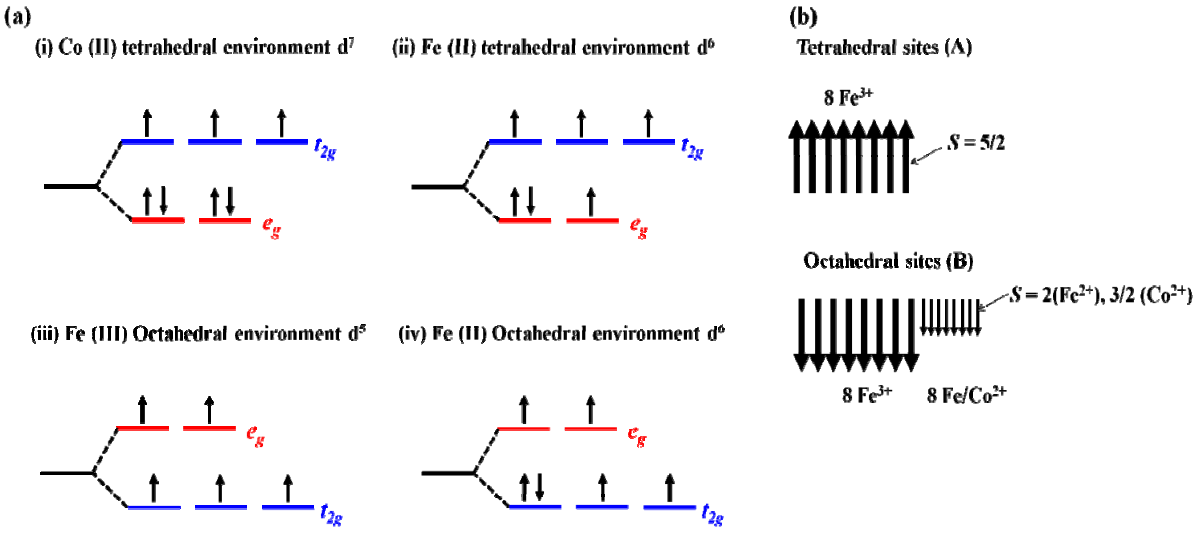

Figure 4. (a) Electronic configuration for the $Co^{2+}/Fe^{2+}/Fe^{3+}$. (b) Schematic representation of the orientation of the magnetic moments for the different types of ions per unit cell.

Therefore, taking into account the ion environment (see Figure 4a), the magnetic moment of each ion (see Figure 4b) and the amount of ions in a unit cell (see Figure 3), the magnetic moment per unit cell for MFe_2O_4 with M=Co, Fe can be calculated as $\left|m_{CoFe_2O_4}\right| = 8m_{Fe^{3+}_{(tet)}} - 8m_{Fe^{3+}_{(oct)}} - 8m_{Co^{2+}_{(oct)}} = 24\mu_B$ and $\left|m_{Fe_3O_4}\right| = 8m_{Fe^{3+}_{(tet)}} - 8m_{Fe^{3+}_{(oct)}} - 8m_{Fe^{2+}_{(oct)}} = 32\mu_B$, where μ_B is the Bohr magneton.[43,44,48]

1.1.4. Synthesis method: high-temperature decomposition of organo-metallic precursors

The background of this approach to prepare iron oxide NPs relies on the synthesis of quantum dots that was applied for transition metals for the first time by Rockenberger et al.[43] It is based on the pyrolysis of metal-fatty acid salts in organic media in the presence of different surfactants. The most widely used metallorganic precursors for the synthesis of MFe_2O_4 (M= Co,Fe) NPs are $Fe(Cup)_3$, $Fe(CO)_5$, $Fe(oleate)_3$, $Fe(acac)_3$, $Co(acac)_2$ and $Co(acac)_3$; using 1-octadecennne, phenil-ether, benzyl-ether among others as organic media, and oleic and decanoid acids, oleylamine and 1,2-hexadecanediol as surfactants (see Figure 5).[33-42]

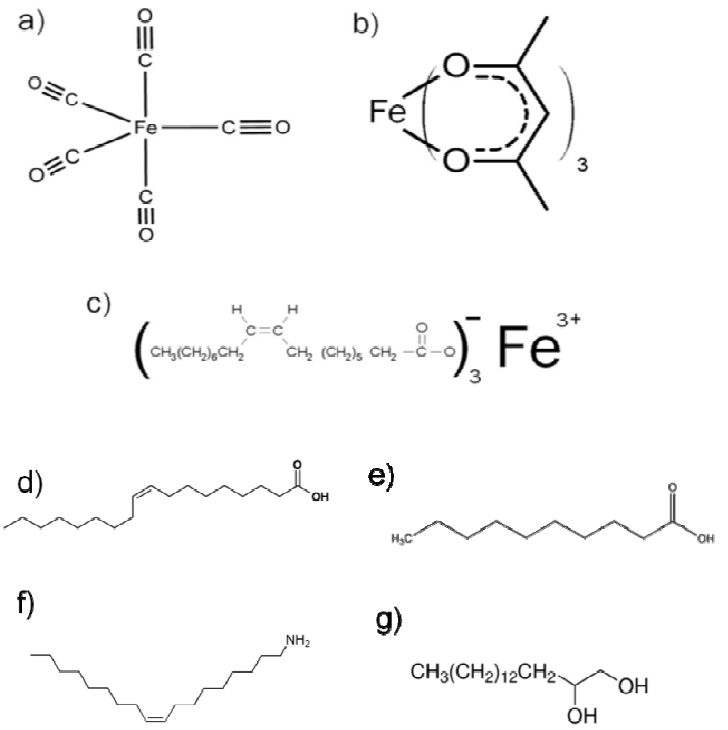

Figure 5. Chemical structure of the most widely used reactants in the synthesis of iron oxide NPs. a)-c) Several iron metallorganic precursors; a) iron pentacarbonyl, b) iron acetylacetonate (III) and c) iron oleate. d)-g) Surfactants; d) oleic acid, e) decanoic acid, f) oleylamine, g) 1,2-hexadecanediol.

This preparation method allows tuning the NP structure by the simple modification of the reaction conditions such as the concentration of the reactants,[49] the solvent used,[42] the reaction heat rate[50] or the reaction time.[51] For instance, Figure 6 shows Fe_3O_4 NPs synthesized in a wide range of sizes by solely changing the concentration of the fatty acid (decanoic acid) in the reaction mixture.[49]

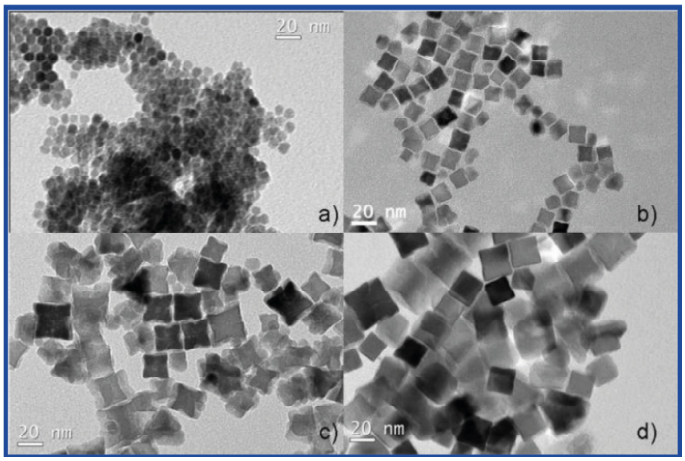

Figure 6. Fe_3O_4 NPs with a wide size-range obtained by using different concentrations of decanoic acid in the reaction mixture. (a) 6 mmol. (b) 5 mmol. (c) 4 mmol. (d) 3 mmol.

The experimental set-up is of key importance in this kind of synthesis method,[33-42] since to achieve NPs with well-controlled structural and magnetic properties some requirements must be fulfilled, including a monitored atmosphere and a suitable flask where the reaction mixture can be heated at constant stirring. We have developed a simple and economical set-up with the aim to obtain monodisperse and highly crystalline NPs (see Figure 7).[52] The main parts of the experimental set-up are as follows:

(a) Reaction flask: The reaction takes place in a flask having three necks (see Figure 7 (1,2)). The first one is used to introduce a thermocouple to monitor the temperature of the reaction mixture in a continuous mode. The second one is an inlet for nitrogen gas in order to keep the reaction mixture in an inert and controlled atmosphere. The third one is connected to the reflux tube so that the condensate returns again to the reaction chamber.

(b) Temperature controller: This device, which is connected to a heating mantle, is responsible of the control of the reaction temperature at all times (see Figure 7 (3)).

(c) Heating mantle: It supplies heat to the reaction mixture (see Figure 7 (4)).

(d) Magnetic stirring: The stirring of the reaction mixture is controlled by varying the rotation speed of the magnetic bar (see Figure 7 (5)).

(e) Thermocouple: It is a transducer formed by the union of two different metals that produces a voltage which is a function of the temperature difference between one junction, a "hot spot" and the other, a "cold spot" (reference junction) (see Figure 7 (6)). In our set-up, it is a type K thermocouple that monitors the temperature of the reaction mixture.

(f) Pipes: The control of the atmosphere is crucial to avoid unwanted reactions. For this purpose, the experimental set-up is connected through two pipes to a vacuum pump (to remove oxygen and other gases) and to a nitrogen bottle (to replace the atmosphere of the reaction flask with an inert gas), respectively (see Figure 7 (7,8)).

(g) Reflux tube: This part of the set-up is used for preventing the evaporation of the reactants and solvent of the reaction mixture at high temperatures. A continuous flow of cold water surrounding the reflux tube condenses the emitted vapours in order to reintroduce the condensate in the reaction flask (see Figure 7 (9)).

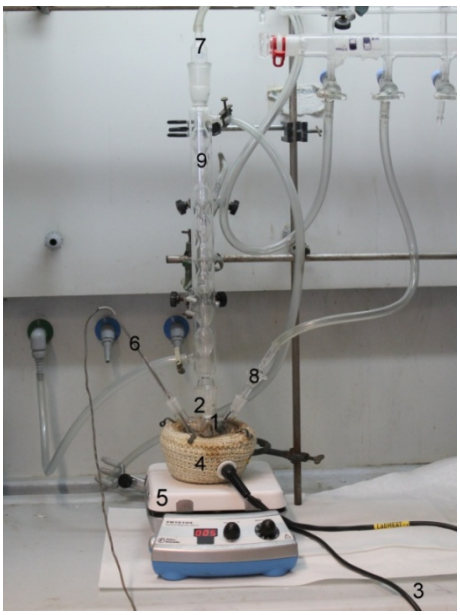

Figure 7. Experimental set-up for the synthesis of NPs. (1,2) Reaction flask of three necks made of resistant glassware. (3) Temperature controller connected to a heating mantle. (4), (5) Magnetic stirring. (6) Thermocouple. (7) Outlet for vacuum pumping. (8) Inlet for nitrogen gas. (9) Reflux tube.

1.1.5. Stabilization of the NPs in aqueous media

The stabilization of magnetic NPs in aqueous media is crucial to obtain magnetic colloidal ferrofluids that are stable against aggregation in a biological medium and under the action of external magnetic fields.[16-20] Unfortunately, NPs synthesized by the organic decomposition method are hydrophobic due to the coating with fatty acids used in the reaction.[33-42,49-51] Therefore, NPs must be coated with hydrophilic either organic or inorganic compounds making them compatible with aqueous media. Generally, there are two strategies to functionalize NPs by means of organic (Tables 2) or inorganic compounds (see Tables 2 and 3).[37,38]

Type	Method used	Examples
bifunctional molecules	ligand exchange	DMSA, SILAN-PEG, Phosphonates, dopamine Mecacpto-11undecanoic, 2-Brom, 2-metilpropionic, Dendrimers, TMAOH
Double bond of the oleic acid	oxidation and break	ozone, potasium permanganate
Polymers	collating	pluronic F-127, PMMA-PEO, PAA+-Octolamine, PEI, ciclodextrines
	ligand exchange	PAA-PAH, PNIPAm-b-PNIPAm, HOOC-PEG-COOH
	Synthesis of NPs in presence of a polymer	HOOC-PEG-COOH, Polyestirenes, norborane
	polymerization in presence of NPs	2-brompropionilester
Liposomes	formation of miscelles	PEG-PE+PC

Table 2. Routes to transfer hydrophobic NPs to water by organic coatings.

Type	Method used	Examples
Silica	ligand exchange	Silsesquioxane, APS
	Sol-gel process	TEOS
	Microemulsions	Ciclohexane/IGEPAL/TEOS/ammonia
Quantum dots	heterogeneous nucleation	CdSe
Gold	heterogeneous nucleation	$Au(acac)_2$, Au metallic
		PAA+-Octolamine, PEI, ciclodextrines
	salt reduction	$HAuCl_4$
	bifunctional molecule	$HS(CH_2)_{19}COOH$

Table 3. Routes to transfer hydrophobic NPs to water by inorganic coatings.

In this work, NPs have coated by silica (microemulsion method) and dimercaptosuccinic acid -DMSA- (ligand exchange) to stabilize them in water, since they are simple methods, highly reproducible and relatively economical.

(a) Microemulsion method: It is based on the encapsulation of magnetic NPs at the interface of a microemulsion formed by water droplets in oil phases.[53-55] Figure 8 summarizes the reaction mechanism that takes place at the water-oil interface. First, the hydrolysis of the silica precursor (TEOS) occurs at the micelles' surface. Then, the hydrolysed TEOS initiates the coating process in contact with a magnetic nanoparticle. Once the particle is completely coated with silica, it is incorporated inside the vesicle. Moreover, depending on the reaction conditions (relative amount of aqueous components, amount of particles in the oil phase and the time elapsed) the size and the shape of the particles can be tuned.

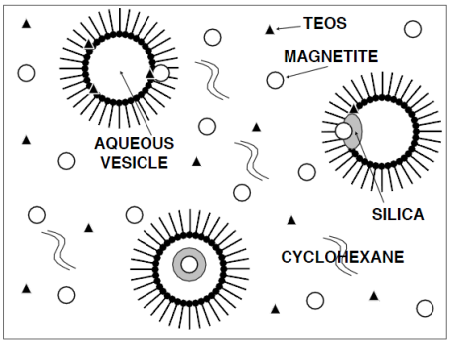

Figure 8. Schematic representation of the coating process of magnetic NPs by the microemulsion method.

(b) Ligand exchange: In this method, DMSA molecules exchange with the fatty acid molecules linked on the particle surface by electronic affinity. As can be seen in Figure 9, the carboxylate groups (COO-) are 'anchoring chemical-groups' that bind to particle surface. Besides, the thiol groups (SH) stabilize the NPs in the aqueous environment.[56-63] Prof. M. P. Morales and Dr. M. Marciello are acknowledged for allowing me to perform the experiments and characterization techniques at the facilities of the ICMM-CSIC during a research stay in 2012.

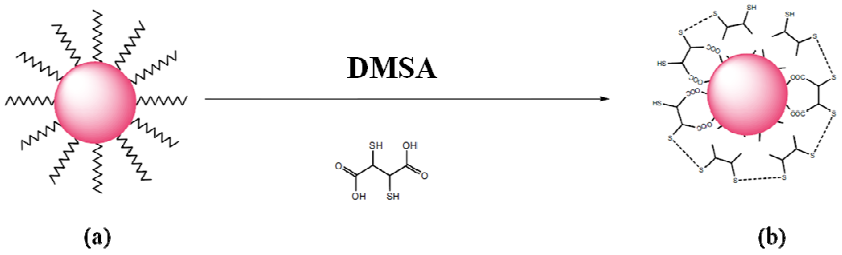

Figure 9. DMSA ligand exchange. Schematic representation of the ligand exchange process. (a) Hydrophobic coating: fatty acid. (b) Hydrophilic coating: DMSA.

1.2. Magnetism in nanoparticles

1.2.1. Anisotropy energy

The magnetic anisotropy energy depends on the orientation of the magnetization with respect certain reference axes in the magnetic system. Therefore, it is one of the factors determining the spatial arrangement of the system magnetization. There are several contributions to the anisotropy energy that, in general, can be considered independent of each other. For instance, in bulk materials, magnetocrystalline and magnetostatic energies are the most significant contributions. However, when the size of the system is reduced towards the nanometre scale, surface anisotropy can be of the same order of magnitude as the latter. This is because the number of atoms at the surface raises dramatically once the size decreases.[1] For instance, in a $Fe_{3-x}O_4$ spherical nanoparticle of 100 nm, atoms at the surface are about 5.9% but, when the size is reduced to 5 nm, as many as 78.5% of the atoms are lying on the surface.[64] Consequently, for single-domain magnetic NPs the main contributions to the anisotropy energy are as follows.

(a) Magnetocrystalline anisotropy (E_{cr}): It is associated with the symmetry of the crystal field acting on the magnetic atoms, and for the simple case of uniaxial anisotropy it can be written as

$$E_{cr}(\theta) = K_1 V \sin^2 \theta \qquad (1)$$

where K_1 is the first order anisotropy constant and V is the particle volume.

(b) Magnetostatic anisotropy (E_{ma}): It is a self-energy that originates at the interaction between the magnetization and the magnetic field that the particle creates around. For a single-domain particle, this energy is related to the components of the particle magnetization along the axis system and can be expressed exactly only when the particle has an ellipsoidal shape. Then, the magnetostatic energy is given by

$$E_{ma} = \frac{1}{2V}(N_x m_x^2 + N_y m_x^2 + N_z m_z^2) \tag{2}$$

where m_x, m_y and m_z are the components of the particle magnetization; N_x, N_y and N_z are the demagnetizing factors relative to the particle shape and V is the particle volume. For an ellipsoid of revolution with the major axis along the z-direction Equation (2) can be simplified as

$$E_{ma} = \frac{m^2}{2V}\left(N_x - N_z\right)\sin^2\theta \tag{3}$$

where θ is the angle between the magnetization and the z-axis. In this case, E_{ma} has uniaxial symmetry and if the ellipsoid is prolate, the effective anisotropy constant is positive. For uniaxial magnetocrystalline anisotropy and if the two uniaxial axes coincide, the two contributions simply add yielding a total effective uniaxial anisotropy.

(c) Surface anisotropy (E_{su}): The origin of this anisotropy energy at the surface is related to the lack of symmetry of the crystal field and the existence of a discontinuity for the magnetic interactions.[65] This leads to a superficial energy density of the form

$$D_{su} = K_s \cos^2\theta' \tag{4}$$

where θ' is the angle between the local magnetization and the perpendicular to the surface, and K_s is the surface anisotropy constant which is in the order of magnitude of 0.1 to 1 erg/cm^{-3}.[66] For an ellipsoid of revolution, Equation (4) can be integrated to get the net surface anisotropy energy of the particle which is given by

$$E_{su} = FK_sS\sin^2\theta \tag{5}$$

where F is a geometrical factor and θ is referred to the usual axis system

Interestingly and given all of the above, the effective anisotropy of a particle can often be assumed to have uniaxial character, being the corresponding energy determined by a unique anisotropy constant, K. Therefore, the total anisotropy energy can be written as

$$E_{eff} = KV \sin^2 \theta \tag{6}$$

Figure 10 shows E_{eff} as a function of the angle θ formed between the particle magnetization and the effective anisotropy axis. The most significant features of this angular dependence of the anisotropy energy are the existence of two states at $\theta = 0$ and $\theta = \pi$ corresponding to energy minima which are separated from each other by an energy barrier of height $E_B = KV$. So, in equilibrium, particle magnetization is pointing along one of these two angles and fluctuates between them due to thermal excitation. Taking into account the volume distribution $f(V)$ in a real ensemble of NPs, it is a matter of fact that the dynamics of the particles' magnetization will behave as if it was driven by an energy barrier distribution $f(E_B)$.

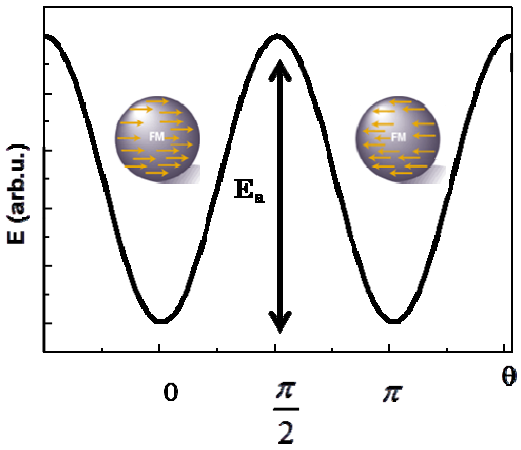

Figure 10. Dependence of the effective anisotropy energy of a single-domain particle with uniaxial character as a function of the angle between the particle magnetization and the anisotropy axis.

1.2.2. Single domain particles

It is well established that a magnetic material splits in domains, which are regions with uniform magnetization separated by domain walls (Bloch walls), in order to minimize its magnetostatic energy.[67] The formation of a domain structure is governed by various energy contributions coming from: the exchange interactions, the anisotropy energy and the magnetostatic energy. Therefore, the final interplay among these energies is what determines the actual spatial arrangement and shape of the magnetic domains. Once the system becomes smaller, both the size of the domains and the number of them in the multidomain structure are reduced. Thus, below a certain critical size, the energy cost to generate a domain wall becomes greater than the corresponding reduction in the magnetostatic energy due to the splitting of a larger domain in two. As a consequence, the

system no longer divides in smaller domains, keeping the magnetic structure of a single domain.[68,69] For spherical particles, the characteristic radius below which they will be in a single-domain configuration is given by [70,71]

$$R_{sd} = \frac{9E_\sigma}{\mu_0 m_s^2} \tag{7}$$

where m_s is the saturation magnetization, E_σ is the total domain wall energy per unit area and μ_0 is the vacuum magnetic permeability. As an example, it is shown in Table 4 the critical diameter for single-domain spherical particles of common magnetic materials.[69]

Material	Ds (nm)
Fe	14
Co	70
Ni	55
Fe_3O_4	128
γ- Fe_2O_3	166
$CoFe_2O_4$	40

Table 4. Typical values of the critical diameter for single-domain spherical particles.

1.2.3. Magnetic relaxation

The particles' magnetization can be reoriented by thermal excitation or the action of an external field through two main mechanisms: Néel and Brown relaxation processes.[72,73] The first one implies the reversal of the particle moment through fluctuations between the orientations corresponding to the anisotropy energy minima. The second mechanism corresponds to a physical rotation of the particle as a whole with its magnetization anchored to the initial orientation with respect the particle axis system. Figure 11 shows a schematic representation of these two mechanisms of relaxation that fully govern the dynamical properties of an ensemble of magnetic NPs. In the following, they are further described.

(a) Néel's Model: In this model, it is supposed that the particle spins are rigidly coupled and rotate in a synchronous manner when m is reversed. Néel considered only the case of uniaxial symmetry and the model was developed for $E_B / k_B T \gg 1$, where k_B is the Boltzmann constant, so that $k_B T$ is an estimation of the available thermal energy at a given temperature.[73] In this framework, the characteristic time of the thermal fluctuations of the

magnetization of a particle with uniaxial anisotropy is given by Arrhenius' law:

$$\tau_N = \tau_0 \exp\left(\frac{KV}{k_B T}\right) \tag{8}$$

where τ_0 is a characteristic attempt time. This mechanism is dominant in small particles and the unique existent in a frozen colloidal suspension where particles cannot physically rotate.

(b) Brown's Model: Brown's relaxation can only occur when the particles are dispersed in a solvent in the form of a colloidal suspension (the so-called magnetic liquid or ferrofluid). In this case, the characteristic relaxation time for the particle rotation as a whole is given by[72]

$$\tau_B = \frac{V_H \eta}{k_B T} \tag{9}$$

where V_H is the hydrodynamic volume of the particle and η is the solvent viscosity.

In a ferrofluid, when the two mechanisms of relaxation are present and assuming that they are independent, the effective characteristic time of the magnetic relaxation can be expressed as

$$\frac{1}{\tau} = \frac{1}{\tau_B} + \frac{1}{\tau_N} \tag{10}$$

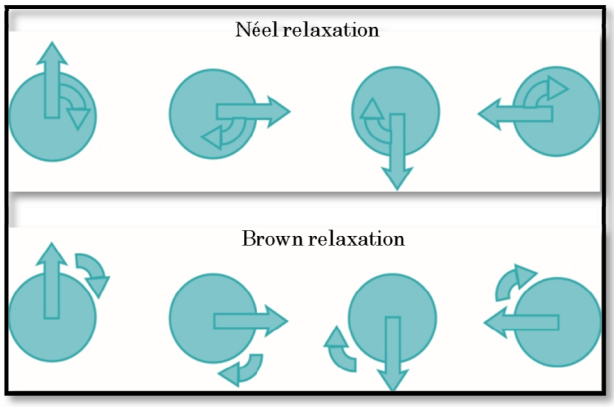

Figure 11. Schematic representation of the relaxation mechanisms of the Brown and Néel models.

1.2.4. Superparamagnetism

When a magnetic system is so small as to be single domain, the local magnetization is uniform at any applied magnetic field so that the system magnetization behaves as a super-spin that relaxes according to thermal fluctuations with a characteristic time τ given by Equation (10). When Néel

relaxation is the dominant mechanism the anisotropy energy barrier for magnetization reversal may be overcome, and then, the particle magnetization can thermally fluctuate like a single spin in a paramagnetic material but with a magnetic moment very much larger, even at low applied magnetic fields.[43,74]

It is to say that this phenomenon is time dependent due to the statistical nature of the thermal energy. Thus, for non-interacting particles, the magnetic behaviour depends strongly on the value of the characteristic measuring time τ_m of the specific experimental technique with respect to the relaxation time τ associated with Néel's law. Therefore, considering that τ varies exponentially with $E_B / k_B T$ ratio, very different magnetic regimes can be observed in an ensemble of magnetic NPs as a function of the temperature. If relaxation is much faster than the experimental time frame ($\tau_m \gg \tau$), the rapid fluctuations of the particle magnetization mimic the atomic paramagnetism and the measured value of the magnetization is small. This regime is known as superparamagnetism due to its similitudes with the atomic paramagnetism. On the contrary, if $\tau_m \ll \tau$, the particle magnetization remains blocked during the observation time (blocked state). In the intermediate regime, the probability that the magnetization has not been reversed after an observation time t is given by

$$P(t) = \exp\left(-\frac{t}{\tau}\right) \tag{11}$$

The validity of Equation (11) is supported by the results of various single-particle experiments.[75-77] Moreover, from this equation it can be deduced that the relaxation of the magnetization towards the equilibrium of an ensemble of identical nanoparticles will follow exponential time decay.

The temperature at which $\tau_m \simeq \tau$ is called blocking temperature (T_B). T_B is the temperature corresponding to the transition between the regimes associated with the superparamagnetic and blocked states. Interestingly, this temperature depends not only on the particle size but also on to the time scale of the experimental technique. It can be strongly modified by the existence of inter-particle interactions as well.

Nowadays, the most used techniques of magnetic characterization to study the superparamagnetic relaxation are dc susceptibility where τ_m is around 100 s, and ac susceptibility where $\tau_m = 10^{-1} - 10^{-5}$ s for a typical equipment and $\tau_m = 10^{-5} - 10^{-8}$ s for high frequencies.[30] Superparamagnetism can be also studied by Mössbauer spectroscopy with $\tau_m = 10^{-7} - 10^{-9}$ s and neutron scattering with $\tau_m = 10^{-8} - 10^{-12}$ s depending on the specific experiments.[43,74] Then, NPs with characteristic relaxation times between

$10^{-7} - 100$ s will be seen as superparamagnetic when they are measured by means of a dc susceptibility technique, but they will appear as blocked in ferro- or ferrimagnetic states when they are measured by Mösbauer spectroscopy or neutron scattering. In other words, both superparamagnetic and blocked states are not intrinsic states of the NPs since their observation depends on the relation between the relaxation time of the particles and the experimental time frame.

Taking into account Arrhenius' law and all the above, the following relationship between the minimum volume of the blocked particles V_B and the corresponding blocking temperature T_B can be obtained

$$V_B = \frac{\ln(\tau_m / \tau_0) k_B}{K} T_B \tag{12}$$

In a typical dc experiment $\tau_m = 100$ s (SQUID magnetometry) and assuming that $\tau_0 = 10^{-9}$ s, one obtains that

$$V_B = \frac{25 k_B}{K} T_B \tag{13}$$

1.2.5. Magnetic characterization

The dc magnetic characterization performed in this thesis has been carried out by SQUID magnetometry. This characterization comprises measurements of hysteresis loops at various temperatures, zero-field-cooled/field-cooled (ZFC-FC) susceptibility and magnetic relaxation experiments.

(a) Hysteresis loops: Magnetic hysteresis is the property of a magnetic material through which a remnant magnetization is retained depending on the previous magnetic history after the applied magnetic field is removed. The measurement of hysteresis loops at constant temperature enables the determination of the following magnetic parameters of a sample constituted of a size distribution of nanoparticles: the saturation magnetization M_s that is the value of the magnetization when all the particle moments are aligned along the external applied magnetic field; the remnant magnetization M_r that is the value of the residual magnetization when the applied magnetic field is removed; and the coercive field H_c which can be defined as the magnetic field that has to be applied in order to cancel the sample magnetization (see Figure 12). In addition, analysing the profile of the magnetization curves as well as the coercive field, one can obtain relevant information about de size distribution of the particles and detect the eventual presence of other magnetic phases in the sample.

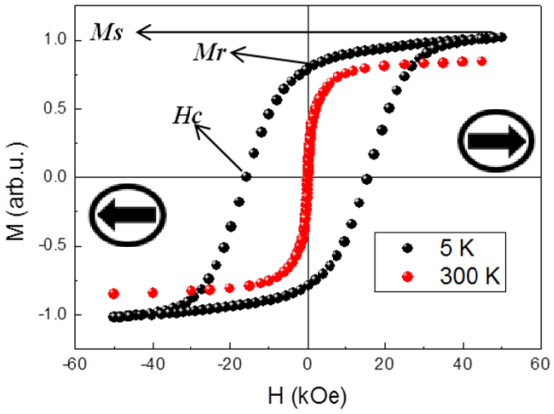

Figure 12. Hysteresis loops for 8 nm $CoFe_2O_4$ NPs. Solid black circles correspond to a temperature below T_B (where the particles show typical ferrimagnetic behaviour in the blocked state). Solid red circles correspond to a temperature above T_B where particles are superparamagnetic.[78]

As previously stated, the actual value of H_c at a given temperature depends on the size of the particles, so it can be used as a signature of the occurrence of size effects in this kind of systems.[1,43] Figure 13 shows the different situations that one can find when measuring the hysteresis loop of a nanoparticle. Figure 13A displays the reversible hysteresis loop with zero coercive field of a small particle in the superparamagnetic state. Besides, the profile of this magnetization curve is similar to that of a paramagnetic substance. For a particle bigger enough to just reach the blocked state, the coercive field is also very small but the profile of the magnetization curve looks like that of a ferro- or a ferrimagnetic material (see Figure 13B). As the size of the particle increases, longer relaxation times are observed, thus stabilizing the blocked state and increasing the coercive field (see Figure 13C). Finally, above the critical size for a single-domain formation, the particle is in a multidomain configuration associated with a lower value of the coercive field (see Figure 13D).

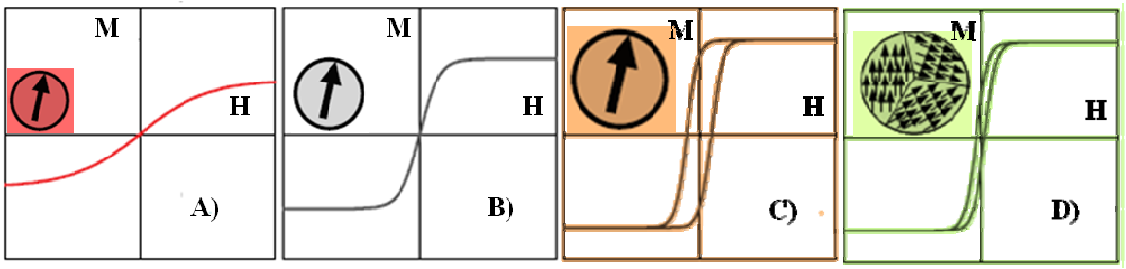

Figure 13. Hysteresis loops as a function of the particle size.

(b) Isothermal magnetization curves for superparamagnetic particles: The distribution of activation magnetic volumes can be obtained from the isothermal magnetization curves in the superparamagnetic state. This distribution of magnetic volumes is somehow related to the size distribution of the particles when inter-particle interactions are negligible. Thus, here we will assume that the activation magnetic volumes coincide with the volumes of the particles. Therefore, in the superparamagnetic regime and for a non-interacting ensemble, the projection of a particle magnetization in the direction of the applied magnetic field m' can be described as a Langevin function of the form[79]

$$\frac{m'(H,T)}{m} = \coth\left(\frac{mH}{k_B T}\right) - \frac{k_B T}{mH} = L\left(\frac{mH}{k_B T}\right) \tag{14}$$

where it is assumed that $k_B T$ is large enough to neglect the effect of the particle anisotropy on the magnetization orientation so that the particle behaves as an isotropic single-domain. Taking into account that in real samples there is always certain dispersion in the volume of the particles (size distribution), the values of the particles' magnetization will follow a distribution that often can be approximated by a lognormal distribution $P(m)$ given by

$$P(m) = \frac{1}{m\,\omega_m\sqrt{2\pi}} \exp\left[\frac{\ln^2\left(m/m_0\right)}{2\omega_m^2}\right] \tag{15}$$

where m_0 is the mean geometric particle moment and $\sigma_m = \exp(\omega_m)$ is the geometric standard deviation of the particle moment. ω_m is related to the geometric standard deviations of both the volume and the diameter of the particles through the relationship $\omega_m = \omega_v = 3\omega_d$. Therefore, by summing up the values of the particles' magnetization giving by Equation (14) in accordance with $P(m)$ in Equation (15) and adding a linear-field term originating at a residual paramagnetic susceptibility, the magnetization of the sample can be written as[78]

$$M(H,T) = M_S \frac{\int m\,P(m)\,L(mH/k_B T)\,dm}{\int m\,P(m)\,dm} + \chi_p H \tag{16}$$

where M_S is the saturation magnetization of the sample and H is the applied field. Consequently, the parameters of the particle-magnetization distribution in a real sample can be estimated by fitting isothermal magnetization curves in the superparamagnetic regime to Equation (16).

(c) Zero-field-cooled/field-cooled (ZFC/FC) measurements: This kind of magnetic measurements is very useful to obtain information about the effective distribution of magnetic volumes, to verify the existence of inter-particle interactions as well as to estimate the average value of the particle anisotropy. The protocol implies the measurement of the sample magnetization as a function of the temperature after submitting the sample to a certain magnetic history. Typically, the sample is cooled down from room temperature to 4-2 K in zero magnetic field; then a static magnetic field is applied ($H < H_c$) and M_{ZFC} is measured while the temperature is increased. Once room temperature is reached, sample is cooled down again to low temperature. After that, the sample is warmed up to 300 K and M_{FC} is collected under the same magnetic field (see Figure 14 for a scheme of the protocol).[79,80]

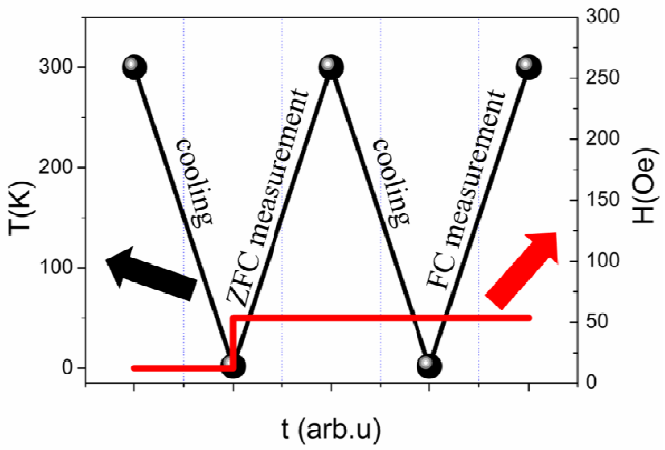

Figure 14. Example of the temperature and field profiles *versus* time in a ZFC/FC protocol. H = 50 Oe.

In a superparamagnetic material the processes that take place in a ZFC measurement are as follows. First, while the sample is cooled down at zero magnetic field, particle moments become blocked in random directions so that the magnetization of the sample is very small well below the mean value of the blocking temperature of the particles. After applying the measuring magnetic field and as the temperature is increased, the smaller particles align progressively in the direction of the magnetic field and the magnetization increases steadily. This process keeps on until reaching the blocking temperature T_B , where the majority of the particles become aligned with the magnetic field since they are transiting between the blocked and the superparamagnetic states. Once overtaken this temperature, the magnetization decreases due to thermal excitation. Therefore, M_{ZFC} develops a peak around the blocking temperature. On the contrary, a peak is not present in the M_{FC} curve, since the field cooling process gives rise to

a progressive alignment of the particle moments along the direction of the magnetic field as the temperature decreases and more particles become blocked. Then, M_{FC} shows a monotonous decrease of the magnetization due to thermal excitation as the temperature is raised. Figure 15 shows a typical example of measurements of $M_{ZFC}-M_{FC}$ for samples of $Fe_{3-x}O_4$ NPs with sizes ranging from 6 to 17 nm.

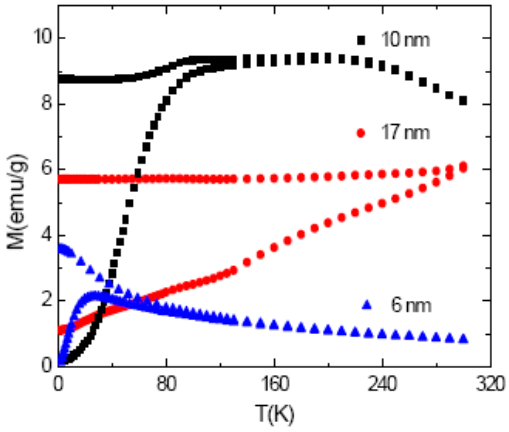

Figure 15. $M_{ZFC}-M_{FC}$ curves as a function of the temperature for $Fe_{3-x}O_4$ NPs with H= 50 Oe.[52]

M_{ZFC} curves can be fitted by applying Gittleman's model to obtain the distribution of magnetic volumes and the effective anisotropy constant of the particles.[81] This model describes the magnetization of an ensemble of non-interacting NPs with a size distribution $P(m)$ as the result of two contributions: one coming from the blocked particles (m_{bl}) and the other from the superparamagnetic ones (m_{spm}), as it is given by the following expression

$$M_{ZFC}(T) = \int_0^{M_s V_B(T)} m_{spm}\, P(m)\, dm + \int_{M_s V_B(T)}^{\infty} m_{bl}\, P(m)\, dm \qquad (17)$$

where V_B is the critical blocking volume at the temperature T given in Equation (13) that separates NPs in two classes: those in the blocked sate ($V \geq V_B$) and the superparamagnetic ones ($V_B > V$). The magnetization of superparamagnetic NPs follows the Langevin function of Equation (14). Besides, for small values of the magnetic field, the Langevin function can be approximated by

$$m\, L(mH / K_B T) \approx m^2 H / 3k_B T \qquad (18)$$

Moreover, blocked NPs behave as single-domain particles with an anisotropy field of $2K / M_s$, so when subjected to an external magnetic field H the induced magnetization is given by

$$m_{bl} = mM_s H / 3KT \qquad (19)$$

Substituting Equations (18) and (19) in Equation (17), the ZFC susceptibility is written as

$$\frac{M_{ZFC}}{H}(T)=\frac{1}{3k_BT}\int_0^{M_SV_B(T)} m^2P(m)\,dm+\frac{M_S}{3K}\int_{M_SV_B(T)}^{\infty} mP(m)\,dm \qquad (20)$$

(d) Magnetic relaxation experiments: When the magnetization of NPs is repeatedly measured with an observation time frame which is comparable to the reversal time of a certain fraction of the particles, the results will evolve with time, phenomenon called magnetic relaxation. The study of this non-equilibrium phenomenon constitutes a common method to characterize the energy spectrum of the particle system, since it is a macroscopic signature of the existence of a distribution of energy barriers separating local minima which correspond to different orientations of the particle moments.[11] Usually, these experiments are carried out after cooling the sample under a magnetic applied field down to the measuring temperature, at which the magnetic field is switched off.[41] Then, the magnetization decay is recorded as a function of time. This procedure is repeated at several temperatures below and above T_B in order to fully characterize the distribution of energy barriers that governs the dynamic response of the system. In Figure 16, it is shown an example of the magnetization decays at several temperatures for a sample constituted by NPs of 5 nm $Fe_{3-x}O_4$.[82]

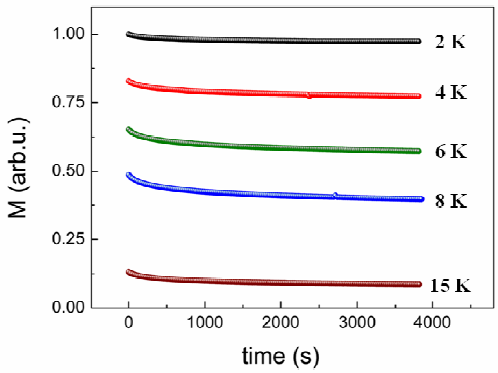

Figure 16. The magnetization decay at zero field as a function of time for a sample constituted of 5 nm $Fe_{3-x}O_4$ NPs after field-cooling the sample under 50 Oe down to the measuring temperature and switching off the magnetic field. [82]

For instance, starting from the field-cooled state at a given temperature, and then switching off the field, the time evolution of the magnetization for non-interacting particles can be written as

$$M(t)=M_{FC}\frac{\int mP(m)e^{-t/\tau(m)}dm}{\int mP(m)dm} \qquad (21)$$

where it has been assumed that the probability that the magnetization of a particle has been reversed in the time t is given by Equation (11). Substituting $\tau(m)$ by Arrhenius law (Equation (8)) in the exponential function of Equation (21) we can define the double exponential function $\rho(m,t)$ as

$$\rho(m,t) = e^{-(t/\tau_0)e^{(-KV(m)/k_BT)}} \tag{22}$$

which varies abruptly from 0 to 1 at $V_C = (k_BT/K)\ln(t/\tau_0)$ or $m_C = M_S V_C$. The usual simplification is based on approximating $\rho(m,t)$ by a step function whose discontinuity $m_C(t)$ moves to higher values of m as time elapses at constant temperature. Therefore, the integral in the numerator in Equation (21) is cut off at the lower limit by the value of $m_C(t)$, which is the only time-dependent parameter, and Equation (21) is finally expressed as

$$M(t) \simeq M_{FC} \frac{\int_{M_S V_C}^{\infty} m\,P(m)\,dm}{\int m\,P(m)\,dm} \tag{23}$$

From Equation (23), it is deduced that $M(t)$ is a function of time and temperature only through the variable $m_C(t)$. Therefore, $T\ln(t/\tau_0)$ acts as a scaling variable in such a way that measuring the magnetization as function of the temperature at a given time is equivalent to measure the magnetization as a function of $\ln(t/\tau_0)$ at a fixed temperature. This kind of time-temperature scaling is characteristic of activated processes governed by the Arrhenius law.[75-77] Figure 17 shows an example of $T\ln(t/\tau_0)$ scaling for 8 nm $CoFe_2O_4$ NPs.[78]

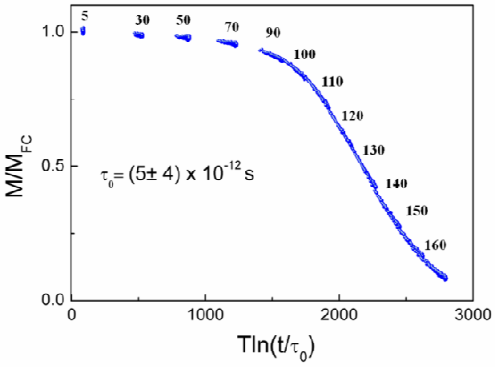

Figure 17. Scaling of the relaxation curves for a sample of 8 nm $CoFe_2O_4$ NPs , measured at several temperatures, with an attempt time of τ_0 = (5 ±4) x 10^{-12}s.[78]

1.3. Magnetic Force Microscopy (MFM)

1.3.1. Overview

In the 80s, Binning and Rohrer developed the Scanning Tunnelling Microscope (STM) which was based on measuring the tunnel current flowing between a sharp metallic tip and a sample at very close distances (0.5 nm).[83] Thanks to this development, they earned the Novel Price in Physics in 1986.

Years later and as a consequence of this invention, other microscopes were developed such as the Near-field Scanning Optical Microscope (SNOM) or the Scanning Force Microscope (SFM), among which stand out Atomic Force Microscopy (AFM) and Magnetic Force Microscopy (MFM). This last one appeared in 1987 as a variation of the AFM.[84,85] One of the greatest benefits of SFM in contrast to STM is the capability to study nonconductive samples, for instance, insulating or biology samples.[86] This is due to the specific mode of operation of this microscope, which measures the interaction forces between the tip and the sample. In addition, it is possible to perform measurements in conditions of controlled atmosphere (removing moisture, keeping a constant temperature), in liquids, in high vacuum (HV) or in ultra-high vacuum (UHV). Moreover, thanks to the high resolution of MFM, it is a perfect tool to study magnetism at nanometre scale. It is based on the interaction force between the tip and the magnetic field that a magnetic sample induces around. In general, it works in dynamic mode, for which the cantilever oscillates to their resonance frequency that changes in amplitude (A), phase (ϕ) and in frequency (ω) depending on the force gradients.

1.3.2. Experimental set-up

In this section, we are going to describe the experimental set-up used for the MFM experiments which were performed using Nanotec Electrónica systems and WSxM software for data acquisition.[87] All the experiments were performed during my two research stays in the laboratory led by Dr. Agustina Asenjo Barahona at the Instituto de Ciencia de Materiales de Madrid (ICMM) within the period 2012-2013. Figure 18 shows the experimental set-up used for the MFM experiments that is based on a piezo-acustic excitation system, where a small piezo integrated in the cantilever generates the oscillation at the desired frequency. In addition, a piezoelectric scanner is used for faster scanning the sample surface.[86] It is able to move the sample in all spatial directions using a tubular piezo-

element with a single interior electrode and four external electrodes. For the detection system, a laser spot is focalized into the oscillating cantilever and the reflection of the beam is detected by a four quadrant photodiode. Each quadrant generates a voltage which is proportional to the intensity of the incident beam, in such a way that lateral and normal deflections of the cantilever from the equilibrium position can be precisely determined by subtracting the signals between different quadrants.

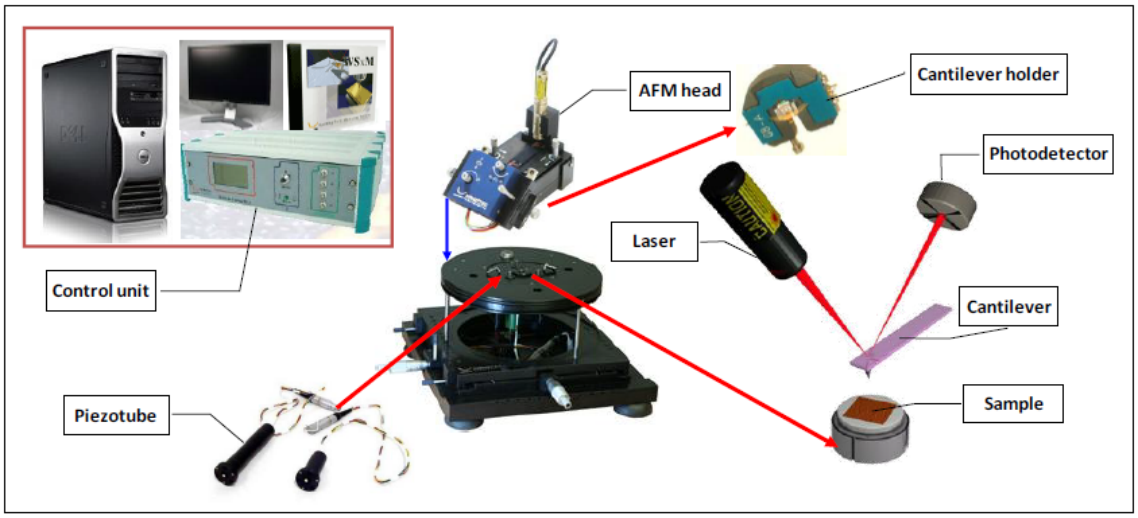

Figure 18. Schematics of the experimental set-up of the microscope used throughout this thesis.

In order to carry out experiments with an applied field (in geometries corresponding to in-plane and out-of-plane), a controlled current is made to flow through two electromagnets that generate fields up to ±100 mT along the out-of-plane direction (OP) and ±125 mT for the in-plane (IP) geometry, respectively. An exceptional mechanical stability has been achieved by substituting magnetostrictive components by materials with a negligible magnetoelastic response.[88]

As it was mentioned before, in a SFM, it is measured the interaction forces between the tip and the sample. For this reason, one of the most important components in a MFM is the force detector (see Figure 19). It consists in a cantilever with an integrated tip, generally conic or pyramidal, obtained by microfabrication techniques (Budget Sensors Tech) using as typical materials Si and Si_3N_4 nanocrystals. Tips can be coated with several coatings depending on the specific application (magnetic or conductive materials, etc.).

Depending on the mechanical properties of the cantilever which are specific of each material used (its density, geometry, etc.), one has to consider the following key parameters to select the suitable force detector for each experiment: the force constant (K), the resonance frequency (ω_0) and the quality factor (Q).

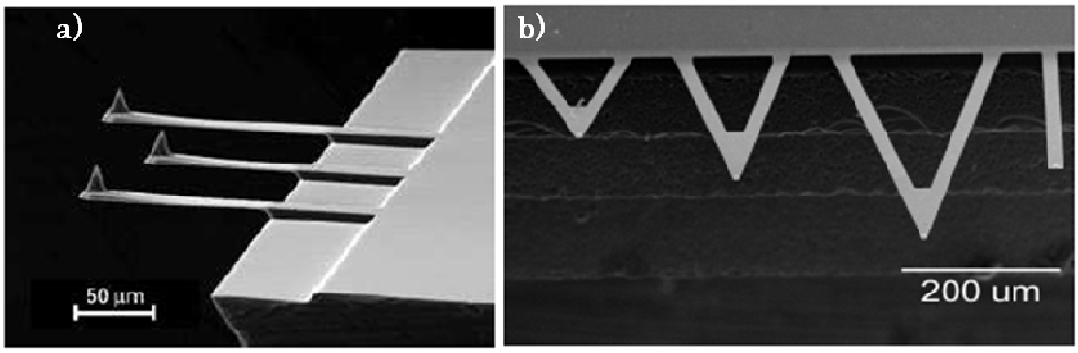

Figure 19. (a) Semi-lateral view of three rectangular micro-cantilevers where the tips can be seen at their ends; (b) Top view of three triangular and one rectangular micro-cantilevers.[89]

Each cantilever is integrated in a chip with macroscopic dimensions (mm), in such a way that it can be manipulated with pliers. Due to the cantilever geometry, a good approximation for the values of the forces can be obtained by the Hooke law

$$F_N = K_Z \Delta Z \tag{24}$$

$$F_l = K_T \Delta X \tag{25}$$

where K_Z and K_T are the force constants corresponding to the normal and the lateral defection forces, respectively ($K_Z \ll K_T$). Consequently, normal forces, which act on the tip perpendicular to the cantilever plane, produce a vertical deflection ΔZ. Analogously, lateral forces acting perpendicular to the cantilever axis provoke a torsion ΔX.

The appropriate choice of force constants is of key importance to obtain quantitative information in a SFM. Due to the fact that companies normally provide only approximate nominal values, it is necessary to perform the direct determination of those values through methods described elsewhere.[90]

1.3.3. Fundamentals of MFM

In dynamic MFM, force gradients are determined through the experimental frequency shift of the oscillating cantilever. When a magnetic coating is present in the sensing probe, the interaction between the stray field emerging from the sample and the magnetization distribution within the tip gives rise to a force gradient that can be mapped. Therefore, the magnetostatic force arising from the tip-sample interaction is

$$\vec{F}_{t-s} = \mu_0 \int \vec{\nabla}(\vec{M}_{tip} \cdot \vec{H}_{sample}) dV_{tip} = \mu_0 \hat{k} \int \sum_{i=x,y,z} \frac{\partial}{\partial z}(M_{tip,i} H_{sample,i}) dV_{tip} \tag{26}$$

where $\hat{k}$ is the unit vector along Z, and it has been assumed that the cantilever spreads out on the xy plane, in such way that the normal force is exerted in the z direction.

There are two approximations depending on how far away the tip is from the sample. If the tip is far enough, a dipolar approximation can be assumed that accounts for the total magnetization $\vec{m}_{tip} = \int \vec{M}_{tip} dV_{tip}$ and gets rid of the integral in the Equation (26).[91]

$$\vec{F}_{t-s} = \mu_0 \hat{k} \left[m_x \frac{\partial H_{sample,x}}{\partial z} + m_y \frac{\partial H_{sample,y}}{\partial z} + m_z \frac{\partial H_{sample,z}}{\partial z} \right] \tag{27}$$

Therefore, the frequency shift can be expressed as

$$\Delta\omega \approx \frac{-\omega_0 \mu_0}{2K_z} \left[m_x \frac{\partial^2 H_{sample,x}}{\partial z^2} + m_y \frac{\partial^2 H_{sample,y}}{\partial z^2} + m_z \frac{\partial^2 H_{sample,z}}{\partial z^2} \right] \tag{28}$$

If the point dipole is oriented along the vertical direction (out-of-plane geometry), then

$$\Delta\omega \approx \frac{-\omega_0 \mu_0 m_{tip}}{2K_Z} \frac{\partial^2 H_{sample,z}}{\partial z^2} \tag{29}$$

Another approximation is to consider the MFM tip as a monopole. This model is suitable for long and elongated sensors.[92] In this case, the magnetization is supposed to be homogeneous along the Z direction, so from Equation (26), it is obtained that

$$\vec{F}_{t-s} = \mu_0 \hat{k} \int \frac{\partial}{\partial z}(M_{tip,z} H_{sample,z}) dV_{tip} = \mu_0 \hat{k} \int M_{tip} \frac{\partial}{\partial z} H_{sample} dz_{tip} = \mu_0 M_{tip} H_{sample} \hat{k} \tag{30}$$

and the frequency shift is then:

$$\Delta\omega \approx \frac{-\omega_0 \mu_0 M_{tip}}{2K_Z} \frac{\partial H_{sample}}{\partial z} \tag{31}$$

1.3.4. Measurement modes

In general terms and in absence of electrical, magnetic or capillarity forces, the interaction between the tip and the sample is due to intermolecular forces. Figure 20 shows the profile of a typical interaction potential between either both atoms and molecules or two surfaces. In particular, it can illustrate the interaction potential between the tip and the sample in a SFM.

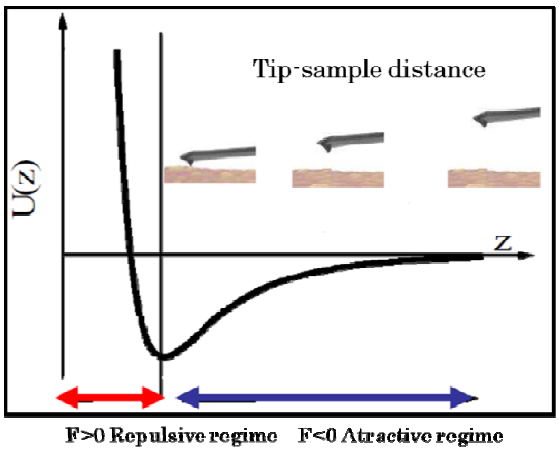

Figure 20. Interaction potential between the tip and the sample as a function of the tip-sample distance (z coordinate in a SFM microscope).

This kind of potentials shows two clear regions, one where the potential is attractive and the other where it is repulsive. The attractive regime corresponds to cases with predominant van deer Waals interactions (this situation is only valid when the experiments are carried out in room atmosphere conditions). Due to tip and sample geometry, this interaction can be approximated by a sphere brought closer to a plane.

$$F_{VdW} = -\frac{A_H R}{r^2} \tag{32}$$

where R is the sphere radius, r is the distance between the sphere and the plane, and A_H is the Hamaker constant (which is of the order of 10^{-19} J). Moreover, the repulsive regime is reached when the electronic clouds of the tip and the sample start to overlap.

These two regimes of the interaction potential define the basic work modes of SFM: *dynamic mode* (both non-contact and intermittent contact modes) and static mode (contact mode). In this section, it is only described the dynamic mode because it is the only one we used in the experiments.

In the dynamic mode, the cantilever is oscillated at its resonance frequency; while the amplitude and the frequency shift of the oscillation are the magnitudes studied in the cantilever-tip system.[92] In this work, we have

only performed the experiments in this mode in order to prevent that the friction between the tip and the particles drags them away.

Two methods of measuring can be applied in the dynamic mode: amplitude modulation (AM) and frequency modulation (FM). The first one (tapping mode) uses the oscillation amplitude as a feedback parameter and the experiment is usually carried out in the air. On the contrary, FM mode is performed in vacuum or high vacuum and adopts the frequency shift as a feedback parameter. Due to the fact that in this work all the measurements were made in air conditions, the next section is only devoted to the AM mode.

(a) Equations of the amplitude and the phase shift in AM mode: The cantilever-tip system is forced to maintain a constant frequency of oscillation which is generally near the free resonance frequency. The amplitude of the oscillation acts as feedback parameter, so that the system follows the equation

$$m\ddot{z} + \frac{\omega_0}{Q} + Kz = F_0 \cos(\omega t) + F_{ts} \tag{33}$$

where z is the direction in which cantilever vibrates, K is the force constant, m is the mass system, ω_0 is the resonance frequency, Q is the oscillation quality factor, ω and F_0 the frequency and the excitation amplitude, respectively, and F_{ts} stands for the interaction between the tip and the sample. We can assume that the dominant forces are: van deer Waals, repulsive forces, accession and capillarity. [93] Assuming that F_{ts} is equal to zero (in the z axis, the system can be described as a forced and damped harmonic oscillator) the solution of Equation (33) can be written as

$$z(t) = Be^{-\alpha t} \cos(\omega_r t + \beta) + A(\omega) \cos(\omega t - \phi) \tag{34}$$

This solution has a transitory term and a stationary term that dominates after a short time. The stationary state is a harmonic sinusoidal function. The dependence of the amplitude on the excitation frequency is as follows

$$A(\omega) = \frac{F_0 / m}{\left[\left(\omega_0^2 + \omega^2 \right)^2 + \left(\frac{\omega \omega_0}{Q} \right)^2 \right]^{1/2}} \tag{35}$$

and the phase shift can be written as

$$\tan \phi = \frac{\omega \omega_0}{Q\left(\omega_0^2 - \omega^2 \right)} \tag{36}$$

Without damping, the amplitude is given by

$$A_0 = \frac{QF_0}{K} \tag{37}$$

On the other hand, if the tip-sample interaction (F_{ts}) can be considered as a perturbation, $F_{ts} = F_z^{ext}$, it is possible to define an effective force constant $K_{ef} = K - \frac{\partial F_z^{ext}}{\partial z}$, in such way that Equation (31) can be rewritten as

$$\Delta\omega = \omega - \omega_0 = -\frac{\mu_0\omega_0}{2K}\frac{\partial F_z^{ext}}{\partial z} \tag{38}$$

This expression shows how resonance frequency of the oscillating system is modified in presence of a force gradient. In the same way, the amplitude variation can be related to the force gradient as follows

$$\Delta A \propto \frac{Q}{2K}\frac{\partial F_z^{ext}}{\partial z} \tag{39}$$

Therefore, the variation of the amplitude is proportional to the quality factor and is very sensitive to changes in the distance between the tip and the sample. This is commonly applied to measure the interaction due to topography (see Figure 21).

In the dynamic mode, the phase locked loop (PLL) is a feedback system whose function consists in keeping constant and close to zero the amplitude shift.[93] This is achieved by varying the excitation frequency in such way that the cantilever is always in the resonance condition in order to keep the phase equal to zero. The PLL output is directly recorded in units of frequency and is equivalent to measure the amplitude shift.

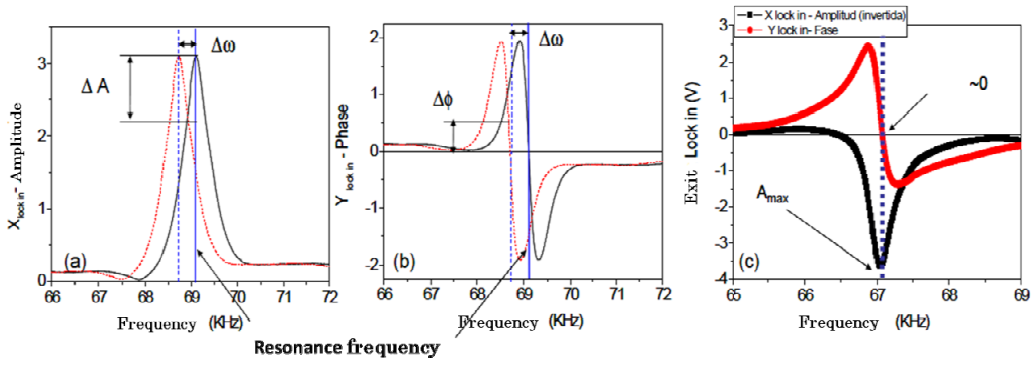

Figure 21. X and Y outputs of the lock-in near the resonance where it is measured: a) the amplitude, and b) the phase (discontinuous line shows what happens in the presence of an interaction). c) Scheme of the result of the PLL feedback. [89]

1.3.5. Interpretation of the images

MFM images agree with frequency-shift maps obtained at a certain tip-sample distance where the magnetostatic coupling is dominant. In the case of magnetic nanoparticles, this range of distance is within 20-80 nm depending on both the size and the nature of the tip.[94] As can be seen in Figure 22 and depending on the relative tip-sample distance, different interactions are dominant. For instance, van deer Waals forces are typically responsible for changes in the cantilever dynamics used to track the topography at separations between 1-10 nm. To extract information about magnetostatic and electrostatic interactions, it is often necessary to withdraw the tip few tens of nanometers until these interactions become dominant.

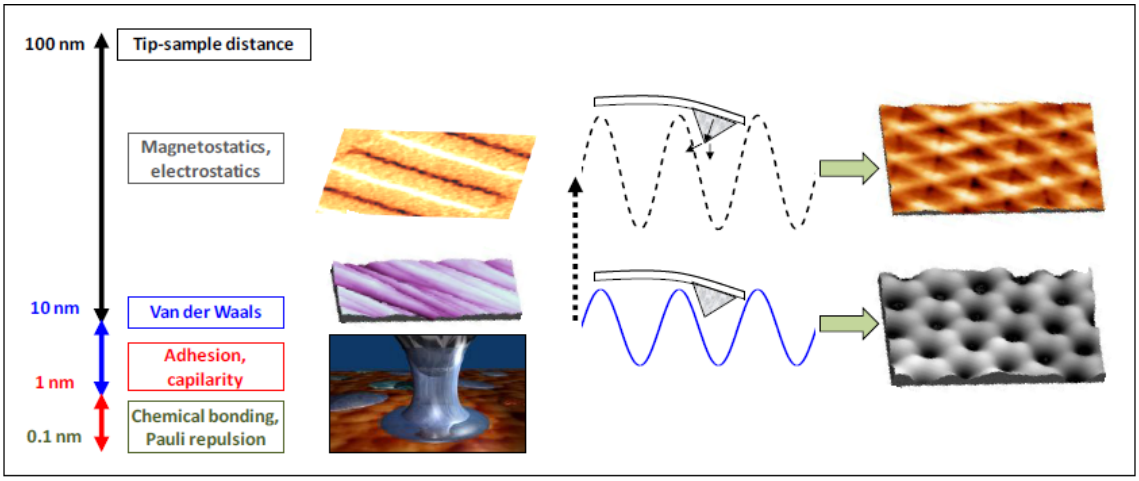

Figure 22. Dominant forces as a function of the tip-sample distance. Schematics of the interactions that govern the cantilever dynamics depending on this distance.

Normally, the operating procedure used, called the lift-mode or retrace-mode, is based on scanning over the sample surface twice at two different separations. First, one scan is carried out at a distance of a few nanometres to obtain the topographic profile. After that, the tip is retraced and the system repeats the same profile obtained during the first scan. Finally, frequency shifts are recoded for the cantilever oscillation during this retrace and are transformed into the MFM image. However, it is worth noting that the interpretation of a MFM signal could be a complex task. For instance, assuming that the sensing magnetization at the tip apex is oriented perpendicular to the sample plane (z-direction), an increase of $\Delta\omega$ corresponds to repulsive forces while attractive forces are associated with a decrease of $\Delta\omega$.

1.4. Motivation

From the fundamental point of view,[1] NPs formed by MFe_2O_4 with (M= Co, Fe) are ideal system models to study the new magnetic phenomena associated with the so-called *particle-like* behaviour, which emerges from the size reduction towards the nanometre scale and contrasts with the well-established magnetic properties of their bulk-counterparts. It is well known that most of the particle-like behaviour and in general the large variability of the magnetic properties observed in this kind of nanomaterials are related to structural features of the NPs rather than being originated from intrinsic finite-size or surface effects, at least for NPs bigger than a few nanometers.[2-9] These structural features, such as crystallographic defects, polycrystalline nature of the NPs, lack of crystallinity at the particle surface, etc., have strong influence on their magnetic properties and can be modified at will through the synthesis method. Therefore, whenever this particle-like behaviour is unwanted for applications with highly demanding requirements, the choice of a suitable synthesis method is of key importance to obtain NPs of high-crystalline quality. On the contrary, particle-like behaviour controlled by the crystalline nature of the NPs could be useful to tailor their magnetic properties for specific applications.

Among the common synthesis methods,[36,37] high-temperature decomposition of metal-organic precursors results the best alternative due to the remarkable final properties of the obtained NPs, such as narrow size distribution, high crystallinity and relatively simple tuning of their size and shape.[33-42] So this will be the chemical route chosen in this work to study the capabilities of this synthesis method to control the final properties of the NPs through their nanostructure.

In addition, to get a deeper insight in the magnetic and structural properties of those materials and to shed light on relevant issues that are still under discussion (dynamic response, magnetic frustration or inter-particle interactions) it could be useful to combine experimental techniques enabling the characterization of the system from macroscopic scales towards single-particle structures.[43,95,96]

Within this framework, we present this work that is divided into three main parts. First, it is studied the effect of the concentration of two common reactants, involved in the thermal decomposition method, on the final properties of magnetic NPs based on iron oxides aiming at optimizing the synthesis procedure and getting a good control of the structure of the final product. In the second part, those NPs obtained in the former way are applied to demonstrate the crucial role of the nanostructure on the physical properties of nanoparticulate systems; specially, the strong interplay existent between structure and both magnetic frustration and interparticle

interactions. Finally, in the third part, MFM experiments with an external applied magnetic field have been performed to directly observe the reversal of the magnetization of isolated particles and the dynamic behaviour of small aggregates.

1.5. References

1 X. Batlle and A. Labarta, J. Phys. D: Appl. Phys. 2002, **35**, R15.

2 P. Grünberg, R. Schreiber, Y. Pang, M. B. Brodsky and H. Sowers, *Phys. Rev. Lett.*, 1986, **57**, 2442–2445.

3 G. Binasch, P. Grünberg, F. Saurenbach and W. Zinn, *Phys. Rev. B*, 1989, **39**, 4828–4830.

4 P. M. Levy and A. Fert, *Phys. Rev. Lett.*, 2006, **97**, 097205.

5 A. Fert, J.-L. Duvail and T. Valet, *Phys. Rev. B*, 1995, **52**, 6513–6521.

6 A. Aharoni, *Phys. Rev. B*, 1973, **7**, 1103–1107.

7 J. Faraudo, J. S. Andreu and J. Camacho, *Soft Matter*, 2013, **9**, 6654.

8 A. Hernández-Mínguez, J. M. Hernandez, F. Macià, A. García-Santiago, J. Tejada, and P. V. Santos. *Phys. Rev. Lett.*, 2005, **95**, 217205.

9 J. R. Friedman, M. P. Sarachik, J. Tejada and R. Ziolo, *Phys. Rev. Lett.*, 1996, **76**, 3830.

10 Ganguly, V. Mehrotra, M. W. Russell, D. R. Huffman, *Science* 1992, **257**, 219.

11 A. Moser, K. Takano, D. T. Margulies, M. Albrecht, Y. Sonobe, Y. Ikeda, S. H. Sun, E. E. Fullerton, Journal of Physics D-Applied Physics 2002, **35**, R157.

12 B. D. Terris, T. Thomson, *Journal of Physics D: Applied Physics* 2005, R199.

13 W. M. Terry, Journal of Physics: *Condensed Matter* 2005, R315.

14 Y. Dahmane, L. Cagnon, J. Voiron, S.Pairis, M. Bacia, L.Ortega, N. Benbrahim and A. Kadri., *Journal of Physics D: Applied Physics*, 2006, R39.

15 M. Z. Zayat, F. del Monte, M. D. Morales, G. Rosa, H. Guerrero, C. J.Serna, D. Levy, *Advanced Materials* 2003, **15**, 1809.

16 J. B. Haun, T.-J. Yoon, H. Lee and R. Weissleder, *Wiley Interdiscip. Rev. Nanomed. Nanobiotechnol.*, 2010, **2**, 291.

17 H. Bin Na, I. C. Song and T. Hyeon, *Adv. Mater.*, 2009, **21**, 2133.

18 C. Sun, J. S. H. Lee and M. Zhang, *Adv. Drug Deliv. Rev.*, 2008, **60**, 1252.

19 Q. A. Pankhurst, J. Connolly, S. K. Jones and J. Dobson, *J. Phys. D. Appl. Phys.*, 2003, **36**, R167.

20 C. S. S. R. Kumar and F. Mohammad, *Adv. Drug Deliv. Rev.*, 2011, **63**, 789.

21 C. B. Catherine, S. G. C. Adam, *Journal of Physics D: Applied Physics* 2003, R198.

22 S. Mornet, S. Vasseur, F. Grasset, E. Duguet, *Journal of Materials Chemistry* 2004, **14**, 2161.

23 P. S. G. V. M. R. Mrinmoy, *Advanced Materials.*, 2008, 9999, NA.

24 M. Rohrer, H. Bauer, J. Mintorovitch, M. Requardt, H. J. Weinmann,

Investigative Radiology , 2005, **40**, 715.

25 M. S. Martina, J. P. Fortin, C. Menager, O. Clement, G. Barratt, C. Grabielle-Madelmont, F. Gazeau, V. Cabuil, S. Lesieur, *J. Am. Chem. Soc.*, 2005, **127**, 10676.A.

26 I. Conde-Leboran, D. Baldomir, C. Martinez-Boubeta, O. Chubykalo-Fesenko, M. del Puerto Morales, G. Salas, D. Cabrera, J. Camarero, F. J. Teran and D. Serantes, *J. Phys. Chem. C*, 2015, **119**, 15698.

27 D. Serantes, K. Simeonidis, M. Angelakeris, O. Chubykalo-Fesenko, M. Marciello, M. del P. Morales, D. Baldomir and C. Martinez-Boubeta, *J. Phys. Chem. C*, 2014, **118**, 5927.

28 P. de la Presa, Y. Luengo, V. Velasco, M. P. Morales, M. Iglesias, S. Veintemillas-Verdaguer, P. Crespo and a. Hernando, *J. Phys. Chem. C*, 2015, **119,** 11022.

29 E. L. Verde, G. T. Landi, J. A. Gomes, M. H. Sousa and A. F. Bakuzis, *J. Appl. Phys.*, 2012, **111**, 123902.

30 C. Haase and U. Nowak, *Phys. Rev. B*, 2012, **85**, 045435.

31 C. Liang, S. Huang, W. Zhao, W. Liu, J. Chen, H. Liu and Y. Tong, *New J. Chem.*, 2015, **39**, 2651–2656.

32 V. F. Puntes, K. M. Krishnan and A. P. Alivisatos, *Science*, 2001, **291**, 2115–2117.

33 J. Rockenberger, E. C. Scher, A. P. Alivisatos, *J. Am. Chem. Soc.*., 1999, **121**, 11595.

34 T. Hyeon, *Chemical Communications* 2003, **9**, 927.

35 T. Hyeon, S. S. Lee, J. Park, Y. Chung, H. B. Na, *J. Am. Chem. Soc.* 2001,

123, 12798.

36 A. G. Roca, R. Costo, A. F. Rebolledo, S. Veintemillas-Verdaguer, P. Tartaj, T. González-Carreño, M. P. Morales and C. J. Serna, *J. Phys. D. Appl. Phys.*, 2009, **42**, 224002.

37 P. Tartaj, P. Morales, S. Veintemillas-verdaguer and T. Gonz, *Physics D: Applied Physics* 2003, **182,** R182.

38 S. Sun and H. Zeng, J. Am. Chem. Soc., 2002, **124**, 8204.

39 S. Sun, H. Zeng, D. B. Robinson, S. Raoux, P. M. Rice, S. X. Wang and G. Li, *J. Am. Chem. Soc.*2004, **4**, 126.

40 J. Park, K. An, Y. Hwang, J.-G. Park, H.-J. Noh, J.-Y. Kim, J.-H. Park, N.-M. Hwang and T. Hyeon, *Nat. Mater.*, 2004, **3**, 891–5.

41 P. Guardia, A. Labarta and X. Batlle, *J. Phys. Chem. C*, 2011, **115**, 390–396.

42 N. Pérez, F. López-Calahorra, A. Labarta and X. Batlle, *Phys. Chem. Chem. Phys.*, 2011, **13**, 19485.

43 B. D. Cullity and C. D. Graham, *Introduction to Magnetic Materials*, 2011.

44 U. Schwertmann and R. M. Cornell, Iron Oxides in the Laboratory, 2008.

45 Z. Szotek, W. M. Temmerman, D. Ködderitzsch, A. Svane, L. Petit, and H. Winter *Phys. Rev. B.*,2006, **74**, 174431.

46 J.H. Van Vleck.,*Physical Review*,1930, **208**, 41.

47 J. H. Van Vleck, *Phys. Rev.*, 1932, **41**, 208–215.

48 L. I. Schiff. *Quantum Mechanics*. McGraw-Hill.,1968.

49 P. Guardia, J. Pérez-Juste, A. Labarta, X. Batlle and L. M. Liz-Marzán, *Chem. Commun. (Camb).*, 2010, **46**, 6108.

50 P. Guardia, N. Pérez, A. Labarta and X. Batlle, *Langmuir*, 2010, **26**, 5843.

51 C. Moya, M. del P. Morales, X. Batlle and A. Labarta, *Phys. Chem. Chem. Phys.*, 2015, **17**, 13143.

52 P. Guardia. Doctoral thesis: Synthesis and characterization of high quality iron oxide nanoparticles of controlled size, shape and magnetic properties. 2010, Barcelona.

53 K. Osseo-Asare and F. Arriagada, *J. Colloid Interface Sci.*, 1999, **218**, 68.

54 F. Arriagada and K. Osseo-Asare, *J. Colloid Interface Sci.*, 1999, **211**, 210.

55 A. I. Figueroa, C. Moya, J. Bartolomé, F. Bartolomé, L. M. García, N. Pérez, A. Labarta and X. Batlle, *Nanotechnology*, 2013, **24**, 155705.

56 Z.P. Chen, Y. Zhang, S. Zhang, J.G. Xia, J.W. Liu, K. Xu, N. Gu, *Colloids Surf. A Physicochem. Eng. Asp.* 2008, **316**, 210.

57 G. Huang, C. Zhang, S. Li, C. Khemtong, S.-G. Yang, R. Tian, J.D. Minna, K.C. Brown, J. Gao, *J. Mater. Chem.* 2009, **19**, 6367.

58 S.I.C.J. Palma et al. / *Journal of Colloid and Interface Science* 2015, **437**, 147.
M. Hatakeyama, H. Kishi, Y. Kita, K. Imai, K. Nishio, S. Karasawa, Y. Masaike, S. Sakamoto, A. Sandhu, A. Tanimoto, et al., *J. Mater. Chem.* 2011, **21**, 5959.

59 L. Lartigue, C. Innocenti, T. Kalaivani, A. Awwad, M. del M. Sanchez Duque, Y. Guari, J. Larionova, C. Guérin, J.-L.G. Montero, V. Barragan-Montero, et al., *J. Am. Chem. Soc.* 2011, **133**, 10459.

60 A. Ruiz, G. Salas, M. Calero, Y. Hernández, A. Villanueva, F. Herranz, S. Veintemillas-Verdaguer, E. Martínez, D.F. Barber, M.P. Morales, *Acta Biomater.* 2013, **9** ,6421.

61 Y.-W. Jun, Y.-M. Huh, J.-S. Choi, J.-H. Lee, H.-T. Song, S. Kim, S. Yoon, K.-S. Kim, J.-S. Shin, J.-S. Suh, et al., *J. Am. Chem. Soc.* 2005, **127**, 5732.

62 Q. N. Fauconnier, J.N. Pons, J. Roger, A. Bee, *J. Colloid Interface Sci.* 1997, **194** , 427.

63 E. Taboada, E. Rodríguez, A. Roig, J. Oró, A. Roch, R.N. Muller, *Langmuir*, 2007, **23**, 4583.

64 J.H. Van Vleck.,*Physical Review*,1930, **208**, 41.

65 J. H. Van Vleck, *Phys. Rev.*, 1932, **41**, 208–215.

66 N. Pérez, P. Guardia, a G. Roca, M. P. Morales, C. J. Serna, O. Iglesias, F. Bartolomé, L. M. García, X. Batlle and a Labarta, *Nanotechnology*, 2008, **19**, 475704.

67 B. A. Lilley, *Philos. Mag.*, 1950, **41**, 792.

68 C. Kittel*, Phys. Rev.*, 1946, **70**, 965.

69 D. L. Leslie-Pelecky, R. D. Rieke, *Chem. Mater*. 1996, **8**, 1770.

70 H. Zijlstra, in Ferromagnetic Materials, Vol 3, E. P. Wohlfarth,ed., North-Holland, Amsterdam, 1982.

71 R. S. Tebble, Magnetic Domains, Methuen and Co., London 1969.

72 L. Néel. *C.R. Acad. Sci. Paris.* , 1949 **228** ,664.

73 E. Stoner, E. Wohlfart, *Philosophical Transactions of the Royal Society of London. Series A.*, 1948, **599**, 240.

74 I. Prigogine and S. A. Rice, Eds., *Advances in Chemical Physics*, John Wiley & Sons, Inc., Hoboken, NJ, USA, 1997, vol. 98.

75 R. Omari, J.J. Préjean ans J. Souletie, J. Phys. (Paris) 1984, **45**, 1809.

76 B. Castaign and J. Souletie, J. Phys. (France)., 1991, **1**, 403.

77 A. Labarta, O. Iglesias, Ll. Balcells, F. Badia, *Phys.Rev.B*. 1993, **48**, 10248.

78 C. Moya, G. Salas, M. del P. Morales, X. Batlle and A. Labarta, *J. Mater. Chem. C*, 2015, **3**, 4522.

79 C. P. Bean and J. D. Livingston, *J. Appl. Phys.*, 1959, **30**, S120.

80 Dorman, *Rev. Phys. Appl.*, 1981, **16**, 275.

81 J. I. Gittleman, B. Abeles, S. Bozowski, *Phys.Rev.B.*, 1974, **9**, 3891.

82 C. Moya, O. Iglesias, X. Batlle, A. Labarta. Quantification of dipolar interactions in Fe_3O_4 NPs. http://arxiv.org/ftp/arxiv/papers/1508/1508.00337.pdf

83 G. Binning, H. Rohrer, Helv. *Phys. Acta*. 1982, **55**, 726.

84 J.J. Sáenz, N. García, P. Grütter, E. Meyer, H. Heinzelmann, R. Wiesendanger, L. *Journal of applied physics* , 1987, **62** (10), 4293.

85 Y. Martin H.K. Wickramasinghe, Appl. Phys. Lett. 1987, **50**, 1455.

86 G. Binning, C.F. Quate, C.H. Gerber, *Phys. Rev. Lett.* 1986, **56**, 930.

87 I. Horcas, R. Fernández, J.M. Gómez-Rodríguez, J. Colchero, J. Gómez-Herrero, A. M. Baró, *Rev. Sci. Instrum.* 2007, **78**, 013705.

88 M. Jaafar, J. Gómez-Herrero, A. Gil, P. Ares, M. Vázquez and A. Asenjo, *Ultramicroscopy*. 2009, **109** (2) 693.

89 M. Jaafar, Doctoral thesis: Procesos de imanación en la nanoescala mediante Microscopía de Fuerzas Atómicas. 2009.

90 C. P. Green, H. Lioe, J. P. Cleveland, R. Proksch, P. Mulvaney, J. E. Sader, *Rev. Sci. Instrum.* 2004, **75**, 1988.

91 U. Hartmann, *Physics Letters A*, 1989, **137** (9) 475.

92 T. Kebe, A. Carl. *J. Appl. Phys.* 2004, **95**, 775.

93 R. García, R. Pérez *Surface Science reports,* 2002, **47**,197.

94 U. Dürig, O. Züger, A. Stalder; *J. Appl. Phys*. 1992, **72**,1778.

95 S. Schreiber, M. Savla, D. V Pelekhov, D. F. Iscru, C. Selcu, P. C. Hammel and G. Agarwal, *Small*, 2008, **4**, 270.

96 A. Balan, P. M. Derlet, A. F. Rodríguez, J. Bansmann, R. Yanes, U. Nowak, A. Kleibert and F. Nolting, *Phys. Rev. Lett.*, 2014, **112**, 107201.

Chapter 2.The synthesis method and the final structure of the nanoparticles

PCCP

Accepted Manuscript

This article can be cited before page numbers have been issued, to do this please use: C. Moya, X. Batlle and A. Labarta, *Phys. Chem. Chem. Phys.*, 2015, DOI: 10.1039/C5CP03395K.

Dynamic Article Links ►
View Article Online
DOI: 10.1039/C5CP03395K

Cite this: DOI: 10.1039/c0xx00000x

www.rsc.org/xxxxxx

ARTICLE TYPE

The role of the oleic acid on the synthesis of $Fe_{3-x}O_4$ nanoparticles over a wide size range

Carlos Moya,* Xavier Batlle, Amílcar Labarta

Received (in XXX, XXX) Xth XXXXXXXXX 20XX, Accepted Xth XXXXXXXXX 20XX
DOI: 10.1039/b000000x

This work reports on the role of the oleic acid concentration on the magnetic and structural properties of $Fe_{3-x}O_4$ nanoparticles synthesized by thermal decomposition of $Fe(acac)_3$ in benzyl-ether. This method allows the synthesis of highly monodisperse particles ranging from 7 to 100 nm in size by only varying the concentration of the oleic acid in the reaction mixture. The structural and magnetic characterizations reveal homogeneous particles in composition, with narrow particle size distribution, which are single-phase magnetite with almost bulk-like values of the saturation magnetization of about 90-99 emu/g at low temperatures and showing the characteristic anomaly in the zero field-cooling magnetization curves associated with the Verwey transition for nanoparticles bigger than about 7 nm. In addition, the analyses of aliquots of the reaction mixtures by Fourier transform infrared spectroscopy at various stages shed light about the nucleation and growing processes of the particles.

Introduction

$Fe_{3-x}O_4$ nanoparticles (NPs) have been widely investigated because of their high value of the saturation magnetization at room temperature, low-toxicity, easy functionalization and fast response to an external magnetic field.[1,2] Those properties make them excellent candidates for potential applications in technology and biomedicine[3], such as catalysis,[4] hyperthermia,[5,6] drug delivery,[7] NMR contrast agents or data storage.[8-10] Besides and from the fundamental point of view,[11] those NPs are ideal system models to study the new magnetic phenomenology associated with the so-called *particle-like* behaviour, which emerges from the size reduction towards the nanometer scale and contrasts with the well-established magnetic properties of their bulk-counterparts. It has been shown that most of the particle-like behaviour and in general the large variability of the magnetic properties observed in this kind of nanomaterials are related to structural features of the NPs rather than being originated from intrinsic finite-size or surface effects, at least for NPs bigger than a few nanometers.[12-15] These structural features, such as crystallographic defects, polycrystalline nature of the NPs, lack of crystallinity at the particle surface, etc., have strong influence on their magnetic properties and can be modified at will through the synthesis method. So that, whenever this particle-like behaviour is unwanted for specifics applications, the choice of a suitable synthesis method is of key importance to obtain nanoparticles of high-crystalline quality.[16] The thermal decomposition of an organic precursor stands up among those methods used to obtain $Fe_{3-x}O_4$ NPs, since it yields monodisperse NPs with excellent magneto-structural properties, such as single-phase NPs which are crystalline monodomains and exhibit high values of the saturation magnetization very close to that of the bulk material.[17-19] Typically, in this method, either decanoic or oleic acids and oleylamine are used as surfactants that react with the metallic organic precursor to form an intermediate Fe^{3+}-complex that in turn decomposes to form $Fe_{3-x}O_4$,[20,21] together with 1,2-hexadecanediol as stabilizer agent and several organic solvents with high boiling points as reaction medium.[14,22] However and although all the chemicals needed for the reaction are well-established, some drawbacks and lack of reproducibility are observed when trying to scale up the method due to the great number of reactants involved, fact that complicates a proper characterization of the reaction mechanisms. In this sense, we reported on the synthesis of iron oxide NPs in a wide size range from a reaction mixture containing only decanoic acid and iron acetylacetonate.[23, 24]

Within this framework, we present a systematic study where we control the size of the obtained $Fe_{3-x}O_4$ NPs from about 7 to 100 nm by only varying the amount of oleic acid in the reaction mixture, using in all the cases benzyl-ether as the carrier solvent. In addition, we show that the samples exhibit excellent magnetic properties very close to those of bulk magnetite. To gain a deeper insight into the reaction mechanisms some aliquots of the reaction mixture at several stages were studied by Fourier transform infrared (FTIR) spectroscopy. The results show that the iron acetylacetonate totally decomposes at 200 ºC to form an intermediate metal-complex, no matter the amount of oleic acid present in the reaction. Therefore, we demonstrate that the nucleation and growth processes of the NPs caused by the further decomposition of the intermediate metal-complex can be controlled by means of solely the concentration of oleic acid.

View Article Online
DOI: 10.1039/C5CP03395K

Experimental Section

Sample preparation

Five samples of $Fe_{3-x}O_4$ NPs were synthesized in order to study the effect of the oleic acid concentration on particle size and magneto-structural properties, by using iron (III) acetylacetonate (Sigma-Aldrich, 99%) as precursor, and oleic acid (Sigma-Aldrich 90) and benzyl-ether (Sigma-Aldrich, 98%) as surfactant and organic solvent, respectively. All the reactants were used in the synthesis without further purification.

Sample R1. 0.36 g of $Fe(acac)_3$ (1 mmol) and 1.73 g of oleic acid (6 mmol) were mixed in 25 mL of benzyl-ether. The reaction mixture was degassed at 60 ºC for 30 min, then, heated up to 200 ºC, and kept at this temperature for 2 h under a nitrogen atmosphere and vigorous stirring. After that, the solution was heated up at 5 ºC/min to reflux temperature (270 ºC) and kept at this temperature for 1 h. After cooling down to room temperature, a mixture of ethanol and 1-propanol with the volume ratio 3:1 was added to the solution. Then, the mixture was centrifuged to precipitate the NPs. The precipitate was decanted, washed several times and finally redispersed in hexane.

Samples R2-R5. Bigger NPs were obtained following the former procedure but reducing the concentration of oleic acid in the reaction mixture as follows: **R2** (1,15 g, 4 mmol), **R3** (0.87g, 3 mmol) **R4** (0.58 g, 2 mmol) and **R5** (without using oleic acid in the reaction mixture). The precipitate for samples **R2-R5** was redispersed in ethanol.

Experimental techniques

The shape and size of the NPs were determined by transmission electron microscopy (TEM) using a MT80-Hitachi microscope. To prepare the samples for TEM experiments, one drop of a dilute suspension of NPs in an appropriate solvent was placed onto a carbon-coated cooper grid and dried at room temperature. The size distributions were obtained by measuring at least 1500 particles and the resultant histograms were fitted to log-normal functions (see Fig. S1 for samples R1, R2, R3 and R4 and Fig. S3d for R5, Supporting information). The mean particle size (D_{TEM}) and the unitless standard deviation of the log-normal distribution (σ) were obtained from these fits (see Table 1). In order to get insight about the crystal quality of the samples, high resolution transmission microscopy (HRTEM) was carried out by using JEOL-2100 microscope (see Fig. 1e-h and Fig. S2 and S3b-c, Supporting information).

The crystallographic structure of the particles was identified by X-ray powder diffraction (XRD) performed in a PANalytical X'Pert PRO MPD diffractometer by using Cu Kα radiation. The patterns were collected within 5 and 120º in 2θ. In all cases, the XRD spectra were indexed to an inverse spinel structure (see Fig. 3). The mean size of the crystal domains (D_{XRD}) obtained from XRD spectra are given in Table 1.

The organic fraction of the samples was evaluated by thermogravimetric analysis (TGA). Measurements were performed in a TGA-SDTA 851e/SF/1100 (Mettler Toledo) at a heating rate of 10 ºC min^{-1} in nitrogen atmosphere from room temperature up to 800 ºC (see Fig. S4, Supporting information).

2 mL aliquots of the reaction mixtures collected at several stages along the reactions to synthesize R1-R5 samples were studied by means of Fourier transform infrared (FTIR) spectroscopy (see Fig. 7 and Fig. S6, Supporting information) with a Thermo SCIENTIFIC NICOLET iZ10 in the energy range between 4000 and 400 cm^{-1} with a spectral resolution of 4 cm^{-1}.

Magnetization measurements in powder samples were performed with a Quantum Design SQUID magnetometer. Hysteresis loops, $M(H)$, were recorded at several temperatures within 5 and 300 K under a maximum magnetic field of ± 50 kOe to study the saturation magnetization M_s and coercive field H_c (see Fig. 4 and S5a, Supporting information). M_s was obtained by extrapolation of the high-field region of $M(H)$ to zero field, assuming the high-field behaviour $M(H) = M_s + \chi \cdot H$, where χ is a residual susceptibility (see Table 1). M_s values were normalized to the magnetic content by subtracting the organic fraction determined by TGA measurements. H_c was defined as $H_c = (|H_c^+| + |H_c^-|)/2$. In order to investigate the presence of various magnetic phases, hysteresis loops were recorded after field cooling the sample from 300 K down to the final measuring temperature under an applied magnetic field of 10 kOe (see Fig. 5 and S5a, Supporting information). The thermal dependence of the magnetization was studied after zero field cooling (M_{ZFC}) and field cooling (M_{FC}) the samples. These curves were collected using the following protocol. The sample was cooled down from 300 to 2 K in zero magnetic field. Then, a static magnetic field of 50 Oe was applied and M_{ZFC} was measured while warming up from 2 to 300 K. Once room temperature was reached, the sample was cooled down again to 2 K while 50 Oe was applied. Finally, the sample was rewarmed up to 300 K and M_{FC} was collected under an applied field of 50 Oe (see Fig. 6 and S5b, Supporting information).

Results and discussion

Structural characterization

TEM images for samples R1-R4 show particles with narrow size distributions (see Table 1 and Fig. S1, Supporting information) and distinct shapes depending on the NP size, that go from pseudo-spherical NPs for R1 to faceted ones for R2-R4 (see Fig. 1a-d). In addition, micrograph images for R1 and R2, those samples with the smallest particles, reveal the formation of self-assemblies in a hexagonal close-packing arrangement of the NPs as a consequence of their monodispersity, shape regularity and the fact that the particles are smaller than about 20 nm in both samples. Besides, HRTEM images show certain degradation on the crystalline quality of the NPs as their size is increased (see Fig. 1e-h). In contrast to the good crystallinity observed in the HRTEM images for samples R1 and R2, samples R3 and R4 show particles with some crystalline defects and irregularities that could be attributed to faster particle growing during the synthesis (see Fig. S2, Supporting information). From these results, it can be concluded the key role of the oleic acid concentration on the reaction mixture to tune the mean particle size, as it is shown in Fig. 2 where an abrupt increase on the average size of the particles is observed as the oleic acid concentration is reduced.

View Article Online
DOI: 10.1039/C5CP03395K

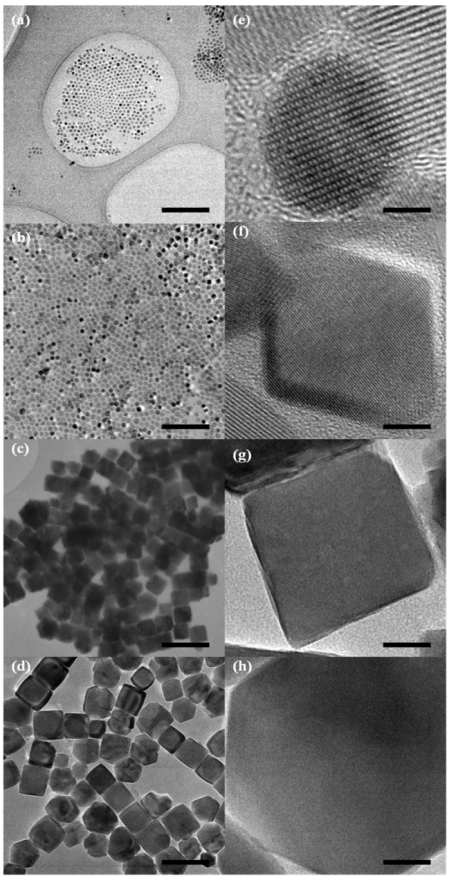

Figure 1. TEM images of iron oxide NPs: (a) R1, (b) R2, (c) R3 and (d) R4. HRTEM images of the same NPs: (e) R1, (f) R2, (g) R3 and (h) R4. Scale bars are as follows. (a)-(d) 150 nm, (e) 2 nm, (f) 4 nm and (g)-(h) 15 nm, respectively.

However, to obtain big NPs or even small ones with acceptable crystalline quality, a certain minimum amount of oleic acid (around to 2 mmol) must be present in the reaction mixture in order to participate in the formation of the intermediate metal-complexes (metal oleates) that in turn regulate the nucleation and growth of the NPs through further decomposition. In addition, oleic acid plays an important role on the final size and dispersity of the particles since it forms a dynamic layer around the nuclei that actively controls the growing process. This was evidenced by synthesizing sample R5 without oleic acid in the reaction mixture. In this way, TEM image in Fig. S3a for sample R5 shows irregular particles in shape with D_{TEM} = 10.6 nm, size much smaller than those obtained with 2-3 mmol of oleic acid. Besides, particles in sample R5 form aggregates as a consequence of poor benzyl-ether coating, and HRTEM images (see Fig. S3b and S3c, Supporting information) reveal the presence of NPs with different grade of crystalline quality that results from a bad control of the particle formation yielding partial coalescence of small crystallites and non-homogeneous particle growing.

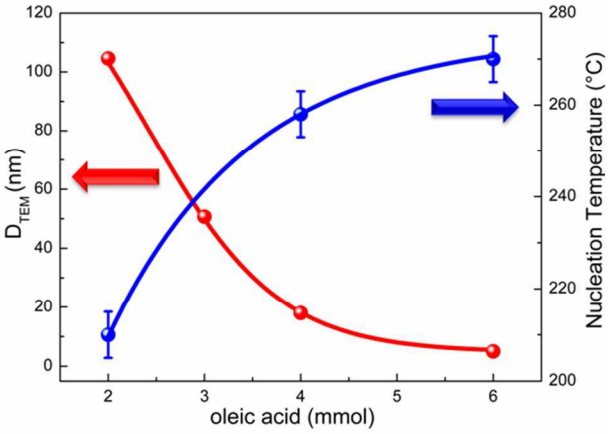

Figure 2. Dependences of the particle size obtained from TEM (red spheres) and the nucleation temperature (blue spheres) as a function of the oleic acid concentration in the reaction mixture. The solid lines are guides to the eye.

Samples R1-R5 were also characterized by XRD diffraction spectroscopy (see Fig. 3 and S3e, Supporting information). All XRD patterns were indexed to a spinel structure without significant traces of any other Fe-oxide compounds. In addition, although there is agreement between D_{TEM} and D_{XRD} for R1 and R2, D_{XRD} is slightly smaller than D_{TEM} for R3-R5 due to the lack of perfect crystallinity of those samples.

TGA spectra for R1-R4 samples show the typical two weight-loss plateaus between 200-400 ºC and 500-750 ºC, that correspond to the removal of both the free oleic acid present in the samples and that attached to the surface of the NPs, respectively.[22] The slight weight-loss below 200 ºC is attributed to the evaporation of adsorbed water molecules.[22] The total weight-loss is within 27% and 3%, where the extreme values correspond to R1 and R4 samples, respectively (see Fig. S4, Supporting information).[22, 24] The reduction in the weight-loss as the size of the particles increases can be explained in terms of the smaller surface to volume ratio for the bigger particles (samples R3 and R4).

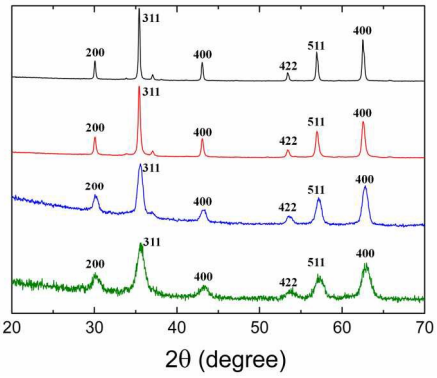

Figure 3. X-ray diffraction patterns together with the indexation of the Bragg peaks to an inverse spinel structure. Samples are showed as follows: R1 (solid green line), R2 (solid blue line), R3 (solid red line) and R4 (black solid line).

View Article Online
DOI: 10.1039/C5CP03395K

Magnetic characterization

First, the magnetic properties of the samples were studied by measuring hysteresis loops at 5 K with a maximum field of ± 50 kOe (see Fig. 4). All curves showed high values of M_s very close to that of bulk magnetite (98 emu/g at 5 K) (see Table 1) and similar to those published elsewhere,[1, 20, 21,23,24] which are associated with an almost perfect bulk-like ferrimagnetic order throughout the whole NPs. In addition, H_c at 5 K rose consistently with particle size from 264 ± 2 up to 327 ± 2 Oe for samples R1 to R3 (see inset to Fig. 4), since particles can be considered as single domain in this range of sizes. The high value of H_c found for R4 may be related to the tendency of those large, faceted particles to pile up forming linear chains (see Fig. 1d).[25] Interestingly, sample R5 showed particle-like behaviour, with a strong reduction of M_s and an increase of H_c in comparison to samples R1-R3 (see Table 1), which is characteristic of crystalline-defective particles.[15]

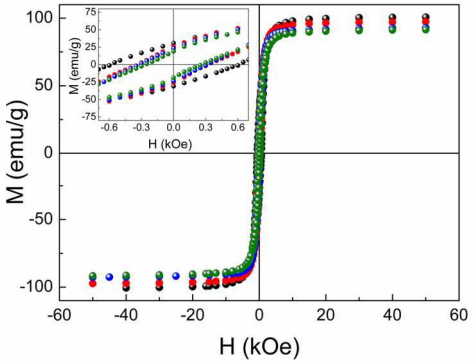

Figure 4. Hysteresis loops at 5 K. Samples are as follows: R1 (green spheres), R2 (blue spheres), R3 (red spheres) and R4 (black spheres). Inset: detail of the low-field region to evaluate the coercive fields.

In order to discard the existence of other magnetic species in the samples, hysteresis loops were recorded at 5 K after cooling the samples under 10 kOe from room temperature (see Fig. 5 and S4, Supporting information). None of the measured loops exhibited the typical features of particles containing ferromagnetic, antiferromagnetic (FeO in wustite phase) and/or ferromagnetic phases in close contact with each other, i.e. shifts along either the magnetic field or magnetization axes – exchange bias effects -.[13,26] Despite this fact, some FC effects on the hysteresis loops are evident in the group of samples R3-R5 in contrast with the invariance of the curves for R1 and R2 after FC. In the cases of R3 and R4, the increase in the magnitude of the magnetization after FC along the whole hysteresis loops could be attributed to a magnetic rearrangement of either some amount of multidomain particles or particle aggregates present in those samples because of their large size or special geometry.[27] On the contrary, the observed slightly effect of FC on the hysteresis loops for sample R5 (see Fig. S5a) could be originated at the enhancement of the magnetic order in NPs where ferrimagnetism is downgraded by crystalline defects.

Finally, the temperature dependence of the magnetic properties was measured. $M_{ZFC} - M_{FC}$ measurements were carried out under a field of 50 Oe and the results for the five samples are shown in Fig. 6 and S5, Supporting Information. $M_{ZFC} - M_{FC}$ curves for sample R1 branch off below about 235 K and M_{ZFC} develops a maximum around 150 K accordingly to the progressive blocking of a distribution of superparamagnetic magnetite NPs of about 7 nm in average size.

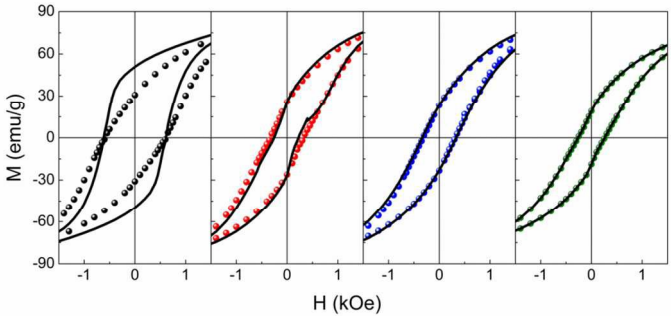

Figure 5. Comparison between the hysteresis loops collected at 5 K before and after FC the sample. Symbols are as follows. R1 (green spheres), R2 (blue spheres), R3 (red spheres) and R4 (black spheres), and the corresponding hysteresis loops of the samples after FC at 10 kOe (solid black lines).

On the contrary, $M_{ZFC} - M_{FC}$ curves for samples R2-R4 exhibit a completely different behaviour: NPs remain blocked even at room temperature as expected for bigger particles. Besides, there is a magnetization jump in the M_{ZFC} curves around $T \approx 120$ K which is attributed to the Verwey transition. Note that this transition is very sensitive to very small changes in the oxygen content of the magnetite phase,[28] so its observation in samples R2-R4 proves their accurate stoichiometry. On the other hand, $M_{ZFC} - M_{FC}$ curves for sample R5 (see Fig. S5b, Supporting information) show some kind of mixing between those two observed behaviours since the mean particle size is in between those for samples R1 and R2 and there might be a coexistence of superparamagnetic and blocked particles even at room temperature.

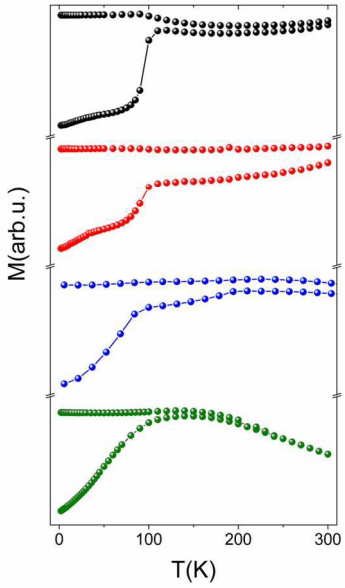

Figure 6. $M_{ZFC} - M_{FC}$ curves as a function of temperature. Samples are as follows: R1 (green spheres), R2 (blue spheres), R3 (red spheres) and R4 (black spheres).

View Article Online
DOI: 10.1039/C5CP03395K

FTIR spectra

So as to study the reaction mechanisms, 4 aliquots (2 mL) of the reaction mixtures collected at different stages of the reactions R1, R2, R4 and R5 were studied by FTIR spectroscopy (see Fig. 7). Figures 7a,b show the spectra of the reactions mixtures at 100 and 200 ºC, respectively. The bands shown in these two spectra are as follows. At long wavelengths (1725-1675 cm^{-1}), two bands appear associated with the stretching modes of the C=O in the COOH group and C=C which correspond to the oleic acid and benzyl-ether molecules, respectively (see the spectra for oleic acid and benzyl-ether in Fig. S6, Supporting Information).[29, 30] In addition, three bands characteristic of aromatic groups (stretching of C=C) are located between 1620-1580 cm^{-1} and 1515-1475 cm^{-1} (see the spectrum of benzyl-ether in Fig. S6, Supporting information). [30] At lower wavelengths, a typical band located at 1525 cm^{-1} and associated with the stretching mode of the C-O group of the $Fe(acac)_3$ is observed (see the spectrum of the $Fe(acac)_3$ in Fig. S6, Supporting information).[31] It is worth noting that the depth of this peak decreases slightly from 100 to 200 ºC (see Fig. 7a,b) suggesting that the $Fe(acac)_3$ starts to decompose below 200 ºC. In addition, the depletion of the peak in this range of temperatures results more abrupt once the amount of oleic acid increases, suggesting that it enhances the decomposition of the $Fe(acac)_3$ and the formation of an intermediate iron complex (Fe^{3+}-oleate).

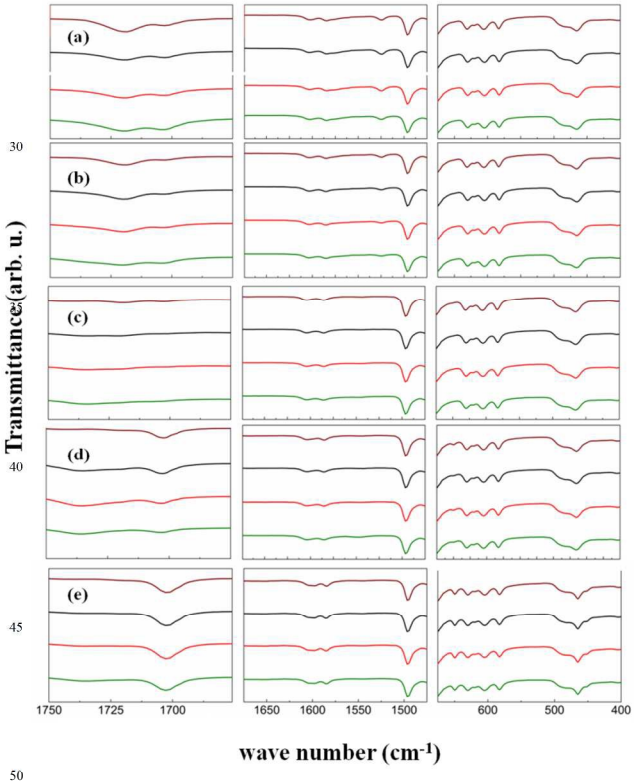

Figure 7. IR spectra for the reaction mixtures at (a) 100 ºC, (b) 200 ºC (0 min), (c) 200 ºC (120 min), (d) 270 ºC (0 min) and (e) 270 ºC (60 min). Curves are as follows: R1 (solid green line), R2 (solid red line), R4 (solid black line) and R5 (solid brown line).

On the other hand, four bands located between 675-400 cm^{-1} are associated with the bending modes of C-H group for the benzyl-ether (see Fig. S6, Supporting information).[30]

After 120 min at 200 ºC, the FTIR spectra of the reaction mixtures shown in Fig. 7c indicated the complete decomposition of $Fe(acac)_3$ (no trace of the peak at 1525 cm^{-1}), and the partial reaction of the benzyl-ether and the oleic acid with the $Fe(acac)_3$ to form Fe^{3+}-complexes since a significant shrinkages of the peaks in between 1725-1675 cm^{-1} were also observed. It is worth noting that the spectra at lower wave numbers (675-400 cm^{-1}) do not show any difference with the spectra at lower temperatures.

When the temperature of the reaction mixtures was risen up to 270 ºC (see Fig. 7d), the spectra for all the samples showed two additional bands between (1720-1685) and (675-630) cm^{-1} that are associated with the stretching modes of C=O and Fe-O groups, respectively. These results indicate the formation of $Fe_{3-x}O_4$ NPs and the attachment of an Fe^{3+}-complex to the NPs' surface. After keeping the reaction mixtures 60 min at this temperature (see Fig. 7e), a dramatically increase of the peaks are observed together with the appearance of a new band between 500-450 cm^{-1} (Fe-O stretching), which in fact is a typical band observed in $Fe_{3-x}O_4$ NPs.[32] From these results one could conclude that both nucleation and growth processes of the NPs take place between 200 and 270 ºC.

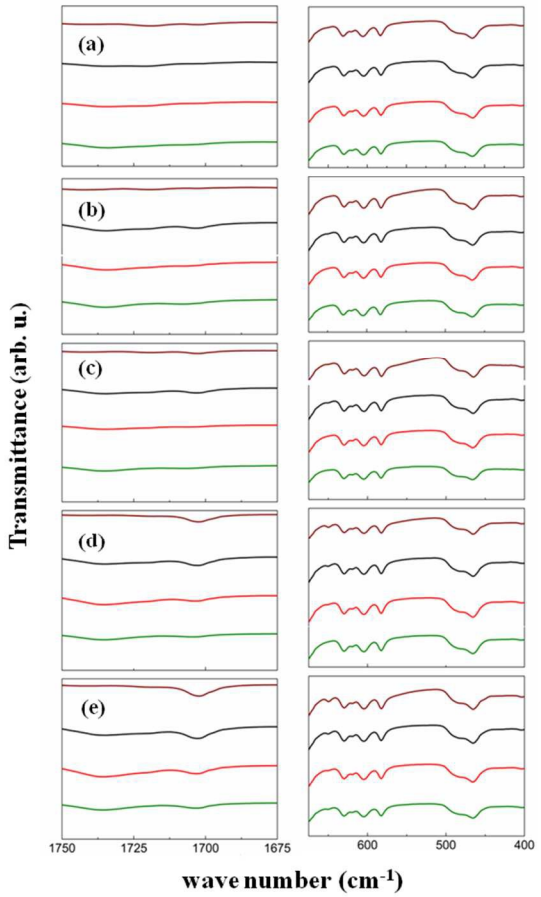

Figure 8. IR spectra for the reaction mixtures between 200 and 270 ºC. (a) 200 ºC, (b) 210 ºC, (c) 230 ºC, (d) 260 ºC and (e) 270 ºC. Curves are as follows: R1 (solid green line), R2 (solid red line), R4 (solid black line) and R5 (solid brown line).

View Article Online
DOI: 10.1039/C5CP03395K

In order to determine the temperatures at which the nucleation and growth processes actually occur, 7 aliquots (1 mL) of the reaction mixtures for samples R1, R2, R4 and R5, taken every 10 ºC between 200-270ºC, were studied by FTIR spectroscopy (see Fig. 8 and Fig. S7 and S8, Supporting information). Figure 8 shows the occurrence of a stepped nucleation process depending on the concentration of oleic acid in the reaction mixture. While at 200 ºC (after 120 min) there is no evidence of particles' nucleation for any reaction mixture (see Fig. 8a), the appearance at 210 ºC (see Fig. 8b) of the two new bands between (1720-1685) and (675-630) cm^{-1} for sample R4 (2 mmols of oleic acid) is a clear indication of the onset of the nucleation process for this low concentration of oleic acid. The nucleation temperatures for the reaction mixtures with higher concentration of oleic acid are around 260 ºC for sample R2 (4 mmols of oleic acid) (see Fig. 8d) and 270 ºC for sample R1 (6 mmols of oleic acid) (see Fig. 8e). At the same time, the spectra at 270 ºC (Fig. 8e) show a significant increase in the intensity of those two peaks for samples R2 and R4 indicating that the growth process comes about already between the nucleation and reflux temperatures. These results are summarized in Fig. 2, where the dependences of the nucleation temperature and the mean size of the NPs on the concentration of oleic acid are plotted together. From the comparison of these two curves it can be concluded that the higher the nucleation temperature the smaller the size of the particles, since the temperature interval in which the growth process takes place is progressively reduced as the nucleation temperature increases. Moreover, the nucleation temperature for the reaction without oleic acid (sample R5) is about 230 ºC (see Fig. 8c), however the final size of the particles is much smaller than expected when comparing with the cases of samples with similar nucleation temperatures (R3 and R4) but with oleic acid present in the reaction mixture. This result confirms the greater affinity of the oleic acid as coordinating group for iron than that of the benzyl-ether alone.

Summarizing these analyses, the formation of monodisperse NPs over a wide size is intrinsically related to the separation of the nucleation and growth processes along the reaction as was described by La-Mer and the amount of the surfactant on the reaction mixture.[23,24,33] In the first stages of the reaction, $Fe(acac)_3$ decomposes forming Fe^{3+}-complexes at 200 ºC in a slow process. The onset of the nucleation process takes place at higher temperature while the reaction mixture is heated up to 270 ºC at a constant rate. However, we have observed that the nucleation temperature is strongly dependent on the amount of oleic acid in the reaction mixture. Once the concentration of oleic acid increases, the nucleation temperature rises as well and consequently the growth process can be tuned.[17,33,34] Besides, the concentration of the surfactant self-regulates the growing of the NPs by becoming attached to the particle surface forming a surfactant coating that hinders the aggregation of more nuclei to the particle (see Fig. 9 for a schematic representation of the role of the oleic acid on the final size and shape of the NPs). Interestingly, it is also possible synthesizing NPs with only the presence in the reaction mixture of benzyl-ether acting simultaneously as solvent and surfactant (sample R5). Although the reaction mechanisms involved in this case are pretty similar to those for R1-R4, the obtained particles are much more polydisperse and crystalline defective (see Fig. S3, Supporting information) since benzyl-ether is both a worse surfactant and coordinating group for iron than oleic acid is.[35]

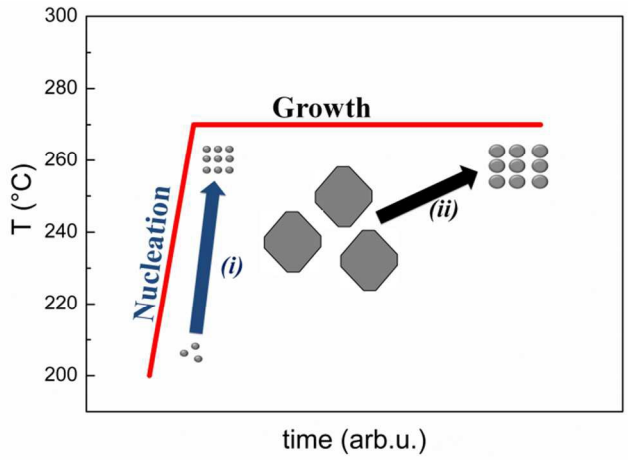

Figure 9. Schematic representation of the role of the oleic acid on the size of the NPs. Arrows at *(i)* and *(ii)* indicate an increase on the concentration of the oleic acid in the reaction mixture and the subsequent effect on the nucleation temperature, and the particle size and shape.

Conclusions

We have shown the effect of the concentration of oleic acid on the synthesis of $Fe_{3-x}O_4$ NPs using benzyl-ether as a solvent. This synthesis method enables the formation of monodisperse NPs ranging from 7 to 100 nm. Structural and magnetic characterization of the samples indicate highly crystalline, single-phase NPs, with values of M_s close to the bulk material and for NPs bigger than 7 nm exhibiting the typical Verwey transition associated with a composition very close to stoichiometric magnetite. In addition, the study by FTIR of the reactions mixtures at various stages contributes to the characterization of the nucleation and growing processes of the NPs. First, $Fe(acac)_3$ decomposes forming an intermediate iron complex at 200 ºC in a slow process. After that and depending on the oleic acid concentration in the reaction mixture, different nucleation temperatures have been observed. Finally, particle growth takes place mainly at the boiling point of the mixture, where the amount of oleic acid plays a self-regulating role on the final particle size by surface coating. Interestingly, the sample synthesized without oleic acid yielded highly defective crystalline NPs of about 10 nm in size, with low values of M_s , in accordance with uncompleted particle formation and poor surfactant coating. All in all, the careful control of the structural and magnetic properties of magnetite nanoparticles is of crucial interest to make them suitable for a number of technological and bio applications.

View Article Online
DOI: 10.1039/C5CP03395K

Acknowledgements

This work was supported by Spanish MINECO (MAT2012-33037), Catalan DURSI (2014SGR220) and European Union FEDER funds (Una manera de hacer Europa).

Notes and references

Departament de Física Fonamental, Institut de Nanociència i Nanotecnologia, Universitat de Barcelona, Martí i Franquès 1, Barcelona 08028, Catalonia, Spain . E-mail: cmoya@ffn.ub.es

Electronic Supplementary Information (ESI) available: For samples R1-R4, particle size distribution and thermogravimetric curves. HRTEM images for samles R3 and R4. For sample R5, TEM and HRTEM images, size distribution, XRD spectrum, hysteresis loop at 5 K and after field cooling the sample under 10 kOe from 300 K down to the final measuring temperature, zero field cooling and field cooling magnetizations as a function of temperature. FTIR spectra for iron (III) acetylacetonate, benzyl-ether and oleic acid. FTIR spectra for the reaction mixtures between 200 and 270 ºC every 10 ºC.

1 B. D. Cullity and C. D. Graham, *Introduction to Magnetic Materials*, 2011.
2 U. Schwertmann and R. M. Cornell, *Iron Oxides in the Laboratory*, 2008.
3 S. Laurent, D. Forge, M. Port, A. Roch, C. Robic, L. Vander Elst and R. N. Muller, *Chem. Rev.*, 2008, **108**, 2064–110.
4 A. Schätz, O. Reiser and W. J. Stark, *Chemistry a European Journal*, 2010, **16**, 8950–67.
5 G. F. Goya, E. Lima, A. D. Arelaro, T. Torres, H. R. Rechenberg, L. Rossi, C. Marquina and M. R. Ibarra, *IEEE Trans. Magn.*, 2008, **44**, 4444–4447.
6 G. Salas, J. Camarero, D. Cabrera, R. Ludwig, I. Hilger, R. Miranda, P. Morales, F. J. Teran and D.- Jena, *J. Phys. Chem. C*, 2014, **118**, 19985
7 J. Chomoucka, J. Drbohlavova, D. Huska, V. Adam, R. Kizek and J. Hubalek, *Pharmacol. Res.*, 2010, **62**, 144–9.
8 C. Sun, J. S. H. Lee and M. Zhang, *Adv. Drug Deliv. Rev.*, 2008, **60**, 1252–65.
9 R. Mejias, S. Pérez-Yagüe, A. G. Roca, N. Perez, A. Villanueva, M. Cañete, S. Manes, J. Ruiz-Cabello, M. Benito, A. Labarta, X. Batlle, S. Veintemillas-Verdaguer, M.P. Morales, D. F. Barber, C. J. Serna, *Nanomedicine*, 2010, **5,** 397.
10 C. Liang, S. Huang, W. Zhao, W. Liu, J. Chen, H. Liu and Y. Tong, *New J. Chem.*, 2015, **39**, 2651–2656.
11 X. Batlle and A. Labarta, *J. Phys. D: Appl. Phys.* 2002, **35**, R15.
12 C. P. Bean and J. D. Livingston, *J. Appl. Phys.*, 1959, **30**, S120.
13 M. Estrader, A. López-Ortega, I. V Golosovsky, S. Estradé, A. G. Roca, G. Salazar-Alvarez, L. López-Conesa, D. Tobia, E. Winkler, J. D. Ardisson, W. A. A. Macedo, A. Morphis, M. Vasilakaki, K. N. Trohidou, A. Gukasov, I. Mirebeau, O. L. Makarova, R. D. Zysler, F. Peiró, M. D. Baró, L. Bergström and J. Nogués, *Nanoscale*, 2015, **7**, 3002–15.
14 C. Moya, M. del P. Morales, X. Batlle and A. Labarta, *Phys. Chem. Chem. Phys.*, 2015, **17**, 13143.
15 C. Moya, G. Salas, M. del P. Morales, X. Batlle and A. Labarta, *J. Mater. Chem. C*, 2015, **3**, 4522–4529.
16 A. G. Roca, R. Costo, A. F. Rebolledo, S. Veintemillas-Verdaguer, P. Tartaj, T. González-Carreño, M. P. Morales and C. J. Serna, *J. Phys. D. Appl. Phys.*, 2009, **42**, 224002.
17 S. Sun and H. Zeng, *J. Am. Chem. Soc.*, 2002, **124**, 8204–8205.
18 S. Sun, H. Zeng, D. B. Robinson, S. Raoux, P. M. Rice, S. X. Wang and G. Li, 2004, **4**, 126–132.
19 J. Park, K. An, Y. Hwang, J.-G. Park, H.-J. Noh, J.-Y. Kim, J.-H. Park, N.-M. Hwang and T. Hyeon, *Nat. Mater.*, 2004, **3**, 891–5.
20 P. Guardia, A. Labarta and X. Batlle, *J. Phys. Chem. C*, 2011, **115**, 390–396.
21 N. Pérez, F. López-Calahorra, A. Labarta and X. Batlle, *Phys. Chem. Chem. Phys.*, 2011, **13**, 19485–9.
22 A. G. Roca, M. P. Morales, K. O'Grady and C. J. Serna, *Nanotechnology*, 2006, **17**, 2783–2788.
23 P. Guardia, J. Pérez-Juste, A. Labarta, X. Batlle and L. M. Liz-Marzán, *Chem. Commun. (Camb).*, 2010, **46**, 6108–10.
24 P. Guardia, N. Pérez, A. Labarta and X. Batlle, *Langmuir*, 2010, **26**, 5843–7.
25 D. Serantes, K. Simeonidis, M. Angelakeris, O. Chubykalo-Fesenko, M. Marciello, M. del P. Morales, D. Baldomir and C. Martinez-Boubeta, *J. Phys. Chem. C*, 2014, **118**, 5927–5934.
26 J. Nogués, J. Sort, V. Langlais, V. Skumryev, S. Suriñach, J. S. Muñoz and M. D. Baró, *Phys. Rep.*, 2005, **422**, 65–117.
27 D. L. Leslie-Pelecky, R. D. Rieke, *Chem. Mater.* 1996, ***8***, 1770.
28 E. J. W. Verwey *Nature*, 1939, **144**, 327.
29 To see the spectrum of the oleic acid: http://pubchem.ncbi.nlm.nih.gov/substance/24278605#section=Source
30 To see the spectrum of the benzyl ether: http://webbook.nist.gov/cgi/cbook.cgi?ID=C538863&Mask=80
31 To see the spectrum of the $Fe(acac)_3$: http://webbook.nist.gov/cgi/cbook.cgi?ID=C14024181&Mask=80
32 A. G. Roca, M. P. Morales, C. J. Serna, *IEEE Trans.Magn,* 2006, **42**, 3025.
33 V. K. LaMer and R. H. Dinegar, J. Am. Chem. Soc., 1950, **72**, 4847.
34 T. Sugimoto; Monodispersed particles. Elsevier: Amsterdam, Holland, 2001
35 J. de la Fuente and V. Grazu, Nanobiotechnology, Volume 4: Inorganic Nanoparticles vs Organic Nanoparticles, 2012.

View Article Online
DOI: 10.1039/C5CP03395K

Table 1. Summary of the structural, microstructural and magnetic parameters of the samples.

Samples	D_{TEM} (nm)	σ	D_{XRD} (nm)	% weight-loss	M_s at 5k (emu/g)	M_s at 300 K (emu/g)	H_c at 5K (Oe)	H_c at 300 K (Oe)
R1	7.4	0.15	7.1 (0.4)	27	90(1)	75(1)	264(2)	SPM*
R2	16.2	0.14	15.4 (1.0)	17	91(1)	82(1)	320(1)	9(2)
R3	50.7	0.20	44.0 (1.5)	7	96(2)	90(2)	327(2)	82(2)
R4	104.6	0.11	94.0 (2.0)	3	99(2)	91(1)	598(10)	94(2)
R5	10.6	0.21	9.0 (0.5)	2	62 (2)	54 (2)	345 (5)	SPM

*SPM stands for superparamagnetic. Numbers in parentheses correspond to the experimental error.

Electronic Supplementary Material (ESI) for Physical Chemistry Chemical Physics.

Supporting Information

The role of the oleic acid on the synthesis of $Fe_{3-x}O_4$ nanoparticles over a wide size range

Carlos Moya, Xavier Batlle and Amílcar Labarta*

Departament de Física Fonamental, Institut de Nanociència i Nanotecnologia,

Universitat de Barcelona, Martí i Franquès 1, Barcelona 08028, Catalonia, Spain

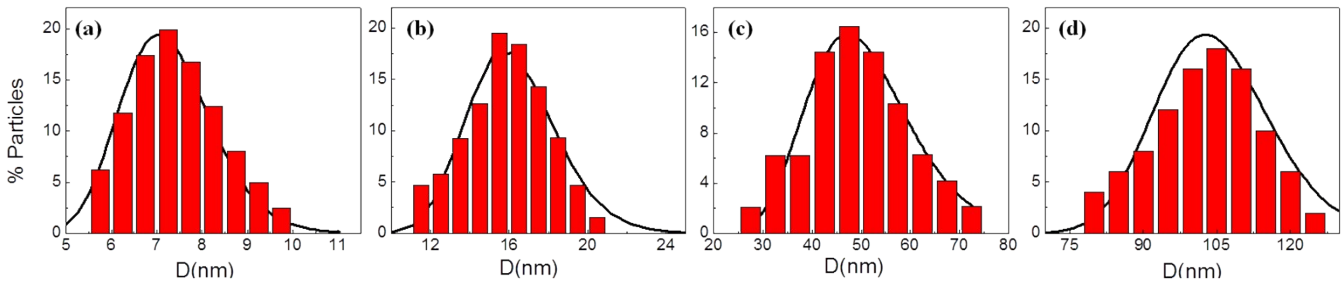

Figure S1. Histograms for the particle size of samples: (a) R1, (b) R2, (c) R3 and (d) R4.

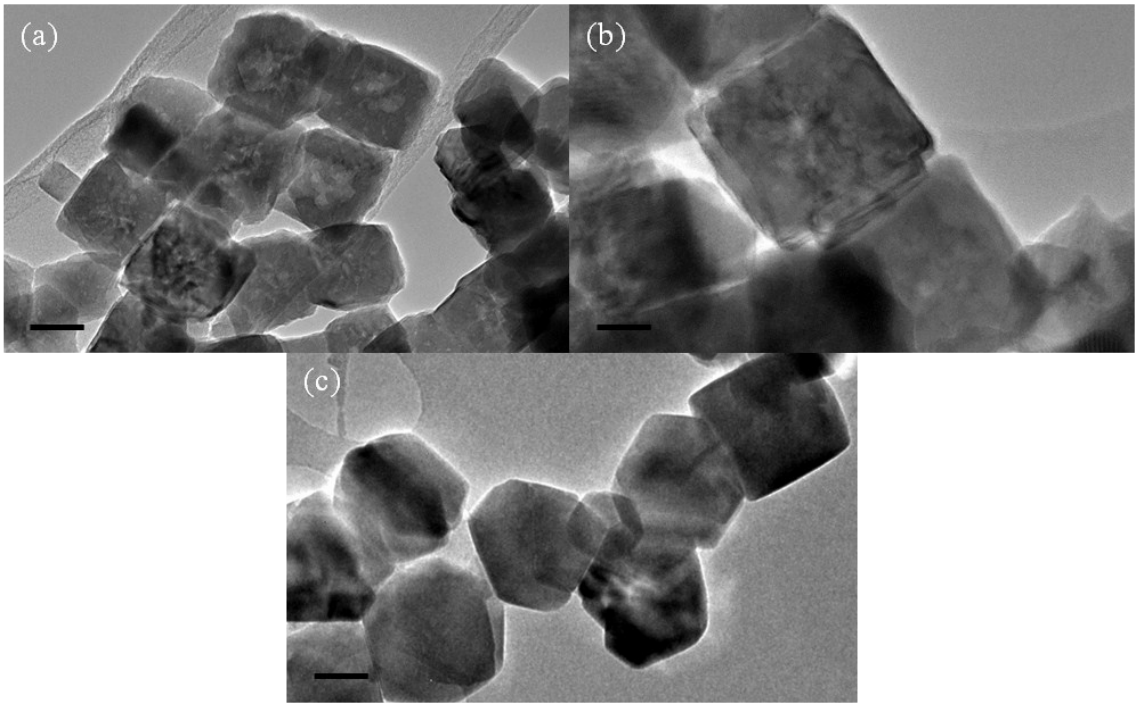

Figure S2. HRTEM images for samples with bigger NPs. (a) and (b) correspond to R3. (c) R4. Scale bars: (a) 30 nm, (b) 15 nm, (c) 50 nm.

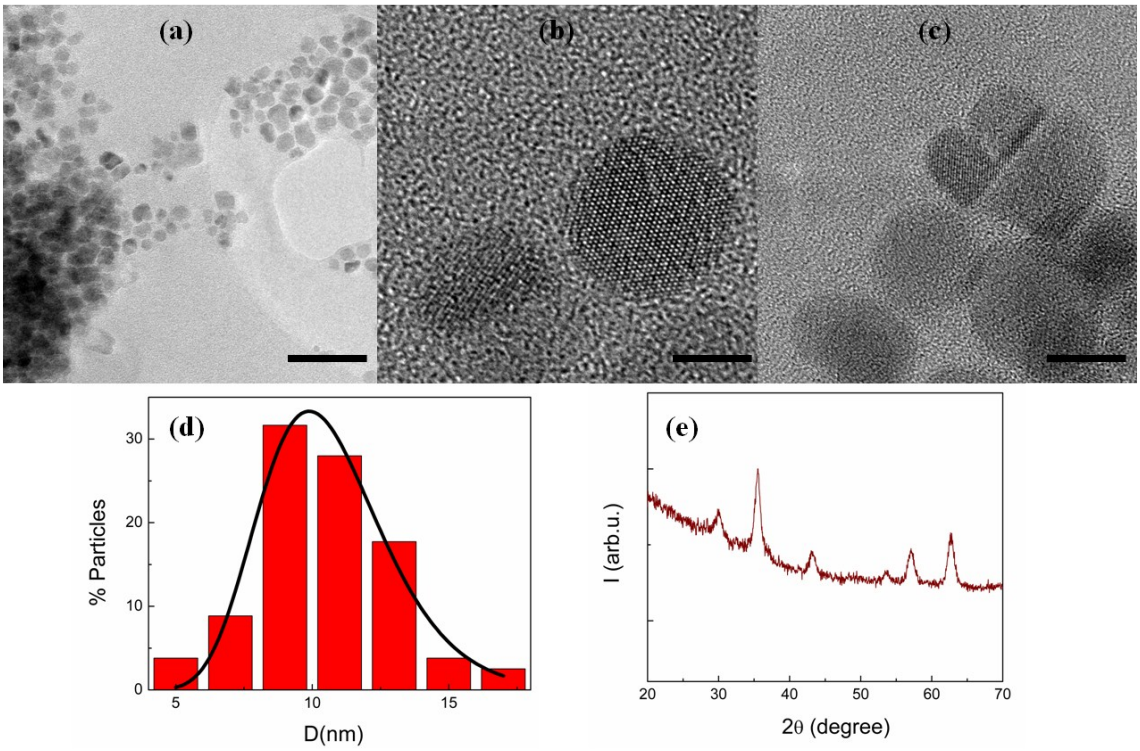

Figure S3. Structural characterization of sample R5. (a) TEM image at low resolution, (b) and (c) HRTEM images. Scale bars: (a) 50 nm, (b) 5 nm and (c) 7nm. (d) Particle-size distribution. (e) XRD spectrum of the sample.

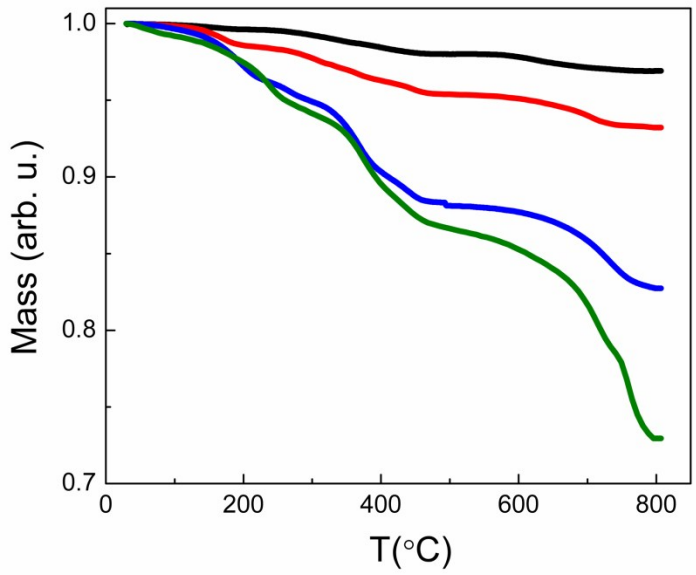

Figure S4. Thermogravimetric curves for the samples as follows: R1 (green solid line), R2 (blue solid line), R3 (red solid line) and R4 (black solid line).

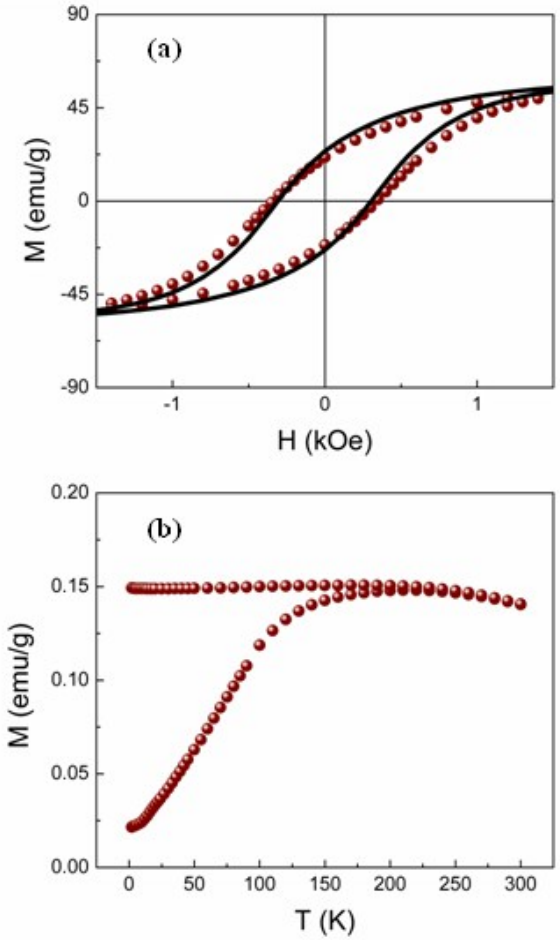

Figure S5. Magnetic characterization of the sample R5. (a) Hysteresis loop at 5 K (brown spheres) and after FC at 10 kOe (black solid line). (b) $M_{ZFC} - M_{FC}$ curves for the same sample.

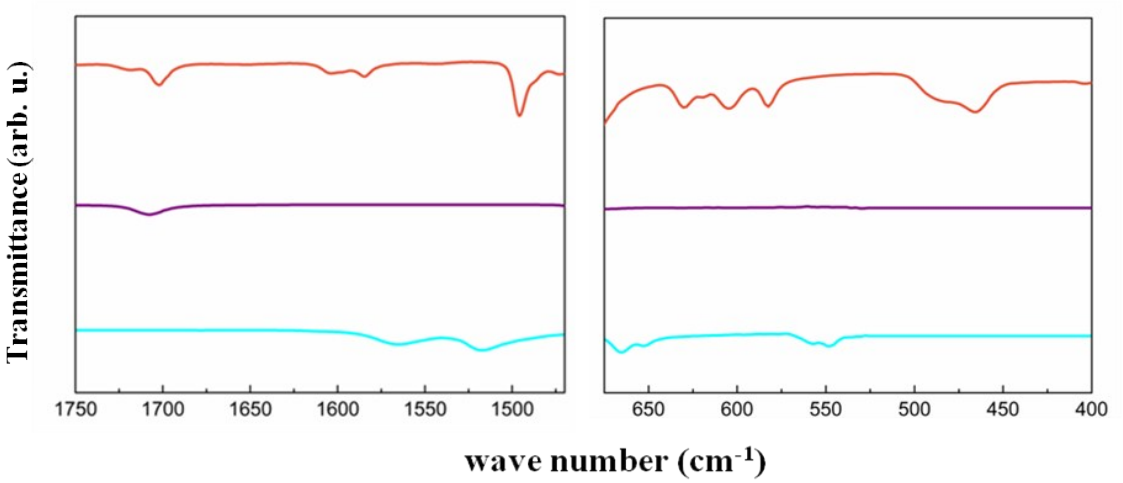

Figure S6. IR spectra of the reactants: $Fe(acac)_3$ (turquoise solid line), oleic acid (purple solid line) and benzyl-ether (red solid line).

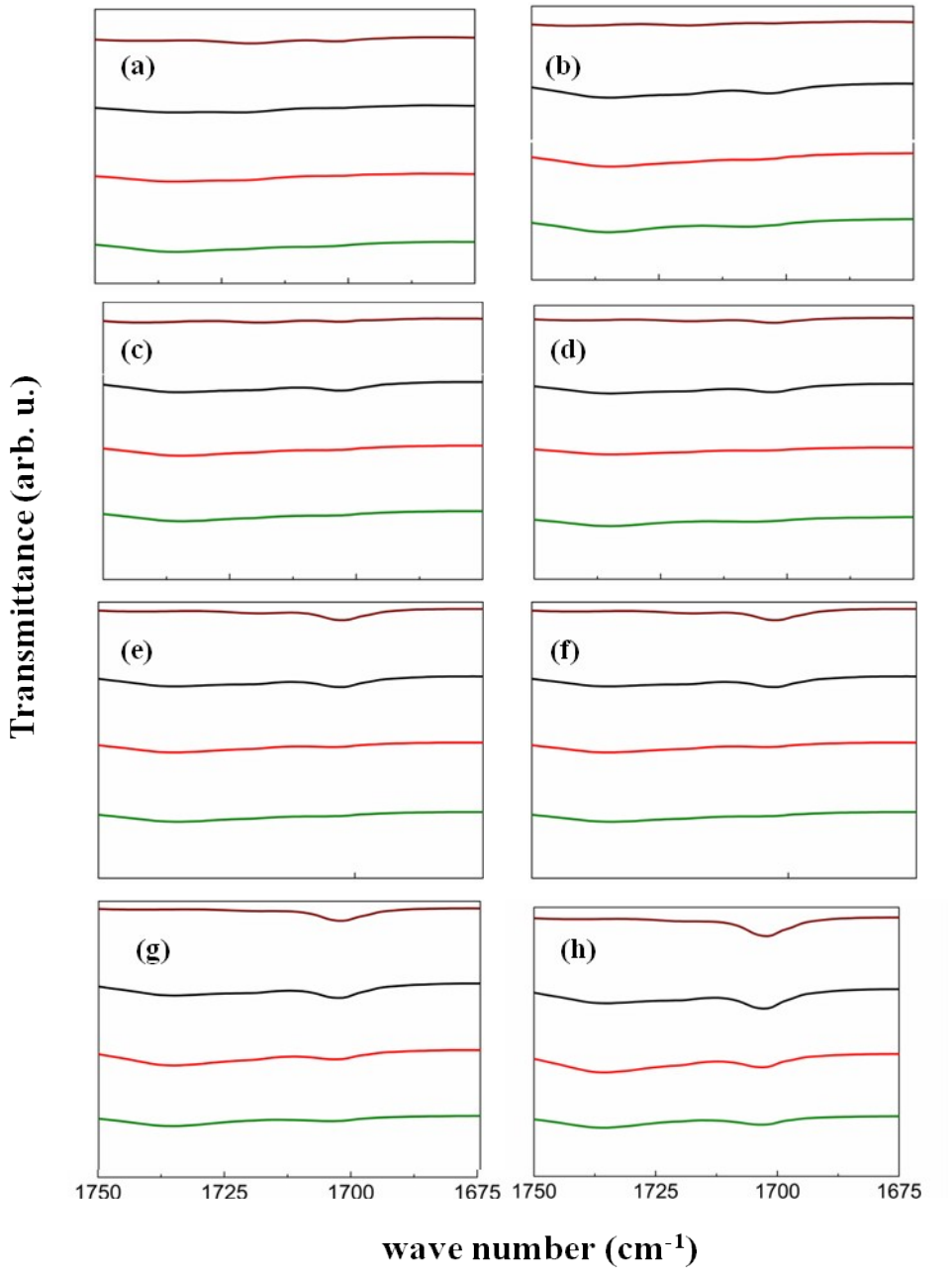

Figure S7. IR spectra for the reaction mixtures in the wave number range between 1750 and 1675 cm^{-1} at (a) 200 ºC, (b) 210 ºC, (c) 220 ºC (d) 230 ºC, (e) 240 ºC, (f) 250 ºC, (g) 260 ºC and (h) 270 ºC. Curves are as follows: R1 (solid green line), R2 (solid red line), R4 (solid black line) and R5 (solid brown line).

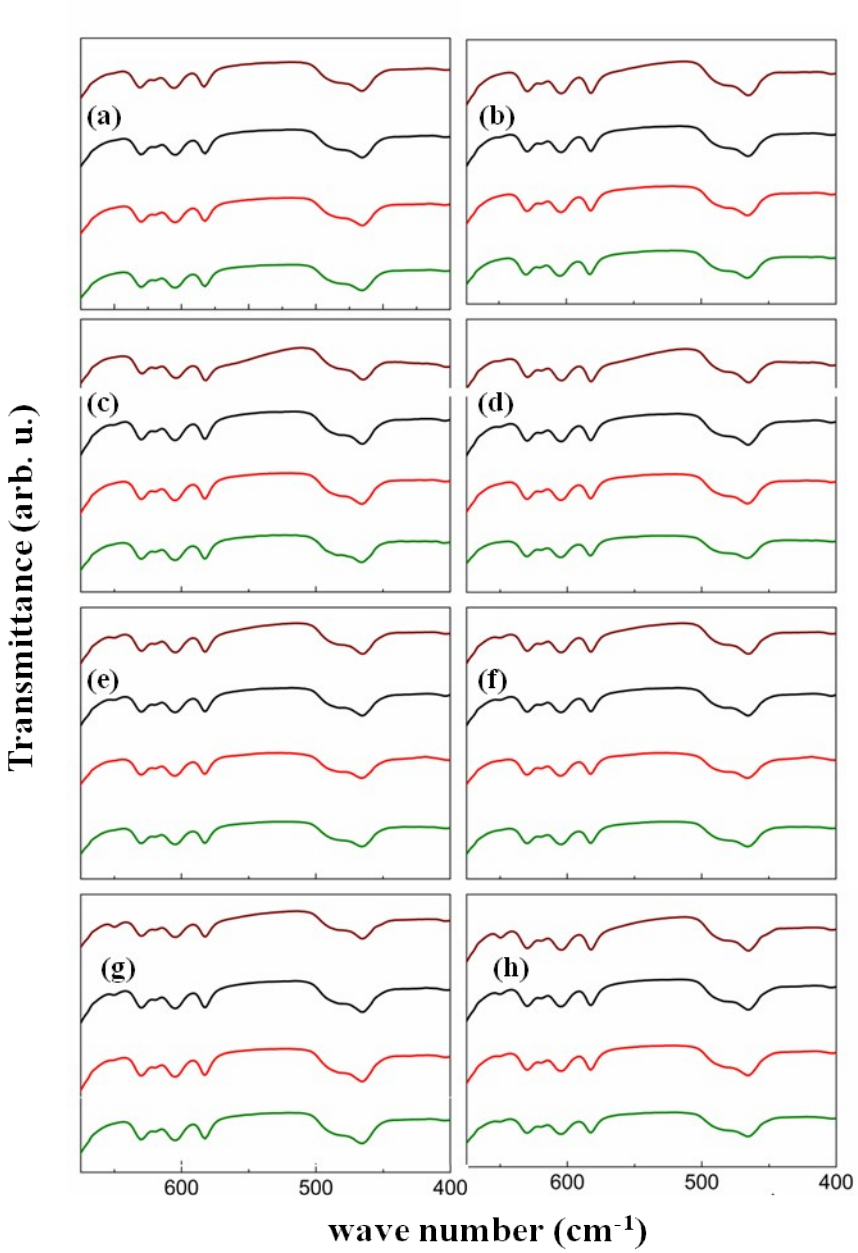

Figure S8. IR spectra for the reaction mixtures in the wave number range between 675 and 400 cm^{-1} at (a) 200 ºC, (b) 210 ºC, (c) 220 ºC (d) 230 ºC, (e) 240 ºC, (f) 250 ºC, (g) 260 ºC and (h) 270 ºC. Curves are as follows: R1 (solid green line), R2 (solid red line), R4 (solid black line) and R5 (solid brown line).

PCCP

PAPER

View Article Online
View Journal

Cite this: DOI: 10.1039/c5cp01052g

Tuning the magnetic properties of Co-ferrite nanoparticles through the 1,2-hexadecanediol concentration in the reaction mixture†

Carlos Moya,*[a] María del Puerto Morales,[b] Xavier Batlle[a] and Amílcar Labarta[a]

Received 19th February 2015,
Accepted 12th April 2015

DOI: 10.1039/c5cp01052g

www.rsc.org/pccp

This work reports on the effect of the 1,2-hexadecanediol content on the structural and magnetic properties of $CoFe_2O_4$ nanoparticles synthesized by thermal decomposition of metal–organic precursors in 1-octadecene. Although pseudo-spherical particles having an average size of about 8 nm and similar stoichiometry have been observed in all studied samples, a high level of variability in the crystal quality and, in turn, in the magnetic properties has been found as a function of the amount of 1,2-hexadecanediol added to the reaction mixture. The magnetic study reveals that samples progress from glassy magnetic behavior to bulk-like, ferrimagnetic order as the crystal quality improves. The analysis of the reaction mixtures by Fourier transform infrared spectroscopy at various stages of the reaction shows the key role of the 1,2-hexadecanediol in favoring the decomposition of the metal–organic precursor, formation of an intermediate $Co^{2+}Fe^{3+}$–oleate complex and, finally, the nucleation of nanoparticles at lower temperatures.

Introduction

Currently, Co-ferrite nanoparticles (NPs) are of great interest due to their high magnetic performance, including high values of the magnetocrystalline anisotropy, saturation magnetization and the magneto-optical coefficients.[1] These make these systems excellent candidates for several technological and biomedical applications, such as information storage media,[2] detection of biomolecules by magnetic separation,[3] cancer treatment by magnetic hyperthermia[4,5] and contrast enhancement agents in magnetic resonance imaging.[6,7] However, Co-ferrite NPs show magnetic properties with high variability depending on the preparation method, which limits the standardization of those procedures for large scale applications. Consequently, the choice of a suitable synthesis method, where one can get control over the size, shape, stoichiometry and the crystallinity of the particles, is of key importance to make progress in the fundamental understanding of the properties of nanoparticulate Co-ferrite systems as compared to those of bulk-counterparts.[8] Among the conventional synthesis methods,[9] the decomposition of organic precursors at high temperature is one of the best routes to synthesize particles with narrow size distribution, high crystal quality and an atomic metal composition very close to that of stoichiometric compounds.[10,11] In this method, 1,2-hexadecanediol is commonly added to the reaction mixture as a reducing agent.[10] However, in the past, we investigated the role of 1,2-hexadecanediol in the synthesis of iron oxide NPs[12,13] and we found that this reactant was not actually necessary to synthesize magnetite NPs with bulk-like properties in a wide range of sizes.[14–16] Aiming at clarifying the role of this reactant, we synthesized 8 nm Co-ferrite NPs from a reaction mixture containing metal acetylacetonates, oleic acid as a surfactant and 1-octadecene.[17] Although we obtained a narrow size distribution and the sample was single phase with a stoichiometry very close to that of bulk Co-ferrite, NPs showed magnetic glassy behavior associated with a highly defective crystal structure,[17] in contrast to the previous case of magnetite NPs. Within this framework, in this work we demonstrate the crucial role of 1,2-hexadecanediol content in the reaction mixture as a tuning parameter that progressively improves the crystal quality and magnetic properties of Co-ferrite NPs from highly defective crystal structures with glassy behavior to NPs exhibiting single crystalline domains with bulk-like magnetism. The reaction was studied by Fourier transform infrared (FTIR) spectroscopy at several reaction stages as the time elapsed and the results

[a] Departament de Física Fonamental, Institut de Nanociència i Nanotecnologia, Universitat de Barcelona, Barcelona, Spain. E-mail: cmoya@ffn.ub.es
[b] Instituto de Ciencia de Materiales de Madrid, CSIC, C/Sor Juana de Inés de la Cruz 3, Campus de Cantoblanco, Madrid, Spain. E-mail: puerto@icmm.csic.es

† Electronic supplementary information (ESI) available: For R2: TEM and HRTEM characterization and particle size distribution. Hysteresis loops at 5 and 300 K, hysteresis loops after field cooling the sample under 10 kOe from 250 K to the final measuring temperature, and zero field cooling and field cooling magnetizations as a function of temperature. FTIR spectra of iron(III) acetylacetonate, cobalt(II) acetylacetonate, $Co^{2+}Fe^{3+}$–oleate complexes and 1-octadecene. See DOI: 10.1039/c5cp01052g

showed that the decomposition of metal acetylacetonates to form a mixed-metal oleate complex takes place at earlier times and lower temperatures as the 1,2-hexadecanediol content is increased.

Experimental section

Sample preparation

In order to clarify the effect of 1,2-hexadecanediol content and reaction time on the structural and magnetic properties of $CoFe_2O_4$ nanoparticles,[17] four samples were synthesized using iron(III) acetylacetonate (Sigma-Aldrich, 99%), cobalt(II) acetylacetonate (Sigma-Aldrich, 97%), 1,2-hexadecanediol (Sigma-Aldrich, 90%), oleic acid (Sigma-Aldrich 90) and 1-octadecene (Sigma-Aldrich 90%). All reactants were used in the synthesis without further purification.

Samples R1a, R1b and R1c. 0.71 g of $Fe(acac)_3$ (2 mmol), 0.26 g of $Co(acac)_2$ (1 mmol), 0.72 g of 1,2-hexadecanediol (2.5 mmol) and 2.59 g of oleic acid (9 mmol) were mixed in 20 mL of 1-octadecene. After heating to 200 °C and keeping the temperature constant for 2 h, the solution was heated to reflux temperature, cooled to room temperature and washed several times with a mixture of hexane and acetone with a volume ratio of 1 : 3. Finally, NPs of sample R1a were collected by centrifugation at 8000 rpm. Two additional samples, R1b and R1c, were synthesized using the same route as that for R1a but the amount of 1,2-hexadecanediol being 1.435 g (5 mmol) and 2.87 g (10 mmol), respectively. Note that the concentration of 1,2-hexadecanediol for R1c is the standard one described in the literature.[10–12]

Samples R1 and R2. These particles were synthesized following a similar procedure to that used for the former reactions but without the addition of 1,2-hexadecanediol to the reaction mixtures. Particles of 8 nm in size were obtained from 0.71 g of $Fe(acac)_3$ (2 mmol), 0.26 g of $Co(acac)_2$ (1 mmol) and 2.59 g of oleic acid (9 mmol) in 20 mL of 1-octadecene. The solution was heated to 200 °C under an argon flow, vigorously stirred and kept at this temperature for 2 h. After that, the solution was heated to reflux temperature, cooled to room temperature immediately and washed several times with a mixture of hexane and acetone with a volume ratio of 1 : 3. NPs of sample R1 were collected by centrifugation at 8000 rpm. Sample R2, containing particles of about 12 nm in size, was prepared exactly by the same procedure as R1 but keeping it at reflux temperature for 1 h.

Experimental techniques

The particle shape and size were determined by transmission electron microscopy (TEM) using a MT80-Hitachi microscope. To prepare the samples for TEM experiments, one drop of dilute suspension of NPs in hexane was placed onto a carbon-coated copper grid and dried at room temperature. The size distributions were obtained by measuring at least 2000 particles and the resultant histograms were fitted to log-normal functions (see Fig. 1i for samples R1 and R1a–c and Fig. S1c for R2, ESI†). The mean particle size (D_{TEM}) and standard deviation (σ) were obtained from these fits (see Table 1). In order to get insight into the crystal quality of the samples, high resolution transmission microscopy (HRTEM) was carried out by using Titan high-base and JEOL-2100 microscopes (see Fig. 1e–h and Fig. S1b, ESI†).

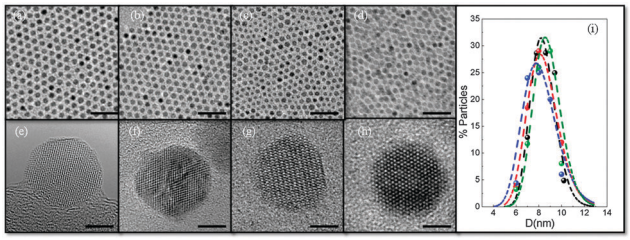

Fig. 1 TEM images of the Co-ferrite NPs: (a) R1, (b) R1a, (c) R1b, and (d) R1d. HRTEM images of the Co-ferrite NPs: (e) R1, (f) R1a, (g) R1b, and (h) R1d. Scale bars are 40 nm in length for (a), (b), (c) and (d), and 3 nm for (e), (f), (g) and (h). (i) Particle size distributions obtained by fitting TEM histograms to a log-normal distribution function: R1: black dashed line, R1a: red dashed line, R1b: blue dashed line and R1c: green dashed line. Experimental histograms are shown as solid spheres with the same color code.

The crystallographic structure of the particles was identified by X-ray powder diffraction (XRD) performed using a PANalytical X'Pert PRO MPD diffractometer with Cu Kα radiation. The patterns were collected within 5 and 120° of 2θ. In all cases, the XRD spectra were indexed to an inverse spinel structure (see Fig. 2). The mean size of the crystal domains (D_{XRD}) obtained from XRD spectra is given in Table 1.

The Fe and Co content in the samples were determined by inductively coupled plasma-optimal emission spectrometry (ICP-OES) by using a Perkin Elmer OPTIMA 3200RL after digesting the sample in a mixture of $HCl : HNO_3$; 5 : 25, and finally diluting them with distilled water (see Table 1).

The organic fraction of the samples was evaluated by thermogravimetric analysis (TGA). Measurements were performed using a TGA-SDTA 851e/SF/1100 (Mettler Toledo) at a heating rate of 10 °C min^{-1} in a nitrogen atmosphere from room temperature up to 800 °C.

2 mL aliquots of the reaction mixtures collected at several times along the reactions to synthesize R1 and R1a–c were studied by means of Fourier transform infrared (FTIR) spectroscopy using a Thermo SCIENTIFIC NICOLET iZ10 in the energy range between 4000 and 400 cm^{-1} with a spectral resolution of 4 cm^{-1}.

Magnetization measurements in powder samples were performed using a Quantum Design SQUID magnetometer (see Fig. 3 and Fig. S2b, ESI†). Hysteresis loops, $M(H)$, were recorded at several temperatures within 5 and 300 K under a maximum magnetic field of ±50 kOe to study the saturation magnetization M_s, and the coercive field H_c. M_s was obtained by extrapolation of the high-field region of $M(H)$ to the zero field, assuming the high-field behaviour: $M(H) = M_s + \chi \cdot H$, where χ is the residual susceptibility (see Table 1). M_s values were normalized to the magnetic content by subtracting the organic fraction determined by TGA measurements. H_c was defined as $< H_c = (|H_c^+| + |H_c^-|)/2$, and the shift of the hysteresis loop along the

Table 1 Summary of the structural, microstructural and magnetic parameters of the samples[a]

Samples	D_{TEM} (nm)	σ (nm)	D_{XRD} (nm)	T_p (K)	Co : Fe (KP-OES)	T_{irr} (K)	M_s at 5 K (emu g^{-1})	M_s at RT (emu g^{-1})	H_c at 5 K (kOe)	H_c at RT (kOe)
R1	8.6	5.2	2.1 (0.6)	150	1.0 : 2.0	170	25 (1)	20 (1)	6.8 (0.2)	SPM[b]
R1a	8.4	5.0	3.2 (0.4)	ISO	1.0 : 2.0	213	38 (1)	31 (2)	7.3 (0.3)	SPM
R1b	8.8	5.3	6.2 (0.4)	222	1.0 : 2.0	250	70 (2)	60 (2)	15.1 (0.3)	SPM
R1c	8.1	4.9	8.0 (0.2)	270	1.0 : 2.0	300	79 (2)	67 (1)	17.2 (0.2)	0.007 (0.001)
R2	12.2	7.4	2.9 (0.4)	>300	1.0 : 2.0	>300	35 (1)	30 (1)	9.1 (1)	0.066 (0.001)

[a] The values in parentheses indicate the experimental error of the data. [b] Stands for superparamagnetic behaviour.

field axis as $H_s = (|H_c^+| - |H_c^-|)/2$. In order to study H_s, hysteresis loops were recorded after field cooling the sample from 250 K down to the final measuring temperature under an applied magnetic field of 10 kOe. The thermal dependence of the magnetization was studied after zero field cooling (M_{ZFC}) and field cooling (M_{FC}) the samples (see Fig. 4 and Fig. S2a, ESI†). These curves were collected using the following protocol. The sample was cooled down from 300 to 2 K in a zero magnetic field. Then, a static magnetic field of 50 Oe was applied and M_{ZFC} was measured while heating from 2 to 300 K. Once room temperature was reached, the sample was cooled down again to 2 K while 50 Oe was applied. Finally, the sample was reheated to 300 K and M_{FC} was collected under the applied field of 50 Oe.

Results and discussion

Structural and magnetic properties

TEM images for samples R1and R1a–c (see Fig. 1a–d) show almost spherically shaped particles with narrow size distributions centered at around 8 nm ($\sigma \sim 5$) (see Fig. 1i and Table 1). Particles self-assemble in a hexagonal close-packing arrangement as a consequence of both the high monodispersity of all samples and the oleic acid coating that prevent particle aggregation and keep them apart from each other a few nanometers. Consequently, the concentration of 1,2-hexadecanediol in the reaction mixture did not significantly affect either the mean size or size distribution of the particles. Interestingly enough, when the reaction mixture without 1,2-hexadecanediol was left for 1 h at the reflux temperature (sample R2), spherical NPs with D_{TEM} = 12 nm and σ = 7.4 nm were obtained (see Fig. S1a and c, ESI†) indicating that the reaction time is one of the crucial parameters determining the final size distribution of the particles.[9]

However, the 1,2-hexadecanediol content in the reaction mixture gave rise to large nanostructural modifications inside the particles that could only be revealed by HRTEM images. Despite the similar values of D_{TEM} and σ for R1 and R1a–c, a gradual improvement of the crystalline quality of the NPs was observed (see Fig. 1e–h) as the 1,2-hexadecanediol content was increased. While particles in R1 and R1a showed highly defective structures, with several in-volume defects and domain boundaries between randomly oriented, smaller crystal domains that add up to form crystallite aggregates, sample R1b was almost free of crystallographic defects and NPs of R1c were all single crystal domains with high structural order up to the particle surface.

Moreover, NPs in R2 showed also highly defective structures, as this sample was synthesized without 1,2-hexadecanediol, but with bigger crystal domains (see Fig. S1b, ESI†) because of the longer reaction time at the reflux temperature. From these results, it is unambiguously concluded that the 1,2-hexadecanediol reactant is essential to obtain single crystal particles since it somehow modifies the reaction process. It is worth noting that despite the large variation in the crystal quality of the particles, they are all single phase (core–shell structures are not observed) and their compositions, determined by ICP-OES measurements, correspond to atomic Co : Fe ratios very close to 1 : 2 as expected for stoichiometric Co-ferrite.

The crystal quality of the samples was also studied by XRD and the obtained diffraction patterns are shown in Fig. 2. The diffraction peaks significantly sharpen when going from sample R1 to R1c as D_{XRD} increases from about one fourth of the particle diameter obtained by TEM to roughly the particle diameter (see Table 1). All XRD patterns were indexed to an inverse spinel structure without any significant traces of any other Fe and/or Co phases.

The degradation in the crystal quality of the NPs, when the 1,2-hexadecanediol content in the reaction mixture is reduced, has dramatic consequences on their magnetic properties. The hysteresis loops at 5 K in Fig. 3 range from that of R1, which resembles the one corresponding to a highly disordered and frustrated glassy-magnet, to those of samples R1b and R1c associated with an almost perfect, bulk-like ferrimagnetic ordering. On the one hand, samples R1b and R1c show values of M_s and

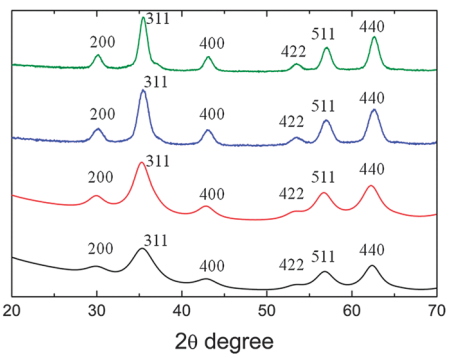

Fig. 2 X-ray diffraction patterns together with the indexation of the Bragg peaks to an inverse spinel structure. Samples are as follows: R1: black solid line, R1a: red solid line, R1b: blue solid line and R1c: green solid line.

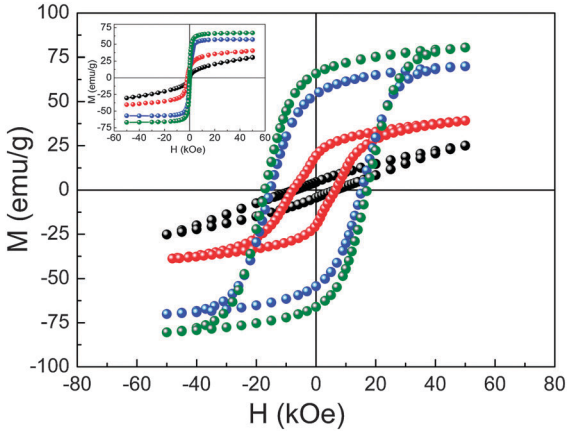

Fig. 3 Hysteresis loops at 5 K. Samples are as follows: R1: black spheres, R1a: red spheres, R1b: blue spheres, and R1c: green spheres. Inset: hysteresis loops at 300 K with the same color code.

H_c (see Table 1) being similar to those published elsewhere for standard NPs of Co-ferrite.[17–22] On the other hand, NPs in R1 and R1a, containing crystal defects, domain boundaries and local anisotropies axes associated with crystal domains within the particles, show a dramatic reduction in M_s and H_c (for instance, for R1, $M_s = 25 \pm 1$ emu g^{-1} and $H_c = 6.8 \pm 0.2$ kOe) as compared to typical values of M_s and H_c for standard Co-ferrite NPs.[17–22]

The crystalline multidomain nature of R1 and R1a NPs makes ferrimagnetic order to be arranged along the local magneto-crystalline anisotropy axes giving rise to magnetic multidomain NPs with frozen spins at the crystallite boundaries due to magnetic frustration. The existence of frozen spins in random directions and local anisotropy axes is also evident from both the high-field linear contribution to the magnetization, which is even present at room temperature (see the main panel and the inset to Fig. 3), and the high values of the closure fields of the hysteresis loops.

Sample R1a reflects an intermediate situation between the glassy behaviour of R1 and the perfect, bulk-like ferrimagnetic ordering of Co-ferrite, since crystal domains are slightly bigger in R1a than in R1. In the case of sample R2, the longer reaction time that the mixture was kept at reflux temperature promoted a further improvement in the crystallinity of the particles with respect R1, thus increasing the ferrimagnetic component of the hysteresis loops even at low temperatures (see Fig. S2a and the inset to Fig. S2a, ESI†).[17] However, a large shift, H_s, of the hysteresis loop along the magnetic field axis is still observable after field cooling the particles down to the measuring temperature under 10 kOe, as shown in Fig. S2b in the ESI.† These horizontal shifts of the loops reveal that they are actually minor loops since the closure fields are so high due to disorder and magnetic frustration, and that the reversible regime is not reached even under the maximum applied magnetic field.[12,23]

M_{ZFC} and M_{FC} curves (see Fig. 4) provide further insight into the magnetic properties as the crystal quality gradually improves from sample R1 to R1c. There are significant differences between

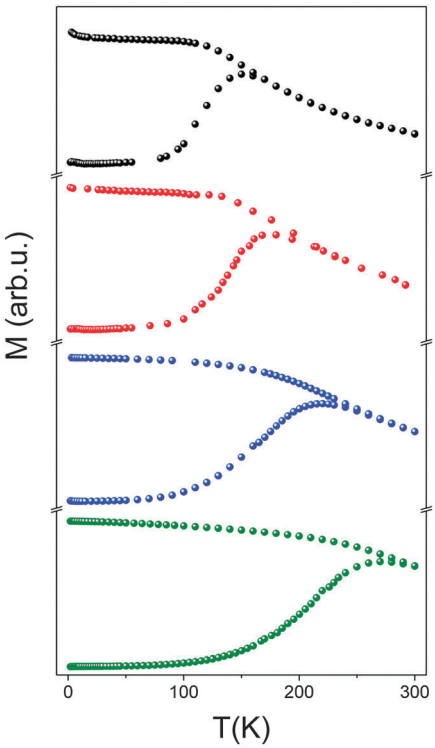

Fig. 4 M_{ZFC}–M_{FC} curves as a function of temperature. Samples are as follows: R1: black spheres, R1a: red spheres, R1b: blue spheres, and R1c; green spheres.

the $M_{ZFC} - M_{FC}$ curves of the four samples obtained by decreasing the content of 1,2-hexadecanediol in the reaction mixture (see Fig. 4). First, the peak of the M_{ZFC} curve, T_p, shifts gradually down to much lower temperatures than expected for the blocking of Co-ferrite NPs of about 8 nm in size (see Table 1 and Fig. 4).[17] Second, for the most structurally defective samples (R1 and R1a), below T_p, M_{FC} is almost constant and M_{ZFC} decreases more steeply suggesting the occurrence of a freezing process around T_p due to magnetic frustration among the crystallites that form particles rather than a simple blocking of particle magnetizations as the sample is cooled down from the superparamagnetic regime.[17] In addition, the irreversibility temperature, T_{irr}, between M_{ZFC} and M_{FC} curves moves down as the glassy behavior of the NPs becomes more prevalent (see Table 1). Finally, the M_{ZFC} and M_{FC} curves for R2 (Fig. S2c in the ESI†) suggest the formation of a ferrimagnetic component due to a partial improvement of the crystal quality, which is superimposed to the magnetic glassy behavior.

FTIR spectra

In order to elucidate the role of 1,2-hexadecanediol in the formation of the Co-ferrite NPs, 3 aliquots (2 mL) of the reaction mixtures collected at different stages of the reaction for R1 and R1a–c were studied by FTIR spectroscopy (see Fig. 5). All spectra show two bands located at 1649 and 1749 cm^{-1}.[24–26] The first band corresponds to the stretching of the C=C group characteristic of the 1-octadecene (see in Fig. S3 the spectrum of 1-octadecene, ESI†), and the depth of the peak does not

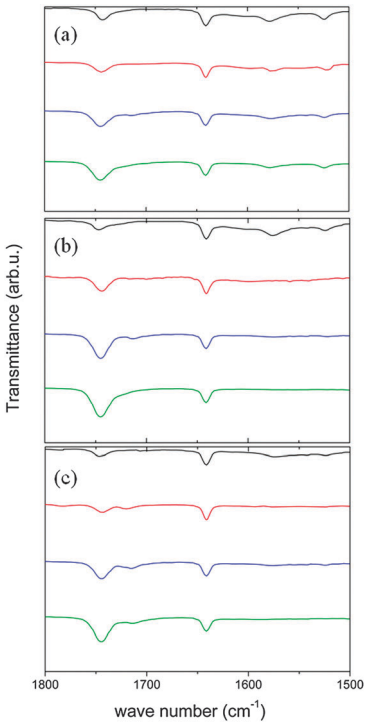

Fig. 5 FTIR spectra of the reaction mixtures at (a) 200 °C (0 min), (b) 200 °C (120 min) and (c) 320 °C (0 min). Curves are as follows: R1: black solid line, R1a: red solid line, R1b: blue solid line, and R1c: green solid line.

evolve with the reaction time since the solvent does not decompose. The second band at 1749 cm^{-1} is associated with the stretching mode of a free carbonyl and its appearance indicates the formation of the mixed $Co^{2+}Fe^{3+}$–oleate complex (see in Fig. S3 the spectrum corresponding to the pure mixed oleate complex, ESI†).

Interestingly, this band is enhanced by the increase in the 1,2-hexadecanediol content for all three studied stages of the reaction (Fig. 5a–c). Moreover, some other revealing differences are observed between the spectra in Fig. 5a–c. Fig. 5a shows the FITR spectra of the reaction mixtures (R1–R1c) once the temperature has just been increased to 200 °C. All the spectra in Fig. 5a show typical bands between 1574 and 1524 cm^{-1} corresponding to the stretching of the C=C and C–O groups of the metal acetylacetonates (see in Fig. S3 the spectra of Fe and Co acetylacetonates, ESI†).[27,28] It is worth noting that a drop in the depth of these peaks is observed when the concentration of 1,2-hexadecanediol in the reaction mixture is increased indicating that this reactant favors the decomposition of the metallic organic precursors. This effect is much more pronounced after 2 h at 200 °C (see Fig. 5b) where the FTIR spectra of the reaction mixtures with 1,2-hexadecanediol do not show any significant trace of acetylacetonates, while the spectrum of R1 still shows that these peaks are almost unaltered. Finally, Fig. 5c shows the FTIR spectra of the reaction mixtures (R1–R1c) at 320 °C. Surprisingly, the spectrum of R3 still shows the bands between 1574 and 1524 cm^{-1} indicating that the decomposition of the metal acetylacetonates has not yet been fully completed.[27,28] Besides, a new band appears at around 1715 cm^{-1} in the reaction mixtures R1a–c associated with the stretching mode of the C=O groups of the mixed $Co^{2+}Fe^{3+}$–oleate complex that is linked to the particle surface,[25] which is detectable at the three stages of the reaction at least for the two reaction mixtures with the highest 1,2-hexdecanediol concentration. The appearance of this peak signals the onset of the formation of the Co-ferrite NPs.

Summarizing, the analyses of the reaction mixtures by FTIR show that the 1,2-hexadecanediol content favors both the decomposition of Fe and Co acetylacetonates, and the formation of the mixed $Co^{2+}Fe^{3+}$–oleate complex, thus lowering the temperature at which the nucleation of the NPs starts. This is pretty obvious in the case of the reaction mixture for R1c (that with the standard concentration of 1,2-hexadecanediol in the literature), where after 2 h at 200 °C, there are not any traces of metal acetylacetonates and an intense band at around 1749 cm^{-1} reveals that they are fully decomposed to form a mixed-metal oleate complex.[25] In contrast, the reaction mixture for R1 after 2 h at 200 °C clearly shows the presence of iron and cobalt acetylacetonates and only traces of the mixed-metal oleate complex. The processes that take place in the nucleation and growth of NPs may include the crystallization of small clusters, coagulation, and finally coalescence of small subunits to form the NPs and/or particle growth by diffusion.[29,30] Our results suggest that Co-ferrite NPs synthesized with a low concentration of 1,2-hexadecanediol have defective crystallographic structures due to a partial decomposition of Fe and Co acetylacetonates yielding a partial formation of the mixed-metal oleate complex, that in turn, leads to retarded nucleation and a faster growth by aggregation. In contrast, samples with a higher amount of 1,2-hexadecanediol proceed through single nucleation that takes place at lower temperature and a slower particle growth by diffusion (see Fig. 6b for the schematics of the process). In addition, even though the amount of 1,2-hexadecanediol slows down the particle growth leading to more ordered crystalline particles, it seems not to affect the nucleation process in terms of the number of formed nuclei since similar particle sizes and size distributions are obtained no matter the amount of this reagent. So, ions in the reaction mixture diffusing to the nanoparticle surface have more time to find the appropriate position. In fact, apart from the reducing

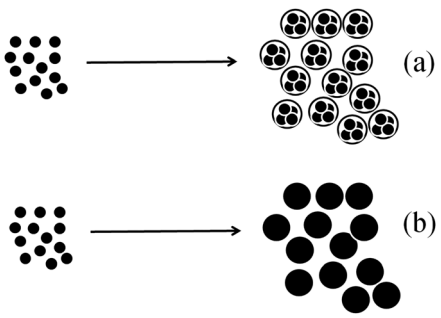

Fig. 6 Schematics of the two types of particle growth observed in the samples: (a) nucleation, growth and partial coalescence of smaller subunits; (b) single nucleation and uniform growth by diffusion.

role of the 1,2-hexadecanediol, it has been shown to serve as a template although not being as efficient as oleic acid and/or oleylamine.[31]

Conclusions

In this work, we have demonstrated the key role of 1,2-hexadecanediol in the formation of Co-ferrite NPs with high crystal quality. The study of the reaction mixtures by FITR showed that this reactant promotes the decomposition of the metal–organic precursors, facilitating the formation of the intermediate mixed-metal complex at lower temperature. Without this reactant it is also possible to synthesize single phase, monodisperse Co-ferrite NPs of similar size and having the correct stoichiometry, but in fact being crystallite aggregates constituted of randomly oriented smaller crystal domains. The crystalline multidomain nature of the particles makes ferrimagnetic order to be arranged along the local magnetocrystalline anisotropy axes, giving rise to high magnetic frustration at the crystallite boundaries thus yielding a magnetic glassy behavior. The final crystal quality of the particles can be gradually improved by the addition of an increasing amount of 1,2-hexadecanediol to the reaction mixture and the various samples prepared reveal the close relationship between the crystal properties and magnetic behavior, since a progression from magnetic glassy behavior towards bulk-like ferrimagnetism is observed. All the foregoing results could be useful to tailor the magnetic properties of Co-ferrite NPs for a specific application demanding lower/higher values of either the saturation magnetization and/or the coercive field. For instance, it may be of interest to decrease the ratio between remanent and saturation magnetizations in order to minimize particle aggregation due to dipolar interactions when they are delivered in the form of a colloidal suspension for *in vivo* applications. Besides, it might allow tuning the effective blocking temperature of the NPs from above room temperature down to about 150 K with the purpose of maximizing the absorption of an external radiofrequency excitation due to Neel relaxation to improve heat dissipation in hyperthermia applications. Moreover, it has been shown that the specific absorption rate in hyperthermia can be enhanced using some kind of multicore particles rather than single particles.[32] It is then suggested that the crystalline multidomain nature of these Co-ferrite nanoparticles could also yield a similar heat dissipation enhancement.

All in all, the 1,2-hexadecanediol concentration in the reaction mixture can be considered as a tunable parameter that controls the final magnetic properties of monodisperse, stoichiometric Co-ferrite NPs.

Acknowledgements

This work was supported by Spanish MINECO (MAT2011-23641, MAT2012-33037, MAT2013-48054-C2), Catalan DURSI (2014SGR220) and European Union FEDER funds (Una manera de hacer Europa). C. Moya acknowledges Spanish MINECO for a PhD contract (BES-2010-038075) and a three month stay at the ICMM-CSIC (Madrid).

Notes and references

1 B. D. Cullity and C. D. Graham, *Introduction to Magnetic Materials*, 2011.
2 T. Fried, G. Shemer and G. Markovich, *Adv. Mater.*, 2013, **13**, 1158.
3 A. G. Pershina, A. E. Sazonov and L. M. Ogorodova, *Russ. J. Bioorg. Chem.*, 2009, **35**, 607.
4 E. L. Verde, G. T. Landi, J. A. Gomes, M. H. Sousa and A. F. Bakuzis, *J. Appl. Phys.*, 2012, **111**, 123902.
5 E. Mazario, N. Menéndez, P. Herrasti, M. Cañete, V. Connord and J. Carrey, *J. Phys. Chem. C*, 2013, **117**, 11405.
6 C. Sun, J. S. H. Lee and M. Zhang, *Adv. Drug Delivery Rev.*, 2008, **11**, 1252.
7 C. Cannas, A. Musinu, A. Ardu, F. Orrù, D. Peddis, M. Casu, R. Sanna, F. Angius, G. Diaz and G. Piccaluga, *Chem. Mater.*, 2010, **11**, 3353.
8 X. Batlle and A. Labarta, *J. Phys. D: Appl. Phys.*, 2002, **35**, R15.
9 A. G. Roca, R. Costo, A. F. Rebolledo, S. Veintemillas-Verdaguer, P. Tartaj, T. González-Carreño, M. P. Morales and C. J. Serna, *J. Phys. D: Appl. Phys.*, 2009, **42**, 224002.
10 S. Sun and H. Zeng, *J. Am. Chem. Soc.*, 2002, **124**, 8204.
11 S. Sun, H. Zeng, D. B. Robinson, S. Raoux, P. M. Rice, S. X. Wang and G. Li, *J. Am. Chem. Soc.*, 2004, **126**, 273.
12 X. Batlle, N. Pérez, P. Guardia, O. Iglesias, A. Labarta, F. Bartolomé, L. M. García, J. Bartolomé, A. G. Roca, M. P. Morales and C. J. Serna, *J. Appl. Phys.*, 2012, **109**, 07B524.
13 P. Guardia, A. Labarta and X. Batlle, *J. Phys. Chem. C*, 2010, **115**, 390.
14 N. Pérez, F. López-Calahorra, A. Labarta and X. Batlle, *Phys. Chem. Chem. Phys.*, 2011, **13**, 19485.
15 P. Guardia, N. Pérez, A. Labarta and X. Batlle, *Langmuir*, 2010, **26**, 5843.
16 P. Guardia, J. Pérez-Juste, A. Labarta, X. Batlle and L. M. Liz-Marzán, *Chem. Commun.*, 2010, **46**, 6108.
17 C. Moya, G. Salas, M. P. Morales, X. Batlle and A. Labarta, *J. Mater. Chem. C*, 2015, **3**, 4522–4529.
18 D. Peddis, F. Orru, A. Ardu, C. Cannas, A. Musinu and G. Piccaluga, *Chem. Mater.*, 2012, **24**, 1062.
19 T. E. Torres, A. G. Roca, M. P. Morales, A. Ibarra, C. Marquina, M. R. Ibarra and G. F. Goya, *J. Phys.: Conf. Ser.*, 2010, **200**, 072101.
20 L. I. Cabrera, Á. Somoza, J. F. Marco, C. J. Serna and M. P. Morales, *J. Nanopart. Res.*, 2012, **14**, 873.
21 Q. Song and Z. J. Zhang, *J. Am. Chem. Soc.*, 2004, **12**, 6164.
22 N. Bao, L. Shen, Y. Wang, P. Padhan and A. Grupta, *J. Am. Chem. Soc.*, 2007, **129**, 12374.
23 J. Nogués, J. Sort, V. Langlais, V. Skumryev, S. Suriñach, J. S. Muñoz and M. D. Baró, *Phys. Rep.*, 2005, **422**, 65.
24 A. P. Herrera, L. Polo-Corrales, E. Chavez, J. Cabarcas-Bolivar, N. C. O. Uwakweh and C. Rinaldi, *J. Magn. Magn. Mater.*, 2013, **328**, 41.
25 J. Park, A. Y. K. Hwang, J.-G. Park, H.-J. Noh, J.-Y. Kim, J.-H. Park, N.-M. Hwang and T. Hyeon, *Nat. Mater.*, 2004, **3**, 891.
26 To see the FTIR spectrum of 1-octadecene: http://webbook.nist.gov/cgi/cbook.cgi?ID=C112889&Mask=80#IR-Spec.

27 To see the FITR spectrum of $Co(acac)_2$: http://www.sigmaaldrich.com/spectra/ftir/FTIR003222.PDF.
28 To see the FTIR spectrum of $Fe(acac)_3$: http://webbook.nist.gov/cgi/cbook.cgi?ID=C14024181&Mask=80.
29 P. Tartaj, M. P. Morales, S. Veintemillas-Verdaguer, T. González-Carreño and C. J. Serna, *J. Phys. D: Appl. Phys.*, 2003, **36**, R182.
30 V. K. LaMer and R. H. Dinegar, *J. Am. Chem. Soc.*, 1950, **72**, 4847.
31 A. C. Christopher and R. B. Andrew, *J. Mater. Chem.*, 2008, **18**, 4146.
32 P. Hugounen, M. Levy, D. Alloyeau, L. Lartigue, E. Dubois, V. Cabuil, C. Ricolleau, S. Roux, Ć. Wilhelm, F. Gazeau and R. Bazzi, *J. Phys. Chem. C*, 2012, **116**, 15702.

Electronic Supplementary Material (ESI) for Physical Chemistry Chemical Physics.

Supporting Information

Tuning the magnetic properties of Co-ferrite nanoparticles through the 1,2-hexadecanediol concentration in the reaction mixture

Carlos Moya,[a*] María del Puerto Morales,[b] Xavier Batlle,[a] Amílcar Labarta[a]

[a] Departament de Física Fonamental, Institut de Nanociència i Nanotecnologia, Universitat de Barcelona, Barcelona (Spain) 08028

[b] Instituto de Ciencia de Materiales de Madrid, CSIC. C/Sor Juana de Inés de la Cruz 3, Campus de Cantoblanco. 28049 Madrid, Spain

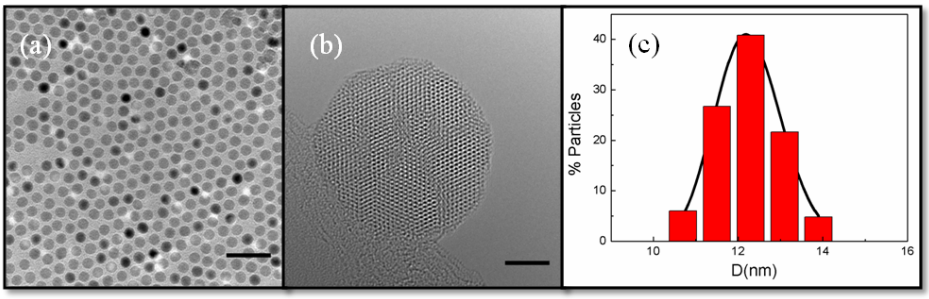

Figure S1. TEM characterization for sample R2. (a) Low-resolution TEM image, (b) HRTEM image, and (c) Particle size distribution obtained from TEM data. Scale bar is 50 nm for (a) and 3 nm for (b).

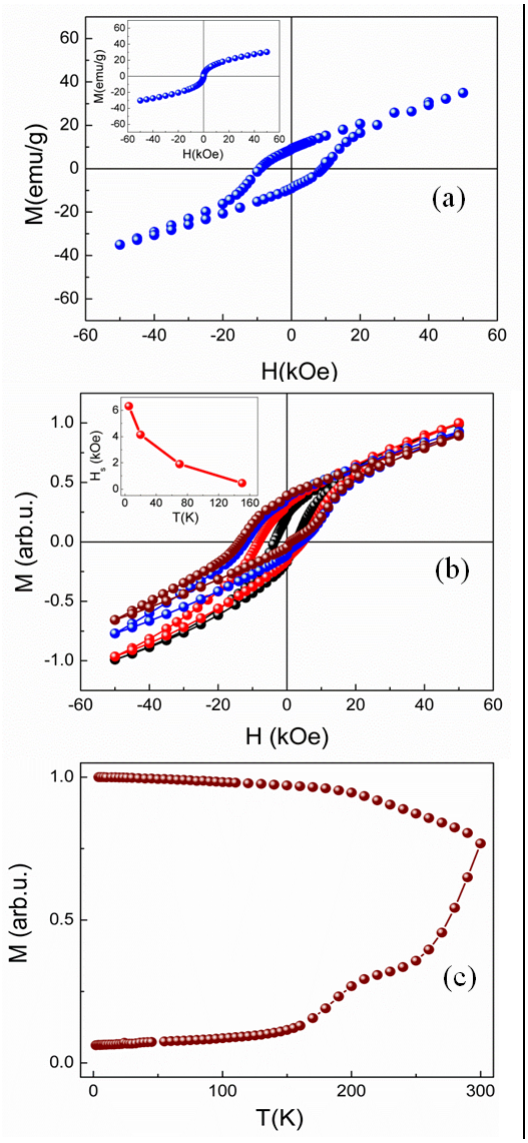

Figure S2. Magnetic properties of sample R2. (a) Hysteresis loop at 5K. Inset: hysteresis loop at room temperature. (b) Hysteresis loops after field cooling the sample under 10 kOe from 250 K down to the final measuring temperature. Symbols are as follows: T = 5 K brown spheres, 20 K blue spheres, 70 K red spheres and 150 K black spheres. Inset: loop shift, H_s, as a function of the temperature. (c) Zero field cooling and field cooling magnetizations as a function of temperature.

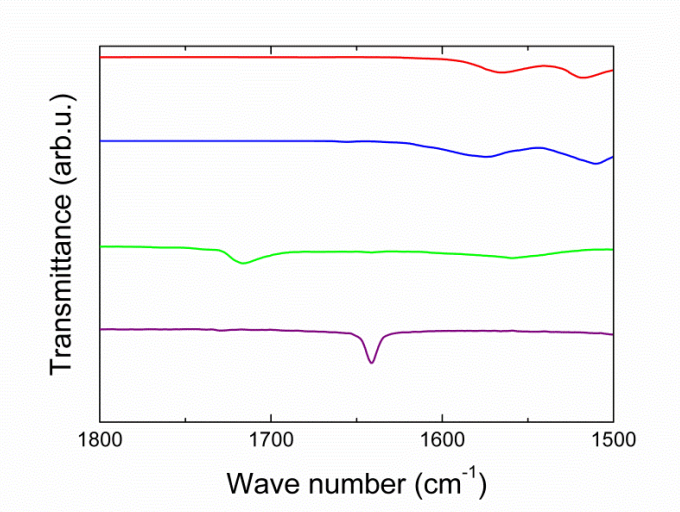

Figure S3. FTIR spectra for iron (III) acetylacetonate (red solid line), cobalt (II) acetylacetonate (blue solid line), $Co^{2+}Fe^{3+}$-oleate complex (green solid line) and 1-octadecene (purple solid line).

Chapter 3.Structure and magnetic frustration in Co-ferrite nanoparticles

Journal of
Materials Chemistry C

PAPER

View Article Online
View Journal

Cite this: DOI: 10.1039/c4tc02889a

Inducing glassy magnetism in Co-ferrite nanoparticles through crystalline nanostructure†

Carlos Moya,*[a] Gorka Salas,[bc] María del Puerto Morales,[b] Xavier Batlle[a] and Amílcar Labarta[a]

Received 15th December 2014,
Accepted 20th March 2015

DOI: 10.1039/c4tc02889a

www.rsc.org/MaterialsC

This work reports on the study of three samples of 8 nm Co-ferrite particles prepared by standard methods based on the thermal decomposition of metal–organic precursors. Although all samples are single phase according to conventional techniques of structural and chemical characterization, they show strongly sample-dependent magnetic properties ranging from bulk-like ferrimagnetism to glassy magnetic behaviour. We show that the presence of crystallite domains associated with crystallographic defects throughout the particles leads to highly-frustrated ferrimagnetic cores that are responsible for the glassy phenomenology, while only samples almost free of structural imperfections show bulk-like magnetic properties. These results suggest the key role of the crystal quality in the large variability of magnetic properties previously reported for Co-ferrite nanoparticles. Besides, achieving control of the amount of structural defects in monodisperse, stoichiometric Co-ferrite nanoparticles can be an additional nano-structuring procedure to tailor their final magnetic properties.

Introduction

Magnetic nanomaterials are extensively studied at present because of the wealth of new phenomena occurring at the nanoscale. Among them magnetic nanoparticles (NPs) are excellent examples of nanosystems providing a plethora of either tailored or enhanced properties with respect to those of their bulk counterparts.[1] Particularly, ferrite nanoparticles with composition MFe_2O_4 (M = Fe, Co) are currently attracting a lot of interest due to their potential applications in biomedicine, such as the detection of biomolecules by magnetic separation, contrast improvement in nuclear magnetic resonance imaging and cancer treatment by magnetic hyperthermia.[2–5] Co-ferrite NPs are especially suitable for those applications because of their high values of magneto-crystalline anisotropy, saturation magnetization and magneto-optical coefficients.[6] In addition, Co-ferrite NPs show a high magnetic response.

However, once size is reduced to the nanometer scale, NPs display particle-like magnetic behavior including finite-size effects such as superparamagnetism, oddly shaped hysteresis loops, and glassy behavior, among others.[1] In addition, there might be a breakdown of the usual scaling laws linking magnetic properties to size.[1] These effects are due to the influence of the particle surface on magnetic order *via* bond breaking and charge rearrangement, and to the closeness of the particle size to critical magnetic length scales like the domain wall width and spin-exchange length.[7] Besides, in spinel ferrite NPs, structural modifications at the grain boundaries and other crystallographic defects may provoke the destabilization of the ferrimagnetic order yielding a variety of non-collinear magnetic structures that become frozen in a kind of glassy state at low temperature.[8] The most important features characterizing this glassy state comprise the existence of high-field irreversibility in the magnetization curves, occurrence of shifted hysteresis loops after field cooling, reduction of the coercive field and the increase in magnetic viscosity.[9] In the case of spinel ferrites such as $Co_xFe_{3-x}O_4$, further complexity arises due to the likely size-dependent cation distribution of the tetrahedral and octahedral sites in the close-packed oxygen structure, which strongly affects their saturation magnetization and magnetic anisotropy.[10] All the foregoing could cause the strongly sample-dependent magnetic properties that have been previously reported for Co-ferrite NPs, suggesting that the synthesis is affected by a number of factors limiting the reproducibility and crystal quality of the final samples.[11–13] The crucial role of the structural quality in the magnetic properties of the Co-ferrite NPs is thus proposed since only NPs almost

[a] Departament de Física Fonamental and Institut de Nanociència i Nanotecnologia (IN2UB), Universitat de Barcelona, Martí i Franquès 1, 08028 Barcelona, Spain. E-mail: cmoya@ffn.ub.es
[b] Instituto de Ciencia de Materiales de Madrid, CSIC. C/Sor Juana de Inés de la Cruz 3, Campus de Cantoblanco, 28049 Madrid, Spain
[c] IMDEA Nanociencia, Ciudad Universitaria de Cantoblanco, C/Faraday 9, E-28049 Madrid, Spain

† Electronic supplementary information (ESI) available: PDF material contains particle size distributions of the samples, the HRTEM image of $CoFe_2O_4$ NPs with contrast colours, EDX and EELS experiments for sample R3, X-ray patterns of the samples, hysteresis loops after FC under 10 kOe from 250 K down to the final measuring temperature for sample R3 and $M_{ZFC}-M_{FC}$ curves for all the samples. See DOI: 10.1039/c4tc02889a

free of structural defects show the magnetic performance suitable for many applications.[14] At the same time, getting control of the amount of structural defects in monodisperse, stoichiometric Co-ferrite NPs can be an additional nano-structuring procedure to tailor their final magnetic properties. In this framework, we have addressed these issues by studying various samples of Co-ferrite NPs prepared by high-temperature decomposition of metal–organic precursors in an organic solvent with distinct reactants, in order to establish a close relationship between the actual magnetic behaviour and the structural properties of the NPs. We have shown that samples with compositions corresponding to stoichiometric Co-ferrite exhibit a wide variety of magnetic phenomena ranging from almost perfect bulk-like ferrimagnetic order with high coercive fields for Co-ferrite NPs of high crystallinity, to glassy magnetic behaviour for the most structurally defective samples.

Experimental details

Preparation of the samples

Three samples of Co-ferrite NPs were synthesized by high-temperature decomposition of various Fe and Co organic precursors in 1-octadecenne, using oleic acid as a surfactant in all cases and following standard methods reported elsewhere.[15–21] Metal oleates, used as organic precursors, were prepared by the reaction of the corresponding metal chlorides, $CoCl_2{\cdot}6H_2O$ (Sigma-Aldrich, 99%), $FeCl_3{\cdot}6H_2O$ (Sigma-Aldrich, 98%) and sodium oleate (Riedel-deHaën, 85%). Co-ferrite nanoparticles were prepared from oleate precursors of Fe and Co, iron(III) acetylacetonate (Sigma-Aldrich, 99%), cobalt(II) acetylacetonate (Sigma-Aldrich, 97%), 1,2-hexadecanediol (Sigma-Aldrich, 90%), oleic acid (Sigma-Aldrich 90%), oleylamine (Sigma-Aldrich 70%) and 1-octadecene (Sigma-Aldrich 90%). All reactants were used in the synthesis without further purification.

Synthesis of metal oleates

Cobalt(II) oleate. $CoCl_2{\cdot}6H_2O$ (9.60 g, 40 mmol) was mixed with sodium oleate (32.60 g, 88 mmol) in a mixture of ethanol, distilled water and hexane (80 mL each). The reaction mixture was kept for 15 minutes under vigorous stirring. Then, the aqueous phase was removed and the organic phase was washed four times with a mixture of water and ethanol. Then, the organic solvent was removed and the Co(II) oleate was dried in a rotary evaporator. The resulting product was a purple solid.

Iron(III) oleate. For the synthesis of iron(III) oleate, $FeCl_3{\cdot}6H_2O$ (10.80 g, 40 mmol) and sodium oleate (45.00 g, 148 mmol) were dissolved in a mixture of distilled water, ethanol and hexane (60, 80 and 140 mL, respectively). The resulting solution was heated at 70 °C for 4 h under reflux. When the reaction was completed, organic products were washed three times with distilled water. Finally, hexane was removed in vacuum resulting in a waxy black solid.

Cobalt(II) iron(III) oleate. The mixed-metal compound $Co^{2+}Fe_2^{3+}$-oleate was prepared by dissolving sodium oleate (23.76 g, 64 mmol), $CoCl_2{\cdot}6H_2O$ (1.90 g, 8 mmol) and $FeCl_3{\cdot}6H_2O$ (4.41 g, 16 mmol) in a mixture of water, ethanol and hexane (40, 40 and 80 mL, respectively). The reaction mixture was stirred and refluxed at 60 °C for 4 h. Then, the aqueous phase was removed and the organic phase was washed three times with a mixture of ethanol and distilled water. A viscose brown liquid was obtained after evaporation of the hexane and ethanol at 100 °C.

Preparation of Co-ferrite NPs

Sample R1. Co and Fe acetylacetonates as metallic precursors: $Co(acac)_2$ (0.26 g, 1 mmol), $Fe(acac)_3$ (0.71 g, 2 mmol), 1,2-hexadecanediol (2.87 g, 10 mmol), oleic acid (1.88 g, 6 mmol) and oleylamine (2.29 g, 6 mmol) were added to 1-octadecenne (20 mL). The mixture was heated at 200 °C for 2 h under stirring in a flow of nitrogen gas. Then, the solution was heated up to reflux for 1 h. After that, the solution was cooled down to room temperature and transferred to a 50 mL centrifugation tube together with 20 mL of a mixture of 2-propanol and ethanol with a volume ratio of 1 : 3. After centrifugating three times at 9000 rpm for 15 min, a black powder was obtained, which was then dispersed in hexane for storage.

Sample R2. Co and Fe oleates as metallic precursors: a mixture of $Co(oleate)_2$ (0.62 g, 1 mmol), $Fe(oleate)_3$ (1.79 g, 2 mmol) and oleic acid (2.59 g, 9 mmol) were slowly heated under a nitrogen atmosphere in 1-octadecene (20 mL) up to 80 °C. Then, the solution was quickly heated up to reflux temperature for 1 h. The reaction mixture was washed with a mixture of 2-propanol and ethanol with a ratio of 1 : 3 and centrifuged. The procedure was repeated several times, until a clear solution was obtained. After that, the reaction product was re-dispersed in hexane.

Sample R3. Co and Fe acetylacetonates as metallic precursors: $Fe(acac)_3$ (0.71 g, 2 mmol), $Co(acac)_2$ (0.26 g, 1 mmol) and oleic acid (2.59 g, 9 mmol) were mixed in 1-octadecene (20 mL). As for R1, after heating up to 200 °C and maintaining at this temperature for 2 h, the solution was heated to reflux temperature, cooled down to room temperature and washed several times with a mixture of hexane and acetone with a volume ratio 1 : 3, and, finally, NPs were collected by centrifugation at 8000 rpm.

Experimental techniques

The particle shape and size were determined by transmission electron microscopy (TEM) using a MT80-Hitachi microscope. To get a deeper insight into the crystal quality and stoichiometry of individual NPs, high resolution TEM (HRTEM) images were obtained using Titan high-base. Electron energy loss spectroscopy (EELS) and energy-dispersive X-ray spectroscopy (EDX) data, both techniques with a spatial resolution of about 1 nm, were recorded using Titan low-base. TEM samples were prepared by placing a drop of a diluted suspension of NPs in hexane on a carbon-coated copper grid and further evaporation of the solvent at room temperature. Particle size distributions were determined by measuring at least 2000 particles for each sample and the resultant histograms are shown in Fig. S1 in ESI.†

Crystal structures were identified by X-ray powder diffraction performed in a PANalytical X'Pert PRO MPD diffractometer by using Cu Kα radiation. The patterns were collected within 5 and

Table 1 Summary of the structural, microstructural, and magnetic parameters of the samples studied[a]

Samples	D_{TEM} (nm)	σ^b	D_{XRD} (nm)	Co : Fe (ICP-OES)	T_p (K)	T_{irr} (K)	M_s at 5 K (emu g^{-1})	M_s at 300 K (emu g^{-1})	H_c at 5 K (kOe)	H_c at 300 K (kOe)
R1	7.8	0.12	7.7(0.4)	1.0 : 2.0	280	290	77(2)	64(2)	15.6(0.1)	0.016(0.01)
R2	7.2	0.25	6.9(0.5)	1.0 : 2.1	>300	>300	60(2)	47(2)	14.5(0.1)	0.084(0.01)
R3	8.6	0.13	2.1(0.6)	1.0 : 2.0	150	170	25(1)	20(1)	6.8(0.2)	SPM[c]

[a] The values in parentheses indicate the experimental error of the data. [b] Unitless standard deviation of the log-normal distribution. [c] SPM stands for superparamagnetic.

100° in 2θ. In all cases, the XRD spectra were indexed to an inverse spinel structure. The mean particle diameters obtained from XRD (D_{XRD}) are given in Table 1.

The Fe and Co contents in the samples were determined by inductively coupled plasma-optical emission spectrometry (ICP-OES) by using a Perkin Elmer model OPTIMA 3200RL after digesting the samples in a mixture of HCl : HNO_3; 5 : 25, and finally diluting them with distilled water.

The organic fractions of the samples – Co and Fe acetylacetonates or oleates – were evaluated by thermogravimetric analysis (TGA). Measurements were performed in a TGA-SDTA 851e/SF/1100 (Mettler Toledo) at a heating rate of 10 °C min^{-1} in a nitrogen atmosphere from room temperature up to 800 °C.

DC magnetization measurements were performed using a Quantum Design SQUID magnetometer. Hysteresis loops $M(H)$ were measured under a maximum applied field of ±50 kOe within 2 and 300 K in order to evaluate the coercive field H_c, and saturation magnetization M_s. The coercive fields at positive and negative sides of the magnetic field axis were determined by linear regression of the magnetization data around the interceptions of the hysteresis loop with the field axis. H_c was defined as $H_c = (|H_c^+| + |H_c^-|)/2$, and the shift of the hysteresis loop along the field axis as $H_s = (|H_c^+| + |H_c^-|)/2$. In order to study H_s, hysteresis loops were recorded after field cooling (FC) the sample from 250 K down to the final measuring temperature under an applied magnetic field of 10 kOe.

The thermal dependence of the magnetization was measured after zero field cooling (M_{ZFC}) and field cooling (M_{FC}) the samples. These curves were collected using the following protocol: the sample was cooled down from 300 to 2 K in zero magnetic field, then a static magnetic field of 50 Oe was applied and M_{ZFC} was recorded while the sample was warmed up from 2 to 300 K. Then, the sample was again cooled down to 2 K under 50 Oe and M_{FC} was collected while rewarming up to 300 K.

Magnetization relaxation was measured after field cooling the sample under 50 Oe from room temperature down to each measuring temperature, switching off the field and then recording magnetization decay as a function of time at zero field and several temperatures.

Results and discussion

Structural characterization and sample composition

TEM images of R1, R2 and R3 show spherical shaped particles that tend to self-assemble in a hexagonal close-packing pattern (see Fig. 1). Fig. 1 also shows the regularity and good monodispersity of the NPs for R1 and R3 and a wider size distribution for R2. The presence of the oleic acid coating at the particle surface prevents particle aggregation and keeps them a few nanometers apart from each other. The particle size distributions for the three samples were determined from TEM images and the resultant histograms (see Fig. S1a–c in the ESI†) were fitted to log-normal distributions with the mean particle sizes (D_{TEM}) and unitless standard deviations (σ) indicated in Table 1. Interestingly, although R1, R2 and R3 samples were prepared using different reactants and protocols, all of them consist of

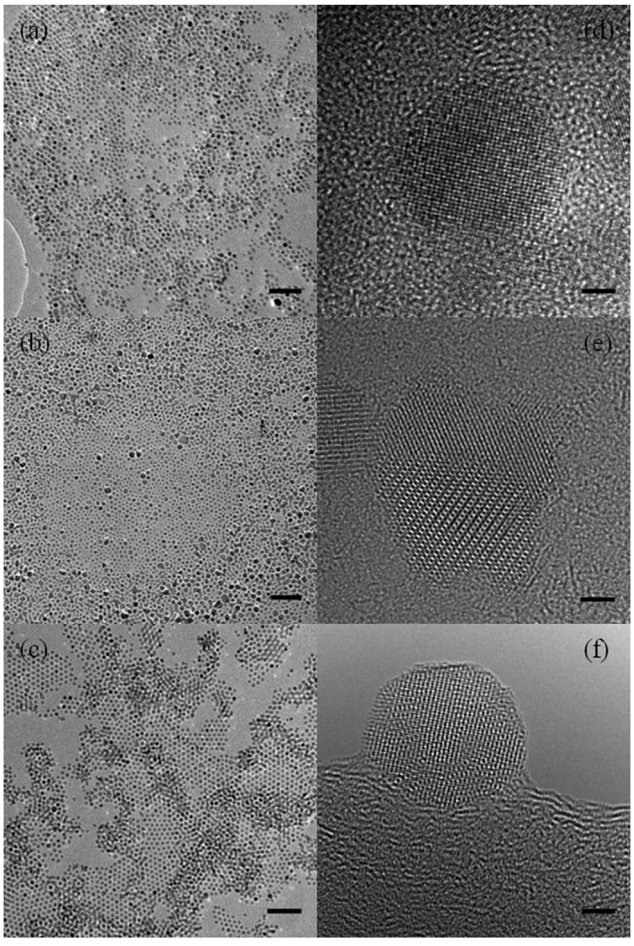

Fig. 1 TEM images of $CoFe_2O_4$ NPs: (a) R1, (b) R2, (c) R3. HRTEM images of $CoFe_2O_4$ NPs: (d) R1, (e) example of a particle from the R2 sample showing two crystal domains inside, (f) R3. Scale bars in (a), (b), (c) correspond to 85 nm and in (d), (e), (f) to 2 nm.

NPs with similar morphology and size distributions which facilitates the comparison of their magnetic properties. Fig. 1d–f show HRTEM images of samples R1, R2 and R3, respectively. R1 NPs are single crystal domains almost free of crystallographic defects up to the particle surface. In contrast, NPs of sample R3 show much poorer crystal quality with several in-volume defects and domain boundaries between randomly oriented smaller crystal domains that add up to form particles as crystallite aggregates (see Fig. S2b, ESI†). NPs of R2 exhibit higher crystal quality than those of R3 but still not being completely free of crystallographic defects and some of them even having about two non-coherent crystal domains randomly distributed throughout the particle (see Fig. S2b and S3, ESI†).

All samples appear to be a single chemical phase of cobalt ferrite as ICP-OES analyses indicate a Co : Fe atomic ratio close to 1 : 2 in all cases, and no core–shell structures are observed by HRTEM. In the case of sample R3 (the most crystal defective particles), spatially resolved EDX and EELS analyses have also corroborated the homogenity of the composition up to the particle surface (see Fig. S4–S8, ESI†) and discarded the existence of other CoFe-based phases.

The XRD spectra of R1, R2 and R3, which are shown in Fig. S9a–c in the ESI,† respectively, have been indexed to an inverse spinel structure corresponding to stoichiometric $CoFe_2O_4$ without any significant traces of other phases. Using the Debye–Scherrer equation applied to the [400] reflection, the mean sizes (D_{XRD}) of the crystal domains have been determined for the three samples (see Table 1). D_{TEM} and D_{XRD} values are in perfect agreement for sample R1, as these NPs are crystal monodomains. In contrast, D_{XRD} is about four times smaller than D_{TEM} for R3 NPs in accordance with the crystal multidomain character of those highly defective particles. Finally, D_{XRD} is just slightly smaller than D_{TEM} for R2 indicating the existence of some crystallographic defects within the volume of some of the particles.

Mechanisms of particle growth

The different size and crystallinity of the samples R1, R2 and R3 are intrinsically related to both the decomposition temperatures of the reactants involved in the reactions and reaction steps. While for the synthesis of R1 and R3 metal organic precursors are $Fe(acac)_3$ and $Co(acac)_2$,[15–21] for R2 they are the corresponding Fe and Co oleates.[17–19]

Typically, the synthesis of $CoFe_2O_4$ NPs by thermal decomposition of acetylacetonates as metal organic precursors is divided into two main steps.[20,21] First, the reaction mixture is kept for 2 h at 200 °C. In this step Fe and Co acetylacetonates decompose at about 200 °C (see Fig. 2a) to form a polynuclear mixed-metal $Co^{2+}Fe_2^{3+}$-oleate that also starts to decompose yielding the nucleation of the NPs. After that, the reaction mixture is heated up and kept at boiling temperature, where the intermediate metal complex decomposes completely and the growth of the NPs takes place. As pointed out by LaMer,[23] one of the crucial aspects to synthesize monodisperse NPs relies on the fact that nucleation and growth processes must occur at different temperatures, as happens in the syntheses of samples R1 and R3.[22,23] In addition, the final contents of Fe and Co in both R1 and R3 samples are stoichiometric (see Table 1).

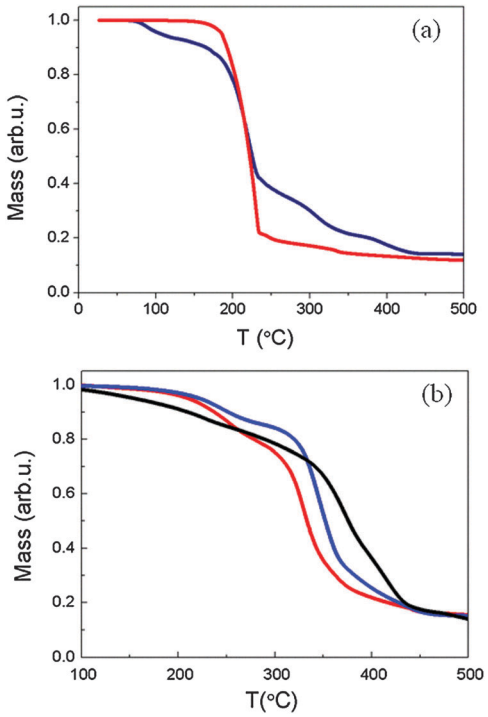

Fig. 2 (a) TGA curves of Fe^{3+}-acetylacetonate (red solid line) and Co^{2+}-acetylacetonate (blue solid line). (b) TGA curves of Fe^{3+}-oleate (red solid line), Co^{2+}-oleate (black solid line) and the mixed-metal $Co^{2+}Fe_2^{3+}$-oleate (blue solid line).

Despite the narrow distribution of particle sizes and stoichiometric composition of both samples, R3 shows a much more defective crystal structure related to a partial coalescence of smaller subunits (crystallite cores) rather than a uniform growth by diffusion.[22] This is probably due to the absence of 1,2-hexadecanediol in the R3 reaction and the specific role of this reactant: it enhances the decomposition of the organic precursors to form a polynuclear mixed-metal complex, thus homogenizing the growth of the NPs by diffusion.

On the other hand, R2 shows a broader particle size distribution having also a slight excess of Fe content and lower crystallinity than sample R1 (see Table 1 and Table S1b, ESI†). These results can be attributed to the different decomposition rates of Fe and Co oleates, since in this case an intermediate mixed-metal complex is not formed and the nucleation and growth of the NPs occur by the parallel decomposition of the two oleates.[19] This is clear from Fig. 2b where TGA curves corresponding to Fe^{3+}-oleate and Co^{2+}-oleate are shown. The TGA curve of mixed-metal (Co^{2+}–Fe^{3+})-oleate has also been included for comparison in Fig. 2b. Two different weight-loss rates are observed for Fe^{3+}-oleate. The first appears between 200 and 250 °C and corresponds to the partial dissociation of the complex by elimination of CO_2.[24] In this first step there is a weight loss of 25% associated with the loss of one oleate ligand. The second jump in the TGA curve (50% of weight loss between 300 and 350 °C) corresponds to the loss of the two remaining oleate ligands yielding the final

product. In contrast, Co^{2+}-oleate shows a constant weight loss rate between 200 and 500 °C (85% of weight loss), suggesting the progressive loss of the two oleate ligands.

Crystal quality and magnetic glassy behaviour

The different crystal quality of the samples is also reflected in the magnetization hysteresis loops shown in Fig. 3 and in the values of M_s and obtained from them. On one hand, for the conventional sample R1 at 5 K, $M_s = 77 \pm 2$ emu g^{-1} and $H_c = 15.6 \pm 0.1$ kOe, both values being in agreement with those reported elsewhere for high magnetic quality Co-ferrite NPs.[16,18] We note that the expected bulk value at low temperature is $M_s = 475$ emu cm^{-3} (80 emu g^{-1}).[6] On the other hand, R2 shows a slight decrease in both quantities (see Table 1) as a consequence of the hindering effect that the crystal defects, domain boundaries and the existence of local anisotropy axes associated with crystal domains within the particles may have on the long-range ferrimagnetic order. In any case, this effect has a very limited impact since the hysteresis loops of samples R1 and R2 look very much the same and highly resemble that expected for bulk $CoFe_2O_4$. In contrast, the degradation of the ferrimagnetic order is much more evident for R3, where the hysteresis loop at 5 K is totally different from the former curves for R1 and R2, resembling those of frustrated and disordered magnets, such as random anisotropy or cluster glass systems.[1] We attribute this behavior to the crystalline multidomain nature of the R3 NPs, where ferrimagnetic order tends to be arranged along the local magnetocrystalline anisotropy axes yielding magnetic multidomain NPs, in contrast to the single magnetic domains observed on high crystal quality Co-ferrite particles of similar size, as is the case of R1 and to some extent even R2. Moreover, frozen spins by magnetic frustration and local anisotropy axes at the crystal domain boundaries are known to give both a significant high-field linear contribution to the magnetization and hysteresis loops with high irreversibility (the hysteresis loops close at the highest applied magnetic field).[1]

Consequently, the saturation magnetization value of 25 emu g^{-1} at 5 K indicated in Table 1 for R3, which is about one third of that of R1, arises mainly from the spins inside the core of the crystal domains, since those spins are the only ones that keep a ferrimagnetic-like ordering. This suggests that the high magnetic frustration present in R3 NPs is due to their crystalline multidomain structure (see Fig. 1f). In addition, a large shift, H_s, of the hysteresis loop along the magnetic field axis is observed after cooling the particles down to about 80 K under 10 kOe, as shown in Fig. S10 in ESI.† The temperature dependence of H_s is displayed in the inset of Fig. 3. Note that the cooling field of 10 kOe is smaller than the irreversibility field below 80 K, so this horizontal shift of the loops may not correspond to a true exchange bias phenomenon,[25] but just to minor loops of the hysteresis loop,[26] as expected when a ferro/ferrimagnet is not saturated under the maximum applied magnetic field.

A further insight into the strong reduction of M_s at low temperature may be gained by evaluating the distribution of the magnetic moments of the crystal domain cores with ferrimagnetic-like order, from the magnetization curves in the superparamagnetic (SPM) regime. In the SPM regime, crystal anisotropy barriers are overcome by thermal excitation so that ferrimagnetic-like cores in the crystal domains magnetize following the applied magnetic field. Then, SPM magnetization curves can be fitted by a log-normal distribution $P(m)$ of Langevin functions $L(x)$ plus a linear contribution to the magnetization, $\chi_p H$, coming from the highly frustrated spins at crystal domain boundaries and the particle surface, as[27]

$$M(H,T) = M_C \frac{\int mP(m)L(mH/k_B T)\mathrm{d}m}{\int mP(m)\mathrm{d}m} + \chi_p H \qquad (1)$$

where m is the magnetic moment per ferrimagnetic-like core, k_B is the Boltzmann constant, M_C is the mean value of the contribution of the ferrimagnetic-like cores to the saturation magnetization and χ_p is the paramagnetic susceptibility. In the case of R3 NPs, the SPM regime is reached above about 200 K, so we used isothermal magnetization curves at 250 and 300 K, scaled in a H/T plot, to perform this fitting (see Fig. 4).

The fitted $P(m)$ distribution, shown in the inset to Fig. 4, can be transformed into the distribution of magnetic domain sizes

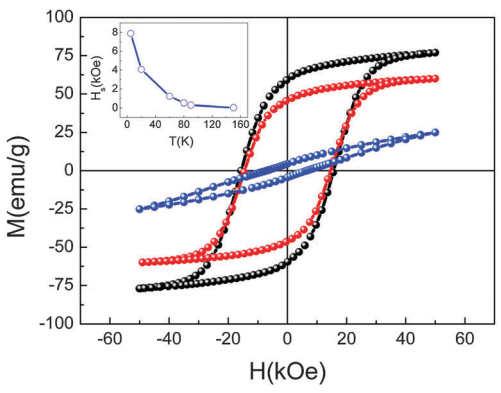

Fig. 3 Hysteresis loops of Co-ferrite NPs synthesized following different methods: R1 (black spheres), R2 (red spheres), R3 (blue spheres). Inset: temperature dependence of the horizontal loop shift, H_s, after field cooling sample R3 under 10 kOe from 250 K down to the measuring temperature.

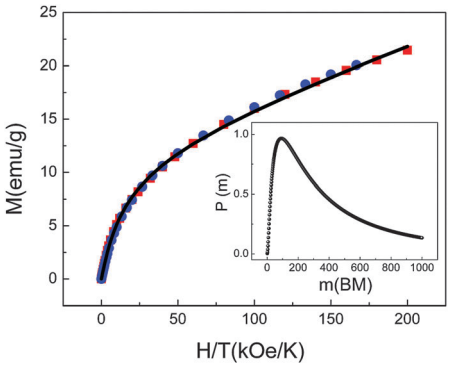

Fig. 4 Isothermal magnetization curves of sample R3 in the superparamagnetic regime, measured at 250 K (red squares) and 300 K (blue circles), as a function of H/T. The black solid line corresponds to the fit of the data to eqn (1). Inset: magnetic moment distribution of the ferrimagnetic-like crystallites obtained from the fit of the magnetization curves to eqn (1).

by assuming the $CoFe_2O_4$ bulk value of 475 emu cm^{-3} (80 emu g^{-1}) for the specific magnetization of the ferimagnetic-like crystallite cores.[6] The mean size of those crystallite magnetic domains and the value of the standard deviation are 1.9 nm and 0.4 nm, respectively, in very good agreement with crystalline features in HRTEM images (see Fig. S2c, ESI†) and D_{XRD} = 2.1 ± 0.6 nm (Table 1).

Additionally, the mean saturation magnetization of the ferrimagnetic-like cores deduced from this fitting is M_C = 28.5 emu g^{-1}, which is in quantitative agreement with the value obtained from the hysteresis loop at 5 K and 5 T (25 emu g^{-1}), temperature at which frustrated spins are essentially frozen so that the major contribution to the hysteresis loop comes from the ferrimagnetic-like cores.

This demonstrates the consistency of the estimation of the distribution of ferrimagnetic-like cores at the crystallite domains by fitting the magnetization curves in the SPM regime.

In addition, M_{ZFC} and M_{FC} curves, shown in the inset to Fig. 5, provide further evidence of the high magnetic frustration existing among ferrimagnetic-like crystallites in R3 NPs at low temperature.

There are significant differences between M_{ZFC}–M_{FC} curves for R3 and a conventional sample, such as R1, for example. First, the peak of the M_{ZFC} curve is located at a temperature (T_p = 150 K) much lower than what is expected for Co-ferrite NPs of about 8 nm in size (see Table 1 and Fig. S11, ESI†). Second, M_{FC} is almost constant below T_p indicating the existence of strong interactions between the magnetic domains and/or the onset of a highly frustrated magnetic state at T_p.[1] The latter is also supported by the rapid decrease of M_{ZFC} below T_p, suggesting the occurrence of a freezing process due to high magnetic frustration rather than a simple blocking of particle magnetization as the system is cooled down from the SPM regime.[1]

Moreover, M_{ZFC} is also very different from what could be expected for the simple blocking process of the distribution of ferrimagnetic-like crystallites, $P(m)$, which we have found by fitting the magnetization curves in the SPM regime (see Fig. 4). Fig. 5 shows a comparison between experimental M_{ZFC} and the corresponding curve calculated from $P(m)$ assuming the bulk values for the anisotropy constant and specific magnetization of Co-ferrite[3] ($K_v = 20 \times 10^5$ erg cm^{-3} and M_0 = 475 emu cm^{-3},[6] respectively), and using the following expression based on the Gittleman model,[28] for the blocking process of an assembly of non-interacting particles:

$$\frac{M_{ZFC}(T)}{H} = \frac{1}{3k_BT}\int_0^{M_0V_p(T)} m^2P(m)\mathrm{d}m + \frac{M_0}{3K_v}\int_{M_0V_p(T)}^{\infty} mP(m)\mathrm{d}m \quad (2)$$

where $V_p(T) = 25\ k_BT/K_v$. The two curves only coincide in the SPM regime (see T_{irr}, Table 1) where magnetic correlations among ferrimagnetic-like crystallites are weak and the net magnetizations of the NPs are mostly dominated by thermal activation of the small magnetic domains inside each particle. However, below around T_p the two curves quickly diverge as the temperature decreases and the calculated M_{ZFC} develops a sharp peak at low temperature associated with the progressive blocking of the small ferrimagnetic-like crystallites. In contrast, experimental M_{ZFC} curve shows a quite pronounced reduction of the magnetization towards zero as the magnetizations of the ferrimagnetic-like crystallites become frozen in random directions due to frustrated magnetic interactions at the boundaries of the crystallite domains.

The existence of high energy barriers originating from the magnetic frustration among crystallites constituting each particle has also been confirmed by measuring the time dependence of the relaxation of the magnetization. Relaxation curves for R3 at several temperatures are analyzed in Fig. 6 in terms of the $T\ln(t/\tau_0)$ scaling where,[29] in order to make all the curves collapse onto a single master curve, the characteristic attempt time has been set to $\tau_0 = (5 \pm 4) \times 10^{-12}$ s and each curve has been divided by an arbitrary reference magnetization value that is pretty close to $M_{FC}(T)$.

The effective distribution of energy barriers, $f(E)$, calculated by numerical derivative of the scaling relaxation curve,[30] is shown in Fig. 7. It is evident from Fig. 7 that $f(E)$ is much broader and right-shifted to higher energies than both (i) the distribution of energy barriers of anisotropy corresponding to the volume distribution of the ferrimagnetic-like cores (see $P(m)$ in the inset to Fig. 4); and (ii) the distribution of energy barriers of anisotropy

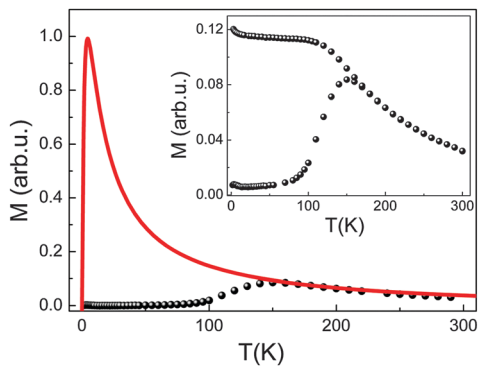

Fig. 5 M_{ZFC} for R3 (black spheres). The solid red line represents the M_{ZFC} curve calculated from eqn (2) with the distribution of magnetic moments for the ferrimagnetic-like cores shown in the inset to Fig. 4. Inset: M_{ZFC}–M_{FC} for R3.

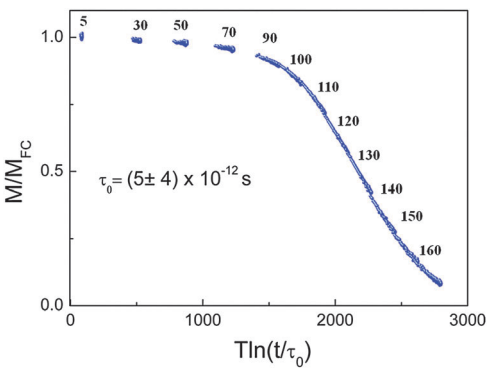

Fig. 6 Scaling of the relaxation curves for R3, measured at several temperatures, with an attempt time of $\tau_0 = (5 \pm 4) \times 10^{-12}$ s.

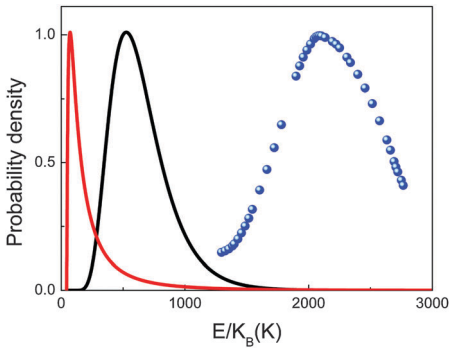

Fig. 7 Comparison between the distribution of energy barriers of anisotropy corresponding to the volumes of the ferrimagnetic-like cores (red solid line) and the particle size distribution obtained from TEM images (black solid line). Those calculations were performed assuming the value of $K_v = 20 \times 10^5$ erg cm^{-3} for bulk Co-ferrite. The effective distribution of energy barriers calculated by the derivative of the scaling relaxation curve in Fig. 6 (blue spheres) is also represented.

corresponding to the particle size distribution obtained from TEM images (see S1c, in ESI†), thus indicating the key role of magnetic frustration among particle crystallites in determining the magnetic performance of those highly structural defective Co-ferrite NPs with stoichiometric composition.

Conclusions

We have studied three samples of 8 nm Co-ferrite NPs synthesized by standard methods based on the thermal decomposition of metal–organic precursors.[13–19] Despite all three samples having very similar stoichiometry and distribution of particle sizes, and being nominally single-phase $CoFe_2O_4$ according to the conventional methods of chemical and structural characterization performed, they show strongly sample-dependent magnetic properties, ranging from bulk-like ferrimagnetism to glassy magnetic behaviour. Interestingly enough, spatially-resolved composition characterization has discarded either the formation of core–shell structures or the presence of other chemical phases within the particles. This raises the question about the effect that the actual crystallographic quality of the Co-ferrite NPs may have on their magnetic behaviour. As a matter of fact, crystallographic defects locally destabilize ferrimagnetic order yielding non-collinear arrangements of the spins that become frozen in a kind of glassy state at low temperature, largely spoiling the magnetic performance of the NPs. In particular, the paradigmatic situation corresponds to the presence of a number of small crystallite domains throughout the particles, which causes highly-frustrated ferrimagnetic-like cores that bring about much of the phenomenology typical of a glassy state. The existence of those small ferrimagnetic-like cores is also confirmed by fitting the magnetization curves in the SPM regime, leading to a distribution of magnetic volumes that is much smaller than the real size of the particles (D_{TEM}). These results highlight the key role of the crystal quality in the sample-dependent magnetic properties previously reported for Co-ferrite NPs. All in all, the structural defects in monodisperse, stoichiometric Co-ferrite NPs can be used as an additional nano-structuring procedure that tunes their final magnetic properties from bulk-like ferrimagnetism to glassy behaviour. In particular, Co-ferrite NPs with highly defective crystal structures show unexpected magnetic properties associated with an internal enhancement of the magnetic frustration that strongly reduces both the saturation magnetization and coercive field.

Acknowledgements

This work was supported by Spanish MINECO (MAT2011-23641, MAT2012-33037, MAT2013-48054-C2), Catalan DURSI (2014SGR220), and European Union FEDER funds (Una manera de hacer Europa) and MULTIFUN project no. 246479. C. Moya acknowledges Spanish MINECO for a PhD contract (BES-2010-038075) and a three month stay at the ICMM/CSIC where the particles were synthesized. Dr Nicolàs Pérez (UB) is acknowledged for critical discussion of the results.

Notes and references

1 X. Batlle and A. Labarta, *J. Phys. D: Appl. Phys.*, 2002, **35**, R15.
2 R. Mejías, S. Pérez-Yagüe, A. G. Roca, N. Pérez, A. Villa nueva, M. Cañete, S. Mañes, J. Ruiz-Cabello, M. Benito, A. Labarta, X. Batlle, S. Veintemillas-Verdaguer, M. P. Morales, D. F. Barber and C. J. Serna, *Nanomedicine*, 2010, **5**, 397.
3 Q. A. Pankhurst, J. Connolly, S. K. Jones and J. Dobson, *J. Phys. D: Appl. Phys.*, 2003, **36**, R167.
4 C. Sun, J. S. H. Lee and M. Zhang, *Adv. Drug Delivery Rev.*, 2008, **60**, 1252.
5 J. M. Perez, L. Josephson and R. Weissleder, *ChemBioChem*, 2004, **5**, 261.
6 B. D. Cullity and C. D. Graham, *Introduction to Magnetic Materials*, 2011.
7 N. Pérez, P. Guardia, A. G. Roca, M. P. Morales, C. J. Serna, O. Iglesias, F. Bartolomé, L. M. García, X. Batlle and A. Labarta, *Nanotechnology*, 2008, **19**, 475704.
8 J. Geshev, *J. Magn. Magn. Mater.*, 2008, **320**, 600.
9 E. S. Leite, J. A. H. Coaquira, W. R. Viali, P. P. C. Sartoratto, R. L. Almeida, P. C. De Morais and S. K. Malik, *J. Phys.: Conf. Ser.*, 2010, **200**, 072060.
10 Y. H. Hou, Y. J. Zhao, Z. W. Liu, H. Y. Yu, X. C. Zhong, W. Q. Qiu, D. C. Zeng and L. S. Wen, *J. Phys. D: Appl. Phys.*, 2010, **43**, 445003.
11 D. Peddis, C. Cannas, G. Piccaluga, E. Agostinelli and D. Fiorani, *Nanotechnology*, 2010, **21**, 125705.
12 Y. Cedeño-Mattei, O. Perales-Pérez and O. N. C. Uwakweh, *Mater. Chem. Phys.*, 2012, **132**, 999.
13 Y. Zhang, Z. Yang, B.-P. Zhu, J. Ou-Yang, R. Xiong, X.-F. Yang and S. Chen, *J. Alloys Compd.*, 2012, **514**, 25.
14 S. Gyergyek, D. Makovec, A. Kodre, I. Arčon, M. Jagodič and M. Drofenik, *J. Nanopart. Res.*, 2009, **12**, 1263.
15 S. Sun and H. Zeng, *J. Am. Chem. Soc.*, 2002, **124**, 8204.

16 S. Sun, H. Zeng, D. B. Robinson, S. Raoux, P. M. Rice, S. X. Wang and G. Li, *J. Am. Chem. Soc.*, 2004, **126**, 273.
17 N. Bao, L. Shen, Y. Wang, P. Padhan and A. Gupta, *J. Am. Chem. Soc.*, 2007, **129**, 12374.
18 Q. Song and Z. J. Zhang, *J. Am. Chem. Soc.*, 2004, **126**, 6164.
19 L. I. Cabrera, Á. Somoza, J. F. Marco, C. J. Serna and M. P. Morales, *J. Nanopart. Res.*, 2012, **14**, 873.
20 N. Pérez, F. López-Calahorra, A. Labarta and X. Batlle, *Phys. Chem. Chem. Phys.*, 2011, **3**, 19485.
21 P. Guardia, N. Pérez, A. Labarta and X. Batlle, *Langmuir*, 2010, **26**, 5843.
22 P. Tartaj, M. P. Morales, S. Veintemillas-Verdaguer, T. Gonzàlez-Carreño and C. J. Serna, *J. Phys. D: Appl. Phys.*, 2003, **36**, R182.
23 V. K. LaMer and R. H. Dinegar, *J. Am. Chem. Soc.*, 1950, **72**, 4847.
24 G. Salas, C. Casado, F. J. Teran, R. Miranda, C. J. Serna and M. P. Morales, *J. Mater. Chem.*, 2012, **22**, 21065.
25 J. Nogués and I. K. Schuller, *J. Magn. Magn. Mater.*, 1999, **192**, 203.
26 X. Batlle, N. Pérez, P. Guardia, O. Iglesias, A. Labarta, F. Bartolomé, L. M. García, J. Bartolomé, A. G. Roca, M. P. Morales and C. J. Serna, *J. Appl. Phys.*, 2012, **109**, 07B524.
27 C. P. Bean and J. D. Livingston, *J. Appl. Phys.*, 1959, **30**, S120.
28 J. Gittleman, B. Abeles and S. Bozowski, *Phys. Rev. B: Condens. Matter Mater. Phys.*, 1974, **9**, 3891.
29 A. Labarta, O. Iglesias, L. Balcells and F. Badia, *Phys. Rev. B: Condens. Matter Mater. Phys.*, 1993, **48**, 10240.
30 O. Iglesias, F. Badia, A. Labarta and L. Balcells, *Z. Phys. B: Condens. Matter*, 1996, **100**, 17.

Electronic Supplementary Material (ESI) for Journal of Materials Chemistry C.

Supporting information

Inducing glassy magnetism in Co-ferrite nanoparticles through crystalline nanostructure

Carlos Moya,*[a] Gorka Salas,[b,c] María del Puerto Morales,[b] Xavier Batlle [a] and Amílcar Labarta [a]

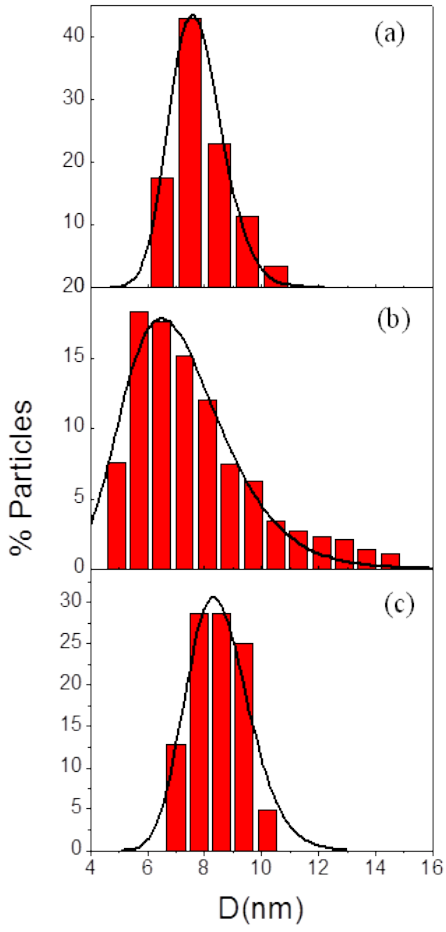

Figure S1. Particle size distributions for the three samples: (a) R1, (b) R2, (c) R3.

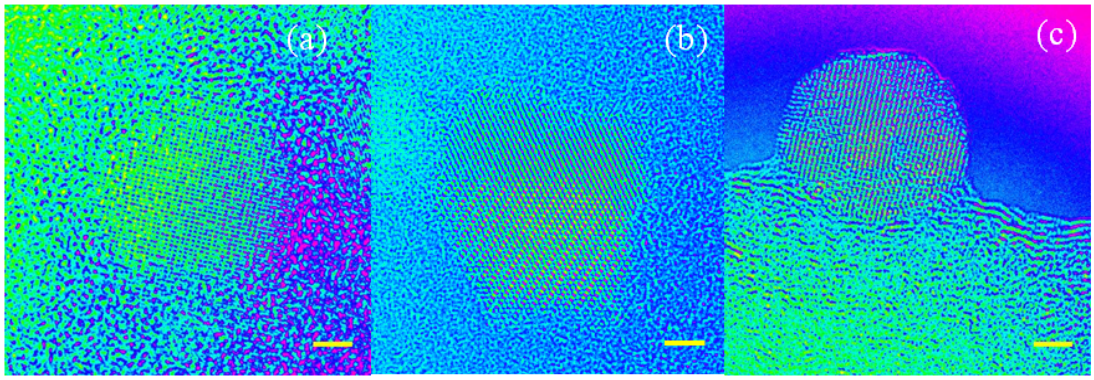

Figure S2. HRTEM micrographs of $CoFe_2O_4$ NPs with color contrast: **(**a) R1, (b) R2, (c) R3. Scale bars correspond to 2 nm.

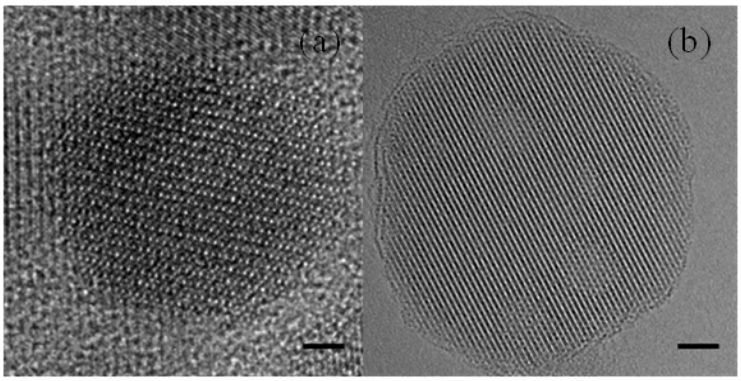

Figure S3. HRTEM micrographs of $CoFe_2O_4$ NPs for R2 with different degree of crystallinity. Scale bars in (a) and in (b) correspond to 1.5 and 2 nm respectively.

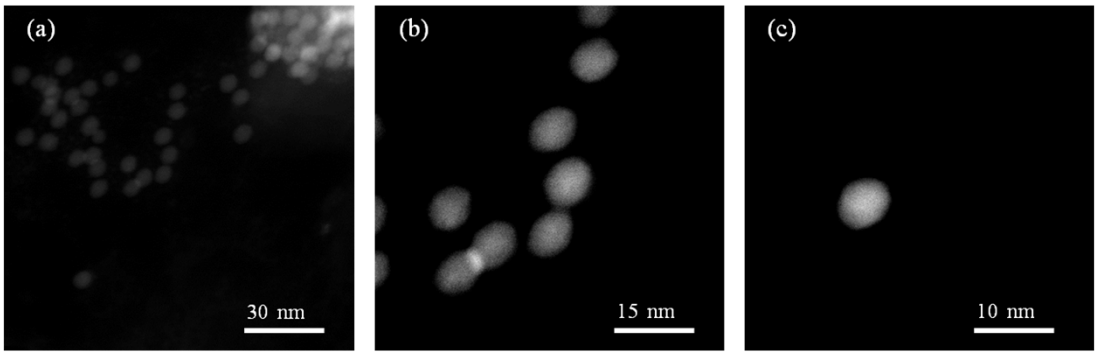

Figure S4. High-angle annular dark field (HAADF) images of several nanoparticles for R3.

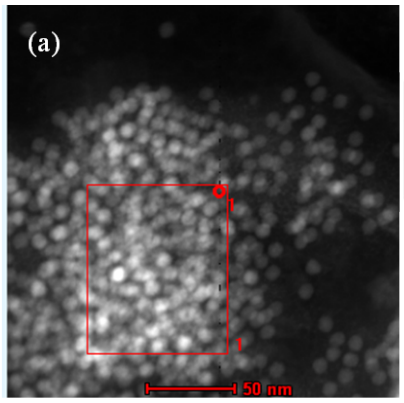

(b)

Element quantification	%
Fe	67(7)
Co	33(4)

(c)

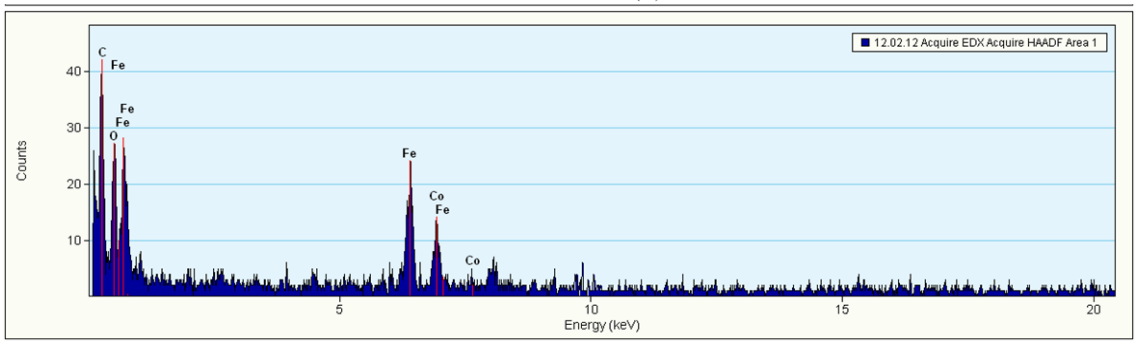

Figure S5. (a) HAADF Energy dispersive X-ray Spectroscopy (EDX) image of several NPs in R3, (b) Fe and Co percentage quantification, (c) EDX spectrum for the red area in a).

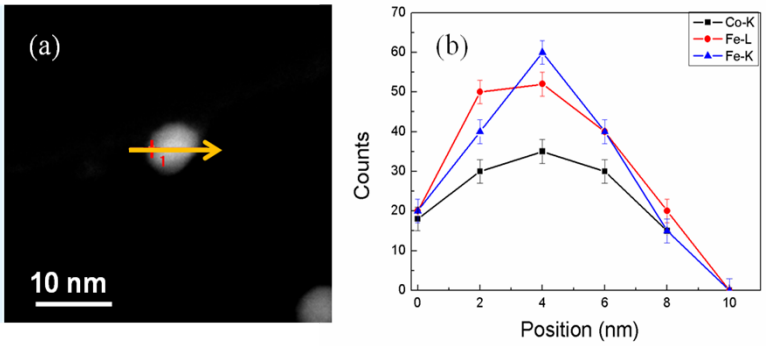

Figure S6. R3: (a) HAADF EDX image of a particle and (b) element quantification along the orange arrow.

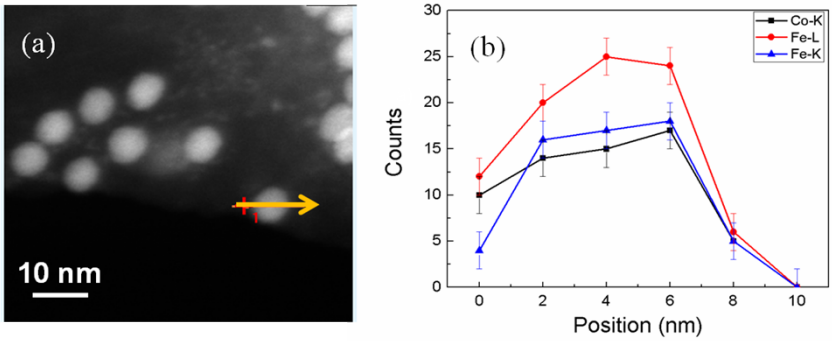

Figure S7. R3: (a) HAADF EDX image of a particle and (b) element quantification along the orange arrow.

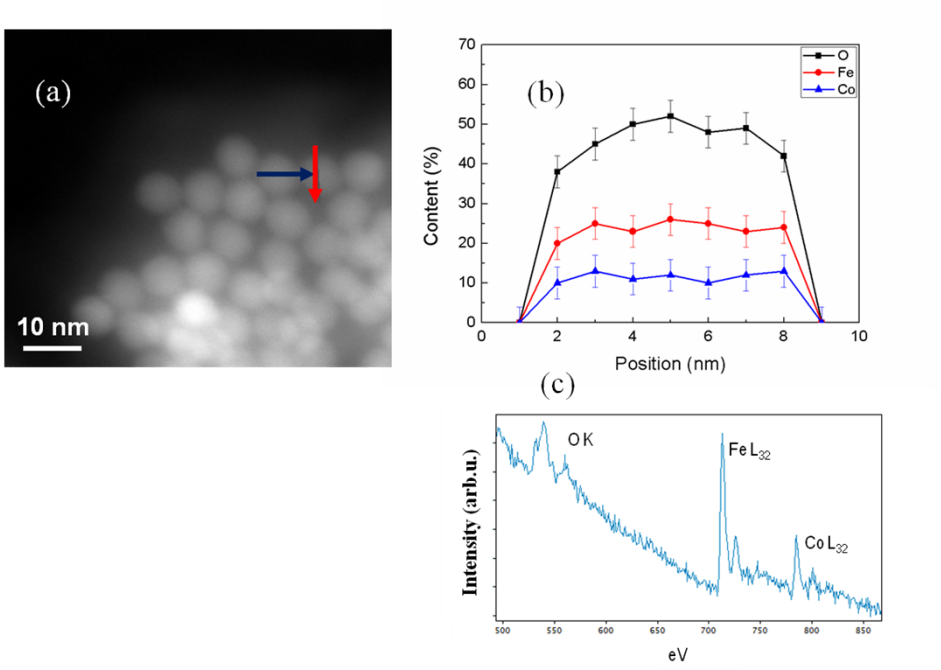

Figure S8. R3: (a) HAADF STEM image of some particles and (b) element quantification along the red arrow. (c) Sample spectrum measured at the point marked with the blue arrow in (a).

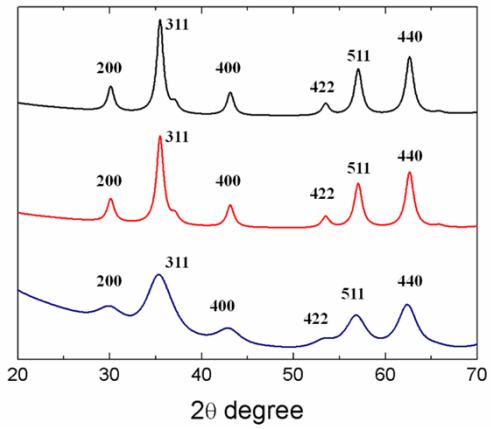

Figure S9. X- ray diffraction patterns together with the indexation of the Bragg peaks to an inverse spinel structure: R1 (black solid line), R2 (red solid line), R3 (blue solid line).

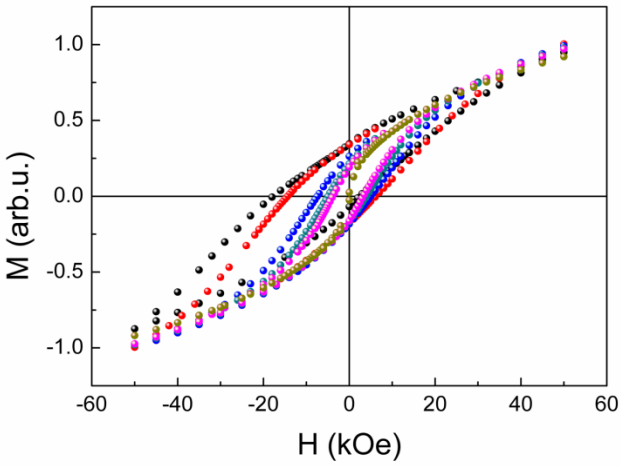

Figure S10. Hysteresis loops after FC sample R3 from 250 K down to the final measuring temperature (T) under an applied magnetic field of 10 kOe. T = 5 K (black spheres), 20 K (red spheres), 60 K (blue spheres), 80 K (green spheres), 90 K (pink spheres) and 150 K (dark yellow).

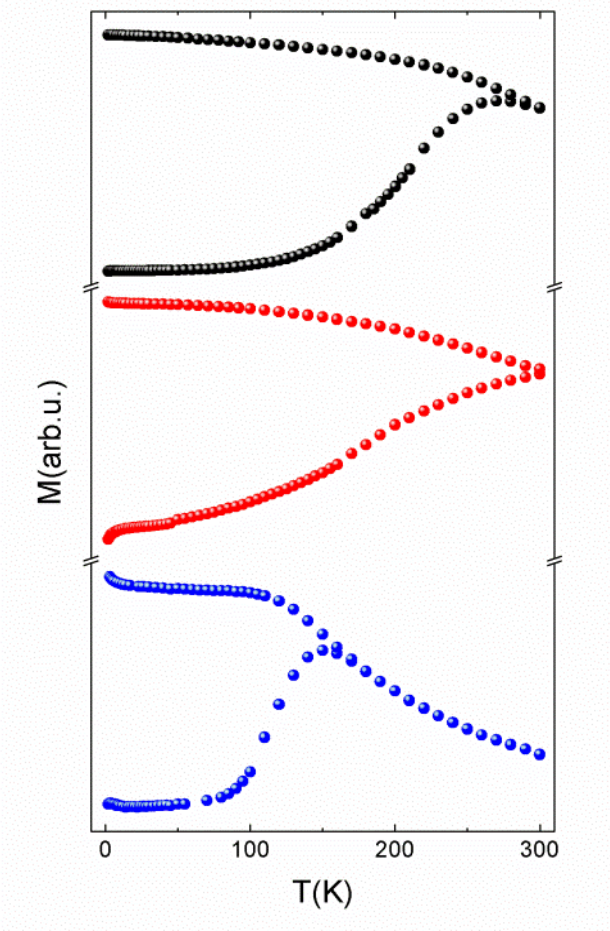

Figure S11. M_{ZFC}-M_{FC} for R1 (black spheres), R2 (red spheres), R3 (blue spheres).

Chapter 4.Effect of interparticle interactions

SiO_2 coating effects in the magnetic anisotropy of $Fe_{3-x}O_4$ nanoparticles suitable for bio-applications

2013 Nanotechnology 24 155705

(http://iopscience.iop.org/0957-4484/24/15/155705)

Nanotechnology **24** (2013) 155705 (8pp) doi:10.1088/0957-4484/24/15/155705

SiO_2 coating effects in the magnetic anisotropy of $Fe_{3-x}O_4$ nanoparticles suitable for bio-applications

A I Figueroa[1], C Moya[2], J Bartolomé[1], F Bartolomé[1], L M García[1], N Pérez[2], A Labarta[2] and X Batlle[2]

[1] Departamento de Física de la Materia Condensada, Instituto de Ciencia de Materiales de Aragón (ICMA), CSIC—Universidad de Zaragoza, E-50009 Zaragoza, Spain
[2] Departament de Física Fonamental and Institut de Nanociència i Nanotecnologia (IN2UB), Universitat de Barcelona, E-08028 Barcelona, Spain

E-mail: figueroa@unizar.es

Received 17 December 2012
Published 22 March 2013
Online at stacks.iop.org/Nano/24/155705

Abstract
We present radio frequency transverse susceptibility (TS) measurements on oleic acid-coated and SiO_2-coated $Fe_{3-x}O_4$ magnetite nanoparticles. The effects of the type of coating on the interparticle interactions and magnetic anisotropy are evaluated for two different particle sizes in powder samples. On the one hand, SiO_2 coating reduces the interparticle interactions as compared to oleic acid coating, the reduction being more effective for 5 nm than for 14 nm diameter particles. On the other hand, the magnetic anisotropy field at low temperature is lower than 1 kOe in all cases and independent of the coating used. Our results are relevant concerning applications in biomedicine, since the SiO_2 coating renders 5 and 14 nm hydrophilic particles with very limited agglomeration, low anisotropy, and superparamagnetic behavior at room temperature. The TS technique also allows us to discriminate the influence on the anisotropy field of interparticle interactions from that of the thermal fluctuations.

(Some figures may appear in colour only in the online journal)

1. Introduction

Magnetic nanoparticles (NPs) constitute an ideal system to study finite-size and surface effects, those yielding new phenomena and enhanced properties with respect to their bulk counterparts [1]. Beyond the scientific interest of their novel phenomenology, their potential technological applications in fields such as biomedicine [2], high-density magnetic recording [3], and magnetic resonance imaging (MRI) [4] have been active subjects of study over the past decades. In particular, magnetite (Fe_3O_4) NPs are one of the most commonly studied systems because of their relatively easy production by chemical routes, low toxicity and fascinating magnetic properties [5–7]. It has been demonstrated that the surrounding environment of the Fe_3O_4 particles strongly affects their magnetic properties [8–12], in such a way that, for example, bulk-like structural, magnetic and electronic behavior may be recovered in 5 nm particles [5–7]. Such effects are obtained in Fe_3O_4 NPs with oleic acid used as surfactant, covalently bonded to the particle surface. These particles are good candidates for biomedical applications [13], once the hydrophobic oleic acid coating is ligand-exchanged to a hydrophilic one, which makes the particles dispersible in aqueous media. Within this framework, magnetic NPs of a few nanometers in size and with the highest possible magnetization are required. They must also show superparamagnetic behavior at room temperature and low interparticle interactions, for which low particle agglomeration is desirable. All these features enable the synthesis of NP dispersions (ferrofluids) which can be injected into biological systems for *in vivo* applications [2, 14].

Following this scheme, it is crucial to evaluate the effects of the hydrophilic particle coating on the magnetic anisotropy of Fe_3O_4 NPs, in order to get optimum particles for

bio-applications. Particle coating also reduces the interparticle interactions as a consequence of the increase in their interparticle distances, thus shifting the superparamagnetic transition well below room temperature. This allows the use of larger particles with larger magnetic moment, which results in larger signals in the superparamagnetic regime [15].

In this paper, we use a hydrophilic coating, namely, SiO_2 on 5 nm and 14 nm Fe_3O_4 NPs, and examine its effects on the interparticle interactions and magnetic anisotropy of the particles by radio frequency (RF) transverse susceptibility (TS) measurements. For completeness, we compare the results on these SiO_2-coated Fe_3O_4 NPs with those obtained for the starting oleic acid-coated particles of the same size. We demonstrate that the SiO_2 coating places the particles further apart. Thus, the effect of the varying dipolar interparticle interactions can be clearly identified in the comparative study of the anisotropy of those particles bearing different coating. We also show that a careful analysis of the TS measurements as a function of temperature allows us to distinguish the effects of thermal fluctuations from those of the interparticle interactions, and their relative weights, in the blocked state of the particles.

2. Synthesis and microstructure

Oleic acid-coated $Fe_{3-x}O_4$ NPs of controlled size were synthesized by thermal decomposition of Fe(III)-acetylacetonate with oleic acid in organic solvent, as extensively described elsewhere [10, 16–18]. Here we express $Fe_{3-x}O_4$ for these magnetite NPs as the actual stoichiometry depends on the amount of Fe^{2+}. The fraction of these ions is very difficult to determine for small particles, as there might be a combination of Fe_3O_4 (magnetite) and γ-Fe_2O_3 (maghemite) forming a solid solution, or even more due to the common over-oxidation of the outermost shell of magnetite NPs [19, 20]. Therefore, the general expression $Fe_{3-x}O_4$ is used in the following. Particles of mean diameter 5 nm and 14 nm, respectively, were prepared and suspended in hexane until final use. SiO_2 coating was performed on the previously obtained $Fe_{3-x}O_4$ NPs using the alkaline catalyzed hydrolysis of tetraethyl orthosilicate in water in oil microemulsions [21, 22], which is a reproducible method that allows controlling the shell thickness and the number of cores per shell [21, 20].

For transmission electron microscopy (TEM) observation, a drop of NP suspension was carefully placed on carbon-coated copper grids and dried. For the magnetic measurements the particles coated with either oleic acid or SiO_2 were extracted from hexane and microemulsion, respectively, by precipitation, allowing the remaining solvent to evaporate at room temperature under moderate vacuum, and the resulting dry powder was then placed in appropriate sample holders.

The size and shape of the NPs were examined by TEM with Hitachi H-7500 (low-resolution) and JEOL JEM 2010 (high-resolution) transmission electron microscopes. Samples for the TEM study were prepared on copper grids coated with carbon. The size distributions of the nanocrystals were determined by analysis of the TEM images. The bright field

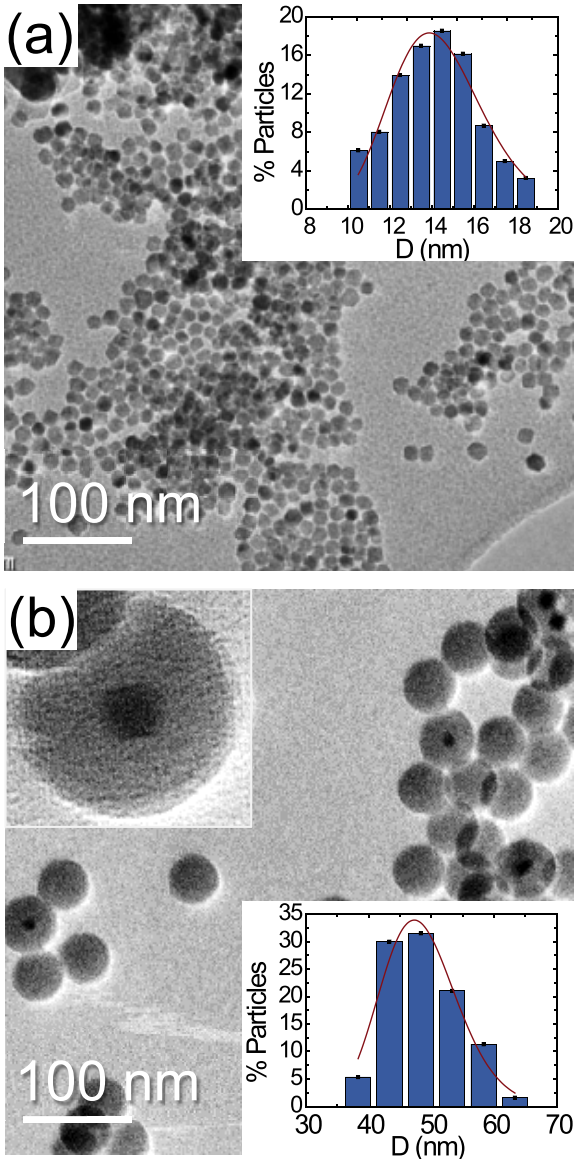

Figure 1. BF TEM images of the oleic acid-coated (a) and SiO_2-coated (b) $Fe_{3-x}O_4$ NPs with average core diameter of 14 nm. Insets show the size distributions obtained in each case. The SiO_2 shell thickness in (b) is about 15–20 nm. Upper inset in (b) shows details of a SiO_2-coated particle.

(BF) TEM images of the 14 nm NPs for both coatings are shown in figure 1 along with the size distributions obtained for each case. The oleic acid-coated particles are very uniform (figure 1(a)), similarly to those previously reported for this range of sizes [10]. SiO_2-coated particles are shown in figure 1(b). Darker and lighter regions correspond to the $Fe_{3-x}O_4$ core (14 nm average diameter) and the SiO_2 shell (about 15–20 nm thick), respectively, shown in detail in the upper inset of figure 1(b). This image reveals that almost all the $Fe_{3-x}O_4$ NPs are single-coated, with very low agglomeration, though an excess of SiO_2 is observed, as some SiO_2 beads without $Fe_{3-x}O_4$ cores are present. We note that 5 nm particles display analogous results, as for the size uniformity and individual SiO_2 coating with similar thickness. TEM measurements reveal that the shape and size

Table 1. Summary of parameters of the $Fe_{3-x}O_4$ NPs. Average particle diameter ($\langle D \rangle$) and standard deviation (σ) of the size distribution as obtained from TEM, blocking temperature (T_B) obtained from χ_{dc}, blocking temperature (T_M) deduced from TS, and anisotropy field (H_{K0}) at $T = 2$ K.

Coating	$\langle D \rangle$ (nm)	σ (nm)	T_B from χ_{dc} (K)	T_M from TS (K)	H_{K0} (kOe)
Oleic acid	5	3	35(2)	35(2)	0.69(3)
	14	9	∼300	215(5)	0.90(4)
SiO_2	44	27	16(1)	14(1)	0.65(3)
	49	29	170(1)	140(1)	0.89(4)

of the starting oleic acid-coated $Fe_{3-x}O_4$ particles are not modified by the SiO_2 coating. The average diameter and standard deviation obtained from the size distributions for the four samples are listed in table 1.

3. Magnetic properties

The magnetic properties (zero-field cooling, ZFC, and field cooling, FC, susceptibility) of the oleic acid-coated $Fe_{3-x}O_4$ particles have been previously reported in [8, 10], and reveal their superparamagnetic behavior. The blocking temperature (estimated as the maximum of the ZFC curve), T_B, of the particles with average sizes of 5 and 14 nm, is 35 and 300 K, respectively. The SiO_2-coated samples also exhibit superparamagnetic behavior, with a reduced T_B (see table 1) as compared to the oleic acid-coated samples. Such an effect will be discussed in section 5 in terms of the dipolar interaction between particles.

4. Transverse susceptibility

TS measurements were performed using a radio frequency (RF) self-resonant circuit oscillator based on a simple inverter cell with CMOS transistors in cross-coupled topology, operating at a resonant frequency of around 12 MHz. The sample in powder form is placed in a gel-cap that snugly fits into the core of an inductive copper coil (L), which is part of the self-resonant circuit oscillator. This is inserted into the sample space of a commercial physical property measurement system (PPMS) from Quantum Design using a customized RF coaxial probe. The oscillating RF field, H_{RF}, produced by the RF current flowing in the coil windings, is oriented perpendicular to the static field, H_{dc}, produced by the PPMS superconducting magnet, and this arrangement sets up the transverse geometry. The temperature, T, and H_{dc} are varied using the PPMS within 2–300 K and ±15 kOe, respectively. In the experiment, a TS scan is performed at a fixed temperature, while the shift in the resonant frequency is measured as the static field is varied from positive to negative saturation (unipolar TS scan), and vice versa (bipolar TS scan). The frequency shift, Δf, arises from a change in the coil inductance L, determined by the change in transverse permeability μ_T of the sample, which is, at the same time, proportional to the transverse susceptibility, χ_T. The quantity

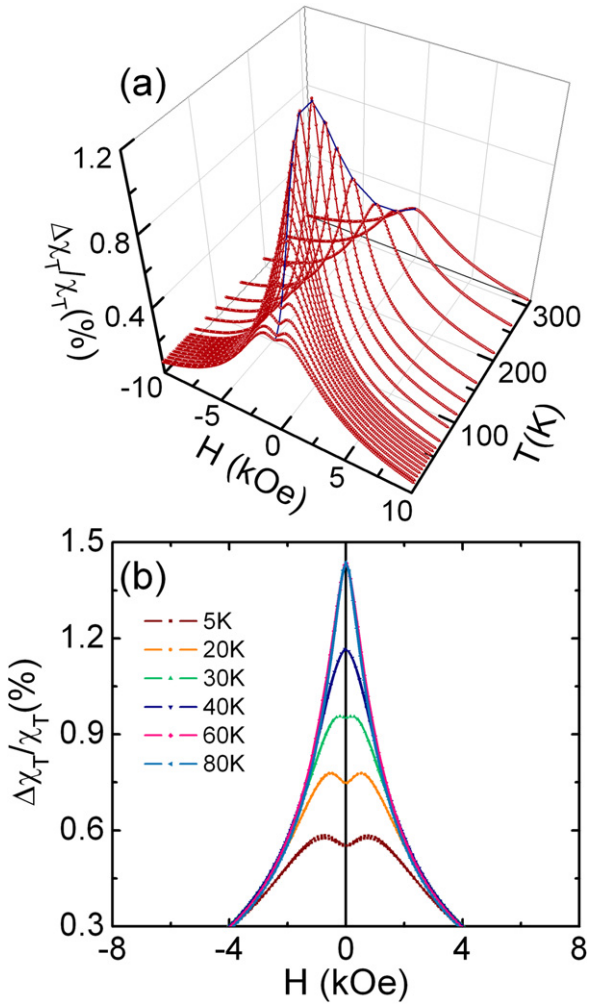

Figure 2. TS results for 5 nm oleic acid-coated $Fe_{3-x}O_4$ NPs. (a) 3D plot of TS unipolar scans at several temperatures. (b) TS bipolar scans at selected temperatures.

of interest is the TS ratio, which is expressed as

$$\frac{\Delta\chi_T}{\chi_T}\% = \frac{\chi_T^{sat} - \chi_T(H_{dc})}{\chi_T^{sat}} \times 100 \propto \frac{\Delta f}{f_0}\% \qquad (1)$$

where χ_T^{sat} is the transverse susceptibility at the saturating field $H^{sat} = 15$ kOe. A complete description of the measurement system can be found in [23]. This technique has been used over the years with great success to study the anisotropy of different systems of magnetic nanoparticles [24–26], including iron oxide NPs [27].

Figure 2(a) shows the 3D plot of unipolar TS scans for the 5 nm oleic acid $Fe_{3-x}O_4$ NPs at several temperatures. At low temperatures the curves show two peaks, located symmetrically about the origin of the magnetic field axis, characteristic of the blocked regime. According to the theoretical model developed by Aharoni *et al* [28], a unipolar TS scan should reveal the existence of those two symmetric peaks at the anisotropy fields, H_K, and a third one at the switching field, H_S. The absence of the peak at H_S in the TS scans, as well as the rounded characteristic shape of the peaks observed in our case or in similar NP systems [25],

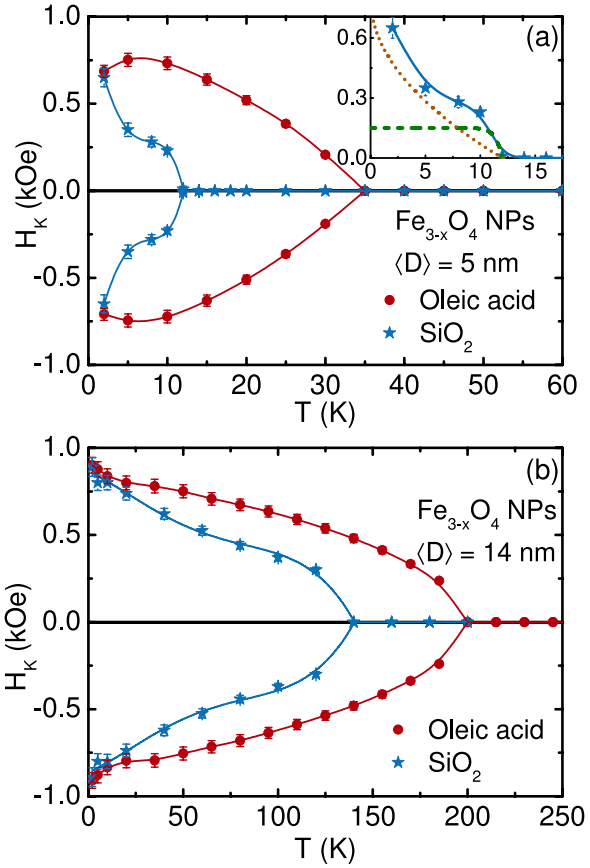

Figure 3. Comparison of the temperature dependence of the values of the anisotropy field (H_K) obtained from the TS scans for the oleic acid- and SiO_2-coated $Fe_{3-x}O_4$ NPs with average diameters of (a) 5 nm and (b) 14 nm. Inset in (a) shows the positive values of $H_K(T)$ for the 5 nm SiO_2-coated particles, along with two guides to the eye curves to illustrate its dependence on temperature (see text in section 5): (dotted line) $\beta < 1$ for thermal fluctuations and (dashed line) $\beta > 1$ for dipolar interactions.

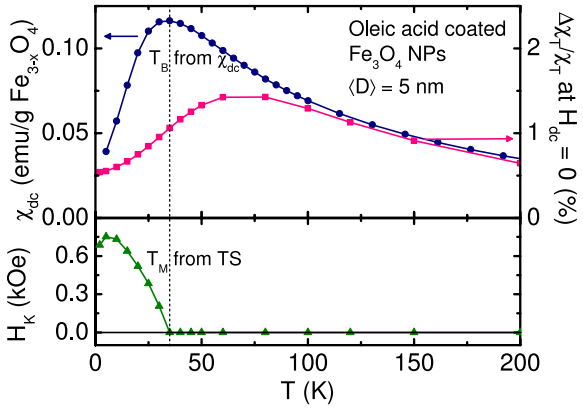

Figure 4. Comparison of the temperature dependence of (i) the ZFC curve (•) obtained from dc susceptibility measurements (χ_{dc}) at 50 Oe; (ii) the curve obtained from the transverse susceptibility values at $H_{dc} = 0$ (■) (top panel), and (iii) the anisotropy field (H_K) (bottom panel), for the oleic acid-coated 5 nm $Fe_{3-x}O_4$ particles. The dashed line marks the T_B from the ZFC curve, which matches the blocking temperature, T_M, obtained from TS.

are attributed to the presence of a distribution of anisotropy fields, which causes the peak at the switching field to merge indistinguishably with one of the peaks at the anisotropy field [29].

As the temperature increases from 2 K, the double-peak structure of the isothermal unipolar scans becomes less pronounced and merges into a single central peak, as depicted in figure 2(b). This trend is consistent with a gradual transition from a blocked state towards a superparamagnetic one, which will be discussed further in section 5. Analogous results for the TS measurements have been obtained for the other three samples.

The H_K values obtained from the TS profiles for the four samples are plotted in figure 3, as a function of temperature. Let us remark that the direct determination of H_K is one of the main assets of the TS technique. We define T_M as the minimum temperature at which $H_K = 0$, corresponding to the blocking temperature where the double-peak structure in the TS profiles disappears. T_M values obtained for the four samples are listed in table 1. Note that these values are in agreement with those of T_B obtained from the ZFC curves measured by conventional SQUID magnetometry (also listed in table 1).

H_K values are found to be lower than 1 kOe in all cases. For most temperatures, H_K are higher for the oleic acid-coated than for the SiO_2-coated samples (see figure 3), for both particle sizes. This is due to a reduction in the T_B value for the SiO_2-coated particles, a fact that will be also discussed in section 5. At about 2 K, though, H_K values are the same within the experimental error for each group of particles (5 nm with both coatings on one side, and 14 nm with both coatings on the other), which reveals that at very low temperature the strong magnetic behavior of the magnetite core overcomes any effect of the coating. H_K at $T = 2$ K will be expressed as H_{K0} in the following, and the values found for the four particle systems studied here are listed in table 1.

5. Discussion

In order to provide a deeper understanding of the TS measurements, in figure 4 we perform a direct comparison between the ZFC curve as obtained from the χ_{dc} SQUID measurements [8, 10] (top panel, left-hand side y-axis) and the TS ratio, $\Delta\chi_T/\chi_T(T)$, at $H_{dc} = 0$ (top panel, right-hand side y-axis) as a function of temperature for the 5 nm oleic-coated particles. As the temperature increases, the TS ratio at $H_{dc} = 0$ increases, similarly to the observed behavior of the ZFC curve, although it has a maximum at a higher temperature. This is consistent with the well-known increase [1] in the temperature of the ac susceptibility maximum as the exciting frequency increases (with respect to the dc measurements), since TS is measured at a frequency of 12 MHz. Such a feature for TS has been previously described in [27]. Both χ_{dc} and TS measurements coincide in the superparamagnetic region, as has been proven elsewhere [23].

For completeness, the temperature dependence of the positive H_K values is also plotted on figure 4 (bottom panel, left-hand side y-axis). Notice the nice accordance between

T_M from TS and T_B from the maximum of the ZFC curve (see dashed line in figure 4), as mentioned in section 4, demonstrating that in the blocked state (below T_B) the particles have finite H_K values.

According to these results, with the TS measurements we are observing, on the one hand, a phenomenon related to a dc behavior of the particles, i.e., their superparamagnetic-blocking transition occurring at a characteristic temperature, detectable from the $H_K(T)$ plot and the ZFC from χ_{dc} measurements; and, on the other hand, we observe a dynamic process evidenced in the shift of the $H_{dc} = 0$ ac susceptibility maximum to higher temperatures with increasing frequency. This is possible given that in a TS experiment we are applying both a bias and a dynamic magnetic field at the same time, thus we are able to observe and disentangle both phenomena in the particles. Let us detail their magnetic response as follows.

The magnetic susceptibility of a nanoparticle with uniaxial anisotropy may be expressed in terms of the component along the anisotropy axis $\chi_\parallel$ and perpendicular to it $\chi_\perp$. The frequency response of these components is drastically different [30] since the relaxation time along each of the two orthogonal directions depends strongly on the anisotropy of the particle. For strong anisotropy, as in the case of our magnetite particles, the relaxation time parallel to the axis is $\tau_\parallel = \tau_0 \exp(U/(k_B T))$, whereas the transverse relaxation time is $\tau_\perp = \tau_0$. The prefactor τ_0 is weakly temperature and volume dependent. This microscopic relaxation time $\tau_\perp$ is related to the intra-potential-well dynamics, being typically of the order of 10^{-10} s, and U is the anisotropy barrier to magnetic moment reversal. The relaxation time $\tau_\parallel$ corresponds to thermally activated processes that can be very slow and are related to jumps over the anisotropy barrier. By contrast, $\tau_\perp$ corresponds to the intra-potential-well redistribution of the magnetic moments. Therefore, at the RF frequencies typical of the present TS experiment (where $\tau_{exp} = 1/\omega_{exp} \approx 10^{-7}$ s), the response along the perpendicular direction may be taken as instantaneous, and no relaxation is encountered. Along the parallel direction, the magnetic response is out of equilibrium, χ_{irrev}, and can be described by a Debye-like factor, while in the perpendicular direction it is always reversible, χ_{rev} [31].

In the TS susceptibility experiment a dc field, H_{dc}, is applied in a fixed direction and a RF ac field, H_{RF}, in the perpendicular one. If the sample consists of a randomly oriented collection of identical, uniaxial nanoparticles, it can be shown that:

- For $H_{dc} = 0$, the ac susceptibility $\chi_{H_{RF}}$ in the direction of H_{RF} is:

$$\chi_{H_{RF}} = \chi_{irrev} + \chi_{rev} = \tfrac{1}{3}\left[\chi_\parallel (1 + i\omega\tau_\parallel)^{-1} + 2\chi_\perp\right] \quad (2)$$

  which means that the two components give a contribution. The first term χ_{irrev} corresponds to the response from the particles in the superparamagnetic state, where the magnetic moments jump over the anisotropy barrier, while the second χ_{rev} describes the response from the blocked particles whose magnetic moment are confined at the bottom of the potential well. Our RF experimental susceptibility for the $\langle D \rangle = 5$ nm oleic acid-coated nanoparticles, measured at $H_{dc} = 0$ is explained with equation (2), with $U/k_B = 300$ K and $\tau_0 = 5 \pm 4 \times 10^{-10}$ s, parameters that are available in the literature for these particles [19]. Indeed, with these values and $f = 12$ MHz, the maximum in $\chi_{H_{RF}}(H_{dc} = 0)$ is predicted at about 85 ± 25 K, which agrees reasonably with our result of $T_{max} = 70$ K.
- For $H_{dc} \neq 0$ the bias field breaks the symmetry around the easy axis of each particle, so that χ_{irrev} and χ_{rev} are no longer given by $\chi_\parallel$ and $\chi_\perp$, respectively. The H_{dc} field effect consists in decreasing the inter-well barrier energy, modifying the shape of the bottom potential well, and shifting the orientation of the minimum of magnetic energy. It has been demonstrated that χ_{irrev} decreases strongly as H_{dc} increases, while χ_{rev} depends weakly on the applied field and temperature [32, 33]. The strong decrease of χ_{irrev} is observed clearly in our bipolar scans at fixed T and ramped H_{dc}.

Within the Stoner–Wohlfarth (SW) model, that is, at $T = 0$ where no relaxation effects are allowed, the measured RF susceptibility is given by the reversible susceptibility $\chi_{H_{RF}} = \chi_{rev}$. For a random collection of identical nanoparticles, $\chi_{H_{RF}}$ must then show two peaks due to the anisotropy field at $H_{dc} = H_K$, and a third peak at the coercive field $H_{dc} = H_c$ [28]. When there is an appreciable size distribution the latter peak broadens and overlaps with the peak at H_K. Only two peaks, one at each direction of the applied field remain [25]. At $T = 0$, all particles are blocked, and at H_{dc}, $\chi_h^{blocked} \approx \frac{2}{3}\chi_\perp = \frac{1}{3}\mu_0 M_S^2/K$, with K the uniaxial anisotropy constant of the particle and M_s the saturation magnetization. As H_{dc} increases, the barrier $U(H_{dc})$ decreases till it becomes zero at a field around $H_K = 2K/M_S$. Correspondingly, χ_{rev} increases till it has a maximum at this field. For even higher fields ($H_{dc} > H_K$) it decreases till zero since the moments become saturated.

At $T \neq 0$, and below the blocking temperature, the magnetic moments are subdivided into two subsystems: the blocked and unblocked ones. Its ratio decreases as T increases, till it becomes zero at $T = T_B$. Since the SW model may be applicable only to the blocked particles, it predicts the peak in $\chi_{H_{RF}}(H_{dc} = \pm H_K)$. As T increases, H_K becomes zero at $T = T_B$ and the peak in $\chi_{H_{RF}}(H_{dc} = H_K) = \chi_{rev}(H_K)$ disappears. Also, the unblocked particles, which jump over the barrier due to thermal excitations, do not contribute to the peak at $H_{dc} \approx \pm H_K$. Instead, their contribution is dominated by χ_{irrev} and decreases continuously with increasing field [32]. This explains our observation of a $\chi_{H_{RF}}(T_{max})$ maximum for $H_{dc} = 0$ at a higher temperature than the static susceptibility maximum, and a non-zero peak due to the transverse component only below the static blocking temperature. We note that in a previous work [27] only the thermal activated slow processes had been taken into account, and the observed difference between the ac T_{max} and the T_B determined from the TS peaks at $H_{dc} \neq 0$ could not be explained.

The strong temperature dependence of H_K, observed in figure 3, accounts for both the magnetocrystalline anisotropy

constant thermal variation, which is negligible in this case, and for the influence of the thermal energy that overcomes the anisotropy energy of the particles [34, 24]. The decrease of H_K with increasing T is usually described by the equation $H_K = H_{K0}[1-(T/T_M)^{\beta}]$, where $\beta \sim 0.5$ [35, 36] for an assembly of aligned particles, and $\beta \sim 0.77$ for an assembly of randomly oriented particles [37–39], and H_{K0} corresponds to the intrinsic anisotropy field of the material. The emerging picture is that, at very low temperatures ($T = 2$ K), the magnetite particles are frozen and $H_K \sim H_{K0}$. As T increases, some fraction of the particles become superparamagnetic since the thermal excitations are now capable of reversing the magnetic moment from one orientation to the opposite, and the effective H_K decreases. Thus, well above the blocking temperature, all the particles are superparamagnetic, which is characterized by the random thermal fluctuations of single-domain particle moments, so that the measured H_K of the collection of magnetite particles is zero.

However, the curves of $H_K(T)$ in figure 3 do not follow the simple $H_K = H_{K0}[1 - (T/T_M)^{\beta}]$ relation, since additional effects on the magnetic anisotropy of the particles, such as interparticle interactions [40] and anisotropy field distribution [35, 36], should be taken into account. In fact, the change in slope in the curves in figure 3 for the SiO_2-coated particles suggests that $H_K(T)$ obtained from TS measurements follows a convolution of two contributions: a function of the form $H_K = H_{K0}[1 - (T/T_M)^{\beta}]$ with $\beta < 1$, related to the thermal effects described above, and an additional $H_K(T)$ function with opposite curvature, resulting from the effects of the dipolar interparticle interactions. The inset in figure 3 shows the positive values of H_K versus T for the 5 nm SiO_2-coated particles, along with two curves as guides to the eyes for each of the two temperature dependences described. The $\beta < 1$ decrease of $H_K(T)$ is clearly observed for the SiO_2-coated, while it is not on the oleic acid-coated particles of the same size, since the interparticle interactions are reduced with the SiO_2 coating, a fact that will be further discussed below. Moreover, the $\beta < 1$ dependence is better observed for the SiO_2-coated 5 nm particles than for the 14 nm ones. With this criterion, it is concluded that the influence of interparticle interactions cannot be neglected. The interactions are stronger in the oleic acid-coated NPs and overcome the effects of thermal fluctuations, while in the SiO_2-coated case the interactions become weak enough to allow the thermal component to dominate as the temperature drops below the crossover temperature (inflection point in the $H_K(T)$ curve).

Indeed, the contribution of the dipolar interactions to the energy barrier for magnetization reversal of one particle in an assembly of randomly oriented particles of the same size has been evaluated [41]. It is on the order of 10^{-13} erg, which is comparable to the intrinsic anisotropy barrier, for the oleic acid-coated particles, and at least four orders of magnitude smaller for the SiO_2-coated ones. This corresponds to the upper limit calculated for zero external magnetic field; however, for $H_{dc} \neq 0$ the moments tend to align parallel to the field, the dipolar interaction field is effectively compensated and, as a consequence, the contribution of this interaction to the energy barrier is lowered. This change of curvature in the $H_K(T)$ has not been previously reported for nanoparticle systems, despite the fact that some studies of soft ferrite nanoparticles describe the influence of dipolar interparticle interactions on the anisotropy peaks obtained from similar TS measurements [25]. In the work described in [25], the ferrite interparticle distances were modified by dispersing them in paraffin wax, so that the agglomeration of the nanoparticles may have not been completely avoided, impeding the observation of changes in the $H_K(T)$ curve. In addition, our TS setup allows measuring below 10 K, which is not possible with other TS setups reported in the literature, so that important features at low temperatures are better explored in ours. At any rate, we may conclude that the TS measurements that we present here allow us to distinguish between the effects of thermal fluctuations and interparticle interactions in a NP system, being very sensitive to the latter.

T_M values, and, correspondingly, T_B, are found to be lower for smaller particles, decreasing from 215 K to 35 K for 14 nm and 5 nm oleic acid-coated NPs, respectively, and from 140 K to 14 K for the equivalent SiO_2-coated particles (see table 1 and figure 3). This coating also reduces the values of T_M with respect to those found for the oleic acid-coated case with the same diameter, which is related to the reduction of the dipolar interparticle interactions [25] as consequence of the increased magnetite average interparticle core–core distance by the thick SiO_2 shell, as described above. A stronger reduction in T_M, and in the contribution due to interparticle interactions in the energy barrier, by SiO_2 coating is observed for the smaller 5 nm particles than for the larger 14 nm NPs, despite the fact that the SiO_2 shell thickness is roughly the same in both cases. Indeed, their magnetic moment reduces with the particle volume, and, correspondingly, their dipole–dipole interactions decrease. Consequently, the smaller the particles the more effective the reduction of the interparticle interactions by SiO_2 coating.

Figure 5 shows the comparison of the ZFC curves and the TS ratio at $H_{dc} = 0$ as a function of temperature for the samples of 14 nm in diameter with both coatings. Since these bigger particles have a wider distribution in size and their interparticle interactions are more evident than the case of the smaller particles in figure 4, the peak at the ZFC curve is broader. However, T_M obtained from TS seems to coincide with the inflection point of the ZFC curve. At any rate, the value of the blocking temperature is sharper from the TS study (H_K versus T plot) than from these ZFC measurements, the latter showing a broad maximum.

Finally, the observation of the same H_{K0} values (within experimental errors) for each group of particles reveals that the low-temperature anisotropy field probably corresponds to the average intrinsic anisotropy field (magnetocrystalline, surface and shape contributions), and it is not significantly modified by interparticle interactions. This results from the previous analysis of the energy barrier for magnetization reversal of the particles, so that at low temperatures the dipolar field created by the interparticle interactions is small, further lowered by the $H_{dc} \neq 0$ bias field in our TS experiment, and then it does not alter the intrinsic anisotropy field of the magnetite core of the particles. An estimation of the

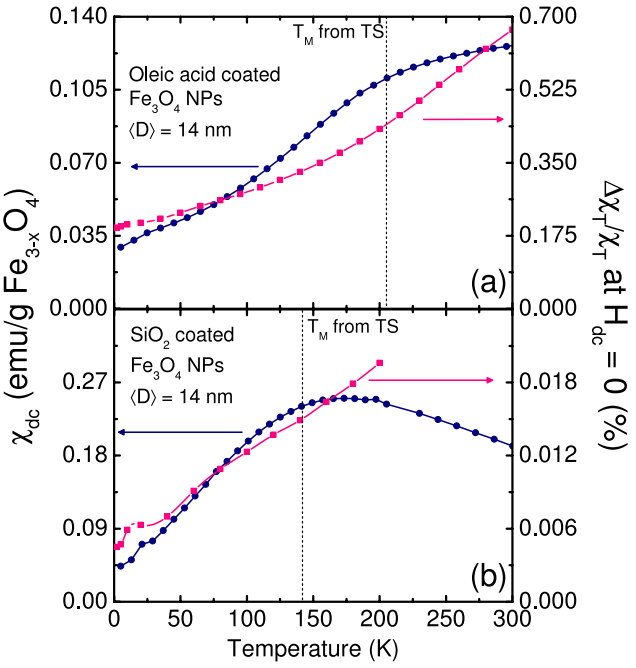

Figure 5. Comparison of the temperature dependence of the ZFC curve from χ_{dc} at 50 Oe (•) to the TS values at $H_{dc} = 0$ (■), for the 14 nm $Fe_{3-x}O_4$ NPs: (a) oleic acid-coated and (b) SiO_2-coated. Dashed line marks T_M.

intrinsic anisotropy constant, K_0, may be directly deduced from the expression $K_0 = \frac{2}{3}M_S H_{K0}$ [15]. With M_S for all samples of the sizes studied here being on the order of 80–90 emu g^{-1} $Fe_{3-x}O_4$ [8, 10], the resulting K_0 values are within 1.6–1.8 × 10^5 erg cm^{-3}, which are close to those values reported for both bulk magnetite (∼1–3 × 10^5 erg cm^{-3}) [42, 15, 19], and high-quality 5 nm particles (∼4–5 × 10^5 erg cm^{-3}) [8, 19].

6. Conclusions

We have demonstrated that SiO_2 coating of the $Fe_{3-x}O_4$ particles strongly reduces the interparticle interactions, which is revealed by three features: (i) the reduction of their contribution to the energy barrier for the magnetization reversal of the particles at low temperatures, (ii) the decrease of the blocking temperature, and (iii) the change in slope of the $H_K(T)$ curves. These features are observed for both particle sizes (5 and 14 nm) but they are more efficient in the case of the smaller ones. The magnetic anisotropy field at low temperatures H_{K0}, directly obtained from the TS measurements, is lower than 1 kOe in all cases and independent of the coating used. TS measurements also allow estimating the intrinsic magnetic anisotropy constant, which is in close agreement with others published in the literature. TS is then a very sensitive and powerful technique to study the interparticle interactions and magnetic anisotropy of nanoparticle systems, allowing the distinguishing between both effects.

To sum up, let us recall that biomedical applications require hydrophilic magnetic particles with high saturation magnetization to manipulate and detect them by application of an external magnetic field [2, 14]; apart from this, a low anisotropy field and superparamagnetic behavior at room temperature (T_B < RT) are desirable since the reduced dipolar interactions above T_B quench the magnetic attractive forces, avoiding the agglomeration of particles. The present work indicates that our 5 and 14 nm SiO_2-coated hydrophilic magnetite nanoparticles fulfil all those requirements (saturation magnetization close to that of the bulk magnetite, H_{K0} below 1 kOe and superparamagnetic behavior at room temperature), which makes them very attractive for such purposes.

Acknowledgments

The financial support of the Spanish MINECO MAT2011-23791, MAT2009-08667 and MAT2012-33037, Aragonese DGA-IMANA E34 (cofunded by Fondo Social Europeo) and Catalan DURSI 2009SGR856 projects, and that received from the European Union FEDER funds (Una manera de hacer Europa) is acknowledged. AIF acknowledges a CSIC JAE2008-Predoc grant. The authors are indebted to the Servicio General de Apoyo a la Investigación-SAI, Universidad de Zaragoza, and the Scientific Facilities of the Universitat de Barcelona. Fruitful discussions with F Luis (ICMA-CSIC, Zaragoza, Spain) are acknowledged. The authors are also indebted to M P Morales and P Tartaj (ICMM-CSIC, Madrid, Spain) for their assistance during the SiO_2 coating.

References

[1] Batlle X and Labarta A 2002 *J. Phys. D Appl. Phys.* **35** R15
[2] Tartaj P, Morales M P, Veintemillas-Verdaguer S, González-Carreño T and Serna C J 2003 *J. Phys. D: Appl. Phys.* **36** R182
[3] Hayashi T, Hirono S, Tomita M and Umemura S 1996 *Nature* **381** 772–4
[4] Kim J *et al* 2006 *Angew. Chem. Int. Edn* **45** 7754
[5] Pérez N, Bartolomé F, García L M, Bartolomé J, Morales M P, Serna C J, Labarta A and Batlle X 2009 *Appl. Phys. Lett.* **94** 093108
[6] Batlle X *et al* 2011 *J. Appl. Phys.* **109** 07B524
[7] Salafranca J, Gazquez J, Pérez N, Labarta A, Pantelides S T, Pennycook S J, Batlle X and Varela M 2012 *Nano Lett.* **12** 2499–503
[8] Guardia P, Batlle-Brugal B, Roca A G, Iglesias O, Morales M P, Serna C J, Labarta A and Batlle X 2007 *J. Magn. Magn. Mater.* **316** e756–9
[9] Pal S, Morales M, Mukherjee P and Srikanth H 2009 *J. Appl. Phys.* **105** 07B504
[10] Roca A G, Morales M P, O'Grady K and Serna C J 2006 *Nanotechnology* **17** 2783–8
[11] Guardia P, Labarta A and Batlle X 2011 *J. Phys. Chem.* C **115** 390–6
[12] Perez N, Lopez-Calahorra F, Labarta A and Batlle X 2011 *Phys. Chem. Chem. Phys.* **13** 19485–9
[13] Mejías R *et al* 2010 *Nanomedicine* **5** 397–408
[14] Frey N A, Peng S, Cheng K and Sun S 2009 *Chem. Soc. Rev.* **38** 2532–42
[15] Cullity B D 1972 *Introduction to Magnetic Materials* (*Addison-Wesley Series in Metallurgy and Materials*) (Reading, MA: Addison-Wesley)

[16] Guardia P, Pérez N, Labarta A and Batlle X 2010 *Langmuir* **26** 5843–7
[17] Guardia P, Perez-Juste J, Labarta A, Batlle X and Liz-Marzan L M 2010 *Chem. Commun.* **46** 6108–10
[18] Park J, An K, Hwang Y, Park J G, Noh H J, Kim J Y, Park J H, Hwang N M and Hyeon T 2004 *Nature Mater.* **3** 891
[19] Pérez N, Guardia P, Roca A G, Morales M P, Serna C J, Iglesias O, Bartolomé F, García L M, Batlle X and Labarta A 2008 *Nanotechnology* **19** 475704
[20] Pérez Rodríguez N 2012 Nanostructure effects on the magnetic properties of magnetite nanoparticles: from synthesis to applications in biomedicine *PhD Thesis* Universitat de Barcelona
[21] Lee D C, Mikulec F V, Pelaez J M, Koo B and Korgel B A 2006 *J. Phys. Chem.* B **110** 11160–6
[22] Arriagada F J and Osseo-Asare K 1999 *J. Colloid Interface Sci.* **211** 210–20
[23] Figueroa A I, Bartolomé J, García del Pozo J M, Arauzo A, Guerrero E, Téllez P, Bartolomé F and García L M 2012 *J. Magn. Magn. Mater.* **324** 2669–75
[24] Poddar P, Wilson J L, Srikanth H, Farrell D F and Majetich S A 2003 *Phys. Rev.* B **68** 214409
[25] Poddar P, Morales M B, Frey N A, Morrison S A, Carpenter E E and Srikanth H 2008 *J. Appl. Phys.* **104** 063901
[26] Frey N A 2008 Surface and interface magnetism in nanostructures and thin films *PhD Thesis* University of South Florida
[27] Spinu L, O'Connor C J and Srikanth H 2001 *IEEE Trans. Magn.* **37** 2188
[28] Aharoni A, Frei E H, Shtrikman S and Treves D 1957 *Bull. Res. Counc. Isr.* **6A** 215–38
[29] Matarranz R, Contreras M C, Pan G, Presa B, Corrales J A and Calleja J F 2006 *J. Appl. Phys.* **99** 08Q504
[30] Shliomis M and Stepanov V 1993 *J. Magn. Magn. Mater.* **122** 176–81
[31] Svedlindh P, Jonsson T and García-Palacios J 1997 *J. Magn. Magn. Mater.* **169** 323–34
[32] Luis F, del Barco E, Hernández J M, Remiro E, Bartolomé J and Tejada J 1999 *Phys. Rev.* B **59** 11837–46
[33] Luis F, Petroff F and Bartolomé J 2004 *J. Phys.: Condens. Matter* **16** 5109
[34] Yoon S 2011 *J. Korean Phys. Soc.* **59** 3069–73
[35] Pfeiffer H 1990 *Phys. Status Solidi* a **118** 295–306
[36] de Julián Fernández C 2005 *Phys. Rev.* B **72** 054438
[37] Pfeiffer H 1990 *Phys. Status Solidi* a **120** 233–45
[38] Pfeiffer H and Schüppel W 1990 *Phys. Status Solidi* a **119** 259–69
[39] Batlle X, Garcia del Muro M, Tejada J, Pfeiffer H, Gornert P and Sinn E 1993 *J. Appl. Phys.* **74** 3333–40
[40] Sollis P M, Bissell P R and Matsutake Y 1997 *IEEE Trans. Magn.* **33** 3046–8
[41] Hansen M and Mørup S 1998 *J. Magn. Magn. Mater.* **184** L262–74
[42] Goya G F, Berquó T S, Fonseca F C and Morales M P 2003 *J. Appl. Phys.* **94** 3520–8

The Journal of Physical Chemistry

Quantification of dipolar interactions in $Fe_{3-x}O_4$ nanoparticles

Carlos Moya,*† Óscar Iglesias,† Xavier Batlle,† Amílcar Labarta†

† Departament de Física Fonamental and Institut de Nanociència i Nanotecnologia (IN2UB), Universitat de Barcelona, Martí i Franquès 1, 08028 Barcelona, Spain

KEYWORDS (magnetite nanoparticles, silica coating, dipolar interactions, numerical simulation)

ABSTRACT: A general method for the quantification of dipolar interactions in assemblies of nanoparticles has been developed from a model sample constituted by magnetite nanoparticles of 5 nm in diameter, in powder form with oleic acid as a surfactant so that the particles were solely separated from each other through an organic layer of about 1 nm in thickness. This quantification is based on the comparison of the distribution of energy barriers for magnetization reversal obtained from time-dependent relaxation measurements starting from either (i) an almost random orientation of the particles' magnetizations or (ii) a collinear arrangement of them prepared by previously field cooling the sample. Experimental results and numerical simulations show that the mean dipolar field acting on each single particle is significantly reduced when particles' magnetizations are collinearly aligned. Besides, the intrinsic distribution of the energy barriers of anisotropy for the non-interacting case was evaluated from a reference sample where the same magnetic particles were individually coated with a thick silica shell in order to make dipolar interactions negligible. Interestingly, the results of the numerical simulations account for the relative energy shift of the experimental energy barrier distributions corresponding to the interacting and non-interacting cases, thus supporting the validity of the proposed method for the quantification of dipolar interactions.

Introduction

Currently, systems formed by magnetic nanoparticles (NPs) are widely investigated due to their potential applications in both information storage and biomedicine, such as for example in hyperthermia, as contrast agents for magnetic resonance imaging and for drug delivery.[1-4] In particular, magnetite ($Fe_{3-x}O_4$) NPs are among the most commonly studied materials due to their low-toxicity, easy production and functionalization, and good magnetic performance, as they exhibit a relatively high specific magnetization and an intermediate value of the magnetocrystalline anisotropy.[5-7] However, the latter could be also considered as an important drawback for biomedical applications of colloidal suspensions of NPs, since it facilitates the formation of big particle aggregates through dipolar interactions among them, either provoking blood thrombi or substantially modifying their magnetic response.[5-8] For instance, recent works have shown a significant variation on the heating efficiency for hyperthermia of a colloidal suspension of NPs depending on the particle concentration and their aggregation state in the heating medium.[9-11] Therefore, proposing a simple method for the quantitative characterization of the inter-particle interactions could be very useful to improve their magnetic performance in such applications. Experimentally, there are two strategies to study the effect of inter-particle interactions in a nanoparticle system. The first one consists on the study, as a function of the particle concentration, of either a colloidal suspension of NPs or a solid matrix where NPs are embedded.[12-13] However, the principal drawback of this method relies on the wide distribution of inter-particle distances and the consequent little accuracy in the determination of a representative mean value, which complicates the interpretation of the data and its generalization. The second strategy is based on the coating of the NPs with either a polymer or an inorganic corona to produce a kind of individual core-shell nanostructure, which in a powder form enables the magnetic cores to keep a quite regular distance from each other. This is indeed a more suitable method than the former to perform a quantitative determination of the inter-particle interactions.[14] In particular, silica coating is an ideal alternative in which particles can be isolated and separated from each other over long distances, so that dipolar interactions can be tuned as a function of the inter-core distance and eventually drastically reduced.[15] On the other hand, numerical simulations have proven to be a useful tool to investigate both the magnetic properties of single NPs and the collective behavior of interacting ensembles of them, providing a general methodology to understand and support experimental results.[10,16,17]

In this framework, we have quantified the effect of dipolar interactions on the magnetic properties of 5 nm $Fe_{3-x}O_4$ NPs in powder form with oleic acid as a surfactant so that the latter separates the NPs from each other solely through an organic layer of about 1 nm in thickness. We propose a simple method to detect the presence of dipolar interactions that consists on the comparison of the distributions of energy barriers for magnetization reversal obtained from time-dependent relaxation measurements, starting from configurations with either random orientation of the particles' magnetizations or collinear arrangement of them prepared by previously field cooling the sample. The validity of these results is supported by both macrospin simulations of a poly dispersed ensemble of spherical NPs and the intrinsic distribution of the energy barriers of anisotropy of the NPs calculated from a reference sample where NPs are individually coated by a thick silica shell in order to make dipolar interactions negligible.

Preparation of the samples and experimental techniques

Two samples have been thoroughly studied and compared. Sample R1 was synthesized by thermal decomposition of the organo-metallic precursor $Fe(acac)_3$ in the presence of oleic acid and oleylamine as surfactants and 1,2-hexadecanediol as stabilizer agent, following a method extensively described elsewhere.[7,18] Monodisperse magnetite $Fe_{3-x}O_4$ NPs of about 5 nm in diameter were obtained. In order to make dipolar interactions among the particles negligible keeping them far apart from each other, magnetite NPs in sample R1 were individually coated with SiO_2 by using a microemulsion method based on a solution of tetraethoxysilane (TEOS) in water-in-oil (w/o), since this is a reproducible procedure where the thickness of the SiO_2 layer and number of magnetite cores inside each silica shell can be easily controlled through the fraction of TEOS and the concentration of $Fe_{3-x}O_4$ NPs.[19,20] This sample is called R2 hereafter.

Samples were prepared for transmission electron microscopy (MT80-Hitachi microscope) by placing one drop of a dilute suspension of NPs onto a carbon-coated cooper grid and letting it dry at room temperature. The size distribution was analyzed by measuring at least 2000 particles and the resultant histograms are shown in Fig. S1a and S1b, Supporting information. Both the crystalline quality of individual NPs and the core-shell nanostructure of the silica-coated NPs were characterized by high-resolution TEM (HR-TEM) micrographs obtained by Titan high-base microscopy (see Fig. 1b-d).

The crystal phase of the iron oxide particles was identified by powder X-ray diffraction performed in a PANalytical X'Pert PRO MPD diffractometer by using Cu Kα radiation (see Fig. S2, Supporting information). The patterns were collected within 5 and 120º for 2θ. The XRD spectra were indexed to an inverse spinel structure.

The Fe content in the samples was determined by inductively coupled plasma-optical emission spectrometry (ICP-OES) by using a Perkin Elmer model OPTIMA 3200RL after digesting the samples in a mixture of $HClO_4$:HNO_3 5:25, and diluting them with distilled water.

Magnetization measurements were performed with a Quantum Design SQUID magnetometer. Hysteresis loops $M(H)$ were measured at several temperatures within 2 and 300 K to study the saturation magnetization (M_s) and the coercive field (H_c) under a maximum magnetic field of ± 20 kOe. M_s was obtained by extrapolating the high-field region of $M(H)$ to zero field, assuming the high-field behavior $M(H) = M_s + \chi \cdot H$, where χ is a residual susceptibility. M_s values were normalized to the magnetic content evaluated from ICP-OES measurements.

The M_s values obtained from the hysteresis loops at 2 K (M_s = 82 ± 2 emu/g and M_s = 76 ± 2 emu/g for R1 and R2, respectively) were just slightly smaller than the bulk one,[21] indicating an almost perfect ferrimagnetic order throughout the whole NPs, as previously observed in samples with very high crystalline quality synthesized by the thermal decomposition method.[7] The coercive field was calculated as $H_c = (|H_c^+| + |H_c^-|)/2$ and the obtained values at 2 K were 690 ± 30 Oe and 650 ± 20 Oe for R1 and R2, respectively.[7,22]

The thermal dependence of the magnetization was studied after zero field cooling (M_{ZFC}) and field cooling (M_{FC}) the samples. These curves were measured using the following protocol: the sample was cooled down from 300 to 2 K in zero magnetic field, then a static magnetic field of 50 Oe was applied and M_{ZFC} was measured while warming up from 2 to 300 K; once room temperature was reached, the sample was cooled down again to 2 K while 50 Oe was applied; after that the sample was warmed up to 300 K and M_{FC} was collected under the applied field of 50 Oe.

The time dependence of the thermo-remnant magnetization in the temperature range 2-30 K was measured after field cooling sample R1 under various fields (50, 200 and 1000 Oe) and sample R2 under 50 Oe, from room temperature down to the measuring temperature, at which the magnetic field was switched off. The magnetization decay was then recorded as a function of time at zero field and at several temperatures.

Structural characterization

TEM images of R1 show spherically shaped particles with a narrow size distribution (Fig. 1a) that was fitted to a log-normal function with values of the mean diameter D_{TEM} = 5.3 nm and the unitless standard deviation of σ= 0.20 (Fig. S1a, Supporting information). Fig. 1a also shows the regularity and monodispersity of the NPs. Besides, HR-TEM image in Fig. 1b demonstrates the high crystalline quality of individual NPs. The mean particle diameter estimated from X-ray data (D_{XRD} = 5.1 ± 0.2 nm) is in agreement with D_{TEM} supporting also the absence of crystalline defects and the fact that the NPs are single-crystal domains. Silica coating of those NPs produced highly regular core-shell nanostructures (sample R2) containing a single magnetic core in most of the cases (see Fig. 1c). The values of the mean diameter and the unitless standard deviation obtained from the histogram of the size distribution are D_{TEM} = 44 nm and σ= 0.19, respectively. HR-TEM image in Fig. 1d indicates that the morphology of the magnetite NPs remains unchanged after silica coating. The thickness of the silica layer coating the magnetite cores is about 20 nm, which is more than enough to make inter-particle dipolar interactions negligible.

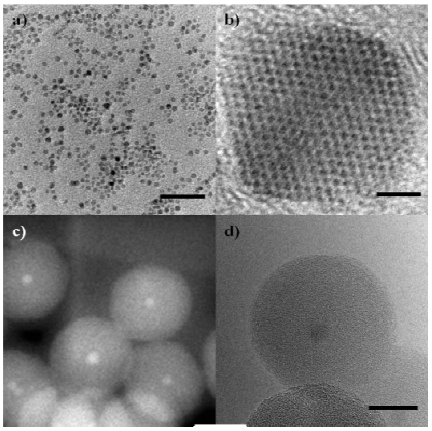

Figure 1. TEM characterization of samples R1 and R2: a) Low-TEM resolution image for R1 NPs. b) High-resolution TEM image for R1. c) Low resolution image of silica-coated NPs (sample R2). d) HAADF image of several silica-coated NPs. Scale bars: a) 50 nm, b) 1 nm c) 30 nm and d) 15 nm.

Magnetic characterization

To get a basic idea of the effect of dipolar interactions on the magnetic properties of the NPs, isothermal magnetization curves for samples R1 and R2 were measured as a function of the magnetic field up to 20 kOe for selected temperatures within 150 K and 300 K, where NPs of the two samples are fully superparamagnetic (SPM). The obtained magnetization curves M as a function of the scaling variable H/T are plotted in Fig. 2. The excellent superposition of the scaled magnetization curves for sample R2 (see main panel of Fig. 2) is a clear indication of its SPM behavior and corroborates the nonexistence of dipolar interactions among the particles when the magnetic cores are well-separated from each other by the silica coating. However, this kind of scaling is not achieved in sample R1 (see inset to Fig. 2), where particles are solely coated by oleic acid and dipolar interactions are significantly affecting their magnetic response.

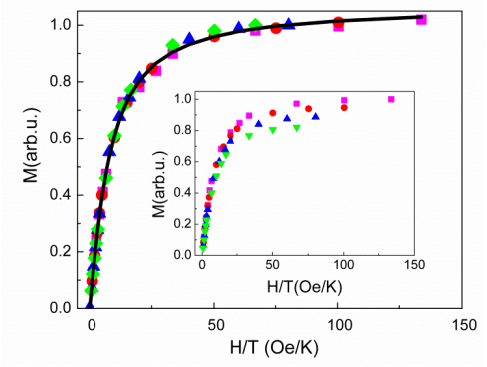

Figure 2. Isothermal magnetization curves for sample R2 measured at 150 K (lilac square), 200 K (red circles), 250 K (blue triangles) and 300 K (green diamonds), plotted as a function of H/T. Inset: Isothermal magnetization curves for sample R1 plotted as a function of H/T. The continuous line is the fit to Eq. (1).

These qualitative results are also confirmed by comparing Mz_{FC} - M_{FC} curves for the two samples (see Figure 3). Whereas Mz_{FC} - M_{FC} data for R2 exhibit the common trends corresponding to non-interacting SPM particles undergoing a blocking process - a sharp peak in Mz_{FC} and a monotonous increase in M_{FC} as the temperature is lowered - , the enhancement of dipolar interactions in sample R1 as compared to sample R2 is suggested by (i) the blocking temperature indicated by the position of the peak in Mz_{FC} is multiplied by a factor of about 1.3, (ii) the ZFC peak is significantly broader, and (iii) M_{FC} becomes flattened below the blocking temperature.[12] Interestingly, all those differences between the M_{ZFC}-M_{FC} curves for the two samples may entirely be attributed to the effect of the inter-particle interactions since the magnetic cores are exactly the same. We can take advantage of this fact in order to get a first quantitative estimation of the changes caused by dipolar interactions on the effective distribution of energy barriers of the NPs.

We first fitted the scaled magnetization curves of sample R2 to

$$M(H,T) = M_S \frac{\int m P(m) L(mH/k_B T)\, dm}{\int m P(m)\, dm} + \chi_p H \qquad (1)$$

where we assume that, in the SPM regime and for non-interacting particles, the magnetization can be described by averaging the Langevin function $L(x)$ accounting for the magnetization m of each particle with the log-normal distribution $P(m)$ of the magnetic moment of the particles[23] plus a linear-field contribution originating at a residual paramagnetic susceptibility χ_p. Taking into account that $m = M_S V_m$, where V_m is the activation magnetic volume of each particle, the fitted $P(m)$ distribution can be transformed in the distribution of activation magnetic volumes being the obtained values of the unitless standard deviation and the mean magnetic diameter $\sigma_V = 0.63$ and D_m = 5.3 nm, respectively, in good agreement with the structural parameters deduced from TEM images. This concordance between the structural and magnetic-volume parameters also supports both the high crystalline quality of the NPs and the nonexistence of significant inter-particle interactions for sample R2.

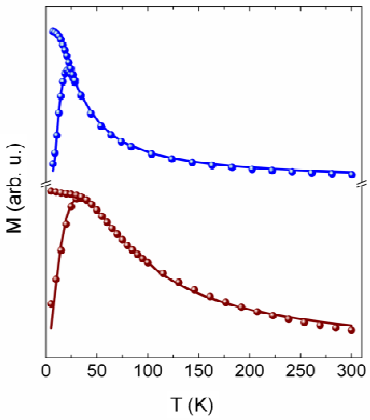

Figure 3. ZFC-FC magnetizations (H=50 Oe). Brown and blue spheres correspond to samples R1 and R2, respectively. Solid blue line and solid brown line correspond to the fit of the ZFC curves for R1 and R2, respectively, to Eq. (2).

It is well-known that the ZFC susceptibility is more sensitive to the distribution of particle volumes than the equilibrium magnetization curves.[24] Consequently, σ_V can be further refined by performing a fit of M_{ZFC}/H to the following expression[25-27]

$$\frac{M_{ZFC}(T)}{H} = \frac{1}{3k_B T}\int_0^{M_S V_p(T)} m^2 P(m)\, dm + \frac{M_S}{3K}\int_{M_S V_p(T)}^{\infty} m P(m)\, dm \qquad (2)$$

deduced from the Gittleman's model, [25] where D_m= 5.3 nm was fixed to the value obtained from the fitting of Eq. (1) to the magnetization curves. In Eq. (2), the first term accounts for the contribution of SPM particles [with volumes $V<$

$V_p(T) = \frac{25k_BT}{K}$] and the second is for the blocked ones [$V > V_p(T)$]. Here k_B is the Boltzmann constant and K the effective anisotropy. As a result of the fitting procedure, we obtained σ_V = 0.54 and K = 3.1x10^5 erg/cm^3, so that the effective anisotropy is about three times the corresponding one for bulk magnetite (K = 1.1x10^5 erg/cm^3),[22] as expected for NPs of a few nanometers in diameter where surface anisotropy is the dominant contribution.[28] Applying the same kind of fitting to the ZFC susceptibility of sample R1 and imposing D_m= 5.3 nm we obtained K = 3.7x10^5 erg/ cm^3 and σ_V = 0.81 which provides a qualitative estimation of the effect of the inter-particle interactions on the distribution of activation magnetic volumes. From these results we can conclude that inter-particle interactions slightly increase the effective anisotropy of the particles but they significantly broaden the distribution of activation magnetic volumes, broadening as well the distribution of effective energy barriers.

The existence of high energy barriers originating from inter-particle interactions has also been studied by measuring the time relaxation of the magnetization at several temperatures following the protocol detailed in Sec. 2. The obtained relaxation curves were analyzed within the context of the so-called $T\ln(t/\tau_0)$ scaling where,[29] in order to make all the curves collapse onto a single master curve, the characteristic attempt time was set to $\tau_0 = (5 \pm 4)\times10^{-10}$ s. The results of this scaling for R1 and R2 after field cooling the samples under the relatively low field of 50 Oe are shown in Fig. 4. The most prominent difference between these two relaxation curves corresponding to the interacting and non-interacting cases, is the extra magnetic viscosity slowing down the magnetic relaxation in sample R1 as a consequence of the magnetic frustration introduced by inter-particle interactions, which are almost completely suppressed in sample R2 by the silica coating.

Besides, it is also evident that the magnitude of the cooling field applied before the relaxation is measured dramatically affects the time decay of the magnetization for sample R1, lowering the magnetic viscosity and making the relaxation look quite similar to the non-interacting case (R2) at intermediate values of the cooling field (200 Oe). As shown in Sec. 5, the latter is a direct consequence of the reduction of the average value of the dipolar field acting on each particle as the initial configuration of the particles' magnetizations becomes collinear through the effect of increasing the cooling field.

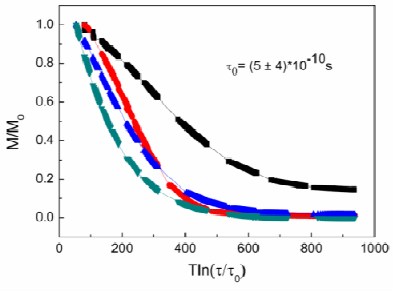

Figure 4. Scaling of the relaxation curves measured at several temperatures (2-30K) with an attempt time of $\tau_0 = (5 \pm 4)\times10^{-10}$ s, after field cooling at a field of 50 Oe for R1 (black line) and R2 (red line), and 200 Oe (blue line) and 1000 Oe (green line) for R1.

Consequently, we propose the study of the relaxation master curve as a function of the cooling field as a simple method to gain a rough estimation of the effect of dipolar interactions on the effective energy landscape of a nanoparticle system. Of course, this method does not provide an exact evaluation of the contribution of the dipolar interactions to the magnetic energy of the system because of both the incomplete suppression of dipolar interactions and the modification of the energy barriers of anisotropy by the cooling field, but at least it can be taken as a clear proof of the existence of inter-particle interactions and a means to get a first approximation of the energy involved.

On the other hand and as shown previously,[30] the $T\ln(t/\tau_0)$ scaling allows determining the effective distribution of energy barriers $f(E)$ explored by the system along the relaxation process by performing the numerical derivative of the master curve with respect to the scaling variable. The distributions so obtained for samples R1 and R2 are shown in Fig. 5. It is worth noting that $f(E)$ for the sample with inter-particle interactions (R1) extends to higher energies and that the energy of the maximum is also higher than for R2 in agreement with the effective distributions of energy barriers obtained by fitting the ZFC data. Thus, the peak of the energy distribution for R2 is placed at a temperature T_{max}= 171 K that is comparable to that corresponding to the mean anisotropy energy barrier given by KV_m/k_B= 175 K, confirming that in sample R2 dipolar interactions are negligible. The peak for sample R1 is shifted to T_{max}= 217 K presumably due to the influence of dipolar interactions on the original distribution of energy barriers, and, as will be shown in Sec. 5, this can be simply accounted through the changes introduced by the local dipolar fields on the anisotropy barriers.

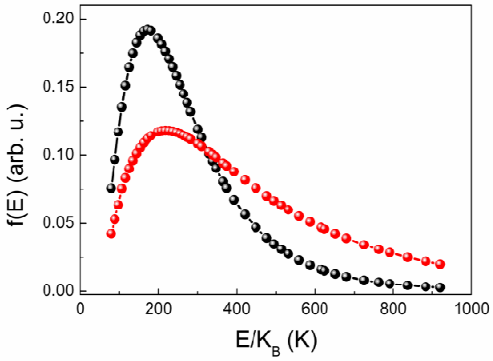

Figure 5. Effective distribution of energy barriers obtained from the scaling curves in Fig. 4 for R1 (red spheres) and R2 (black spheres).

Numerical simulation

In order to gain a deeper insight on the origin of the dependence of the relaxation behavior and the associated effective distribution of energy barriers observed experimentally as a function of the cooling field in a nanoparticle system with inter-particle interactions, we have conducted a series of numerical simulations to compute the dipolar fields and energy barriers of a model of nanoparticle assemblies which mimics the experimental ones. For this purpose, nanoparticle assem-

blies have been built by placing a fixed number N of spheres with diameter D [assemblies with a lognormal distribution of particle sizes $f(D)$ have also been considered] with different spatial arrangements inside a cubic box of varying size aL (where a is the lattice spacing, taken as 1 nm hereafter), adjusted so that the desired volume concentration defined as $c = \frac{V_N}{(aL)^3}$ is achieved (V_N is the total volume of the nanoparticle). We consider that spheres do not overlap and we impose a minimum inter-particle separation given by the thickness of the surfactant layer. We work in the macrospin approximation so that the total particle magnetization is given by $\vec{m_i} = M_s V_i \vec{S_i}$ where $\vec{S_i}$ is a Heisenberg 3D spin of modulus 1, M_s is the saturation magnetization and V_i the particle volume. The interaction energy considered has contributions from magnetic anisotropy, dipolar interaction and Zeeman coupling with the field:

$$E_{ani} = -\sum_i K_i V_i (\vec{S_i}\cdot\vec{n_i})^2,$$
$$E_{dip} = -M_s \sum_i V_i (\vec{S_i}\cdot\vec{H_i}^{dip}), \qquad (3)$$
$$E_H = -\mu_0 M_s \sum_i V_i (\vec{S_i}\cdot\vec{H})$$

where $\vec{n_i}$ are the uniaxial anisotropy directions, H the magnetic field, and we have defined the dipolar field acting in the ith particle as:

$$\vec{H}_i^{dip} = -\frac{\mu_0}{4\pi a^3} M_s \sum_{\{j\}} V_j \left[\frac{\vec{S_j}}{r_{ij}^3} - 3\frac{(\vec{S_j}\cdot\vec{r_{ij}})\vec{r_{ij}}}{r_{ij}^5} \right] \qquad (4)$$

being r_{ij} the interparticle distances in units of a. Typical energy scales for the three contributions for the case of sample R1 can be obtained by setting M_s= 5x10^5 A/m and K= 3.1x10^4 J/m^3. In particular, considering a mean diameter of D_m= 5.3 nm and an inter-particle separation $r_{ij} = d = 7a$, which corresponds to a thickness of the surfactant layer of about a (1 nm in the case of sample R1) and a volume concentration of $c = 0.3$ assuming a close packing of the particles, we get $E_{dip} = \frac{\mu_0}{4\pi d^3}(M_s V_m)^2 = 4.43\times10^{-22}\,\text{J} = 32.1\,\text{K}$ for the characteristic dipolar energy in sample R1. Typical dipolar fields in this sample are of the order of $H_{dip} = \frac{\mu_0}{4\pi d^3} M_s V_m = 114$ Oe, to be compared with the mean anisotropy field of $H_{ani} = \frac{2K}{M_s} = 1240$ Oe.

We have first computed the local dipolar fields generated by $N = 4096$ particles randomly distributed in a box of size aL at various concentrations c. Since dipolar fields depend on the magnetic configuration of the assembly, we have considered two extreme cases: magnetic moments i) aligned along z axis and ii) randomly oriented. In Fig. 6, we show the histograms of the modulus of the dipolar field for the two mentioned magnetic configurations and three values of c. Only the local dipolar fields generated at the sites of the 1000 particles at the central part of the box have been taken into account in order to minimize finite-size effects. Notice that the spread in dipolar field values around a mean value that depends on particle concentration c is caused by the random position of the particles in the simulation box. The exact distribution of H_{dip} values depends also on the magnetic configuration. For increasing concentrations, the spread of H_{mod} histograms increases for the random case while it remains more or less constant for the aligned particles. Most importantly, we observe that, for all concentrations, the magnitude of the dipolar fields is clearly reduced when aligning the particles' magnetization along the z axis. It is worth noting that the situation for sample R1 corresponds approximately to the case with $c = 0.3$, since this is the value of the volume concentration that can be estimated for this sample.

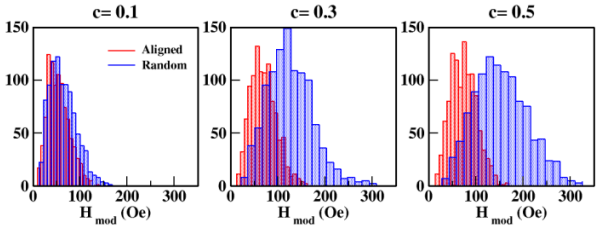

Figure 6. Histograms of the dipolar field moduli for 4096 particles randomly placed in a cubic box of size aL for three different concentrations c = 0.1, 0.3, 0.5, from left to right. Histograms in red are for a configuration with magnetic moments aligned along the z axis while blue ones correspond to randomly oriented magnetic moments. Only contributions from 1000 particles in the central part of the considered box have been taken into account.

This can be more clearly seen in Fig. 7, where the dependence of the mean value of the modulus of the dipolar field on the concentration is plotted. Even for the most diluted case considered here, the relative decrease in dipolar field is approximately 20% and reductions to more than 100% for the highest concentration considered are found. For the case of sample R1 (for $c = 0.3$) this reduction is estimated to be about 100 %. This gives support to the interpretation of the changes in the effective energy barriers observed experimentally for sample R1 as compared to R2 when increasing the cooling field, since changes in the dipolar fields acting on the particles are directly related to the corresponding modification of the energy barriers due to the anisotropy itself. As an estimate of the increase in the energy barriers induced by dipolar interactions, we have calculated the increase in the mean energy barrier by introducing the mean dipolar field obtained in the simulations in the expression for a nanoparticle with easy axis aligned along the field direction $E_b = E_b^0\left(1 + H_{dip}/H_{ani}\right)^2$, where $E_b^0/k_B = KV_m/k_B = 175$ K is the mean energy barrier for non-interacting particles of sample R2. Plugging the estimated values of H_{dip} = 114 Oe (for $c = 0.3$) and $H_{ani} = 1240$ Oe gives E_b/k_B = 209 K which is in close agreement with the peak position in Fig. 5 for sample R1 (T_{max}= 217 K). Consequently, those results unambiguously demonstrate that the observed differences between the distributions of energy barriers for samples R1 and R2 are essentially due to the effect of dipolar interactions present in R1.

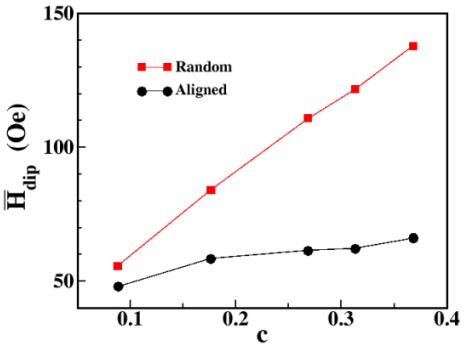

Figure 7. Concentration dependence of the mean value of the dipolar field modulus generated by 4096 particles placed at random in a 3D box of size *aL*. Only the fields on the central part of the simulated box have been taken into account. Black circles correspond to a configuration with magnetic moments aligned along the field direction while red squares correspond to randomly oriented magnetic moments.

Conclusions

We have shown that the average dipolar field acting on each individual particle in an ensemble of interacting particles is strongly reduced when the particles' magnetizations are collinearly aligned, this reduction being more significant as the volume concentration of the magnetic cores increases. As a consequence, we propose a general method to quantify the effect of dipolar interactions on the effective distribution of energy barriers for magnetization reversal, by comparing the master curve for the magnetization relaxation obtained after field cooling the sample at low field (initial state with random orientation of the particles' magnetizations) to that corresponding to intermediate fields where the particles' magnetizations tend to be aligned along the field direction in the initial state. We have also obtained the intrinsic distribution of the energy barriers of anisotropy for the non-interacting case by studying the relaxation of the magnetization for a reference sample where the same magnetic particles were individually coated with a thick silica shell in order to make dipolar interactions negligible. Interestingly, numerical simulations account for the observed energy shift between the distribution of energy barriers corresponding to the interacting and non-interacting cases, thus supporting the proposed method for the quantification of dipolar interactions.

Supporting Information available. Particle size distributions of the samples, X-ray patterns of the samples. This material is available free of charge via the Internet at http://pubs.acs.org.

Corresponding Author
*Corresponding author. Email: cmoya@ffn.ub.es

Author Contributions
The manuscript was written through contributions of all authors. All authors have given approval to the final version of the manuscript.

Acknowledgment
This work was supported by Spanish MINECO (MAT2012-33037) and Catalan DURSI (2014SGR220).

References

(1) Mejías, R.; Pérez-Yagüe, S. ; Roca, A. G.; Pérez, N.; Villanueva, A.; Cañete, M.; Mañes, S.; Ruiz- Cabello, J.; Benito, M.; Labarta, A. ; Batlle, X. ; Veintemillas-Verdaguer, S.; Morales, M. P.; Barber, D. F.; Serna, C. J.; *Nanomedicine*, **2010**, 5, 397.

(2) Haun, J. B.; Yoon, T.-J.; Lee, H.; Weissleder, R. *Wiley Interdiscip. Rev. Nanomed. Nanobiotechnol.* **2010**, *2*, 291–304.

(3) Mejías, R.; Costo, R.; Roca, A. G.; Arias, C. F.; Veintemillas-Verdaguer, S.; González-Carreño, T.; del Puerto Morales, M.; Serna, C. J.; Mañes, S.; Barber, D. F. *J. Control. Release* **2008**, *130*, 168–174.

(4) Puntes, V. F.; Krishnan, K. M.; Alivisatos, A. P. *Science (80-.).* **2001**, *291*, 2115–2117.

(5) Sun, C.; Lee, J. S. H.; Zhang, M. *Adv. Drug Deliv. Rev.* **2008**, *60*, 1252–1265.

(6) Tartaj, P.; Morales, P.; Veintemillas-verdaguer, S.; González-Carreño, T.; Serna, C.J. Phys. *D. Appl. Phys.* **2003**, 36, R182 .

(7) Guardia, P.; Labarta, A.; Batlle, X. *J. Phys. Chem. C* **2011**, *115*, 390–396.

(8) Batlle, X. *; Labarta, A. J. Phys. D: Appl. Phys.* **2002**, 35, R15.

(9) Haase, C.; Nowak, U. *Phys. Rev. B* **2012**, *85*, 045435.

(10) Martinez-Boubeta, C.; Simeonidis, K.; Makridis, A.; Angelakeris, M.; Iglesias, O.; Guardia, P.; Cabot, A.; Yedra, L.; Estradé, S.; Peiró, F.; Saghi, Z.; Midgley, P. A.; Conde-Leborán, I.; Serantes, D.; Baldomir, D. *Sci. Rep.* **2013**, *3*, 1652.

(11) Serantes, D.; Simeonidis, K.; Angelakeris, M.; Chubykalo-Fesenko, O.; Marciello, M.; Morales, M. del P.; Baldomir, D.; Martinez-Boubeta, C. *J. Phys. Chem. C* **2014**, *118*, 5927–5934.

(12) Vargas, J.; Nunes, W.; Socolovsky, L.; Knobel, M.; Zanchet, D. *Phys. Rev. B* **2005**, *72*, 184428.

(13) García del Muro, M.; Konstantinović, Z.; Varela, M.; Batlle, X.; Labarta, A. *J. Magn. Magn. Mater.* **2007**, *316*, 103–105.

(14) Abbasi, A. Z.; Guti, L.; Mercato, L. L.; Herranz, F.; Chubykalo-fesenko, O.; Veintemillas-verdaguer, S.; Parak, W. J.; Hernando, A.; Presa, P. *J. Phys. Chem. C* , **2011**, 115, 6257.

(15) Figueroa, A. I.; Moya, C.; Bartolomé, J.; Bartolomé, F.; García, L. M.; Pérez, N.; Labarta, A.; Batlle, X. *Nanotechnology* **2013**, *24*, 155705.

(16) Ivanov, Y. P.; Iglesias-Freire, O.; Pustovalov, E. V.; Chubykalo-Fesenko, O.; Asenjo, a. *Phys. Rev. B* **2013**, *87*, 184410.

(17) Cabot, A.; Alivisatos, A.; Puntes, V.; Balcells, L.; Iglesias, Ò.; Labarta, A. *Phys. Rev. B* **2009**, *79*, 094419.

(18) Sun, S.; Zeng, H. *J. Am. Chem. Soc.* **2002**, *124*, 8204–8205.

(19) Osseo-Asare, K.; Arriagada, F. *J. Colloid Interface Sci.* **1999**, *218*, 68–76.

(20) Arriagada, F.; Osseo-Asare, K. *J. Colloid Interface Sci.* **1999**, *211*, 210–220.

(21) Cullity, B. D.; Graham, C. D. *Introduction to Magnetic Materials*; 2011.

(22) Guardia, P.; Batlle-Brugal, B.; Roca, a. G.; Iglesias, O.; Morales, M. P.; Serna, C. J.; Labarta, a.; Batlle, X. *J. Magn. Magn. Mater.* **2007**, *316*, e756–e759.
(23) Bean, C. P.; Livingston, J. D. *J. Appl. Phys.* **1959**, *30*, S120.
(24) Luis, F.; Torres, J.; García, L.; Bartolomé, J.; Stankiewicz, J.; Petroff, F.; Fettar, F.; Maurice, J.-L.; Vaurès, A. *Phys. Rev. B* **2002**, *65*, 094409.
(25) Gittleman, J.; Abeles, B.; Bozowski, S. *Phys. Rev. B* **1974**, *9*, 3891–3897.
(26) Peddis, D.; Orru, F.; Ardu, A.; Cannas, C.; Musinu, A.; Piccaluga, G. *Chemistry of Materials,* ***2012****, 6, 1062-1071.*
(27) Moya, C.; Salas, G.; Morales, M. del P.; Batlle, X.; Labarta, A. *J. Mater. Chem. C* **2015**, *3*, 4522–4529.
(28) Pérez, N.; Guardia, P.; Roca, a G.; Morales, M. P.; Serna, C. J.; Iglesias, O.; Bartolomé, F.; García, L. M.; Batlle, X.; Labarta, a. *Nanotechnology* **2008**, *19*, 475704.
(29) Labarta, A.; Iglesias, O.; Balcells, L.; Badia, F. *Phys. Rev. B* **1993**, *48*, 10240–10246.
(30) Del Muro, M. G.; Batlle, X.; Labarta, A. *J. Magn. Magn. Mater.* **2000**, *221*, 26–31.

Quantification of dipolar interactions in $Fe_{3-x}O_4$ nanoparticles

Carlos Moya,*† Óscar Iglesias,† Xavier Batlle,† Amílcar Labarta†

† Departament de Física Fonamental and Institut de Nanociència i Nanotecnologia (IN2UB), Universitat de Barcelona, Martí i Franquès 1, 08028 Barcelona, Spain

E-mail: cmoya@ffn.ub.es

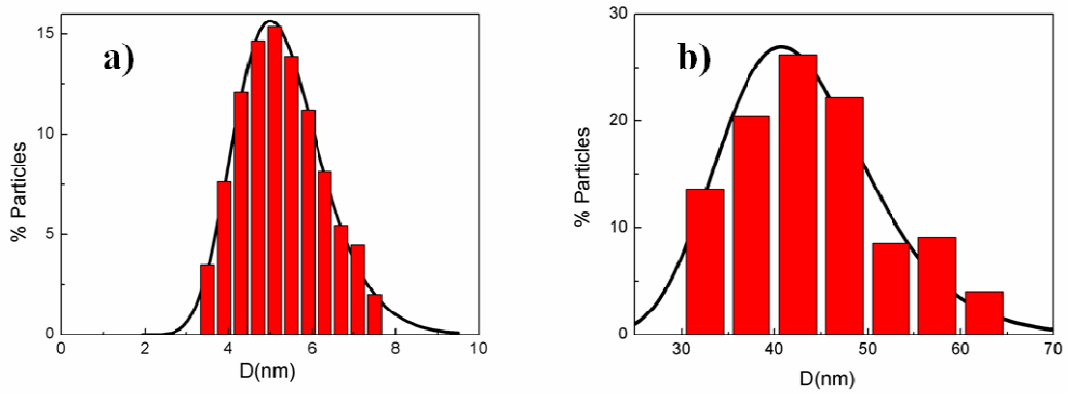

Figure S1. Particle size distribution for samples a) R1, b) R2.

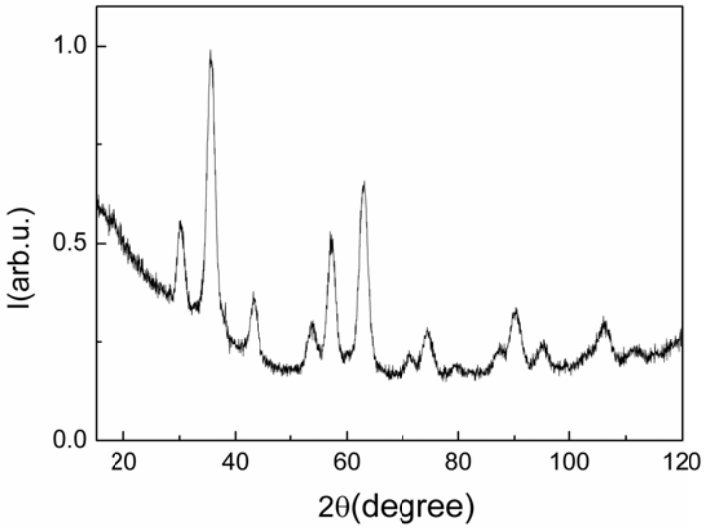

Figure S2. XRD Spectra of sample R1

Chapter 5.Study of the magnetization reversal by MFM

Nanoscale

PAPER

View Article Online
View Journal | View Issue

Cite this: *Nanoscale*, 2015, **7**, 8110

Direct imaging of the magnetic polarity and reversal mechanism in individual $Fe_{3-x}O_4$ nanoparticles†

Carlos Moya,*‡[a] Óscar Iglesias-Freire,‡[b,c] Nicolás Pérez,[a] Xavier Batlle,[a] Amilcar Labarta[a] and Agustina Asenjo[b]

Received 26th January 2015,
Accepted 1st April 2015

DOI: 10.1039/c5nr00592b

www.rsc.org/nanoscale

This work reports on the experimental characterization of the magnetic domain configurations in cubic, isolated $Fe_{3-x}O_4$ nanoparticles with a lateral size of 25–30 nm. The magnetic polarity at remanence of single domain ferrimagnetic $Fe_{3-x}O_4$ nanoparticles deposited onto a carbon–silicon wafer is observed by magnetic force microscopy. The orientations of these domains provide a direct observation of the magneto-crystalline easy axes in each individual nanoparticle. Furthermore, the change in the domain orientation with an external magnetic field gives evidence of particle magnetization reversal mediated by a coherent rotation process that is also theoretically predicted by micromagnetic calculations.

Introduction

Magnetic nanoparticles (NPs) have been actively researched in the last few decades due to their applications in technology such as magnetic recording,[1] catalysis[2] or environmental remediation[3] – and in biomedicine[4] – including biomolecule detection,[5] magnetic hyperthermia[6] or targeted drug delivery.[7] In particular, magnetite $Fe_{3-x}O_4$ NPs are one of the most commonly studied systems because they are easy to produce and functionalize by chemical routes,[8] have low toxicity and magnetic properties.[9] In addition, they are excellent model systems to study finite-size effects, yielding insight into new phenomena and enhanced properties of nanomaterials with respect to their bulk counterparts.[10] Currently, the study of the composition and crystallinity of individual NPs on the sub-nanometer scale can be performed only by electron microscopy techniques, as previously reported.[11] Moreover, the magnetic and the electronic properties of single NPs can be addressed by combining photoemission electron microscopy (PEEM) with synchrotron-based, polarization-dependent X-ray absorption spectroscopy (XAS).[12]

Another remarkable technique that allows the direct imaging of magnetic nanostructures is magnetic force microscopy (MFM),[13,14] a widespread technique that yields information about the distribution of magnetic charges within the surface region of ferrimagnetic samples. Its main advantages consist of a relatively high spatial resolution – allowing local measurements well below the microscopic scale – and versatility – enabling the possibility to apply external magnetic fields.[15] The capability of resolving small nanostructures, such as single nanoparticles, is limited by the finite radius of the tip apex, as well as by the tip–sample distance at which the magnetostatic interactions become dominant (typically 15–50 nm). The radius of the MFM tip can be decreased by using thinner magnetic coatings but the latter results in a lower magnetostatic coupling with the sample. Therefore, a balance must be maintained between resolution and sensitivity when aiming at characterizing magnetic nanostructures.[16] Although partially successful attempts to characterize individual magnetic NPs have been made;[17–26] the unambiguous correlation of the magnetic domain orientation to the crystalline structure is yet to be achieved. Within this framework, we present direct experimental observations of the magnetic domain configuration and magnetization reversal mechanism of individual $Fe_{3-x}O_4$ NPs. In addition, experimental analysis is further supported by micromagnetic calculations.

Experimental details

Samples were synthesized by high-temperature decomposition of Fe(III)–acetylacetonate in organic solvent with decanoic acid

[a]*Departament de Física Fonamental, Institut de Nanociència i Nanotecnologia, Universitat de Barcelona, Barcelona, 08028, Spain. E-mail: cmoya@ffn.ub.es*
[b]*Instituto de Ciencia de Materiales de Madrid (ICMM-CSIC), Cantoblanco, Madrid, 28049 Spain*
[c]*Department of Physics, McGill University, Montreal, H3A 2T8, Canada*

†Electronic supplementary information (ESI) available: PDF material contains TEM images of 27 nm $Fe_{3-x}O_4$ NPs (Fig. S1), thermogravimetric curve for the 27 nm $Fe_{3-x}O_4$ NPs (Fig. S2) and the topography of a scan size of 20 × 20 μm of a sample (Fig. S3). See DOI: 10.1039/c5nr00592b

‡These two authors contributed equally.

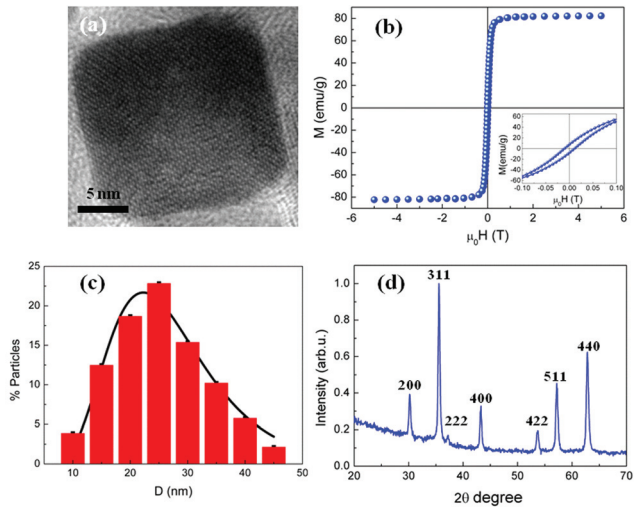

Fig. 1 Structural and magnetic characterization. (a) High resolution TEM image of a single $Fe_{3-x}O_4$ nanoparticle. (b) Hysteresis loops of 27 nm $Fe_{3-x}O_4$ NPs at 300 K and detail of the low field region (inset to Fig. 1b). (c) Particle size distribution obtained by TEM. The solid line corresponds to the fitting of the histogram to a log-normal distribution function. (d) X-ray diffraction pattern together with the indexation of the Bragg peaks to an inverse spinel structure.

as a capping ligand, as reported elsewhere.[8] Particle size distribution was analyzed by measuring around 1500 particles and the resulting histogram was fitted to a log-normal distribution function. Nanocrystals were found to be cubic in shape (see Fig. 1a and S1, ESI†), with a mean diameter of 27.2 nm and a standard deviation of 16.5 nm (see Fig. 1c). Fig. 1d shows iron oxide NPs to possess high crystal quality with an inverse spinel structure and an average particle diameter D_{XRD} = 27.0 ± 1.5 nm.

The saturation magnetization M_S was obtained by extrapolation of the high-field region of the magnetization curves $M(H)$ to zero field, assuming that the high-field behavior is of the type $M_S + \chi H$, where χ is a residual high-field susceptibility.[27,28] M_S values were normalized to the magnetic content by subtracting the organic fraction from the sample mass.

The saturation magnetization obtained from the hysteresis loop at room temperature (RT) (M_S = 80.9 ± 0.2 emu g^{-1}) was slightly smaller than the bulk value,[29] indicating an almost perfect ferrimagnetic order throughout the whole NP, as shown in Fig. 1a and previously reported in samples with very high crystal quality synthesized by the thermal decomposition method.[27,28] The squareness of the hysteresis loop and the existence of a finite value of the coercive field at RT ($\mu_0 \cdot H_c$ = 10.7 ± 2.0 mT) are associated with the blocking of the particle magnetization in a non-superparamagnetic state (see Fig. 1b). In such highly crystalline samples, well defined magneto-crystalline easy axes are expected to favor spins to point along the [111] directions, as has been demonstrated in macroscopic $Fe_{3-x}O_4$ crystals.[30] However, one should keep in mind that the magnetization data result from averaging over an enormous number of NPs – many of them with different orientations and grouped into clusters – in such a way that no direct evidence can be provided for the behavior occurring in isolated NPs. For that purpose, extracting local information about the magnetic properties of single particles becomes necessary.

Results and discussion

Fig. 2 shows the topography and the corresponding MFM images of four isolated $Fe_{3-x}O_4$ NPs, measured at remanence after in-plane saturation along the horizontal direction of the images. It is worth noting that, in contrast to the high accuracy yielded by AFM-based techniques in measuring vertical distances, lateral dimensions of protruding nanostructures are unavoidably overestimated due to the convolution of tip–sample interactions over the tip apex volume. Furthermore, sharp corners are considerably smoothed, as the dimensions of NPs are comparable to the tip apex radius. As a consequence, NPs shown in Fig. 2 appear to be 2–3 times wider than their real size and their cubic geometry is smeared out so that they appear as rather semi-spherical objects[31] (upper row in Fig. 2). In contrast, vertical distances eliminate the convolution effect and yield heights (Fig. 2e) in agreement with the size histogram shown in Fig. 1c.

The MFM images in Fig. 2 show individual NPs at remanence to be single domain with well-defined magnetic polarity, as expected for magnetite NPs of about 30 nm with high crystallinity. Furthermore, KPFM/MFM experiments were performed to discard electrostatic interactions and special attention was paid to the tip selection in order to get tip–particle interaction energy less than the anisotropy energy of a single particle so that the magnetization polarity remains unchanged while the image raster was completed. MFM images showing

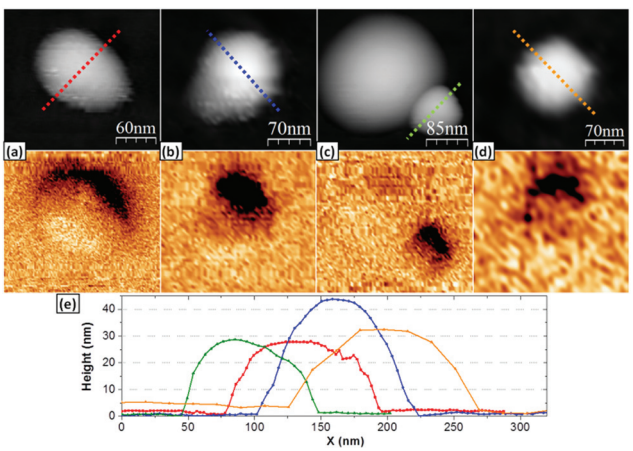

Fig. 2 The remnant state. (a)–(d) Topographic AFM (top row) and the corresponding MFM images (bottom row) of four different $Fe_{3-x}O_4$ NPs measured at remanence after in-plane magnetic saturation along the horizontal direction of the images. (e) Height profiles of those NPs in (a)–(d). Colored profiles in (e) correspond to the respective dashed lines depicted in the (a)–(d) AFM images.

particles with distinct orientations of the magnetic polarity also rule out the eventual influence of the stray field of the tip in the magnetic state of the particles or overlapping[32,33] of electrostatic interactions.[34,35]

Some misorientation of the magnetic polarity[36] – expected from the rather stochastic processes governing the drying step – exists among NPs when comparing the relative orientation of the bright–dark regions in the MFM images of Fig. 2. Interestingly enough, although two neighboring NPs seem to be present in the AFM image of Fig. 2c, only one of them gives rise to contrast in the corresponding MFM map. This suggests the existence of organic residues from the synthesis process, which might be misinterpreted as being $Fe_{3-x}O_4$ NPs in topographic images.

The influence that an external field has over such domain configurations is shown in Fig. 3. Note that the area shown in Fig. 3c corresponds to the zoomed NP shown in Fig. 2c. If these $Fe_{3-x}O_4$ NPs were isotropic, the applied magnetic field would determine a preferential direction in terms of the energy balance, so that, for field values large enough for spins to overcome eventual pinning potentials, domain polarizations would appear aligned with the external field in the MFM images. However, this is not the case in Fig. 3, where the dipolar contrast clearly reflects the existence of other preferential directions for spins to point along. We attribute this to the magneto-crystalline easy axes along the [111] directions of the cubic NPs.

Particularly relevant from these results is the fact that the orientations of the particle domains change when reversing the external field, in such a way that it is not a simple reversal of the dipolar polarity. This can be readily seen when comparing the MFM images shown in the left and right columns of Fig. 3, corresponding to magnetic field values larger than the coercive field of the NPs (at RT) with opposite directions. In each NP, the domain polarization changes from an orientation roughly inclined towards the right (↗ for positive values of the field) to another one inclined towards the left (↖ for negative fields), as the magnetic field is reversed. Thus, the particle spin configuration accommodates the magneto-crystalline easy axis that is closest to the direction of the external field. The similarity between the spin configurations observed in different NPs of the sample can be explained by the previous magnetic history followed by the system, in which magnetic fields close to the saturation field were applied. Most pronounced differences between the magnetic configurations of the NPs would be expected if the samples were in the virgin state.

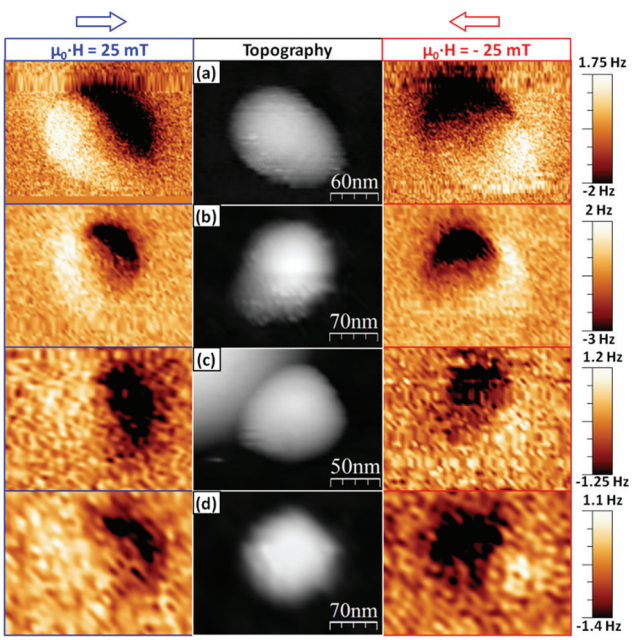

Fig. 3 The domain polarity. Topographic (center) and MFM images (left & right) of the same NPs in Fig. 2(a)–(d), in the presence of in-plane magnetic fields with opposite directions (see blue and red arrows on top of the figure).

Besides revealing the polarity and orientation of the particle domains, these MFM images provide additional information. The recorded switch in the spin orientation from one easy axis (for positive fields) to another one (for negative fields) is an experimental fingerprint of the reversal process being carried out by a coherent rotation mechanism. In order to support this hypothesis, some numerical calculations were performed by means of the OOMMF code[37] to simulate the magnetization distribution in cubic $Fe_{3-x}O_4$ NPs. The 3D Oxsii mode was used with the following parameters: saturation magnetization, M_S = 4.66 kA m^{-1}, was obtained from the hysteresis loop (see Fig. 1b); exchange stiffness constant for magnetite,[38] A = 13.2 × 10^{-12} J m^{-1}; magneto-crystalline anisotropy constant for bulk magnetite,[29] k_1 = 12 kJ m^{-3} and a cubic cell size of (2 × 2 × 2) nm^3.

The simulated hysteresis loop of a single NP is displayed in Fig. 4. This curve describes the reversal of the particle magnetization in the case of an in-plane field applied along the [100] direction (horizontal direction), similarly to the experimental situation. In the remnant state ($\mu_0 \cdot H$ = 0), the NP presents a single domain configuration with its spins mainly aligned along the [111] axis. This causes the ratio of the remnant magnetization to the saturation magnetization to be 0.58. The simulation predicts the reversal mechanism to follow a coherent rotation of the spins, as is displayed in Fig. 4b, with a coercive field of $\mu_0 \cdot H_C$ = 26 mT. Since the dimensions of these NPs are rather small, it would be costly in terms of the exchange energy to generate any kind of domain wall to carry out the reversal process. Thus, the NPs behave as a macrospin, tending to accommodate anytime the closest crystalline easy axis, giving rise to the change of orientations shown in Fig. 4a and c as the magnetic field reverses its polarity. So, as the micromagnetic simulations suggest that the switching between easy axes during the magnetization reversal process observed in the MFM images (see Fig. 3) can be associated with a coherent rotation mechanism rather than with nucleation and propagation of domain walls.

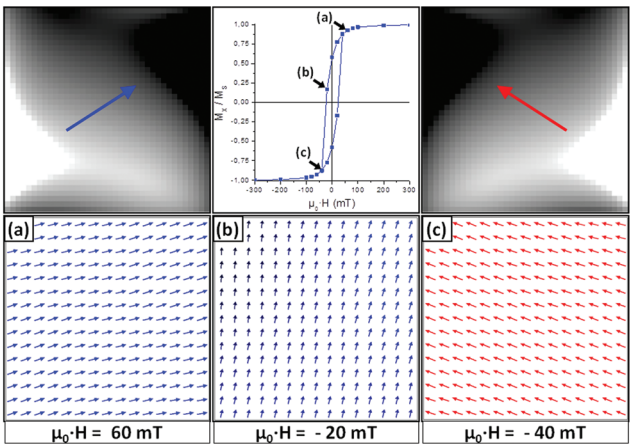

Fig. 4 Micromagnetic simulations. (Upper center) OOMMF simulated hysteresis loop for an individual NP with an in-plane field applied along the [100] direction (horizontal direction). Bottom (a), (b) and (c) images: distribution of the magnetization for the three situations highlighted by black arrows in the previous hysteresis loop. The upper left and upper right images display the simulated MFM contrast for the configurations presented below in the bottom (a) and (c) images, respectively.

Experimental section

Samples for transmission electron microscopy (MT80-Hitachi TEM) analysis were prepared by drying one drop of a dilute suspension of NPs deposited onto a carbon-coated copper grid at room temperature (RT). In order to gain deeper insight into the crystal quality and stoichiometry of individual NPs, high resolution TEM images (HR-TEM) were obtained with a JEOL-2100F microscope. The organic fraction of the samples was evaluated by thermogravimetric analysis (TGA) using a TGA-SDTA 851e/SF/1100 (Mettler Toledo) set-up, at a heating rate of 10 K min^{-1} under a nitrogen atmosphere from room temperature up to 1073 K (see Fig. S2, ESI†). Hysteresis loops of a powdered sample of NPs were measured with a Quantum Design SQUID magnetometer under a maximum applied magnetic field of ±5 T at 5 and 300 K. Samples for AFM-MFM observations were prepared by placing one drop of a dilute suspension of NPs onto a carbon–silicon wafer and drying it in an oven at 348 K for 1 hour in order to ensure that all solvent traces were completely removed. We prepared several samples by varying the particle concentration, deposition conditions and the particle size in order to find regions and identify by AFM imaging, isolated particles that were far enough (about a few times the apparent particle diameter) from other particles and aggregates so as to disregard dipolar interactions (see Fig. S3, ESI†).

MFM measurements were carried out at room temperature using a variable field MFM set-up from Nanotec Electrónica.[39] All the experiments were performed using the lift mode (lift height: 40 nm), in which the topographic profile is retraced at a tip–sample distance where magnetostatic interactions become dominant. MFM data are from the change in the resonance frequency of the oscillating cantilever induced by such magnetostatic coupling between the tip and the sample; in all the experiments shown, a phase-locked loop (PLL) was used to keep a constant phase lag between the driving signal and the cantilever oscillation, so that MFM data have units of Hz. BudgetSensors Multi75-G tips, with nominal values of spring constant $k \approx 3$ N m^{-1} and resonance frequency $f_0 \approx 75$ kHz, were used.

Conclusions

Summarizing, this work provides experimental characterization by variable field-magnetic force microscopy of the domain configurations in cubic, isolated $Fe_{3-x}O_4$ NPs with an average lateral size of 25–30 nm and high crystal quality. Single domain structures are reported, whose orientation and polarity are determined by both their magnetocrystalline easy axes and previous magnetic history. As the main result, we have been able to directly observe the orientation of the easy axes in individual ferrimagnetic nanoparticles. Furthermore, experimental evidence of a magnetization reversal mediated by coherent rotation of the particle spins has been obtained in these isolated NPs. These results have also been supported by micromagnetic simulations.

Acknowledgements

This work was supported by Spanish MINECO (MAT2012-33037, CSD2010-00024 and MAT2013-48054-C2) and Catalan DURSI (2009SGR856, 2014SGR220).

Notes and references

1 H. Zeng, J. Li, J. P. Liu, Z. L. Wang and S. Sun, *Nature*, 2002, **420**, 395; S. Sun, C. B. Murray, D. Weller, L. Folks and A. Moser, *Science*, 2000, **287**, 1989.
2 A. Schätz, O. Reiser and W. J. Stark, *Chem. – Eur. J.*, 2010, **16**, 8950.
3 W. Zhang, *J. Nanopart. Res.*, 2003, **5**, 323.
4 Q. A. Pankhurst, J. Connolly, S. K. Jones and J. Dobson, *J. Phys. D: Appl. Phys.*, 2003, **36**, R167.
5 J. M. Perez, L. Josephson and R. Weissleder, *ChemBioChem*, 2004, **5**, 261.
6 R. Mejías, S. Pérez-Yagüe, A. G. Roca, N. Pérez, A. Villanueva, M. Cañete, S. Mañes, J. Ruiz-Cabello, M. Benito, A. Labarta, X. Batlle, S. Veintemillas-Verdaguer, M. P. Morales, D. F. Barber and C. J. Serna, *Nanomedicine*, 2010, **5**, 397.
7 C. Sun, J. S. H. Lee and M. Zhanga, *Adv. Drug Delivery Rev.*, 2008, **60**, 1252.
8 P. Guardia, N. Pérez, A. Labarta and X. Batlle, *Langmuir*, 2009, **26**, 5843.

9 P. Tartaj, M. P. Morales, S. Veintemillas-Verdaguer, T. González-Carreño and C. Serna, *J. Phys. D: Appl. Phys.*, 2003, **36**, R182.
10 X. Batlle and A. Labarta, *J. Phys. D: Appl. Phys.*, 2002, **35**, R15.
11 J. Salafranca, J. Gazquez, N. Pérez, A. Labarta, S. T. Pantelides, S. J. Pennycook, X. Batlle and M. Varela, *Nano Lett.*, 2012, **12**, 2499.
12 A. Balan, P. M. Derlet, A. B. Fraile Rodríguez, J. Bansmann, R. Yanes, U. Nowak, A. Kleibert and F. Nolting, *Phys. Rev. Lett.*, 2014, **112**, 107201.
13 Y. Martin and H. K. Wickramasinghe, *Appl. Phys. Lett.*, 1987, **50**, 1455.
14 J. J. Sáenz, N. García, P. Grütter, E. Meyer, H. Heinzelmann, R. Wiesendanger, L. Rosenthaler, H. R. Hidber and H.-J. Güntherodt, *J. Appl. Phys.*, 1987, **62**, 4293.
15 M. Jaafar, J. Gómez-Herrero, A. Gil, P. Ares, M. Vázquez and A. Asenjo, *Ultramicroscopy*, 2009, **109**, 693.
16 Yu. P. Ivanov, O. Iglesias-Freire, E. V. Pustovalov, O. Chubykalo-Fesenko and A. Asenjo, *Phys. Rev. B: Condens. Matter*, 2013, **87**, 184410.
17 M. Raşa, B. W. M. Kuipers and A. P. Philipse, *J. Colloid Interface Sci.*, 2002, **250**, 303.
18 X. Huang, L. M. Bronstein, J. Retrum, C. Dufort, I. Tsvetkova, S. Aniagyei, B. Stein, G. Stucky, B. McKenna, N. Remmes, D. Baxter, C. C. Kao and B. Dragnea, *Nano Lett.*, 2007, **7**, 2407.
19 S. Schreiber, M. Savla, D. V. Pelekhov, D. F. Iscru, C. Selcu, P. C. Hammel and G. Agarwal, *Small*, 2008, **4**, 270.
20 C. Dietz, E. T. Herruzo, J. R. Lozano and R. Garcia, *Nanotechnology*, 2011, **22**, 125708.
21 X. Li, Z. Li, D. Pang, S. Yoshimura and H. Saito, *Appl. Phys. Lett.*, 2014, **104**, 213106.
22 S. Sievers, K. Braun, D. Eberbeck, S. Gustafsson, E. Olsson, H. W. Schumacher and U. Siegner, *Small*, 2012, **8**, 2675.
23 S. Block, G. Glöck, W. Weitschies and C. A. Helm, *Nano Lett.*, 2011, **11**, 3587.
24 J. D. Wei, I. Knittel, C. Lang, D. Schüler and U. Hartmann, *J. Nanopart. Res.*, 2011, **13**, 3345.
25 N. I. Nurgazizov, T. F. Khanipov, D. A. Bizyaev, A. A. Bukharaev and A. P. Chuklanov, *Phys. Solid State*, 2014, **56**, 1817.
26 Z. Xiaobin and P. Grütter, *Phys. Rev. B: Condens. Matter*, 2002, **66**, 024423.
27 P. Guardia, A. Labarta and X. Batlle, *J. Phys. Chem. C*, 2011, **115**, 390.
28 P. Guardia, B. Batlle-Brugal, A. G. Roca, O. Iglesias, M. P. Morales, C. J. Serna, A. Labarta and X. Batlle, *J. Magn. Magn. Mater.*, 2007, **316**, e756.
29 B. D. Cullity, *Introduction to Magnetism and Magnetic Materials*, Addison-Wesley, MA, 1972.
30 F. Heider, A. Zitzelsberger and K. Fabian, *Phys. Earth Planet. Inter.*, 1996, **93**, 239.
31 J. Zabaleta, M. Jaafar, P. Abellán, C. Montón, O. Iglesias-Freire, F. Sandiumenge, C. A. Ramos, R. D. Zysler, T. Puig, A. Asenjo, N. Mestres and X. Obradors, *J. Appl. Phys.*, 2012, **111**, 024307.
32 P. Grütter, Y. Liu, P. LeBlanc and U. Dürig, *Appl. Phys. Lett.*, 1997, **71**, 279.
33 Ó. Iglesias-Freire, J. R. Bates, Y. Miyahara, A. Asenjo and P. H. Grütter, *Appl. Phys. Lett.*, 2013, **102**, 022417.
34 A. Schwarz and R. Wiesendanger, *Nanotoday*, 2008, **3**, 28.
35 C. S. Neves, P. Quaresma, P. V. Baptista, P. A. Carvalho, J. P. Araujo, E. Pereira and P. Eaton, *Nanotechnology*, 2010, **21**, 305706.
36 M. Jaafar, O. Iglesias-Freire, L. Serrano-Ramón, M. R. Ibarra, J. M. de Teresa and A. Asenjo, *Beilstein J. Nanotechnol.*, 2011, **2**, 552.
37 M. J. Donahue and D. G. Porter, Interagency Report NISTIR 6376, N.I.S.T., Gaithersburg, 1999.
38 H.-C. Wu, S. K. Arora, O. N. Mryasov and I. V. Shvets, *Appl. Phys. Lett.*, 2008, **92**, 182502.
39 http://www.nanotec.es.

Electronic Supplementary Material (ESI) for Nanoscale.

Supporting Information

Direct imaging of the magnetic domain polarity and reversal mechanism in individual $Fe_{3-x}O_4$ nanoparticles

Carlos Moya [1‡], Óscar Iglesias-Freire [2,3‡], Nicolás Pérez [1]*, Xavier *Batlle [1], Amílcar Labarta [1] and Agustina Asenjo [2]*

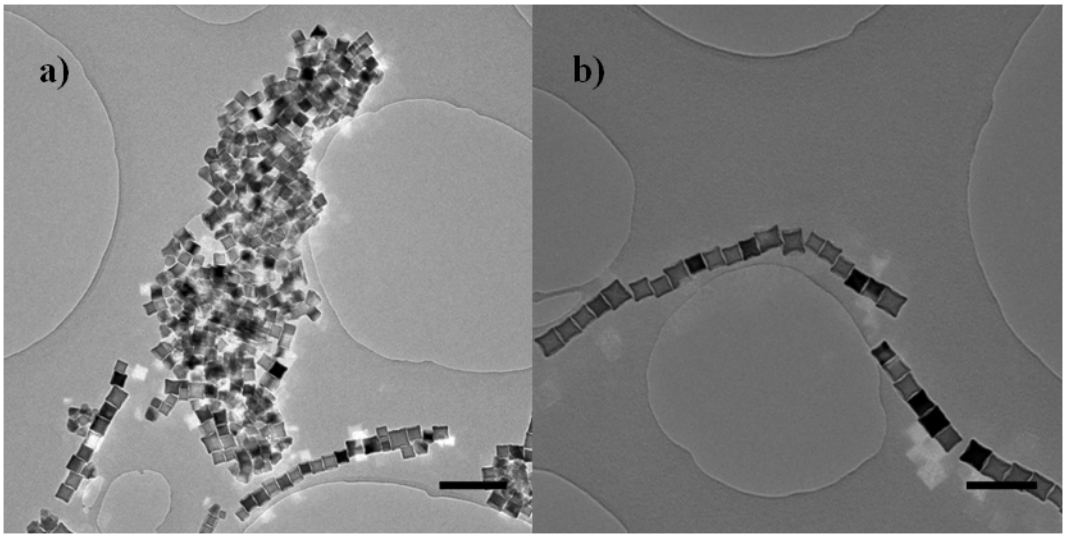

Figure S1. TEM images of 27 nm $Fe_{3-x}O_4$ NPs. Scale bars in a) = 200 nm and in b) =125 nm.

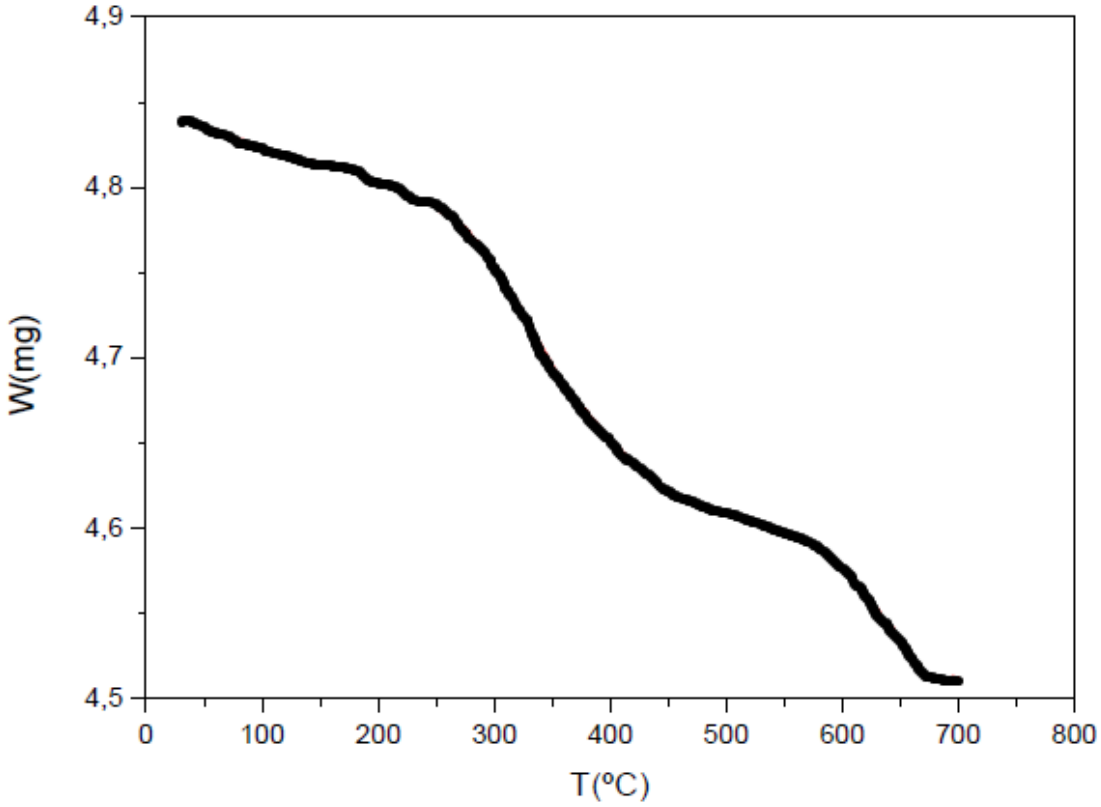

Figure S2. Thermogravimetric curve for the 27 nm $Fe_{3-x}O_4$ NPs.

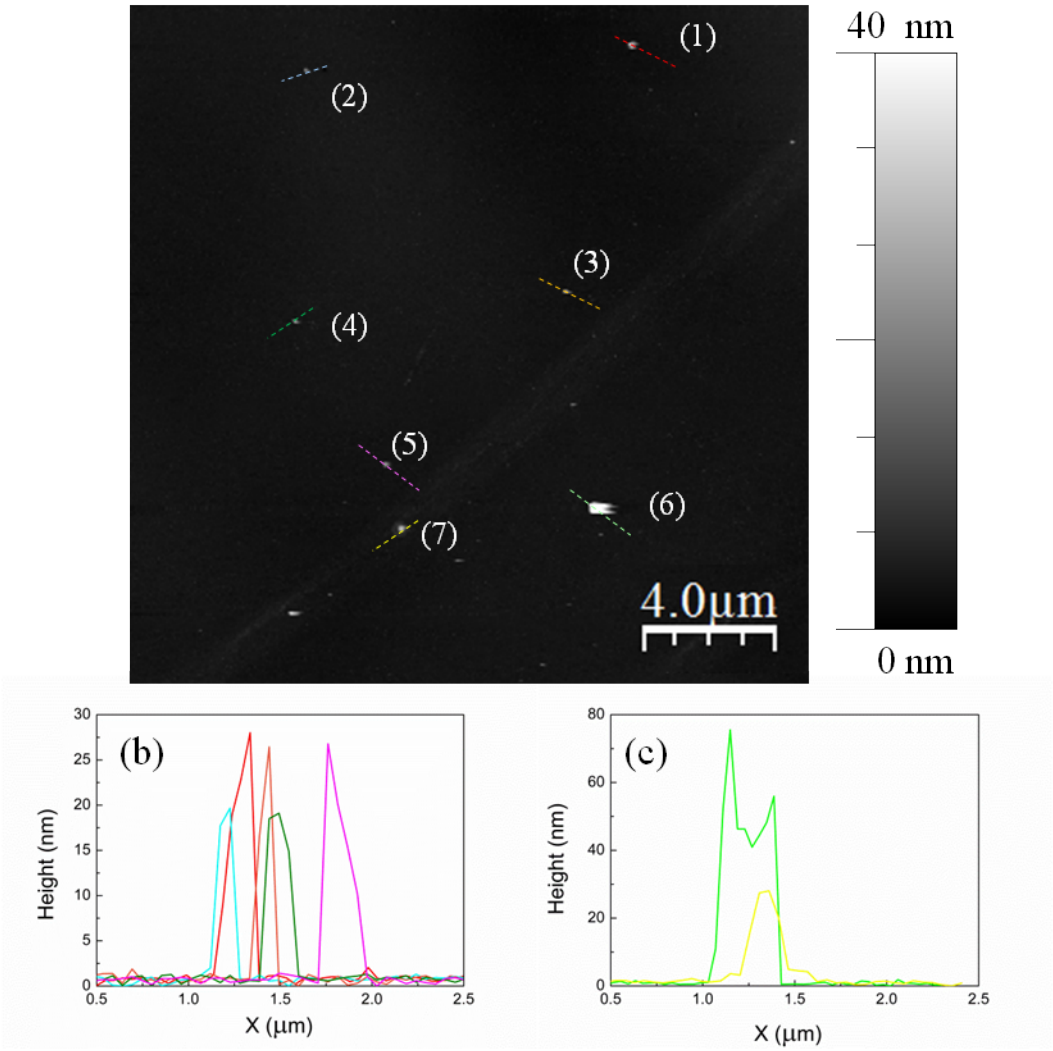

Figure S3. (a) Topography of the scan size (20 x 20 µm). (b) Particle histograms (1)-(5). (c) Particle histograms (6)-(7). Particle (1) is the same as in the Figures 2-3 (a).

Journal Name

RSCPublishing

ARTICLE

Cite this: DOI: 10.1039/xoxxoooooox

Superparamagnetic versus blocked states in aggregates of $Fe_{3-x}O_4$ nanoparticles studied by MFM

Carlos Moya,[*‡a] Óscar Iglesias-Freire,[‡b,c] Xavier Batlle,[a] Amilcar Labarta [a] and Agustina Asenjo [b]

Received ooth January 2012,
Accepted ooth January 2012

DOI: 10.1039/xoxxoooooox

www.rsc.org/

Magnetic domain configurations in two samples containing small aggregates of $Fe_{3-x}O_4$ nanoparticles of about 11 and 49 nm in size, respectively, were characterized by magnetic force microscopy (MFM). Two distinct magnetic behavior were observed depending on particle size. Aggregates constituted of nanoparticles about 11 nm in size showed uniform dark contrast on MFM images, reflecting the predominant superparamagnetic character of those particles and arising from the coherent rotation of the spins within the aggregate as the latter align along the tip stray-field. Applying a variable in-plane field, it is possible to induce a magnetic polarization yielding an increasing dark/bright contrast as the strength of the applied field overcomes the stray-field of the tip, although this polarization completely disappears as the remanent state is back recovered when the magnetic field is switched off. On the contrary, for aggregates of NPs of about 49 nm in size, dark/bright contrast associated with the existence of magnetic domains and magnetic polarization prevails on MFM images all along of the magnetic cycle due to the blocking state of the magnetization of those larger particles, even in the absence of an applied field. All in all, we unambiguously demonstrate the capabilities of magnetic force microscopy to distinguish between blocked and superparamagnetic states in aggregates of magnetic nanoparticles. Micromagnetic simulations strongly support the conclusions stated from the MFM experiments.

Introduction

Magnetite nanoparticles (NPs) have been the focus of a lot of interest due to their easy production by chemical routes,[1] remarkable magnetic properties[2,3] and relative low toxicity;[4] all of them making these NPs suitable candidates for potential applications in biomedicine, such as contrast agents in magnetic resonance imaging (MRI),[5] drug delivery[6] and hyperthermia[7] among others,[8] and in technology, such as in magnetic recording.[9,10] In addition, they are ideal systems to study finite-size effects, yielding new phenomena and enhanced properties with respect to their bulk-counterparts.[11] One of the most common finite-size effects is superparamagnetism (SPM) which not only depends on the particle volume but it is also a time-dependent phenomenon due to the stochastic nature of the thermal activation energy.[11,12] Thus, for non-interacting particles, the observed magnetic behavior depends on the relative characteristic value of the acquisition time, τ_m , of the specific experimental technique with respect to the relaxation time, τ, associated with the probability of the spins to overcome the energy barriers for magnetic anisotropy.[11,12] In addition, SPM regime limits the use of NPs in several bioapplications and magnetic recording.[11] Consequently, special attention has been paid to get an accurate dynamical magnetic characterization in order to distinguish between the SPM and blocked regimes of the net magnetization of NPs ensembles. The majority of those studies have been performed by measuring both DC (τ_m = 100s) and AC susceptibilities (τ_m = 10^{-1}-10^{-5}s for typical experiments), Mössbauer spectroscopy (τ_m = 10^{-7}-10^{-9}s) and neutron scattering (τ_m = 10^{-8}-10^{-12}s).[13,14] A common downside of all these standard characterization techniques lies on the fact that they only provide average information over a very large number of NPs. On the contrary, the direct observation of either a single particle or small clusters of NPs is available by magnetic force microscopy (MFM).[15-19] MFM has proved to be a versatile technique, by means of which it is possible to study the real time evolution of the magnetic domains by variable-field MFM (VF-MFM)[20]or to characterize the evolution of MFM contrast versus tip-sample distance by 3D mode, allowing a complete characterization of small structures.[21,22] In addition, micromagnetic simulations performed with the Object Oriented Micromagnetic Framework (OOMF) code constitutes an ideal tool to interpret the experimental MFM images.[23]

Within this framework, we have addressed the study of SPM and blocked regimes of aggregates by MFM experiments in two samples of $Fe_{3-x}O_4$ NPs with mean diameters of 11 nm (R11) and 49 nm (R49), respectively, that were synthesized by thermal decomposition of organic precursors.[24,25] SPM and ferrimagnetic blocked NPs were independently observed and were fully differentiated for samples R11 and R49, respectively. Interestingly enough, 3D mode and VF-MFM experiments were carried out, aiming at studying the influence that the stray field emerging from the MFM tip has on the magnetic state of the sample, so as to avoid artifacts and misinterpretation of data when images corresponding to the SPM and blocked regimes were compared. Finally, micromagnetic simulations were used to gain some insight into the different mechanisms taking place during magnetization reversal.

Sample preparation

$Fe_{3-x}O_4$ NPs were prepared by high-temperature decomposition of Fe(III)-acetylacetonate with decanoic acid as capping ligand in an organic solvent, as reported elsewhere.[25,26] It has been shown that a wide range of monodisperse particle sizes can be obtained depending on the relative concentration of the reactants and temperature profile of the reaction.[25,26]

Sample R11. For 11 nm NPs, 5 mmol of decanoic acid were mixed with 1 mmol of Fe(III)-acetylacetonate in 25 mL of dibenzyl-ether. First of all, the solution was heated up to 200 ºC at a constant rate of 6.5 ºC/min under nitrogen atmosphere and vigorous stirring. After 2 h at 200 ºC, the reaction mixture was heated up to 270 ºC and kept at this temperature for 1 h. Finally, the solution was cooled down to room temperature, washed three times with ethanol and NPs were collected by centrifugation at 9000 rpm.

Sample R49. NPs 49 nm in size were obtained following the same method explained before but with a larger molar ratio of decanoic acid to Fe(III)-acetylacetonate (1:4) and setting the temperature profile to 3.5 ºC/min for the last reaction stage.

Samples were stored in ethanol until final use.

Structural and magnetic characterization

The samples were prepared for transmission electron microscopy (TEM) (MT80-Hitachi microscope) by placing one drop of a dilute NPs suspension onto a carbon-coated copper grid and drying at room temperature. The size distribution was analyzed by measuring at least 2000 particles and the resulting histograms were fitted to log-normal functions (see Fig. 1d-e and S1a-b, Supporting information). The particles in both samples were found to be faceted (see Fig. 1a-b) and single-crystal domains of 11 and 49 nm in mean size, respectively. The standard deviation of the size distribution were 6 nm for R11 and 30 nm for R49.

The crystalline phase of the iron oxide particles was identified by powder X-ray diffraction. The patterns were collected between 5º to 120º in 2θ in a PANalytical X'Pert PRO MPD diffractometer by using Cu Kα radiation, and they were indexed to an inverse spinel structure (Fig. 1f). The mean particle diameters obtained from XRD data (D_{XRD}) were 11 ± 0.5 nm for R11 and 45 ± 2 nm for R49, in good agreement with estimations from TEM. This also confirms the high crystalline quality of the samples and their single-crystal domain features.

The organic fraction of the samples was evaluated by thermogravimetric analysis (TGA). Measurements were effected in a TGA-SDTA 851e/SF/1100 (Mettler Toledo) at a heating rate of 10 ºC/min from room temperature up to 800 ºC in nitrogen atmosphere (see Fig. S2, Supporting information).

Hysteresis loops $M(H)$ were measured with a Quantum Design SQUID magnetometer at 300 K (see Fig. 1c) to study the coercive field (H_c) and saturation magnetization (M_s) under a maximum magnetic field of ± 50 kOe. M_s was obtained by extrapolation of the high-field region of $M(H)$ curves to zero magnetic field, assuming the high-field behavior,

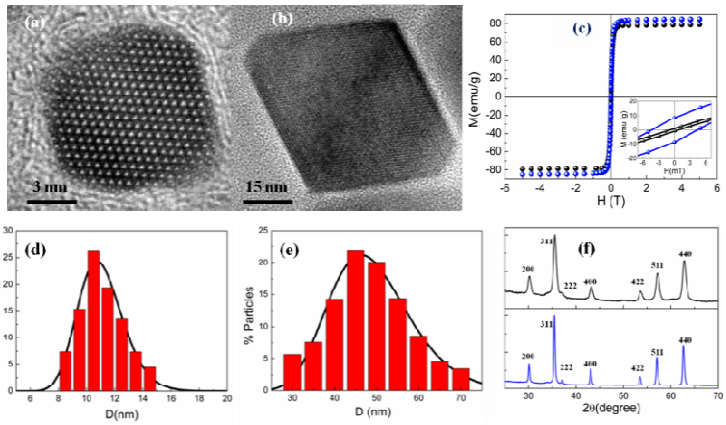

Figure 1. (a) and (b) HRTEM images of sample R11 and R49, respectively. (c) Hysteresis loops of $Fe_{3-x}O_4$ NPs at 300 K . Blue circles: sample R49, black circles: sample R11. Inset: detail of the low field region. (d) and (e) show the particle size distribution for R11 and for R49, respectively. (f) X-ray diffraction pattern with the indexation of the Bragg peaks to an inverse structure for R11 (black line) and for R49 (blue line).

$M(H) = M_s + \chi H$, where χ is a residual susceptibility.[3] M_s values were normalized to the magnetic content by subtracting the organic fraction evaluated by TGA analyses from the sample mass. The values obtained at RT were M_s =78.0 ± 0.7 emu/g for R11 and M_s = 84.3 ± 0.1 emu/g for R49. Those values are just slightly smaller than the bulk one, indicating an almost perfect ferrimagnetic order throughout the whole NPs, as previously observed in samples with very high crystal quality synthesized by the thermal decomposition method.[2], [3], [13], [26] Besides, H_c was defined as $H_c = (|H_c^+| + |H_c^-|)/2$, where H_c^+ and H_c^- are the interceptions of the hysteresis loop with the positive and negative sides of the H-axis, respectively. A magnification of the field range where those interceptions take place is shown in the inset to Fig. 1c. The obtained values of the coercive field are 0.8 ± 0.3 mT for R11 and 4.3 ± 0.5 mT for R49. This very small value of H_c for R11 suggests that the majority of the particles in this sample are SPM at RT, in contrast with the case for R49 where the magnetization of most of the particles remains blocked.

Magnetic force microscopy

Characterization of the aggregates by MFM

Figure 2 shows the topography and MFM images at remanence (zero field) of several aggregates containing a few particles of samples R11 (Fig. 2a-d) and R49 (Fig. 2e-f) and the corresponding topographic and frequency shift profiles. The aggregates of the smaller R11 NPs give rise to a homogeneous attractive interaction between the tip and the sample, displayed as a uniform dark contrast in Fig. 2a-d, which is consistent with a coherent rotation of the spins within the NPs induced by the tip stray-field. This reflects the relatively low value of the net anisotropy energy arising from the small size of the R11 NPs and, consequently, their predominant SPM character.

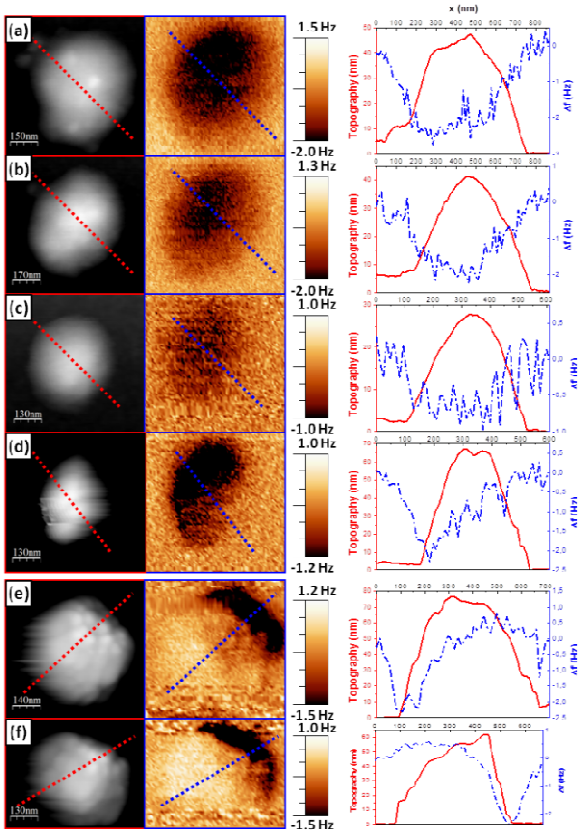

Figure 2. The remanent state. (a)–(f) Topographic *AFM* (left row) and *MFM* images (center row) of six different clusters of $Fe_{3-x}O_4$ NPs (R11: (a)-(d), R49: (e)-(f)), measured at remanence after in-plane magnetic saturation along the horizontal axis of the images. Right-most column: Heights (red solid line) and frequency shifts (blue solid line) profiles of the studied clusters (R11 and R49, respectively).

This kind of attractive tip-induced interactions is expected to occur in either SPM NPs or very soft magnetic nanostructures, the two cases not being unambiguously distinguishable by recording solely conventional MFM images. Therefore, care must be taken to avoid misinterpretation of the MFM data, as has been previously reported. [15,16,27,28] In order to confirm the SPM character of the aggregates of R11 NPs, a study of the dependence of the frequency shift on the tip-sample distance was carried out and the results are shown in Fig. 3.[21,22] To perform this sort of experiments, the same profile across the aggregate is repeatedly scanned while the lift height is varied from 30 to 180 nm. As shown in Fig. 3d, the frequency shift decreases with the distance from (-1.23 ± 0.6) Hz at 30 nm to (-0.06 ± 0.42) Hz at 180 nm, accordingly to a monotonous reduction of the attractive interaction until the signal becomes comparable to the experimental noise. The latter reveals that the net magnetization of the R11 aggregates orients along the vertical direction even for very small values of the stray field emerging from the tip,[15] which in turn confirms the SPM character of these aggregates. However, aggregates of R49 NPs yield MFM images with well-defined magnetic polarity because of the blocked state of their net magnetization at RT (see Fig. 2e-f).

The characterization by MFM imaging of those aggregates has revealed two situations as regards to the interaction between the stray-fields of the tip (B_{tip}) and that generated by the sample (B_{sample}). For sample R11, $B_{tip} > B_{sample}$ and aggregates are observed to be in a SPM regime, while for sample R49, $B_{tip} < B_{sample}$ and a blocked state of the sample magnetization with well-defined magnetic polarity is clearly displayed on the MFM images.

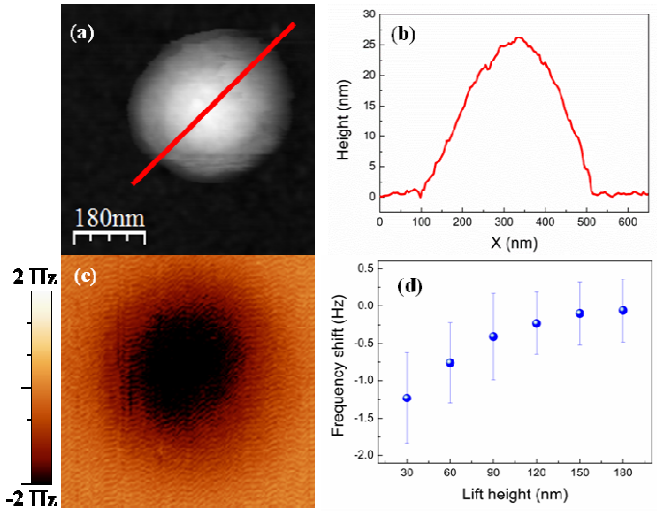

Figure 3. (a) Topography of a cluster of NPs for R11. (b) Height profile of the studied cluster. (c) MFM image of the cluster in (a). (d) Variation of the frequency shift from 30 to 180 nm lift height in a 3D experiment.

Variable field MFM study

A deeper insight into the magnetic nature of those particle aggregates can be gained by recording VF-MFM images as a function of an in-plane applied magnetic field. Results are shown in Fig. 4 for three cases recorded, respectively, at zero field and with a field of 82 mT applied in opposite in-plane directions. Similar magnetic domain structures with opposite polarities can be observed when comparing images at opposite values of the applied field for R11 aggregates (see Fig. 4a-d). Considering that these aggregates are SPM at zero field, the observed magnetic polarization can be understood as just

induced by the action of the external magnetic field, since the associated dark/bright contrast progressively disappears becoming only dark contrast as the magnitude of the field is decreased to zero (see central panels in Fig. 4a-d). So the in-plane polarization is imprinted in the aggregates when the strength of the applied field is large enough to overcome the attractive interaction between the sample and the stray-field of the tip. On the contrary, magnetic domains within the R49 aggregates are not totally saturated at 82 mT and non-symmetric states of the magnetization polarization are observed at both sides of the magnetic cycle (see Fig. 4e-f). At the same time, the dark/bright contrast prevails along the whole magnetic cycle since the net magnetization of these large particles remains blocked during the acquisition time of the MFM images.

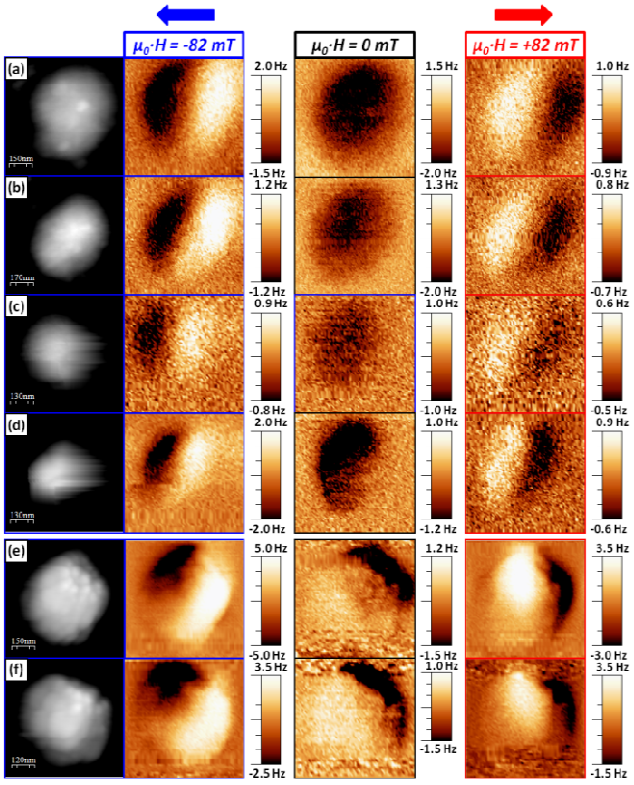

Figure 4. The domain polarity. Topographic (left) and MFM images (right) of the same NPs in Figure 2 (a)-(f) [(a)-(d) for R11 and (e)-(f) for R49], in the presence of in-plane horizontal magnetic fields with opposite direction (+/- 82 mT) and at zero magnetic field.

A detailed sequence depicting the reversal processes of the magnetic domains for the R49 aggregate shown in Fig. 4e is presented in Fig. 5a. A single domain configuration is observed at both sides of the magnetic cycle and along much of the way down to remanence, indicating that the aggregate behaves predominantly as a macro-spin. Interestingly, as the field direction is reversed from negative values a multi-domain structure is observed, where a domain wall seems to be present. That multi-domain structure defines the reversal process until a single domain configuration is reached again, with an uncompleted reversal of the magnetization polarity because the magnitude of the maximum applied field is not enough to achieve complete saturation. Therefore, the larger volume of these aggregates and their multi-particle nature result in a domain wall-mediated reversal of the magnetization, as compared to the coherent rotation of spins taking place in isolated NPs, as reported elsewhere.[18]

Micromagnetic simulations

In order to gain further knowledge on the processes involved in magnetization reversal, micromagnetic simulations were carried out using the OOMMF free source software.[23]The 3D Oxsii mode was used with the following parameters: saturation magnetization, MS = 4.66 kA/m (obtained from the hysteresis loop shown in Fig. 1b); exchange stiffness constant for magnetite,[29] A = $13.2 \cdot 10^{-12}$ J/m; magneto-crystalline anisotropy constant for bulk magnetite,[13] k1 = 12 kJ/m^3 and a cubic cell size of (2x2x2) nm^3. One should recall here that micromagnetic simulations are known to reproduce with high reliability experimental results in a qualitative manner, lacking in general quantitative reproducibility of experiments. Reasons for this can be attributed to thermally activated processes, the influence of structural and/or surface effects.

Figure 5b presents a simulated distribution of the magnetization during the reversal process in a cluster of (3x3) 50 nm-NPs with an additional one on the top of the middle of the square cluster. The external field was applied in-plane along the horizontal axis of the images. The apparent broadening of lateral dimensions intrinsic to AFM experiments mentioned above might cause such a cluster to appear with similar dimensions to the ones displayed in Fig. 4. The direction of the local magnetization is represented by arrows in a blue-red scale which indicates an outbound-inbound component (with respect to the image plane); the simulated MFM image is shown in a black-white scale which stands for a negative-positive divergence of the magnetization (thus, causing the appearance of the magnetic charges to which MFM is sensitive). The sample was initially saturated along the direction of negative polarity and magnetization reversal was studied.

Snapshots of the most relevant steps within the reversal process are shown in Fig. 5b. A single-domain phase is again first observed all the way from saturation to remanence (left image in Fig. 5b) and even for low fields applied upon reversal of the field direction. However, the relatively large lateral dimensions of this cluster of NPs allow for the magnetization to adopt a configuration with increasing in-plane curling. At a certain field value, a magnetic vortex is formed and magnetization reversal takes then place as the vortex moves across the cluster. The simulated MFM contrast emerging from this configuration reproduces up to a good extent the experimental results highlighted in Fig. 5a by green/yellow frames. Note that the exact orientation and shape of the experimental cluster may differ from those of the simulated one. Finally, a single (but reversed) domain is again obtained.

Therefore, our simulations suggest magnetization reversal to be mediated by nucleation and propagation of a vortex domain wall. Additional simulations were performed in

larger clusters of (4x4) NPs with another one on the top and the same mechanism was observed.

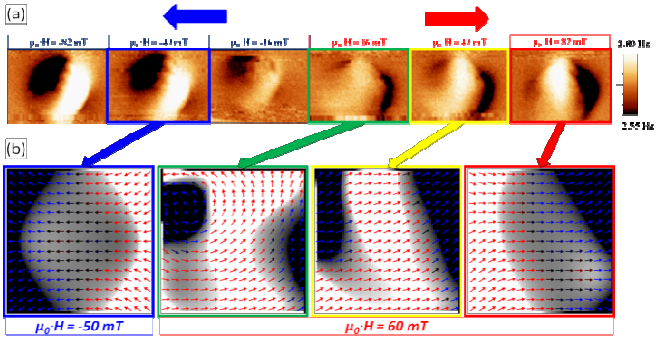

Figure 5. (a) MFM images of the aggregate shown in Fig. 4e in the presence of horizontal in-plane magnetic fields with variable magnitude and direction. (b) Results of the micromagnetic simulations, for a cluster of (3x3) 50 nm-NPs with an additional one on the top of the middle, showing various stages of the magnetization reversal, compared to the MFM images squared in (a) by color frames. The arrows and color code indicate the correspondence between the MFM images and the snapshots of the micromagnetic simulations.

Conclusions

MFM characterization of small aggregates of $Fe_{3-x}O_4$ NPs at RT reveals two distinct magnetic behavior depending on the particle size. Aggregates constituted of NPs about 11 nm in size show homogeneous attractive tip-sample interaction, displayed as a uniform dark contrast on the MFM images, and arising from the coherent rotation of the spins within the aggregate as they align along the tip stray-field. This reflects the predominant SPM character of those small particles observed within the characteristic acquisition time of the MFM technique and at zero applied field. Interestingly enough, applying a variable in-plane field, it is possible to induce a magnetic polarization yielding an increasing dark/bright contrast as the strength of the applied field increases and overcomes the stray-field of the tip. However, this induced polarization completely disappears as the remanent state is back recovered when the applied field is switched off. On the contrary, for aggregates of NPs of about 49 nm in size, dark/bright contrast associated with the existence of magnetic domains and magnetization polarization prevails on MFM images all along of the magnetic cycle, since the net magnetization of these large particles remains blocked during the acquisition time of the MFM images even at zero applied field. Therefore, the larger volume of these aggregates and their multi-particle nature yield a domain-wall mediated reversal of the magnetization, as compared to the coherent rotation of spins taking place in either aggregates of SPM NPs or even isolated particles with blocked magnetization. Micromagnetic simulations suggest such walls to be formed by an in-plane magnetic vortex moving across the cluster.

Experimental Section

MFM measurements were carried out at RT using a VF-MFM set-up from Nanotec Electrónica.[30] All experiments were performed using the lift mode (lift height: 40 nm), in which the topographic profile is retraced at a tip-sample distance for which magnetostatic interactions become dominant. MFM data arise from the change in the resonance frequency of the oscillating cantilever induced by such magnetostatic coupling between the tip and sample. In all the experiments performed, a phase-locked loop (PLL) was used to keep a constant phase lag between the driving signal and the cantilever oscillation, so that MFM data have units of Hz. BudgetSensors Multi75-G tips were used, with nominal values of the spring constant k≈3N/m and resonance frequency f_0≈75 kHz.

Samples for MFM observations were prepared by placing one drop of a dilute suspension of NPs onto a carbon-silicon wafer and letting it dry in an oven at 348 K for 1 h in order to remove all the remaining solvent. All images were collected at 0.5 lines/s and with a resolution of 256x256 pixels, so that the acquisition time was 7.8 ms/pixel. Taking this into account, an estimation of the maximum size for an isolated particle showing SPM behavior can be calculated by assuming a typical Néel relaxation of the magnetization with an relaxation time of about $\tau_0 = 10^{-9}$-10^{-11}s and an anisotropy constant of K_v = 2-4·10^5 erg·cm^{-3}, within the typical values found in magnetite NPs.[31,32] As result, a critical particle size of 11-16 nm is estimated for the observation of the SPM regime in our MFM data (see S3, Supporting information). Thus, NPs with smaller dimensions will exhibit SPM behavior and, consequently, internal magnetic domain configurations will not be observable by MFM.

It is worth noting that AFM techniques are very accurate in measuring vertical distances, whereas lateral dimensions of protruding nanostructures are unavoidably overestimated due to the convolution of tip-sample interactions over the tip apex volume.[18]As a consequence, NPs appear wider than their real size, whereas this convolution effect is not present in vertical displacements of the tip, which yields particle heights (see Fig. 2e-h) in outstanding agreement with the TEM size histogram shown in Fig. 1d-e. Corresponding topographic and MFM images display the exact same location; however, magnetic features may appear offset from the topographic ones, as different regions of the tip are sensitive to interactions with the sample during either AFM or MFM imaging (see Figure S4, Supporting information).

Acknowledgements

This work was supported by Spanish MINECO (MAT2012-33037, CSD2010-00024 and MAT2013-48054-C2) and Catalan DURSI (2014SGR220).

Notes and references

[a] Departament de Física Fonamental, Institut de Nanociència i Nanotecnologia, Universitat de Barcelona, Barcelona, 08028, Spain

[b] Instituto de Ciencia de Materiales de Madrid (ICMM-CSIC), Cantoblanco, Madrid, 28049 Spain
[c] Department of Physics, McGill University, Montreal, H3A 2T8, Canada
*Corresponding author E-mail: cmoya@ffn.ub.es
[‡] These two authors contributed equally.

† Electronic Supplementary Information (ESI) available: PDF material contains TEM images for samples R11 and R49 (Figure S1), Thermogravimetric curves for samples R11 and R49 (Figure S2) and Calculated relaxation time from Arrhenius law for a single $Fe_{3-X}O_4$ NP following Néel relaxation (Figure S3).

1 A. G. Roca, R. Costo, A. F. Rebolledo, S. Veintemillas-Verdaguer, P. Tartaj, T. González-Carreño, M. P. Morales, C. J. Serna, *J. Phys. D. Appl. Phys.* 2009, **42**, 224002.
2 P. Guardia, B. Batlle-Brugal, a. G. Roca, O. Iglesias, M. P. Morales, C. J. Serna, a. Labarta, X. Batlle, *J. Magn. Magn. Mater.* 2007, **316**, e756.
3 P. Guardia, A. Labarta, X. Batlle, *J. Phys. Chem. C* 2011, **115**, 390.
4 Y. Zhang, N. Kohler, M. Zhang, *Biomaterials* 2002, **23**, 1553.
5 H. Bin Na, I. C. Song, T. Hyeon, *Adv. Mater.* 2009, **21**, 2133.
6 M. Arruebo, R. Fernández-Pacheco, M. R. Ibarra, J. Santamaría, *Nano Today* 2007, **2**, 22.
7 R. Mejías, S. Pérez-Yagüe, A. G. Roca, N. Pérez, A. Villanueva, M. Cañete, S. Mañes, J. Ruiz-Cabello, M. Benito, A. Labarta, X. Batlle, S. Veintemillas-Verdaguer, M.P. Morales, D.F. Barber, C. J. Serna, *Nanomedicine*. 2010, **5**, 397.
8 Q. A. Pankhurst, J. Connolly, S. K. Jones, J. Dobson, *J. Phys. D. Appl. Phys.* 2003, **36**, R167.
9 S. Wang, F. J. Yue, D. Wu, F. M. Zhang, W. Zhong, Y. W. Du, *Appl. Phys. Lett.* 2009, **94**, 012507.
10 S. Yun, B. Sohn, J. C. Jung, W. Zin, *Langmuir* 2005, **14**, 6548.
11 X. Batlle, A. Labarta. Journal of Physics D: Applied Physics. 2002, **35**, R15.
12 C. P. Bean, J. D. Livingston, *J. Appl. Phys.* 1959, **30**, S120.
13 B. D. Cullity, C. D. Graham, *Introduction to Magnetic Materials*, **2011**.
14 I. Prigogine, S. A. Rice, Eds. , *Advances in Chemical Physics*, John Wiley & Sons, Inc., Hoboken, NJ, USA, **1997**.
15 C. S. Neves, P. Quaresma, P. V Baptista, P. a Carvalho, J. P. Araújo, E. Pereira, P. Eaton, *Nanotechnology* 2010, **21**, 305706.
16 S. Schreiber, M. Savla, D. V Pelekhov, D. F. Iscru, C. Selcu, P. C. Hammel, G. Agarwal, *Small* 2008, **4**, 270.
17 S. Sievers, K.-F. Braun, D. Eberbeck, S. Gustafsson, E. Olsson, H. W. Schumacher, U. Siegner, *Small* 2012, **8**, 2675.
18 C. Moya, Ó. Iglesias-Freire, N. Pérez, X. Batlle, A. Labarta, A. Asenjo, *Nanoscale* 2015, **7**, 8110.
19 P.Ares, M.Jaafar,A. Gil, J. Gómez-Herrero,A. Asenjo, *Small* **2015**. (DOI: 10.1002).
20 M. Jaafar, J. Gómez-Herrero, A. Gil, P. Ares, M. Vázquez, A. Asenjo, *Ultramicroscopy* 2009, **109**, 693.
21 C. Gómez-Navarro, F. Moreno-Herrero, P. J. de Pablo, J. Colchero, J. Gómez-Herrero, A. M. Baró, *Proc. Natl. Acad. Sci. U. S. A.* 2002, **99**, 8484.
22 M. Jaafar, L. Serrano-Ramón, O. Iglesias-Freire, A. Fernández-Pacheco, M. R. Ibarra, J. M. De Teresa, A. Asenjo, *Nanoscale Res. Lett.* 2011, **6**, 407.
23 Donahue MJ, Porter DG, National Technitian Information Service Document No. PB99 163214, National Institute of Standars and Technology (NIST), 1999 http://www.ntis.gov/Index.aspx.
24 P. Guardia, J. Pérez-Juste, A. Labarta, X. Batlle, L. M. Liz-Marzán, *Chem. Commun. (Camb).* 2010, **46**, 6108.
25 P. Guardia, N. Pérez, A. Labarta, X. Batlle, *Langmuir* 2010, **26**, 5843.
26 X. Batlle, N. Pérez, P. Guardia, O. Iglesias, A. Labarta, F. Bartolomé, L. M. García, J. Bartolomé, A. G. Roca, M. P. Morales, C. J. Serna, *J. Appl. Phys.* 2011, **109**, 07B524.
27 O. Iglesias-Freire, J. R. Bates, Y. Miyahara, A. Asenjo, P. H. Grütter, *Appl. Phys. Lett.* 2013, **102**, 022417.
28 M. Jaafar, O. Iglesias-Freire, L. Serrano-Ramón, M. R. Ibarra, J. M. de Teresa, A. Asenjo. *Beilstein Journal of Nanotechnology*. 2011, **2**, 552.
29 Wu, H.-C.; Arora, S. K.;Mryasov, O. N.; Shvets, I. V. *Appl. Phys. Lett.* 2008, **92**, 182502.
30 http://www.nanotec.es
31 N. Pérez, P. Guardia, a G. Roca, M. P. Morales, C. J. Serna, O. Iglesias, F. Bartolomé, L. M. García, X. Batlle, a Labarta, *Nanotechnology* 2008, **19**, 475704.
32 A. G. Roca, M. P. Morales, K. O'Grady, C. J. Serna, *Nanotechnology* 2006, **17**, 2783.

Supporting Information

Superparamagnetic versus blocked states in aggregates of $Fe_{3-x}O_4$ nanoparticles studied by MFM

Carlos Moya,[*‡a] Óscar Iglesias-Freire,[‡b,c] Xavier Batlle,[a] Amilcar Labarta [a] and Agustina Asenjo [b]

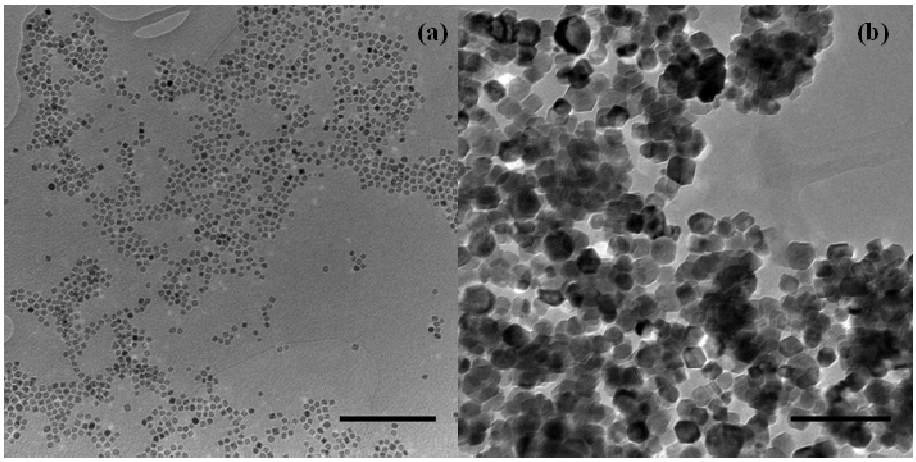

Figure S1. TEM images at low resolution. (a) 11 nm NPs and (b) 49 nm NPs. Scale bars correspond to 200 nm.

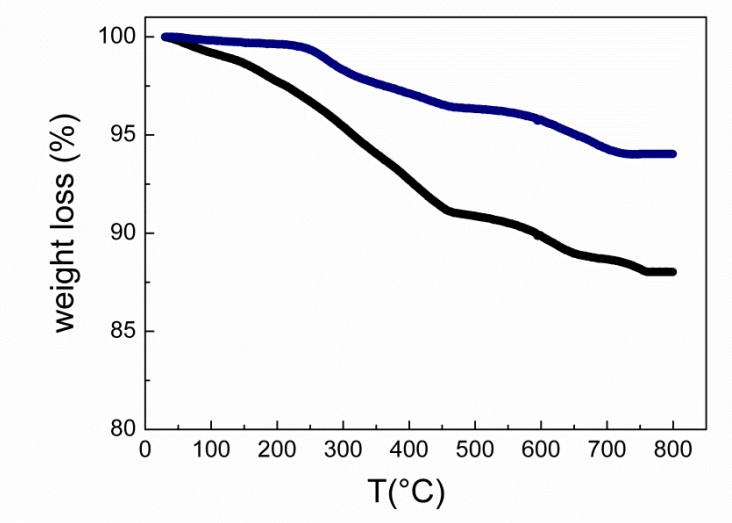

Figure S2. Thermogravimetric curves. Solid black line corresponds to 49 nm NPs and solid blue line corresponds to 11 nm NPs.

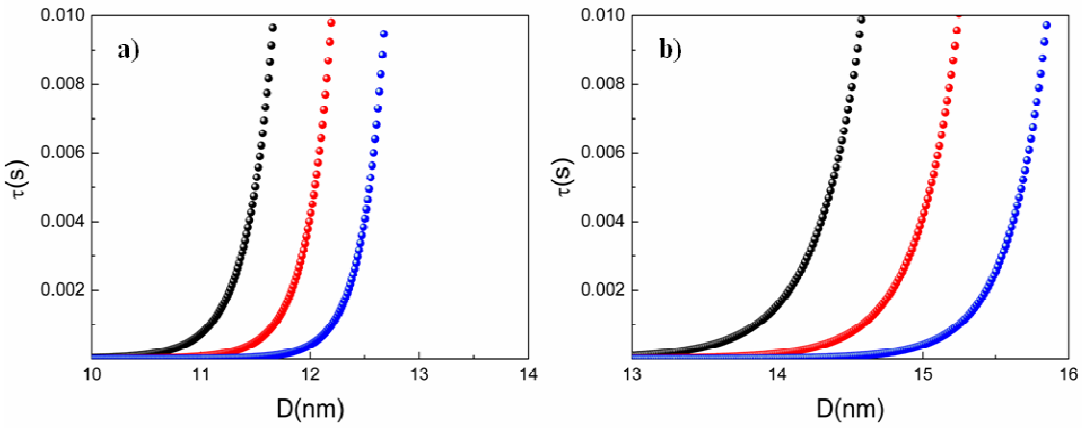

Figure S3. Calculated relaxation time from Arrhenius law for a single $Fe_{3-X}O_4$ NP following Néel relaxation. (a) $K_v = 2.1 \cdot 10^{-5}$ erg cm^{-3} and (b) $K_v = 4.1 \cdot 10^{-5}$ erg cm^{-3}. The values of the characteristic attempt time, τ_0, used in Arrhenius law are as follows. Black spheres: 10^{-9}s, red spheres: 10^{-10}s and blue spheres: 10^{-11}s.

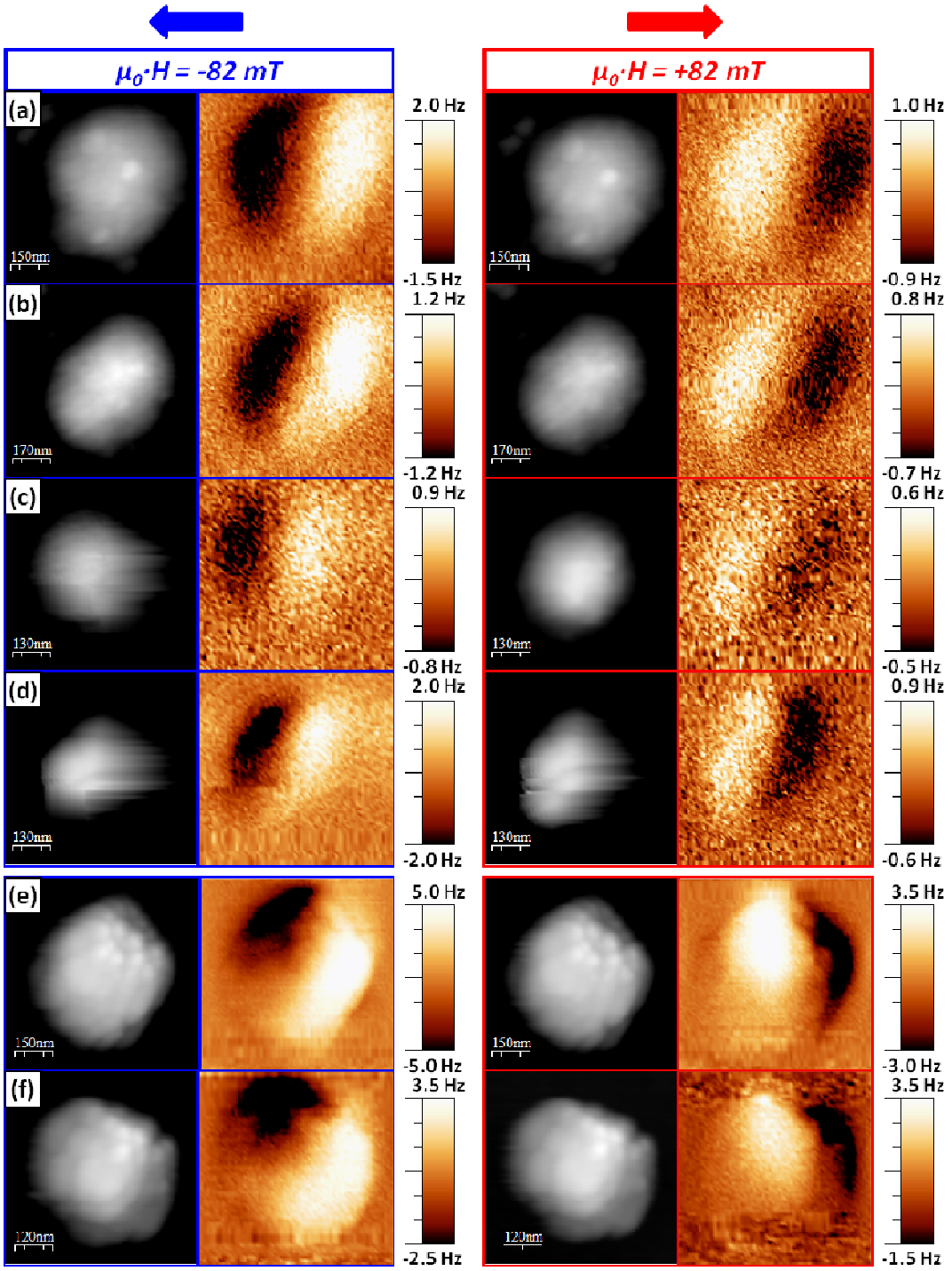

Figure S4. The exact same location for the topographic and MFM images of the aggregates of NPs shown in Figure 4 ((a)-(d) for R11 and (e)-(f) for R49).

Chapter 6.Conclusions

Despite the fact that specific conclusions of the results presented in this thesis have been addressed at the end of each chapter, a summary of the most relevant conclusions are compiled herein.

1) We have studied the effect on the magnetism and structure of MFe_2O_4 (with M= Co,Fe) NPs of the concentration of some reactants present along the high-temperature decomposition of organic precursors that has been the general method used to prepare the particles. Moreover, the reaction mechanisms have been elucidated from the study by FTIR of aliquots of the reaction mixture collected at various stages of the reactions.

a) Firstly, monodisperse $Fe_{3-x}O_4$ NPs in a wide range of sizes between 7 and 100 nm have been synthesized by only modifying the amount of oleic acid in the reaction mixture and using benzyl-ether as a solvent. The structural and magnetic characterization of the samples point out that NPs are single phase, highly crystalline and have values of the saturation magnetization close to the bulk one. Besides, NPs bigger than 7 nm show the typical Verwey transition associated with a composition very close to the stoichiometric Fe_3O_4. All in all, these results confirm the high quality of the particles obtained by this simple method. In addition, the study by FTIR spectroscopy indicates that the nucleation temperature is strongly dependent on the amount of the oleic acid concentration. Once the concentration of the oleic acid increases, the nucleation temperature raises as well and consequently the growth process can be tuned.

b) Secondly, we have demonstrated the key role of 1,2-hexadecanediol on the final crystalline quality of $CoFe_2O_4$ NPs by modifying the concentration of this reactant in the reaction mixture. Although all samples show single-phase NPs, similar stoichiometry and particle size, the final crystalline quality of the NPs can be gradually improved by the addition of an increasing amount of 1,2-hexadecanediol to the reaction mixture. In such a way, it is possible to tune the structure of the NPs from being aggregates of small crystallites exhibiting magnetic glassy behaviour until having highly crystalline NPs with bulk-like ferrimagnetism. The analysis of the FTIR spectra have shown that the content of the 1,2-hexadecanediol in the reaction mixture favours the decomposition of both Fe and Co

acetylacetonates and the formation of the mixed $Co^{2+}Fe^{3+}$-oleate complex, thus lowering the temperature at which the nucleation of the NPs starts. This could be useful to tailor the magnetic properties of Co-ferrite NPs for a specific application demanding lower/higher values of either the saturation magnetization or the coercive field. All in all, the 1,2-hexadecanediol concentration in the reaction mixture can be considered as a tunable parameter that controls the final magnetic properties of monodisperse, stoichiometric Co-ferrite NPs.

2) We have compared the structural and magnetic properties of three samples of 8 nm Co-ferrite NPs synthesized by the decomposition of metallorganic precursors varying the amount of 1,2-hexadecanediol present in the reaction mixture. Tough all three samples had very similar stoichiometry and distribution of particle sizes, and they were all even nominally single-phase $CoFe_2O_4$ according to the conventional methods of chemical and structural characterization performed, they have shown strongly sample-dependent magnetic properties, ranging from bulk-like ferrimagnetism to glassy magnetic behaviour. We have demonstrated that the presence of crystallite domains associated with crystallographic defects throughout the particles leads to highly-frustrated ferrimagnetic cores that were responsible for the glassy phenomenology - largely spoiling the magnetic performance of the NPs -, while only samples almost free of structural imperfections showed bulk-like magnetic properties. It is thus suggested that care should be taken when analysing the magnetic behaviour of ferrimagnetic transition metal oxide nanoparticles since most of the reported large variability of magnetic properties and 'spin glass-like' phenomenology may be just due to the poor crystallinity of the particles yielded by some conventional methods of preparation.

3) The effect of interparticle interactions has been investigated in samples composed of $Fe_{3-x}O_4$ NPs of 5 and 14 nm in size that were coated with either oleic acid or SiO_2 . First, we observed that a strong reduction in the interparticle interactions can be achieved by coating individual NPs with a thick sell of SiO_2. Moreover, we demonstrated that the intrinsic anisotropy of the NPs can be obtained by means of transverse susceptibility measurements even in samples with strong interparticle interactions. This is because experimental results and numerical simulations showed that the mean dipolar field acting on each single particle was significantly reduced when particles' magnetizations were collinearly aligned by the action of an external magnetic field. Based on these results, we developed a general method for the quantification of dipolar interactions in assemblies of NPs. This method consists in the comparison of the distributions of energy

barriers for the magnetization reversal obtained from time-dependent relaxation measurements, starting from configurations with either random orientation of the particles' magnetizations or collinear arrangement of them prepared by previously field cooling the sample. Besides, the intrinsic distribution of the energy barriers of anisotropy for the non-interacting case was evaluated from the same magnetic particles which were individually coated with silica shell in order to make dipolar interactions negligible. Interestingly, the results of the numerical simulations accounted for the relative energy shift of the experimental energy barrier distributions corresponding to the interacting and non-interacting cases, thus supporting the validity of the proposed method for the quantification of dipolar interactions.

4) We have studied the magnetization reversal in isolated $Fe_{3-x}O_4$ NPs and small clusters of them by means of variable-field magnetic force microscopy. In addition, the results and conclusions have been supported by micromagnetic simulations carried out by OOMF.

a) We have directly observed the domain configurations in cubic, isolated $Fe_{3-x}O_4$ NPs with an average lateral size of 25-30 nm and high crystal quality. Single domain structures were shown, whose orientation and polarity result from both the magnetocrystalline easy axes of the particles and previous magnetic history. As the main result, we have been able to directly observe the orientation of the easy axes in individual ferrimagnetic nanoparticles. Furthermore, experimental evidence of a magnetization reversal mediated by coherent rotation of the particle spins has been obtained in these isolated NPs that has also been supported by micromagnetic calculations.

b) The capabilities of MFM to distinguish between blocked and superparamagnetic states in nano-aggregates of a few magnetite nanoparticles with high crystalline quality have been unambiguously demonstrated. Aggregates constituted of nanoparticles about 11 nm in size have shown uniform dark contrast on MFM images, reflecting the predominant superparamagnetic character of those particles and arising from the coherent rotation of the spins within the aggregate as the latter align along the tip stray-field. Applying a variable in-plane field, it has been possible to induce a magnetic polarization yielding an increasing dark/bright contrast as the strength of the applied field overcomes the stray-field of the tip, although this polarization completely disappeared as the remanent state was back

recovered when the magnetic field was switched off. On the contrary, for aggregates of NPs of about 49 nm in size, dark/bright contrast associated with the existence of magnetic domains and magnetic polarization prevailed on MFM images all along of the magnetic cycle due to the blocking state of the magnetization of those larger particles, even in the absence of an applied field.

Capítulo 7.Resumen en castellano

Desde el punto de vista fundamental, los sistemas de (nanopartículas) NPs basados en MFe_2O_4 (M= Fe, Co) resultan sistemas modelo para estudiar la nueva fenomenología magnética encontrada en materiales de escala nanométrica, en comparación con la de sus homólogos masivos. Una gran parte de esta fenomenología propia de la nanoescala se debe a la disminución de la cristalinidad en la superficie y los defectos cristalográficos, en general, o a la naturaleza policristalina del material, la cual tiene una fuerte influencia en las propiedades magnéticas de las NPs, permitiendo a la vez modularlas a través del método de síntesis utilizado. Por lo tanto, el comportamiento magnético de las NPs puede ser modificado a la carta mediante la elección de un método de síntesis apropiado que facilite un buen control de la estructura final de las NPs. La descomposición térmica de precursores órgano-metálicos a alta temperatura destaca entre los métodos de síntesis más comunes, no sólo porque se consiguen NPs monodispersas de alta cristalinidad, sino porque además, con pequeños cambios en la reacción, se pueden variar notablemente las propiedades estructurales de las NPs.

Por otro lado, para obtener una visión más completa de las propiedades magnéticas y estructurales de las NPs, y en particular para avanzar en temas relevantes aún en discusión, como por ejemplo, la respuesta dinámica y los efectos de la frustración magnética o las interacciones entre partículas, es de gran utilidad la combinación de técnicas experimentales que permitan la caracterización del sistema cubriendo desde la escala macroscópica hasta el nivel nanométrico.

Dentro de este contexto, se presenta este trabajo, el cual está dividido en tres partes. En primer lugar, se explicará el efecto de la concentración de algunos reactivos, comunmente utilizados en el método de la descomposición térmica, sobre las propiedades finales de NPs magnéticas basadas en óxidos de hierro. Los objetivos principales que se persiguen son optimizar el método de síntesis y conseguir un buen control de la estructura final del producto. En segundo lugar, se va a demostrar el papel de la nanoestructura en las propiedades finales de sistemas de NPs sintetizadas por estos métodos, prestando especial atención a la fuerte interrelación entre la estructura y la existencia de frustración magnética y a los efectos relacionados con las interacciones entre NPs. Finalmente, se describirán los resultados experimentales obtenidos mediante Microscopía de Fuerzas Magnéticas (MFM) con un campo magnético externo aplicado que tienen

como finalidad la observación de la inversión de la magnetización en partículas aisladas y pequeños agregados de las mismas.

Se ha estudiado el efecto de la concentración de algunos reactivos presentes en la descomposición térmica de los precursores órgano-metálicos sobre el magnetismo y la estructura de NPs de composición MFe_2O_4 (con M = Co, Fe). Además, este trabajo se ha completado con el estudio detallado del mecanismo de reacción a partir de medidas de absorción (FTIR) de diferentes alícuotas de la mezcla de reacción, recogidas a lo largo del proceso de reacción.

En primer lugar, NPs monodispersas de $Fe_{3-x}O_4$ con una amplia gama de tamaños, de entre 7 y 100 nm, se han sintetizado con la simple modificación de la cantidad de ácido oleico en la mezcla de reacción, utilizando como disolvente bencil-éter. La caracterización estructural y magnética de las muestras indica que las NPs son monofásicas, altamente cristalinas y con valores de la magnetización de saturación cercanos a los del material masivo. También se constata la observación de la típica transición de Verwey asociada a una composición muy próxima a la estequiométrica del material. Por lo tanto, estos resultados confirman la alta calidad de las partículas obtenidas por este método. Además, el estudio por espectroscopia de FTIR indica que la temperatura de nucleación depende fuertemente de la cantidad de ácido oleico presente en la mezcla de reacción. Al aumentar la concentración de ácido oleico, también aumenta la temperatura de nucleación, lo cual permite controlar el proceso de crecimiento y en definitiva, el tamaño final de las NPs.

En segundo lugar, hemos demostrado el papel clave del 1,2-hexadecanodiol en la calidad cristalina de las NPs de $CoFe_2O_4$ mediante la variación de la concentración de este reactivo en la mezcla de reacción. Aunque todas las muestras exhiben NPs monofásicas, con similares estequiometrías y tamaños de partículas, la calidad cristalina final de las NPs se incrementa de manera gradual con la adición de una cantidad cada vez mayor de 1,2-hexadecanodiol en la mezcla de reacción. De esta forma, es posible controlar la estructura de las NPs para obtener desde partículas formadas por pequeños cristales que muestran un comportamiento típico de vidrio magnético hasta NPs altamente cristalinas con un comportamiento ferrimagnético muy parecido al del material masivo. El análisis de los espectros de FTIR ha demostrado que el contenido de 1,2-hexadecanodiol en la mezcla de reacción favorece la descomposición de los acetilacetonatos de Fe y Co y la formación de un oleato mixto de Co^{2+} y Fe^{3+}, disminuyendo así la temperatura a la cual se inicia la nucleación de las NPs. Estos resultados podrían ser útiles para diseñar las propiedades magnéticas de las NPs de acuerdo a los requerimientos de una aplicación específica.

En una segunda fase de este trabajo, se han comparado las propiedades estructurales y magnéticas de tres muestras de ferrita de cobalto constituidas por NPs con un tamaño medio de 8 nm que fueron sintetizadas mediante el mismo método descrito con anterioridad. Aunque las tres muestras mostraban similar estequiometría, distribución de tamaños y eran incluso monofásicas, se han observado propiedades magnéticas fuertemente dependientes de la calidad cristalina de cada muestra, que van desde NPs perfectamente ferrimagnéticas a muestras con comportamiento de tipo vidrio de espines.

El efecto de las interacciones entre partículas ha sido investigado en muestras compuestas de NPs de $Fe_{3-x}O_4$ con tamaños medios de 5 y 14 nm, que fueron recubiertas con ácido oleico o sílice. En primer lugar, se ha observado una fuerte reducción en las interacciones entre partículas mediante el recubrimiento de las NPs individuales con una corteza gruesa de SiO_2. Por otra parte, se ha demostrado que puede obtenerse la anisotropía intrínseca de las NPs mediante medidas de susceptibilidad transversa, incluso en muestras con fuertes interacciones entre partículas. El estudio se ha complementado con resultados experimentales junto con simulaciones numéricas que muestran que el campo dipolar medio que actúa sobre cada partícula se reduce cuando las magnetizaciones de las partículas se alinean por la acción de un campo externo. Basándonos en estos resultados, hemos desarrollado un método general para la cuantificación de las interacciones dipolares en conjuntos de NPs. Este método consiste en la comparación de las distribuciones de barreras de energía para la inversión de la magnetización, obtenidas a partir de configuraciones de las NPs correspondientes a la disposición aleatoria de los ejes de anisotropía o a una configuración con las magnetizaciones de las partículas orientadas a lo largo de un campo externo. . Además. la distribución intrínseca de las barreras de energía de anisotropía de las NPs no interactuantes se evaluó a partir de una muestra que contenía las NPs recubiertas individualmente con una corteza de sílice.

Finalmente, se ha estudiado la inversión de la magnetización de NPs de $Fe_{3-x}O_4$, tanto en NPs individuales, como en pequeños grupos de NPs, mediante MFM y un campo magnético variable (VM) externo. Los resultados han sido contrastadas con simulaciones magnéticas llevadas a cabo con el programa OOMF.

Las configuraciones de dominio en NPs cúbicas, altamente cristalinas, de $Fe_{3-x}O_4$, de 27 nm de tamaño medio, se han podido observar directamente. Las estructuras de dominios mostradas (orientación y polaridad) fueron asociadas al eje fácil de imanación de las NPs asociado a la anisotropía magnetocristalina. La interpretación de estos resultados fue confirmada mediante cálculos micromagnéticos de NPs individuales en

similares condiciones (tamaño, mismo material, mismo rango de campo magnético aplicado) a las de las NPs reales. Como resultado principal, hemos sido capaces de observar directamente la orientación de los ejes fáciles asociados a la anisotropía magnetocristalina en NPs individuales ferrimagnéticas.

Por otro lado, se ha utilizado el MFM con el fin de poder distinguir entre los estados bloqueado y superparamagnético en pequeños grupos de NPs con alta calidad cristalina. Los agregados constituidos por NPs de 11 nm de tamaño aproximado mostraron un contraste oscuro uniforme en las imágenes de MFM, que refleja el carácter superparamagnético predominante en estas NPs y que es debido a la rotación coherente de los espines siguiendo el movimiento de la punta. Gracias a la aplicación de un campo magnético variable en el plano ha sido posible inducir una polarización magnética que produce un aumento en el contraste oscuro/brillante debido a que la interacción con el campo aplicado es superior a la interacción con el campo producido por la punta. Por el contrario, en los agregados de las NPs de 49 nm de tamaño, el contraste oscuro/ brillante se ha asociado a la existencia de dominios magnéticos ya que la polarización magnética prevalece en las imágenes de MFM a lo largo de todo el ciclo magnético debido al estado de bloqueo de la magnetización de estas NPs, incluso en ausencia de un campo aplicado.

.

Publications:

1 A. I. Figueroa, C. Moya, J. Bartolomé, F. Bartolomé, L. M. García, N. Pérez, A. Labarta and X. Batlle, *Nanotechnology*, 2013, **24**, 155705.

2 C. Moya, Ó. Iglesias-Freire, N. Pérez, X. Batlle, A. Labarta and A. Asenjo*, Nanoscale*, 2015, **7**, 8110.

3 C. Moya, G. Salas, M. del P. Morales, X. Batlle and A. Labarta, *J. Mater. Chem. C*, 2015, **3**, 4522.

4 C. Moya, M. del P. Morales, X. Batlle and A. Labarta, *Phys. Chem. Chem. Phys.*, 2015,**17**, 13143.

5 C. Moya, X. Batlle and A. Labarta, *Phys. Chem. Chem. Phys.*. Accepted on September 15th.

6 C. Moya, Ó. Iglesias-Freire, X. Batlle, A. Labarta and A. Asenjo. Submitted to *Nanoscale*.

7 C. Moya, Ó. Iglesias, X. Batlle and A. Labarta. *Journal of Physical Chemistry C*. Accepted on September 17th.

Other Publications:

8 C. López, A. González, C. Moya, R. Bosque, X. Solans and M. Font-Bardía, *J. Organomet. Chem.*, 2008, **693**, 2877.

9 C. López, C. Moya, P. K. Basu, A. González, X. Solans, M. Font-Bardía, T. Calvet, E. Lalinde and M. Teresa Moreno, *J. Mol. Struct.*, 2011, **999**, 49.